



TOR VERGATA
UNIVERSITÀ DEGLI STUDI DI ROMA

DOTTORATO DI RICERCA IN FISICA

CICLO DEL CORSO DI DOTTORATO XXXIII

Search for flavour-changing neutral-current top quark decays to c-quark and Z boson using the ATLAS detector at the LHC

LORENZO MARCOCCIA

A.A. 2020/2021

DOCENTE GUIDA: Prof. LUCIO CERRITO

COORDINATORE: Prof. ROBERTO BENZI

A dissertation submitted to the University of Rome Tor Vergata in accordance with the requirements of the degree of DOCTOR OF PHILOSOPHY in the Department of Physics.

Ringraziamenti

Abstract

The main focus of this thesis is the search for the $t \rightarrow Zc$ process in the proton–proton collisions data collected by the ATLAS detector at the Large Hadron Collider located at CERN.

The flavour-changing neutral-current (FCNC) processes are forbidden at tree-level and highly suppressed at loop-level which is why they are very rare phenomena in the Standard Model of particle physics. However, this processes have an higher probability to occur in several theories beyond the Standard Model where the suppression could be relaxed and the loop diagrams mediated by new bosons could contribute.

The FCNC top-quark decays $t \rightarrow Zc$ are searched in $t\bar{t}$ pair events with one top quark decaying through the $t \rightarrow Zc$ channel and the other through the dominant Standard Model mode $t \rightarrow Wb$. The analysed data were recorded at a center-of-mass energy of 13 TeV and correspond to the full Run-2 dataset with an integrated luminosity of 139 fb^{-1} .

The data are consistent with Standard Model background contributions, and, at 95% confidence level the search sets observed (expected) upper limits of 11.8×10^{-5} (9.5×10^{-5}) on the $t \rightarrow cZ$ branching ratio, constituting the most stringent limit to date and improving the previous ATLAS results by a factor of 2 (3.4).

Contents

Abstract	iii
Contents	v
Introduction	1
1 Motivation and theory framework	3
1.1 The gauge principle in quantum field theory	3
1.1.1 Quantum Chromodynamics	5
1.1.2 The electro-weak sector	6
1.2 Top quark physics	9
1.2.1 Production	9
1.2.2 Decay channels	10
1.3 Physics motivation	11
1.4 Theories for physics beyond the Standard Model	12
1.4.1 Quark singlets	14
1.4.2 Two Higgs Doublet Model	15
1.4.3 Minimal Supersymmetric Standard Model	16
2 The LHC accelerator and the ATLAS experiment	18
2.1 The LHC accelerator	19
2.2 The ATLAS detector	23
2.2.1 Magnet System	24
2.2.2 Inner Detector	24
2.2.3 Calorimetric System	25
2.2.4 Muon Spectrometer	27
2.2.5 Trigger and Data Acquisition	29

3 The Trigger system upgrade for High-Luminosity LHC	30
3.1 ATLAS Barrel Muon Trigger	31
3.2 BI upgrade for Phase-II	34
3.2.1 RPC upgrade	37
3.2.2 Trigger scheme	39
3.3 Hit digitization in the BI region	41
3.3.1 The cluster size model	41
3.3.2 Timing	47
3.4 L0 barrel trigger efficiency	48
3.4.1 BM and BO retrofitting	49
3.4.2 Dropping BIR and BIM chambers	52
3.5 Summary and considerations	54
4 Data modeling and object reconstruction	55
4.1 Event simulation	55
4.2 Object reconstruction	57
4.2.1 Electrons	57
4.2.2 Muons	57
4.2.3 Jets	59
4.2.4 Soft Muon Tagging	59
4.2.5 Recurrent Deep-Learning DL1 _r	59
4.2.6 Missing transverse momentum	60
4.2.7 Overlap removal	60
5 Analysis strategy, "Data and Monte Carlo samples"	61
5.1 Analysis strategy	61
5.2 Data and Monte Carlo samples	63
5.2.1 Data sample	64
5.2.2 Monte Carlo simulated samples	65
6 Search for FCNC t → Zc	70
6.1 Event selection and reconstruction	70
6.1.1 Top quarks reconstruction	71
6.1.2 Main sources of background	72
6.2 Signal Region with SMT requirement	73
6.2.1 Reconstruction of the soft muon decay chain	76
6.3 Separation of signal from background events	78
6.3.1 Input variables	78
6.3.2 GBDT training and evaluation	80
6.3.3 GBDT performance and overtraining checks	80
6.4 The alternative selection using the c-tagger DL1 _c	84
6.5 Additional Signal Regions	87
6.5.1 SR1tZc selections	87
6.5.2 SR2tZc selections	87
6.5.3 Orthogonality between Signal Regions	88
6.5.4 Event yields in the Signal Regions	90
6.6 Background estimation	91

6.6.1	Control Regions definition	91
6.6.2	Event yields in the Control Regions	93
6.7	Separation of signal from background events using DL1 r_c	93
7	Extraction of the limit on the branching ratio $t \rightarrow Zc$	95
7.1	Systematic uncertainties	95
7.1.1	Sources of systematic uncertainties	95
7.1.2	Acceptance and shape uncertainties	99
7.2	Fit strategy	100
7.3	Summary of fits	102
7.4	Signal + Background fit in SRs+CRs with realistic Asimov data	102
7.5	S+B fit in SRs+CRs with unblinded data	115
7.6	Results	126
Conclusions		128
Appendix A Monte Carlo samples		129
Appendix B Mass Resolution		132
Appendix C Charm tagging using DL1r		134
Appendix D BDT optimization		136
D.1	Input variables	137
D.2	Hyper-parameters optimisation	143
Appendix E Kinematic distributions in the Signal Regions		144
E.1	SR1tZc	145
E.2	SR2tZc	147
E.3	SR3tZc	149
Appendix F Kinematic distributions in the Control Regions		151
F.1	t̄t CR	152
F.2	t̄tZ CR	154
F.3	Side-band CR1	156
F.4	Side-band CR2	158
Appendix G Background only fit in CRs		160
Appendix H Signal + Background fit in SRs+CRs using SMT		168
Appendix I Background-only fit in SRs+CRs with unblinded data		181
References		193

Introduction

Developed between the late 1960s and the mid-1970s, the standard model (SM) of particle physics represents our best understanding of physics phenomena at the most fundamental scales. It provides a unified picture for all known elementary particles and the way they interact via 3 of the 4 fundamental forces.

Over the decades, the SM has been tested extensively by a broad variety of experiments. It is able to successfully explain almost all experimental results over a wide energy range, at times with a precision unmatched in any other field of physics. However, the SM is not the ultimate "theory of everything", there are some critical points that arise both from theoretical considerations and experimental results that does not fit in the SM and may indicate a presence of new physics Beyond the Standard Model (BSM).

Many are models of "new physics" that attempt to describe and explain these phenomena. One way to test these models and to search for new physics is through the study of the top-quark, the heaviest elementary particle predicted by the Standard Model and discovered in 1995 by the CDF and DØ experiments at the Tevatron collider.

In the SM, top quark decays almost exclusively into bW , while flavour-changing neutral current (FCNC) decays, such as $t \rightarrow Zc$, are forbidden at tree level. FCNC decays occur at one-loop level but are strongly suppressed by the GIM mechanism, with a suppression factor of 14 orders of magnitude relative to the dominant decay mode. However, in the BSM models, the suppression could be relaxed and the loop diagrams mediated by new bosons that could contribute, leading to couplings of many orders of magnitude higher than those expected by the SM. Therefore, any significant signal of top-quark FCNC decays will indicate the existence of new physics.

In this thesis, a search for FCNC top-quark decays in a c-quark and a Z boson is presented taking into account also the FCNC process of production of a single top-quark in association with a Z boson. The analysed data were recorded at a center-of-mass energy of 13 TeV by the ATLAS detector at the Large Hadron Collider located at CERN and correspond to the full Run-2 dataset with an integrated luminosity of 139 fb^{-1} .

Additional work, concerning the ATLAS detector development, will also be presented in this thesis. The goal of this work was the development of a new model for the Resistive Plate Chambers (RPC) detectors in the Barrel Inner (BI) region and, using this model, to perform trigger efficiency studies that will help to plan the work for the Phase-II upgrade (2024-2025) that will lead LHC to High-Luminosity LHC (HL-LHC).

My original contributions presented in this thesis include:

- the construction of a model implementing a realistic digitization in the BI region, and some performance studies for the L0 barrel trigger;
- the definition and optimisation of SR3tZc, and the investigation of the best c-tagging technique for this analysis;
- the determination of the backgrounds in SR3tZc, and the separation of signal from background events using a multivariate analysis;
- the full design of the analysis, including the fit strategy and the extraction of the signal limit.

This thesis is organised as follows. The SM is introduced in Chapter 1, including a more detailed discussion on some BSM theories that have predictions on the FCNC top decay. In Chapter 2 the LHC accelerator and the ATLAS detector are presented. A brief description of the trigger system for HL-LHC is given in Chapter 3 together with the studies performed for the Phase-II upgrade. In Chapter 4 the data modelling and the object reconstruction is presented. Chapter 5 describes the analysis strategy developed for the search for FCNC couplings between top-quark and Z boson. Chapter 6 is devoted to the main analysis, with the description of Signal and Control Regions used for the statistical analysis described in Chapter 7 in order to extract the observed upper limits at 95% confidence level (CL) for the FCNC $t \rightarrow Zc$ process.

CHAPTER 1

Motivation and theory framework

The construction of the Standard Model is the result of a long series of experiments and brilliant ideas in both theoretical and experimental fields. Towards the end of the 1960s, knowledge of what we consider to be the constituent elements of nature and the fundamental interactions among them, was organised in the so-called Standard Model (SM).

More recently, a missing piece towards the completion of the SM, the Higgs boson, was discovered by the ATLAS and CMS collaborations.

The ambition is to find a theoretical representation of all phenomena experimentally accessible. Since particle physics is characterized by phenomena that are both relativistic than quantistic, the description of the Standard Model relies on the formalism of *Quantum Field Theories* (QFT), synthesis of quantum mechanical and relativistic theory. In these terms, the concept of field is associated both to material particles and to forces. Particles are mere manifestations of fields: they are identified with the quanta of the material fields and force fields and the interaction among particles is determined by the exchange of virtual quanta of the field.

To search for extensions of the SM, it is possible to postulate a scale of the new physics high enough to manifest itself through deviations of known observables, usually at high energies.

In this chapter, a concise description of the SM will be presented, from the gauge principle to the description of several theories of physics beyond the Standard Model which are crucial for the search of FCNC decay of the top quark.

1.1 The gauge principle in quantum field theory

The mathematical framework of the SM is based on a quantum field theory description of the particles and their interactions. The structure is a consequence of the invariance of physics under certain general symmetries: these invariances are called *gauge* because there is freedom in the choice of a certain number of parameters that can precisely "calibrate" the model. Each symmetry

is therefore associated with a set of transformations that frame the "gauge group of the theory". The theory is introduced starting from the Lagrangian formalism developed in the classical mechanism, extending this formalism to classical field theory and finally to quantum field theory.

Lagrangian is defined as the difference between the kinetic energy and the potential energy of the system, as below:

$$\mathcal{L}(q, \dot{q}) = \frac{m}{2}(\dot{q})^2 - V(q) \quad (1.1)$$

where q is a set of generalized coordinates and m is the mass of the particle.

The *action* is defined as $S = \int dt \mathcal{L}(q, \dot{q})$.

Using a variational approach it can be shown that for any possible variation of the path of the particle, $\partial(q)$, the equation of motion of the system is the one that minimizes the *action*. The results are the so called *Euler-Lagrange* equations:

$$\frac{\partial \mathcal{L}}{\partial q} - \frac{d}{dt} \left(\frac{\partial \mathcal{L}}{\partial \dot{q}} \right) = 0 \quad (1.2)$$

The next step is the extension of the classical mechanics formalism to field theory. One possible way is to generalize the path of a particle which is a function of time $q(t)$, into a function of space-time coordinates $\phi(x)$ which is the vectorial (or tensorial) representation of the field with Lorentz invariance properties of the space-time.

The sub-set of dimension-four vectorial representations used in particle physics is called spinors and they can be decomposed into left-handed and right-handed components, depending on their chirality: ψ_L and ψ_R . The usual representation for Lorentz and parity transformations is the *Dirac* spinor $\Psi = (\psi_L, \psi_R)$, which allows describing properly the dynamics of relativistic particles.

At this point, the Lorentz-invariant Lagrangian is the following:

$$\mathcal{L}_D = \bar{\Psi}(i\gamma^\mu \partial_\mu - m)\Psi \quad (1.3)$$

where γ are an extension of the Pauli matrices into a four dimension space and they are called Dirac matrices.

The QFT is also built on the *Noether's* theorem that relates symmetries of the system to conserved observables.

Through this theorem, symmetries become a fundamental building block of the physical theory. A particular set of transformations, called gauge transformations, which by construction leave invariant the Lagrangian of the SM, constitute a building principle of the SM itself.

Let us now consider the global $U(1)^1$ transformation of the form:

$$\Psi \rightarrow e^{i\theta}\Psi \quad (1.4)$$

It can be easily demonstrated that \mathcal{L}_D is invariant under such a transformation and the related conserved observable is the current $\bar{\Psi}\gamma^\mu\Psi$.

¹ $U(1)$ is the one-dimensional unitary group, i.e. any of its elements can be expressed as a 1×1 matrix whose inverse is equal to its transpose conjugate ($U^{-1} = \bar{U}^*$).

However, the Lagrangian is no longer invariant under the transformation: $\theta \rightarrow \theta(x)$ which means that the gauge invariance is required in each point of the space-time.

The inclusion of an additional field, the photon, which mediates the forces, makes the Lagrangian explicitly invariant and it allows to choose a *gauge* of the theory, in fact the action of free electromagnetic field is invariant under $A_\mu \rightarrow A_\mu - \partial_\mu \theta$, with A_μ being the four-vector of the electrostatic and magnetic potential: (V, \vec{A}) .

The above example is useful to understand how the SM is constructed. It is a gauge theory which, analogously to what described in this section, is invariant under:

$$SU(3)_c \otimes SU(2)_L \otimes U(1)_Y \quad (1.5)$$

The $SU(3)_c$ describes the strong force (see next section) while $SU(2)_L \otimes U(1)_Y$ term describes the electro-weak sector (see Section 1.1.2). A more detailed discussion follows.

1.1.1 Quantum Chromodynamics

The strong interaction between quark and gluons is described by the *Quantum Chromodynamics* (QCD). It is a gauge theory based on non-abelian $SU(3)_c$ ² and associated to the three colour charges (red, green and blue). A total number of 8 generators T^a of the group, also called Gell-Mann matrices, represent bosons mediating the force, called *gluons*. They are massless, in contrast with the weak mediators.

The QCD Lagrangian, can be expressed as:

$$\mathcal{L}_{QCD} = \bar{\psi}(i\gamma^\mu D_\mu - m)\psi - \frac{1}{4}G_{\mu\nu}^a G_a^{\mu\nu} \quad (1.6)$$

where the index a represents the 8 $SU(3)_C$ generators, $\frac{1}{4}G_{\mu\nu}^a G_a^{\mu\nu}$ is the kinetic term of the gluons (G^a is the gluon field strength tensor) and the covariant derivative D_μ is defined as

$$D_\mu = \partial_\mu - ig_s T_a G_\mu^a \quad (1.7)$$

The coupling constant α_s ($\frac{g_s^2}{4\pi} \sim 1$), is dependent on the transferred momentum Q^2 that corresponds to a dependence on the separation between quarks:

$$\alpha_s(Q^2) = \frac{33 - 2n_f}{12\pi} \ln \left(\frac{Q^2}{\Lambda_{QCD}^2} \right) \quad (1.8)$$

where n_f is the number of quark flavours and Λ_{QCD}^2 is the QCD scale parameter, measured to be ~ 200 MeV that sets the scale between different regimes of the theory.

In fact one can discern two cases:

$$\alpha_s(Q^2) \xrightarrow[Q^2 \gg \Lambda_{QCD}^2]{} 0$$

²S stands for "special", meaning that the group matrices have determinant 1. C stands for "colour", which is the conserved quantity associated with the symmetry

$$\alpha_s(Q^2) \xrightarrow[Q^2 \ll \Lambda_{QCD}^2]{} \infty$$

In the first case, the quark coupling is asymptotically cancelled, in the limit $Q^2 \rightarrow \infty$, quarks can be considered as free particles and this phenomena is called *Asymptotic Freedom*. On the contrary, when the separation becomes relevant, the coupling is so strong to confine quarks in hadronic structures and this different phenomena is called *Confinement*. The only bound states that occur are completely antisymmetric in the colour variables (the colour singlets), which is equivalent to saying that the possible compositions of quarks must be "white".

Interaction between particles that carry charges of colour, takes place through the exchange of gluons of the octet, therefore, not only between quarks and gluons but also between gluons and gluons. This is a very important difference between QED (*Quantum Electrodynamics*) and QCD. In QED, in fact, photons have no charge and cannot couple with each other.

1.1.2 The electro-weak sector

The first model of the weak interaction was proposed by Fermi in 1933, who proposed an effective field theory at low energies. According to this theory, charged current interactions are approximated by a point-like interaction with a coupling called G_F [1, 2]. At energies $\mathcal{O}(100 \text{ GeV})$ the theory breaks and the real propagator of the interaction is the W^\pm boson.

In 1957, a famous experiment conducted by Wu [3] proved that parity is maximally violated by the charged weak interaction: it only couples to particles of left-handed chirality (and antiparticles of right-handed chirality). There also exists a neutral weak interaction, which couples both to left-handed and right-handed particles.

This discovery motivated the introduction of the vector-axial (V-A) structure of the Lagrangian of the weak force.

The model of the weak interaction was subsequently promoted to a gauge theory by requiring local invariance under symmetries of the $SU(2)$ group, and it was associated with a conserved quantity called the *weak isospin*.

Each generation of left-handed fermions forms a doublet satisfying $I_3 = \pm \frac{1}{2}$, while right-handed fermions correspond to singlets of null isospin, as follows:

$$\chi_L = \begin{pmatrix} \nu_l \\ l \end{pmatrix}_L \quad l_R \quad (1.9)$$

where $l = (e, \mu, \tau)$, and a right-handed neutrino singlet is not introduced since there is still no observation of such a particle. A similar representation is given for quarks where both up (u, s, t) and down-types (d, c, b) have a right-handed component, singlet under $SU(2)_L$.

The transitions between quark doublet members corresponds to $SU(2)$ raising (τ^+) and lowering (τ^-) operators, giving the charge raising and lowering currents [4]:

$$J^+ \sim g(\bar{u} d_c) = g(\bar{u} \bar{d}_c) \begin{pmatrix} 0 & 1 \\ 0 & 0 \end{pmatrix} \begin{pmatrix} u \\ d_c \end{pmatrix} = g(\bar{q} \tau^+ q) \quad (1.10)$$

$$J^- \sim g(\bar{d}_c u) = g(\bar{u} \bar{d}_c) \begin{pmatrix} 0 & 0 \\ 1 & 0 \end{pmatrix} \begin{pmatrix} u \\ d_c \end{pmatrix} = g(\bar{q} \tau^- q)$$

where overall numerical factors have been omitted, d-quark is 'Cabibbo-rotated' ($\theta_c \sim 13^\circ$) and g is the dimensionless weak coupling constant and quarks.

If there exist an appropriate symmetry, based on some underlying gauge theory, then a current involving τ_3 is also expected, since these operators are related via the commutation relation $[\tau^+, \tau^-] = 2\tau_3$. Hence, with such a gauge theory symmetry, one would expect the existence of a neutral current (identified by the Z^0 boson) of the form :

$$\begin{aligned} J^0 &\sim 2g(\bar{q}\tau_3q) = g(\bar{u}u - \bar{d}_c d_c) \\ &= g[\bar{u}u - \bar{d}_c d \cos^2 \theta_c - \bar{s}_c s \sin^2 \theta_c - (\bar{d}s + \bar{s}d) \cos \theta_c \sin \theta_c] \end{aligned} \quad (1.11)$$

The terms $\bar{d}s$ and $\bar{s}d$ correspond to strangeness-changing neutral currents (SCNC), which are heavily suppressed in nature.

For example, the decay branching ratio $K^+ \rightarrow \mu^+ \nu_\mu$ is 63.5%, whereas that for $K_L^0 \rightarrow \mu^+ \mu^-$ is $\sim 10^{-8}$.

A mechanism to suppress this unwanted strangeness-changing neutral currents was suggested in 1970 by Glashow, Iliopoulos and Maiani (GIM) and it will be described in the next section.

1.1.2.1 GIM mechanism

Until the beginning of the 1970s, the only three light quarks u, d and s known at this time could explain the observed hadron spectrum, and the observed weak decays of pions and kaons were mostly in good agreement with the predictions of the *Cabibbo mechanism*. Glashow, Iliopoulos and Maiani proposed the existence of a second orthogonal doublet, additional to $(\frac{u}{d_c})$, containing a new quark c (charm) with charge $\frac{2}{3}$, as follows [5]:

$$q' = \begin{pmatrix} c \\ s_c \end{pmatrix} = \begin{pmatrix} c \\ -d \sin \theta_c + s \cos \theta_c \end{pmatrix} \quad (1.12)$$

Adding this term gives the total neutral current:

$$\begin{aligned} J^0 &\sim 2g(\bar{q}\tau_3q + \bar{q}'\tau_3q') = g(\bar{u}u + \bar{c}c - \bar{d}_c d_c - \bar{s}_c s_c) \\ &= g[\bar{u}u + \bar{c}c - \bar{d}d - \bar{s}s] \end{aligned} \quad (1.13)$$

That is, the unwanted terms cancel, leaving a flavour diagonal result.

The GIM mechanism gives also the prediction of the charmed quark, before the J/Ψ discovery occurred in 1974.

In the three-quarks picture, and according to the Cabibbo mechanism alone, $s \rightarrow d$ transitions via *Flavour Changing Neutral Current* FCNC processes would be possible at all orders of the perturbation expansion.

For example, the process $K_L^0 \rightarrow \mu^+ \mu^-$ FCNC decay could take place, in terms of known quark (u and d-quarks), via the "box-diagram" of Figure 1.1(a).

The calculated rate is larger than what was observed experimentally.

However, including the diagram of Figure 1.1(b), the total amplitude is:

$$\mathcal{M} = \mathcal{M}_{(a)} + \mathcal{M}_{(b)} \sim f(m_u)g^4 \cos \theta_c \sin \theta_c - f(m_c)g^4 \cos \theta_c \sin \theta_c \quad (1.14)$$

Thus, the c-quark induces a cancellation, giving a BR compatible with the experiments, but not a total cancellation because $m_c \neq m_u$. Hence, the prediction on the mass of the c-quark that in the end is ~ 3 GeV. In addition to this major prediction, the GIM mechanism led to the prediction

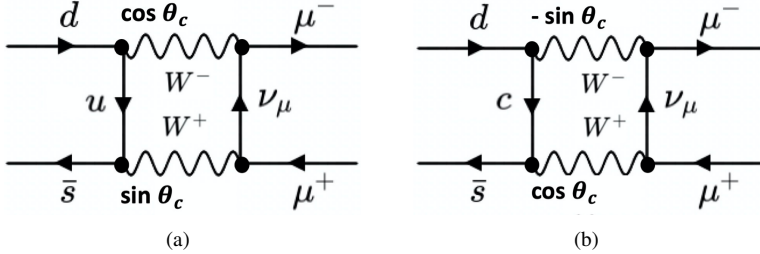


Figure 1.1 – Feynman diagrams of $K_L^0 \rightarrow \mu^+ \mu^-$ via (a) u-quark exchange and (b) c-quark exchange

that FCNC processes are forbidden at tree-level Leading Order. The branching ratios of several FCNC decays of the top quark in the SM are given in Table 1.1. The FCNC production is also

	$t \rightarrow uZ$	$t \rightarrow c\bar{Z}$	$t \rightarrow u\gamma$	$t \rightarrow c\gamma$	$t \rightarrow ug$	$t \rightarrow cg$	$t \rightarrow uH$	$t \rightarrow cH$
BR	8×10^{-17}	1×10^{-14}	3.7×10^{-16}	4.6×10^{-14}	3.7×10^{-14}	4.6×10^{-12}	2×10^{-17}	3×10^{-15}

Table 1.1 – Branching ratios for top quark FCNC interactions in the SM [6].

sensitive to numerous new physics models, as is mentioned in more details in Section 1.4. The GIM hypothesis represents a generalization of Cabibbo's idea. The introduction of the fourth quark (c) restored the symmetry in the (then known) numbers of quark and leptons. These ideas were extended by Kobayashi and Maskawa (1973), who introduced a framework of six quarks and it will be described in the next section.

1.1.2.2 CKM matrix

In 1973 Kobayashi and Maskawa extended the Cabibbo's mechanism allowing to describe the transitions within and in-between 3 generations of quarks using the so-called CKM 3×3 matrix [7, 8], which relates the weak eigenstate of down-type to their mass eigenstate:

$$\begin{pmatrix} d' \\ s' \\ b' \end{pmatrix} = V_{CKM} \begin{pmatrix} d \\ s \\ b \end{pmatrix} = \begin{pmatrix} |V_{ud}| & |V_{us}| & |V_{ub}| \\ |V_{cd}| & |V_{cs}| & |V_{cb}| \\ |V_{td}| & |V_{ts}| & |V_{tb}| \end{pmatrix} \begin{pmatrix} d \\ s \\ b \end{pmatrix} \quad (1.15)$$

By convention, the up-type quarks are taken to be pure states. Therefore, partners of the up-type quarks within the weak isospin doublets are the weak eigenstates d' , s' and b' which are the pure states.

The CKM matrix is fully defined by 4 independent parameters, which must be determined experimentally. These parameters are: 3 mixing angles and 1 CP-mixing phase, which violates the CP³ symmetry in the SM [9]. The diagonal elements of the CKM matrix are close to 1, reflecting

the fact that transitions are favoured between quarks of the same generation. The CKM matrix is unitary, i.e. the sum of the transition probabilities for any quark flavour is equal to 1. If this assumption was to be disproved, it could imply the existence of a fourth quark generation.

1.2 Top quark physics

The heaviest known elementary particle described by the Standard Model is the top quark. In 1995, the top quark discovery at FERMILAB [10, 11] was a great success for the SM predictions e.g. the corroboration of existence of a weak isospin partner of the top quark. Due to its large mass, the predicted lifetime $\tau_t \approx 5 \times 10^{-25}$ s (in agreement with theoretical expectations [12]) entail that it decays before hadronising.

In the next sections, the production mechanism is reported, as well as an overview of the decay channels.

1.2.1 Production

The top quark can either be produced as pairs, via strong interaction, or as a single top quark via electroweak interaction that does not preserve the flavour.

The main parton sub-processes that lead to top-pair production are the quark-antiquark annihilation ($q\bar{q} \rightarrow t\bar{t}$, Figure 1.2(a)) and the gluon-gluon fusion ($gg \rightarrow t\bar{t}$, Figures 1.2(b) and 1.2(c)).

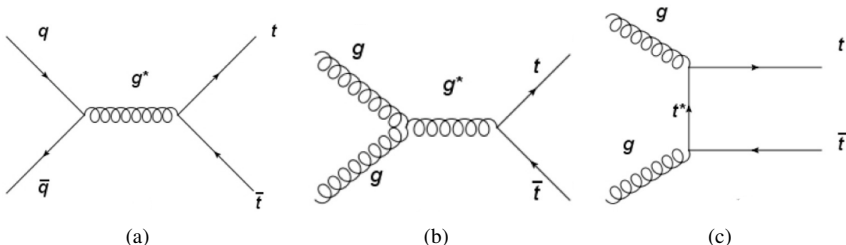


Figure 1.2 – Feynman diagrams of $t\bar{t}$ production via (a) quark-antiquark annihilation ($q\bar{q} \rightarrow t\bar{t}$), (b) and (c) gluon-gluon fusion ($gg \rightarrow t\bar{t}$)

Since in protons there are no valence antiquarks, the quark-antiquark annihilation is suppressed by the parton distribution functions (PDF) of the antiquark in the proton. Therefore, at the LHC the dominant process turns out to be the gluon-gluon fusion, while in a proton-antiproton collider, such as Tevatron, the dominant process is the quark-antiquark annihilation, in fact:

- Tevatron: $q\bar{q} \rightarrow t\bar{t} \approx 86\%$, $gg \rightarrow t\bar{t} \approx 15\%$
- LHC: $q\bar{q} \rightarrow t\bar{t} \approx 20\%$, $gg \rightarrow t\bar{t} \approx 80\%$

³Charge transformation followed by a parity transformation.

Top-pairs can be produced also by the weak interaction when two quarks exchange Z^0 or a γ ; however the cross-section of these type of processes is negligible when compared to the production cross-section through strong interaction.

Although at the LHC the top quarks are mainly produced in the process described above, a not negligible number of tops are produced singly by weak interaction. The production cross section, in this case, is equal to approximately 1/3 of the top-pair production cross-section, which is $\sigma_{t\bar{t}} = 831.8^{+19.8+35.1}_{-29.2-35.1} \text{ pb}$ [13], at $\sqrt{13} \text{ TeV}$ and taking into account a top quark mass of 172.5 GeV.

1.2.2 Decay channels

Since the top quark mass is larger than the W boson mass, the top decays through the weak interaction, mainly in to $t \rightarrow W^+ b$; according to the SM in 100% of the possible cases.

The other channels ($t \rightarrow W^+ s$, $t \rightarrow W^+ d$) are strongly suppressed by the CKM matrix elements (see Section 1.1.2.2). Exploiting the matrix unitarity and the B meson oscillation measurements, it is possible to extract the following BRs[14]:

$$\begin{aligned}\text{BR}(t \rightarrow W^+ b) &\sim 0.998 \\ \text{BR}(t \rightarrow W^+ s) &\sim 1.9 \cdot 10^{-3} \\ \text{BR}(t \rightarrow W^+ d) &\sim 10^{-4}\end{aligned}$$

Therefore, the top decay total width is given by, in good approximation, the decay ($t \rightarrow W^+ b$), thus equals to $\Gamma_t = 1.44 \text{ GeV}$. The W boson may decay in only two ways: "leptonically" ($W \rightarrow l\nu$) or "hadronically" ($W \rightarrow q\bar{q}'$). This leads to three different categories of $t\bar{t}$ decays: dileptonic, semi-leptonic or hadronic.

Figure 1.3 summarizes the BRs associated to each channel.

At hadron colliders, the dominant hadronic mode is the most difficult to isolate due to the large QCD background.

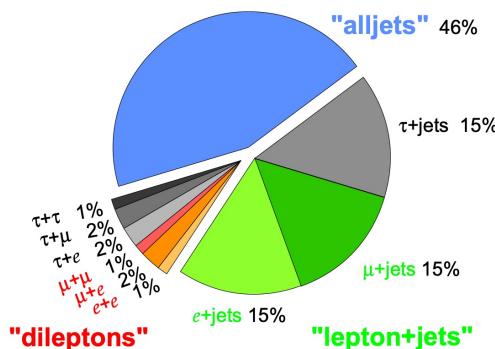


Figure 1.3 – Branching ratios associated to each $t\bar{t}$ decay channel [15].

1.3 Physics motivation

The heaviest particle in the Standard Model (SM), the top quark, decays almost exclusively to a W-boson and a bottom quark [16]. In proton–proton (pp) collisions, top quarks are produced dominantly in pairs, via the strong interaction, but also singly, via the electroweak interaction. Within the SM, "flavour-changing neutral-current" (FCNC) processes are forbidden at tree level due to the Glashow-Iliopoulos-Maiani mechanism [5] (see Section 1.1.2.1) and the approximate diagonality of the Cabibbo-Kobayashi-Maskawa matrix [16] causes the suppression of such processes at higher orders (see Section 1.1.2.2).

Nonetheless, there are several scenarios beyond the Standard Model (BSM) that can significantly enhance the FCNC processes in the top quark sector, opening a door for its detection at the Large Hadron Collider (LHC) [6, 17–21] and some of them will be discussed in Section 1.4.

The analysis presented in the following details a search for FCNC $t \rightarrow Zc$ decay.

In a model independent way, the anomalous couplings can be described by the so called effective field theory (EFT). This theory considers an extension of the SM Lagrangian \mathcal{L}_{SM} by operators in higher-dimensions of the mass, suppressed by the scale of new physics Λ as shown in Equation (1.16). Dimension-5 operators are not considered in this analysis due to the introduction of lepton-flavour violating processes. Therefore, the anomalous couplings can be approximated with dimension-6 operators $O_i^{(6)}$ whose strength is given by the Wilson coefficients $C_i^{(6)}$.

$$\mathcal{L} = \mathcal{L}_{SM} + \frac{1}{\Lambda^2} \sum_i C_i^{(6)} O_i^{(6)} \quad (1.16)$$

Experimental limit on the branching ratio of FCNC $t \rightarrow Zc$ decays was previously established by experiments at the Large Electron-Positron Collider (LEP) [22–25], the Hadron-Electron Ring Accelerator (HERA) [26], the Tevatron [10, 27] and the Large Hadron Collider (LHC) [28–30]. The ATLAS and the CMS collaborations obtained limits at the 95 % confidence level (CL) for this process using data collected at $\sqrt{s} = 13$ TeV and $\sqrt{s} = 8$ TeV, focusing on FCNC top-quark decays [28, 29], or both production and decay modes combined [30]. A summary of the ATLAS and CMS results on the limits on FCNC couplings is shown in Figure 1.4. The actual observed limits on the FCNC tZc coupling from ATLAS is $\text{BR}(t \rightarrow cZ) < 2.4 \times 10^{-4}$ [28].

Recent studies were done on the interference effects on the FCNC tZq and $t\gamma q$ couplings in single-top production and $t\bar{t}$ decay, concluding that these effects are smaller than the variations of the systematics uncertainties considered [31]. Therefore, both decay and production modes are taken into account in this analysis to improve the results on the limit for tZc anomalous coupling.

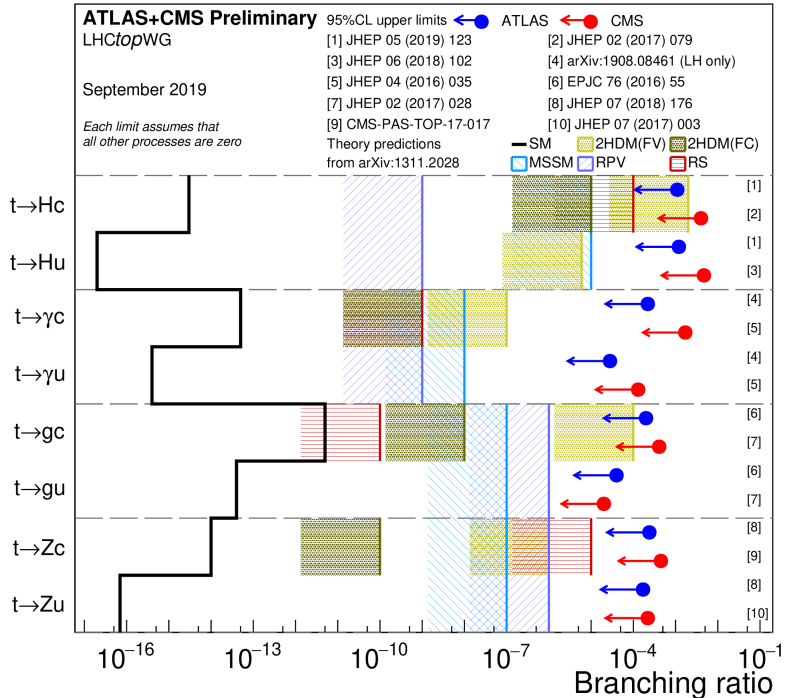


Figure 1.4 – Summary of the current 95% confidence level observed limits on the branching ratios of the top quark decays via flavour changing neutral currents to a quark and a neutral boson $t \rightarrow X q$ ($X = g, Z, \gamma$, or H ; $q = u$ or c) by the ATLAS and CMS Collaborations compared to several new physics models. The ATLAS limits on $t \rightarrow q$ are valid for the case of a purely left-handed coupling. Status of figure: September 2019 (Top2019)

1.4 Theories for physics beyond the Standard Model

The previous sections described the core components of what we call *Standard Model* and report few major successes of many. Its predictive power makes this model the most tested in physics and it reached the culmination of success on 4 July 2012, when the ATLAS and CMS experiments at CERN announced the observation a new particle in the mass region around 125 GeV, the Higgs boson [32].

But in spite of its important achievements, the SM falls short of explaining several important observations that in this section are briefly reported.

- The SM considers neutrinos as massless particles but this is in contradiction with the results of many experiments, which observed, in several different contexts, the *neutrino oscillations*. It is a quantum mechanical phenomenon whereby a neutrino created with a specific lepton family number (e , μ , or τ) can later be measured to have a different lepton family number and this mechanism, implies that the neutrino has a non-zero mass since it arises

from mixing between the flavour and mass eigenstates of neutrinos.

- The SM can not describe *dark matter* and *dark energy*. The first evidence of dark matter came with the observation of the rotational speed of galaxies, which suggests the existence of a huge amount of undetected mass [33].

None of the SM particles could explain this phenomenon and, since a dark matter has never been directly observed, implies that it interacts only weakly with the ordinary matter and radiation, or does not interact at all.

Likewise, dark energy is an unknown form of energy that affects the universe on the largest scales. The first observational evidence for its existence came from supernovae measurements, which showed that the universe does not expand at a constant rate; rather, the expansion of the universe is accelerating.

The data collected by the Planck spacecraft, indicate that dark energy contributes 68% of the total energy in the present-day observable universe. The mass–energy of dark matter and ordinary (baryonic) matter contributes 27% and 5%, respectively, and other components such as neutrinos and photons contribute a very small amount [34].

- After the Big Bang one could expect that the universe produced the same amount of particles-antiparticles and that the constant annihilation of pairs would have resulted in a universe of radiation. What we observe actually is large cosmological matter (but not antimatter) structures. The mechanism suggested by the SM through the CP-symmetry violation of neutral oscillating hadrons is not sufficient to explain alone this phenomenon.
- There are also other strong indications that the SM could be not yet complete. Indeed, it is based on 19 parameters (excluding neutrino masses) that must be determined experimentally and have no known theoretical origin. Moreover, gravity could not be included as a gauge theory because, describing graviton (the associated gauge boson) interactions, the classical theory of Feynman diagrams, and semiclassical corrections with at least two loops lead to *ultraviolet divergences*. These infinite results cannot be removed because quantized general relativity is not perturbatively renormalizable, unlike QED and models such as the Yang–Mills theory. Therefore, when the probability of a particle to emit or absorb gravitons is calculated, the theory loses predictive veracity. Those problems and the complementary approximation framework are grounds to show that a theory more unified than quantized general relativity is required to describe the behaviour near the Planck scale.
- The problem of *naturalness* is also much debated in literature. The Higgs boson is very sensitive to loop corrections and if one considers the theory close to the Planck scale, the corrections involving the top quark may not explain why the Higgs boson mass is so relatively small (~ 125 GeV). Another problem is, in fact, the mass scale of fermions that it ranges across many orders of magnitude without any clear explanation.

Many are models of "new physics" that attempt to describe and explain the phenomena mentioned above but so far there is no evidence of new physics Beyond Standard Model (BSM). In the SM, top quark decays almost exclusively into bW while flavour-changing neutral current (FCNC) decays such as $t \rightarrow qZ$ are forbidden at tree level. FCNC decays occur at one-loop level (Figure 1.5) but are strongly suppressed by the GIM mechanism (Section 1.1.2.1), with a suppression factor of 14 orders of magnitude relative to the dominant decay mode[35].

However, in the BSM models, the suppression could be relaxed and the loop diagrams mediated by new bosons that could contribute, leading to couplings of many orders of magnitude higher than those expected by the SM.

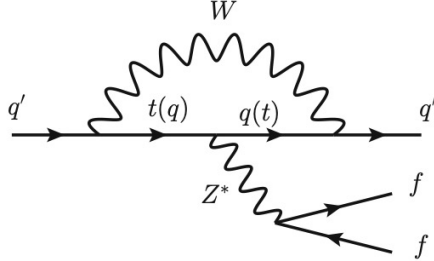


Figure 1.5 – Sketched Feynman diagram for SM $q' \rightarrow q'' f \bar{f}$ induced by the tqZ coupling, where q' and q'' denote the down-type quarks; $q = u, c$, and f can be any possible fermions. In the Standard Model, FCNC processes are forbidden at tree level but occur at one-loop level (see GIM mechanism in Section 1.1.2.1).

Examples of such extensions are the quark-singlet model (QS)[36], the two-Higgs-doublet model with (FC 2HDM) or without (2HDM) flavour conservation[18], the Minimal Supersymmetric Standard Model (MSSM)[19], the MSSM with R-parity violation (RPV SUSY)[20], models with warped extra dimensions (RS)[21], or extended mirror fermion models (EMF) [37]. Reference [38] gives a comprehensive review of the various extensions of the SM that have been proposed. Table 1.2 provides the maximum values for the branching ratios predicted by these models and compares them to the value predicted by the SM.

In this section we will briefly describe some of these theories interesting for the topics of this thesis.

Model:	SM	QS	2HDM	FC 2HDM	MSSM	RPV SUSY	RS	EMF
$\mathcal{B}(t \rightarrow qZ)$	10^{-14}	10^{-4}	10^{-6}	10^{-10}	10^{-7}	10^{-6}	10^{-5}	10^{-6}

Table 1.2 – Maximum allowed FCNC $t \rightarrow qZ$, ($q = u, c$) branching ratios predicted by several models[18–21, 35–38].

1.4.1 Quark singlets

The need to suppress the FCNC mechanism lead to:

- they are not mediated by Z^0 boson at tree-level
- no FCNC mechanism in the scalar sector at tree-level

It is possible to overcome these dogmas using extensions of the SM, like the Quark Singlets (QS) [17] that introduces a vector-like quark ($Q = \frac{1}{3}$ or $Q = \frac{2}{3}$), thus a small violation of the $3 \times 3 V_{CKM}$ unitarity (see Section 1.1.2.2), mediated by Z^0 boson and natural FCNC suppression at tree-level.

Given x_L and x_R , $SU(2)_L$ singlets

$$\begin{pmatrix} d' \\ s' \\ b' \\ x' \end{pmatrix} = \begin{pmatrix} |V_{ud}| & |V_{us}| & |V_{ub}| & |V_{ux}| \\ |V_{cd}| & |V_{cs}| & |V_{cb}| & |V_{cx}| \\ |V_{td}| & |V_{ts}| & |V_{tb}| & |V_{tx}| \end{pmatrix} \begin{pmatrix} d \\ s \\ b \\ x \end{pmatrix}, \quad (1.17)$$

the non orthogonality of the columns leads to terms of the type:

$$J_\mu = \frac{g}{\cos\theta_W} Z_{bd} \bar{b}_L \gamma_\mu d_L Z^\mu \quad (1.18)$$

where

$$Z_{bd} = V_{ud} V_{ub}^* + V_{cd} V_{cb}^* + V_{td} V_{tb}^* \quad (1.19)$$

and Z_{bd} is suppressed by $\frac{m_q}{m_x}$.

In this way it is possible to have deviations from 3×3 unitarity.

For instance, the PMNS matrix in the leptonic sector, in the context of the see-saw mechanism is not 3×3 unitarity [39].

Vector-like quarks provide the simplest model with spontaneous *CP violation* and a framework to have a common origin of all CP violation, because it is a potential solution of the *strong CP problem*.

1.4.2 Two Higgs Doublet Model

The LHC discovery of a Standard-Model-like Higgs $H(125)$ particle in 2012[32] could be a portal to an extended Higgs sector predicted by several models. One of such models is the Two-Higgs-Doublet Model (2HDM) [40]. The most natural extension of the Standard Model scalar sector is the addition of an extra $SU(2)_L$ doublet.

The 2HDM is an *Effective Field Theory* (EFT)⁴ consisting of two complex Higgs doublets, which provide masses to both the up-type and the down-type fermions:

$$\Phi_1 = \begin{pmatrix} \phi_1^+ \\ \phi_1^0 \end{pmatrix} \quad \Phi_2 = \begin{pmatrix} \phi_2^+ \\ \phi_2^0 \end{pmatrix} \quad (1.20)$$

with the minimum of the potential corresponding to

$$\Phi_{1,0} = \frac{1}{\sqrt{2}} \begin{pmatrix} 0 \\ \nu_1 \end{pmatrix} \quad \Phi_{2,0} = \frac{1}{\sqrt{2}} \begin{pmatrix} 0 \\ \nu_2 \end{pmatrix}. \quad (1.21)$$

After the electroweak symmetry breaking (EWSB), there are five physical scalar fields, consisting of neutral bosons h, H, A of which the first two bosons are CP-even, as opposed to the A -boson which is CP-odd and of two charged Higgs states H^\pm .

The model is parametrized by the five Higgs masses (m_H, m_h, m_{H^\pm}, m_A), the ratio of the

⁴An EFT corresponds to a low-energy approximation to a more fundamental underlying theory, characterized by an energy scale Λ (e.g. the mass of new particles)

vacuum expectation values of the two Higgs doublets $\tan \beta = v_2/v_1$ and the mixing angle α between the CP-even Higgs states.

There exist four types of 2HDM which simultaneously forbid the presence of FCNC and preserve CP symmetry:

- in Type I all fermions couple to the second doublet Φ_2 . It follows that BR are independent of $\tan \beta$;
- in Type II or MSSM-like scenario, lepton and down-type quarks couple to the first doublet Φ_1 , whilst up-type quarks couple to Φ_2 ;
- in Type III or lepton specific scenario, quarks couple to Φ_2 while leptons couple to the other doublet;
- in Type IV or flipped model, the coupling of the leptons is reversed with respect to the Type-II model.

1.4.3 Minimal Supersymmetric Standard Model

The FCNC processes have also been studied within the *Minimal Supersymmetric Standard Model* (MSSM), where there are loop corrections of the supersymmetric QCD with gluinos and scalar quarks, as shown in Figure 1.6. In supersymmetric QCD it was shown that there occurs flavour-

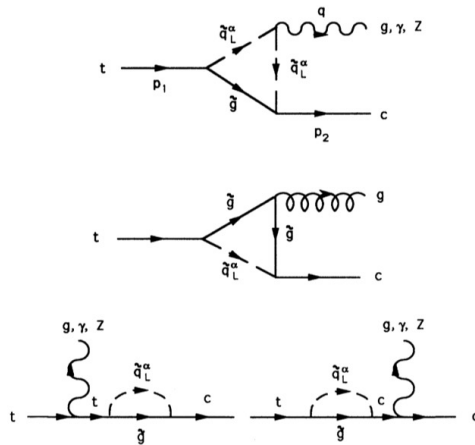


Figure 1.6 – The diagrams with scalar quarks and gluinos within the loop, which contribute to the top quark decay into a charm quark and a Z boson, photon, or gluon[41].

changing strong interactions between the gluino, the left-handed quarks, and their supersymmetric scalar partners, whereas the couplings of the gluino to the right-handed quarks and their partners remains flavour diagonal. To calculate the one-loop diagrams shown in Figure 1.6, we need the couplings of the gluon to the gluinos, of the scalar partners of the left-handed quarks to the gluon, photon, and Z boson, and of the gluino to the left-handed quark and its scalar partner.

After the introduction of non-trivial squark mixing, it is possible to calculate the coupling that

leads to flavour changing in which appears K_{ij} , the supersymmetric version of V_{CKM} :

$$\begin{pmatrix} 1 & \epsilon & \epsilon^2 \\ -\epsilon & 1 & \epsilon \\ -\epsilon^2 & -\epsilon & 1 \end{pmatrix}. \quad (1.22)$$

It is possible to demonstrate that all divergent terms cancel exactly, without the GIM mechanism. Finally, we define $\mathcal{B}(t \rightarrow cZ) = \frac{\Gamma_S(t \rightarrow cZ)}{\Gamma_W(t \rightarrow bW)}$, where:

$$\Gamma_W(t \rightarrow bW) = \frac{\alpha}{16 \sin \Theta_W} m_{top} \left(1 - \frac{m_W^2}{m_{top}^2} \right)^2 \left(2 + \frac{m_{top}^2}{m_W^2} \right) \quad (1.23)$$

Using the following values for the parameters $m_{top} = 174$ GeV, $\alpha_s = 1.4675 / \ln \left(\frac{m_{top}^2}{\Lambda_{QCD}^2} \right)$ with $\Lambda_{QCD} = 0.18$ GeV, it is possible to derive the branching ratio $\mathcal{B}(t \rightarrow cZ)$ as a function of the scalar mass m_S for a gluino mass of 100 GeV (Figure 1.7).

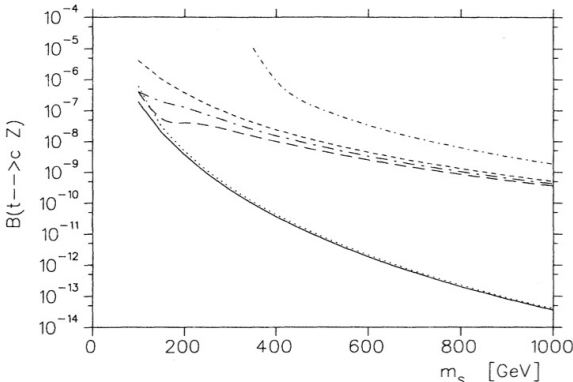


Figure 1.7 – The branching ratio $\mathcal{B}(t \rightarrow cZ)$ as a function of the scalar mass m_S . The gluino mass was taken to be 100 GeV. The solid line is the unphysical case with no squark mixing, the dotted lines are different scenarios of squark mixing[41].

We see that without mixing, $\mathcal{B}(t \rightarrow cZ)$ decreases rapidly with increasing scalar mass. The mixing has a drastic effect. It enhances the branching ratio by up to 5 orders of magnitude for large m_S .

CHAPTER 2

The LHC accelerator and the ATLAS experiment



Figure 2.1 – The LHC ring, aerial view.

The main focus of this chapter is the experimental setup, thus the ATLAS detector, one of the four large experiments at CERN (*Conseil Européen pour la Recherche Nucléaire*) and whose location is shown in Figure 2.1.

Established in 1954, CERN is the largest particle physics laboratory in the world and the organization is based in a north-west suburb of Geneva on the Franco-Swiss border. The analysis presented in this thesis is based on the data collected in Run2 (2015-2018). Since December 2018, LHC has been shut-down (LS2, 2019-2020) to undergo a major upgrade (Phase I Upgrade) which may enable to collect up to 300 fb^{-1} at a c.o.m. energy of 14 TeV by 2023. After that, a second major upgrade (Phase II Upgrade) is planned to the LHC (LS3, 2024-2025) which will increase the interaction rate by a factor of 10; this upgrade will lead LHC to High-Luminosity LHC (HL-LHC).

2.1 The LHC accelerator

Located at CERN, the Large Hadron Collider (LHC) [42] is the world's highest energy particle accelerator. LHC is a circular hadron accelerator, positioned at a depth of about 100 m in the tunnel built for the LEP accelerator. It is 26.6 km long and currently operates by making proton beams collide at an energy $\sqrt{s} = 13$ TeV. The overall accelerator complex is shown in Figure 2.2.

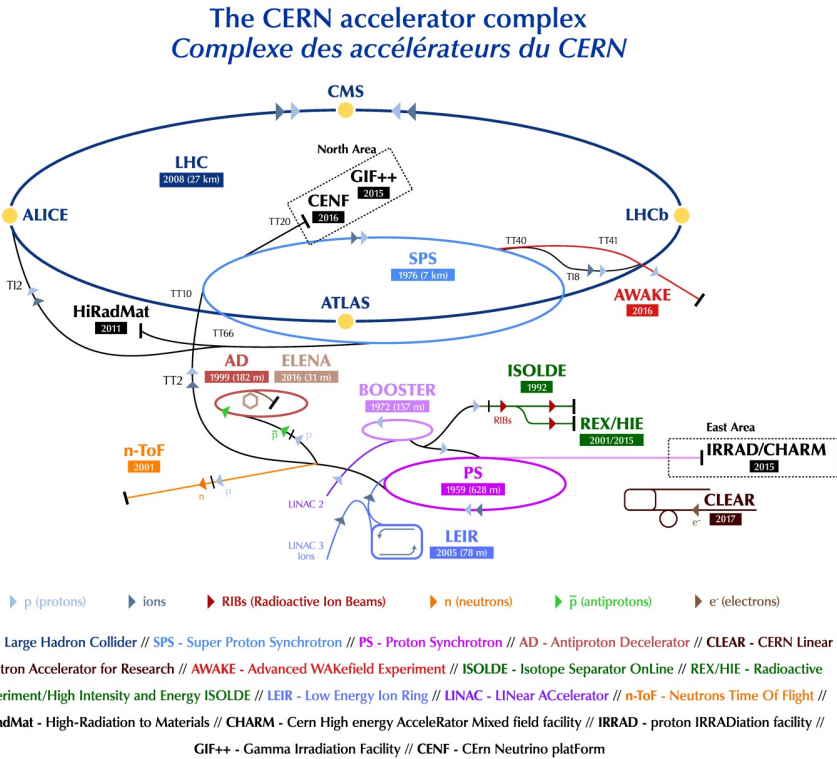


Figure 2.2 – The overall CERN accelerator complex [43].

CERN's choice to replace the LEP leptonic collider with an hadronic one, such as LHC, has brought two fundamental advantages: the first is that for the same infrastructural size it is possible to reach a higher energy in the center of mass, since the energy lost by radiation of synchrotron from a particle in circular motion is $\frac{dE}{dt} \propto \frac{E^4}{m^4 R}$, where R is the bending radius and m is the mass of the accelerated particle travelling at an energy E , hence protons are better than electrons. The second advantage is that the composite structure of the protons allows access to a wider energy spectrum that can be explored simultaneously without having to change the beam parameters. On the other hand, the number of background events also increases. In addition to proton-proton ($p-p$)

p) collisions, the LHC can also collide heavy lead ions (Pb-Pb).

Before reaching the target energy, protons undergo subsequent acceleration steps.

The first step is the proton production from hydrogen gas, after which protons are accelerated up to 50 MeV at the LINear ACcelerator 2 (LINAC 2). These protons are then injected into the Proton Synchrotron Booster (PSB) where their energy reaches 1.8 GeV. The acceleration chain continues into the Proton Synchrotron (PS) which pushes the beam to 25 GeV. After that, the beam is injected into the Super Proton Synchrotron (SPS) where the protons are accelerated up to 450 GeV. Finally, the bunches of protons are injected in the LHC. A typical bunch train corresponds to 2808 bunches for each beam with 25 ns separation, and a bunch contains about 10^{11} protons colliding at a rate up to 40 MHz.

The LHC is designed to accelerate each beam at an energy of 7 TeV thanks to a complex system of dipole and higher order magnets but the LHC performance has not always been that of today. The first protons beams were circulated in the LHC on September 10th of 2008. From 2010 to 2012, the protons beams had an energy of 3.5 TeV. From 2012 to 2013, the energy reached was 4 TeV per beam. Following, the first shutdown, the LHC started to accelerate beams up to an energy of 6.5 TeV in April 5th of 2015.

Since protons are charged particles, a strong magnetic field, produced by 1232 superconducting electromagnets, curves the beams around the circular accelerator. To maintain the superconductivity properties, these magnets require a temperature of 1.9 K ($\approx 271.3^{\circ}\text{C}$). This temperature allows the dipole magnets to generate a magnetic field of 8 T. Besides the bending magnets, a total of 392 quadrupole magnets maintain the beams focused and 16 radio-frequency cavities accelerate particles and keep them in controlled bunches with a constant energy. Four main interaction points are used as collision points corresponding to the location of the four detectors: ALICE, ATLAS, CMS and LHCb.

The number of multiple interactions per bunch crossing is called *pile-up* and it is denoted by μ . Actually there are two different sources of pile-up:

- in-time pile-up occurs when multiple collisions take place in a single bunch crossing
- out-of-time pile-up is due to finite read-out time resolution of the detectors, often larger than 25 ns. In this case, the residual energy from a previous bunch crossing could potentially be associated to the following bunch crossing.

The distribution of $\langle \mu \rangle$ is shown in Figure 2.3, for the different data-taking periods. The average pile-up for 2015-2018 is $\langle \mu \rangle = 33.7$.

The event rate of a given process with cross section σ is given by $\frac{dN}{dt} = \mathcal{L}\sigma$, where \mathcal{L} is a characteristic of the accelerator, known as *instantaneous luminosity* and is given by:

$$\mathcal{L} = \frac{N_b^2 k_b f \gamma}{4\pi \sigma_x \sigma_y} F \quad (2.1)$$

where N_b^2 is the number of particles per bunch, k_b is the number of bunches, γ represents the relativistic gamma factor, f is the revolution frequency of the accelerator, σ_x and σ_y are the horizontal and vertical beam size, F is a geometrical correction factor from the crossing-angle of the two beams at the interaction point (IP).

Given a period of time T , one can define the *integrated luminosity* as $L = \int_0^T dt \mathcal{L}$ which is typically expressed in fb^{-1} (1 b = 10^{-28} m^2).

Figure 2.4 shows the total integrated luminosity over the full LHC data taking period at $\sqrt{s} = 13 \text{ TeV}$ and Table 2.1 summarizes the main design parameters of the LHC.

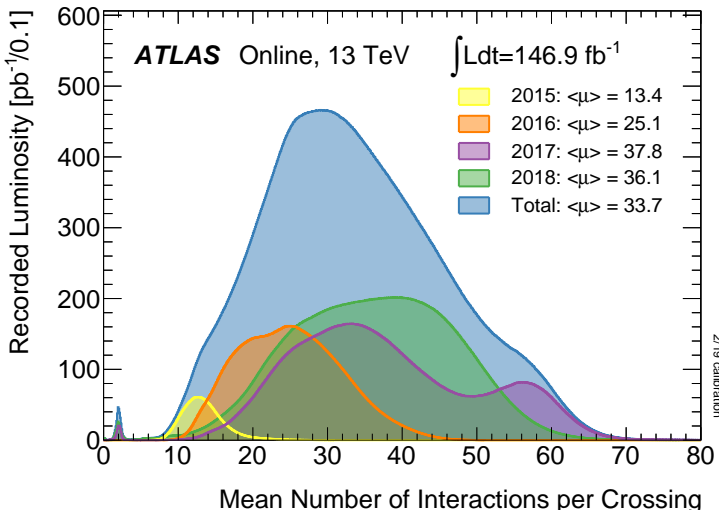


Figure 2.3 – Luminosity-weighted distribution of the mean number of interactions per crossing for the 2015–2018 pp collision data at $\sqrt{13}$. All data recorded by ATLAS during stable beams is shown, and the integrated luminosity and the mean μ value are given in the figure [44].

Parameter	2015	2016	2017	2018
Bunch intensity [$\times 10^{11}$ p]	1.2	1.1	1.25	1.15
Number of bunches	2200	2200	1900	2500
Emittance [μm]	3.5	2.5	2.0	2.2
Crossing angle [μrad]	290	280	300	300
Peak luminosity [$10^{34}\text{cm}^2\text{s}^{-1}$]	0.5	1.5	1.5	2.0

Table 2.1 – Main beam parameters of proton-proton collisions of LHC in Run2.

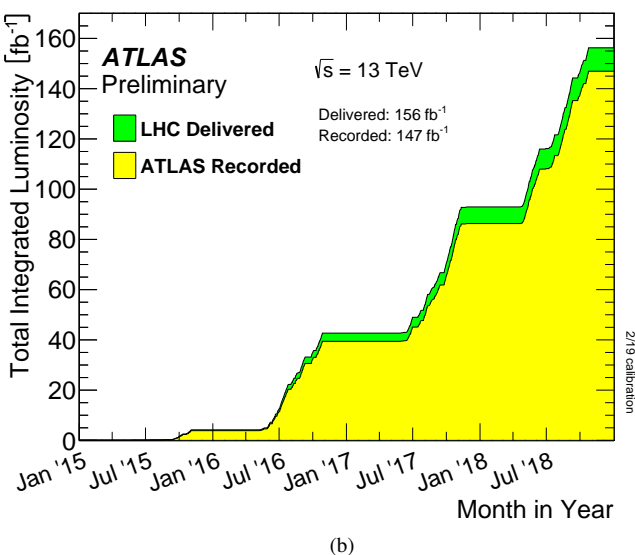
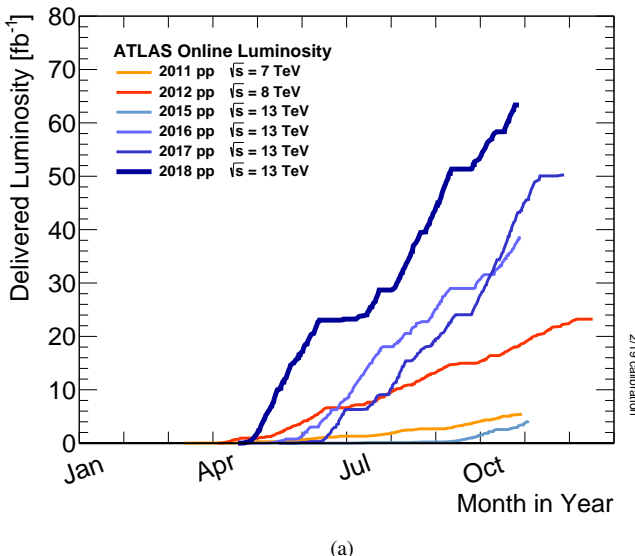


Figure 2.4 – Cumulative luminosity versus (a) day delivered to ATLAS during stable beams; (b) time delivered to ATLAS (green) and recorded by ATLAS (yellow) during stable beams for pp collisions at $\sqrt{13}$ [44].

2.2 The ATLAS detector

ATLAS (A Toroidal LHC ApparatuS) [45] is a multi-purpose apparatus whose primary goal is to identify and measure the properties of particles produced in p–p collision.

The overall ATLAS detector layout is shown in Figure 2.5. The ATLAS detector consist of a concentric cylinder shape (4π coverage), therefore nominally forward-backward symmetric with respect to the interaction point (IP) where the proton beams collide in it. It can be divided into five main parts:

- Magnet System (section 2.2.1);
- The Inner Detector (section 2.2.2);
- The Calorimetric System (section 2.2.3);
- Muon Spectrometer (section 2.2.4).
- Trigger and data acquisition System (section 2.2.5).

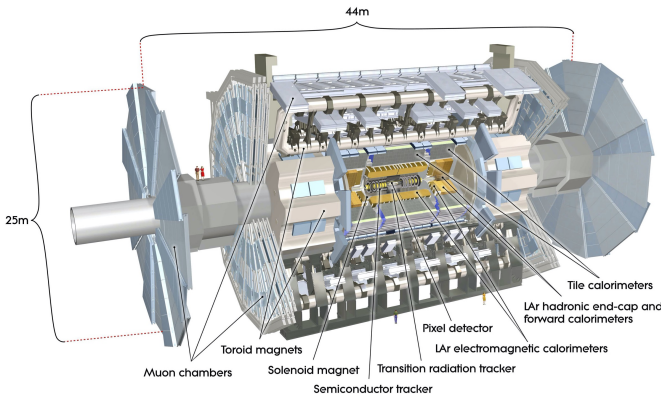


Figure 2.5 – Cut-away view of the ATLAS detector. The dimensions of the detector are 25 m in height and 44 m in length. The overall weight of the detector is approximately 7000 tonnes [45].

Coordinate system

The ATLAS coordinate system is a right-handed Cartesian coordinate system with the origin defined at the IP, in the center of the detector. The z -axis corresponds to the beam pipe while the x and y directions define the transverse plane.

A cylindrical coordinate system is often used due to the geometry of the detector, where ϕ is the azimuthal angle and θ is the polar angle. The ϕ is orthogonal to the beam direction, therefore it is invariant under a Lorentz boost(z -axis), while θ is not an invariant, so the *pseudorapidity* is defined as:

$$\eta = -\ln \left(\tan \left(\frac{\theta}{2} \right) \right) \quad (2.2)$$

Pseudorapidity is an approximation of the *rapidity*¹ for relativist particles ($m \ll p$) with mass m and momentum p .

The distance between two objects is indicated using ΔR , defined as:

$$\Delta R = \sqrt{\Delta\eta^2 + \Delta\phi^2} \quad (2.3)$$

The transverse momentum is the projection of the momentum orthogonal to the beam direction, defined as:

$$p_T = \sqrt{p_x^2 + p_y^2} \quad (2.4)$$

2.2.1 Magnet System

The magnet configuration comprises a thin superconducting solenoid surrounding the inner-detector cavity, and three large superconducting toroids (one barrel and two end-caps) arranged with an eight-fold azimuthal symmetry around the calorimeters. This fundamental choice has driven the design of the rest of the detector.

The inner detector is immersed in a 2 T solenoidal field provided by the central solenoid with inner radius of 1.23 m and a total length of 5.8 m.

It is designed to minimize the amount of material in front of the calorimeter to have a small impact on the energy measurement. This is achieved by hosting the solenoid and the cryostat in the same vacuum vessel of the electromagnetic calorimeter.

The overall dimensions of the magnet system is 26 m long and 20 m diameter and provide an average magnetic field intensity of 0.5 T in the barrel and 1 T in the end-caps regions [46].

2.2.2 Inner Detector

The Inner Detector (ID) [45] is the detector system closest to the beam.

It is composed of three detectors: the semiconductor pixel detector (PIXEL), the microstrip detector SCT (Semi-Conductor Tracker), and the most external, the transition radiation detector TRT (Transition Radiation Tracker). Its overall layout is depicted in Figure 2.6.

The ID is contained in a cylinder, 7 m long and 1.15 m in radius, placed in a 2 T solenoid magnetic field and it is designed to trace charged particles with a minimum moment of 0.1 GeV/c, it allows the measurement of the moment through the track curvature radius and the reconstruction of the main interaction and decay vertices (both primary and secondary).

The innermost part of the ID, which has a radius of about 15 cm, consists of silicon pixels to maximize the precision in the reconstruction of the tracks and the resistance to radiation. The pixel detector records on average three points for each track, which allows a reconstruction of the secondary decay vertices. This detector has a total of approximately 80 million sensitive elements.

The intermediate part, which covers a radius ranging from 30 to 60 cm, uses a microstrip detector (Semi-Conductor Tracker), to provide good spatial resolution. The detection technique of the SCT relies on the same principle as for the pixel detector, however long strips are used compared to the rectangular pixels due to the smaller particle density in the outer layers. It is located around the Pixel detector and is designed to provide eight precision measurements per track, contributing

¹Rapidity is defined as $y = \frac{1}{2} \ln \frac{E+p_z}{E-p_z}$

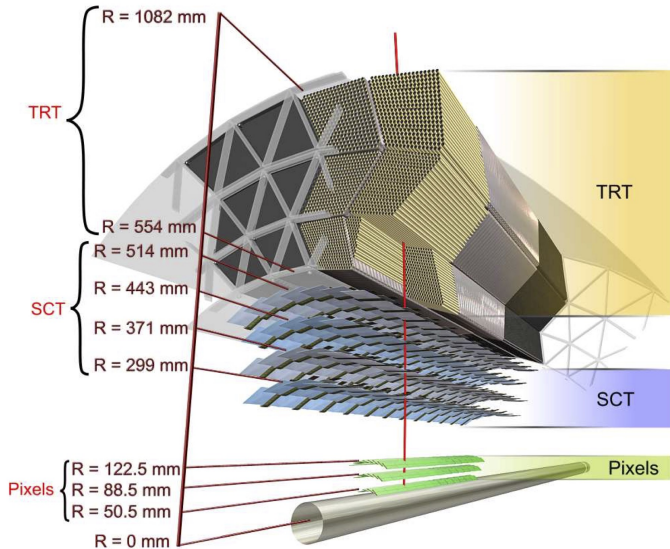


Figure 2.6 – Schematic view of the barrel of the ATLAS inner tracking system [45].

to the measurements of momentum, impact parameter and vertex position. The total number of sensitive items is around 6 million.

The outermost layer ranges from 60 to 95 cm in radius; it is a gas detector (Transition Radiation Tracker) consisting of a set of small diameter tubes, containing Xe (70%), CO₂ (27%), O₂ (3%); it provides a good resolution of the curvature of the track and contributes strongly to its reconstruction.

The tracker contributes to the identification of the electrons, being sensitive to the emission of transition radiation that the particles emit when passing between different materials.

2.2.3 Calorimetric System

Calorimeters must provide good containment for electromagnetic and hadronic showers, they must limit punch-through into the muon system, and finally they must detect the particles that do not lose energy by ionization and are therefore not seen by the internal detector.

It is important that calorimeters cover the largest possible portion of solid angle; in fact, if a particle passes through a region without instrumentation, it is not detected and its energy contributes to the *Missing Transverse Energy* (MET), the precision of which is essential for identifying and studying weakly interacting particles such as neutrinos and, possibly, new BSM particles.

In ATLAS there are two calorimeters: the Electromagnetic Calorimeter (ECAL) and the Hadron Calorimeter (HCAL), as depicted in Figure 2.7 and they cover the range $|\eta| < 4.9$.

The ECAL is divided into a barrel part ($|\eta| < 1.475$) and two end-cap components ($1.375 < |\eta| < 3.2$).

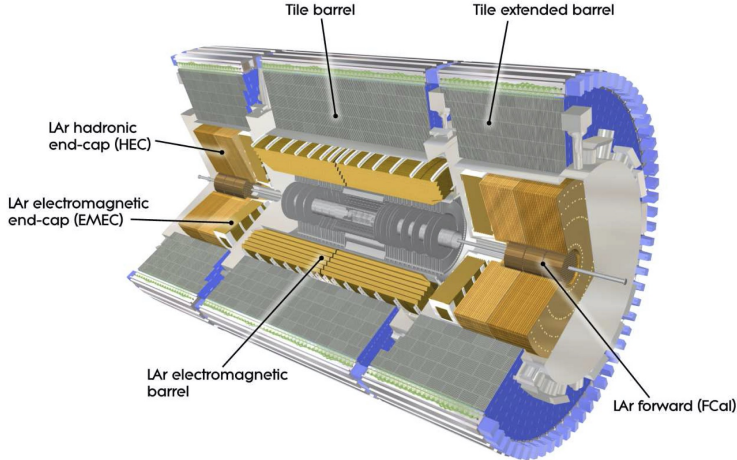


Figure 2.7 – Cut-away view of the ATLAS calorimeter system [45].

each housed in their own cryostat. It is a lead-LAr detector with accordion-shaped kapton electrodes and lead absorber plates over its full coverage. The accordion geometry provides complete ϕ symmetry without azimuthal cracks. The lead thickness in the absorber plates has been optimized as a function of η in terms of ECAL performance in energy resolution.

A schematic representation of the ECAL in the barrel and its main construction parameters are shown in Figure 2.8.

The outer calorimeter is the HCAL, which is divided in Tile Calorimeter (TileCal), the Hadronic End-cap Calorimeter (HEC) and the Forward Calorimeter (FCal).

LAr technology is also used for the hadronic calorimeters, matching the outer $|\eta|$ limits of end-cap electromagnetic calorimeters. The tile calorimeter barrel covers the region $|\eta| < 1.0$, and its two extended barrels the range $0.8 < |\eta| < 1.7$, with a sampling calorimeter using steel as the absorber and scintillating tiles as the active material.

The HEC consists of two independent wheels per end-cap, located directly behind the end-cap electromagnetic calorimeter. The technology is similar to that of the electromagnetic calorimeter in the end-cap region, the active medium is LAr, but the absorption medium is made of copper rather than lead. The FCal ($3.1 < |\eta| < 4.9$) is integrated into the end-cap cryostats, as this provides clear benefits in terms of uniformity of the calorimetric coverage as well as reduced radiation background levels in the muon spectrometer. The FCal consists of three modules in each end-cap: the first, made of copper, is optimized for electromagnetic measurements, while the other two, made of tungsten, measure predominantly the energy of hadronic interactions.

An important quantity in calorimetry is the energy resolution, which is parameterized as:

$$\frac{\sigma_E}{E} = \frac{S}{\sqrt{E}} \oplus \frac{N}{E} \oplus C \quad (2.5)$$

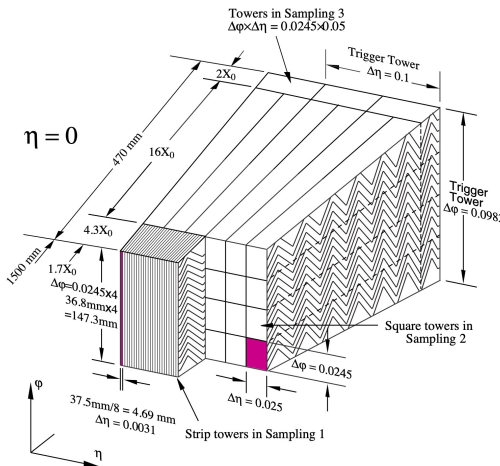


Figure 2.8 – Sketch of the accordion structure of the ECAL [47].

The first term represent the stochastic contribution related to the shower evolution, the second term is related to the read-out electronics and the effect of the pile-up. The last term is a constant, due to systematic effects (e.g. mis-calibrations, dead detector material). The dominant source of uncertainty is linked, at low energy, with the high pile-up whereas, at high energy, C becomes the leading uncertainty.

2.2.4 Muon Spectrometer

The calorimeter is surrounded by the Muon Spectrometer (MS) depicted in Figure 2.9, which is placed at the outermost part of the ATLAS detector.

The outer layers are reached by a few types of particles, mainly muons and neutrinos.

These muons ionize in the material passed through, but the energy, lost in the electromagnetic interaction with other nuclei of the calorimeter, is not sufficient to stop them. The MS identifies muons and measures their momentum.

A series of magnets arranged externally to the calorimeter creates a toroidal-shaped magnetic field that modifies the charged particles direction allowing the measurement of the momentum. For muons with $p_T > 30 \text{ GeV}$ the measurement is much more precise than the measurement obtained by the inner detectors. For lower p_T , on the other hand, the measurement is less accurate, due to the energy loss in the previous layers of the detector and taken in to account to handle *soft muons*, presented in Section 4.2.4.

For both the central part and the end-caps, there are two types of muon detectors:

- a trigger system based on cameras with fast response, such as the *Resistive Plate Chamber* (RPC) and the *Thin Gap Chamber* (TGC),
- precision tracking chambers, such as the *Monitored Drift Tube* (MDT) and the *Cathode Strip Chamber* (CGS).

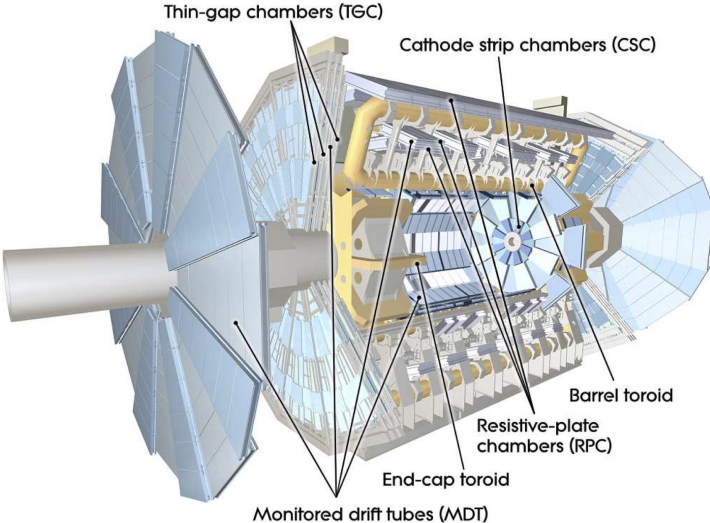


Figure 2.9 – Cut-away view of the ATLAS muon system [45].

In the central region ($|\eta| < 1.05$), the RPCs consist of two parallel planes filled with a mixture of gas that ionizes when a muon passes through. The HV applied between the plates allows the development of avalanches, along the ionization track towards the anode, which constitutes a signal.

In the end-cap ($1.05 < |\eta| < 2.4$), TGCs are used to complement the RPCs in the triggering system for their good time resolution and rate capability.

The TGC is a multi-wire proportional chamber operated in a highly quenching gas mixture. Both TGCs and RPCs can achieve a read-out time of less than 25 ns [48].

The MDTs are used for muons with $|\eta| < 2$, and they are a series of aluminium tubes filled with a gas mixture of Argon and CO₂. A central wire serving as anode allows to collect the electrons that are formed following the passage of the muon into the gas.

The CSCs cover the area while $2 < |\eta| < 2.7$, and are radially-oriented proportional multi-wire chambers, i.e. metal chambers containing a system of parallel and perpendicular anodic wires with strips of opposite polarity.

One important point to stress is that this detector measures the characteristics of any charged particle that passes through it and not just muons. For this reason it is possible that other particles that are not muons, such as pions that manage to overcome the calorimeter are detected as muons. What is presented in this paragraph about the MS is a general overview but much more will be presented in Chapter 3, going deeper on its functioning and its upgrade for the HL-LHC.

2.2.5 Trigger and Data Acquisition

Once fully operational, with the high frequency of collisions typical at LHC, an impressive amount of data is produced (40 MHz of p-p bunch collision frequency), which would be impossible to manage without the application of filters. The *Trigger and Data Acquisition system* (TDAQ) is able to recognize the interesting events for further study.

In Run2 the trigger system consists of two levels of event selection: the *Level-1 trigger* (L1), is an hardware trigger that reduces the rate to 100 kHz, while the *High-Level Trigger* (HLT), is a software trigger, further the reducing event rate to 1 kHz.

The Level-1 trigger is composed by three subsystems: the first is the L1 calorimeter trigger (L1Calo), which uses calorimeter information; the second is the L1 muon trigger (L1Muon), which primarily uses TGC and RPC information to make fast decisions on muon items; the third is the L1 topological trigger (L1Topo) that combines information from L1Calo and L1Muon into the Central Trigger Processor (CTP) which makes the final decision.

At this point, L1 identifies the *Region of Interest* (RoI) with an event rate reduced below 100 kHz. The RoI are then used by the HLT, which has access to the information of all the sub-detectors, targeting the maximum rate of 1 kHz.

Finally, the events are assembled into an event record passes to the offline storage facilities for a complete off-line reconstruction [49].

CHAPTER 3

The Trigger system upgrade for High-Luminosity LHC

Since the beginning, the LHC accelerator has faced operating periods and dedicated shut-downs to upgrade the accelerator machine and the detectors.

In Figure 3.1 a summary of the LHC timeline for operation and upgrade is shown.

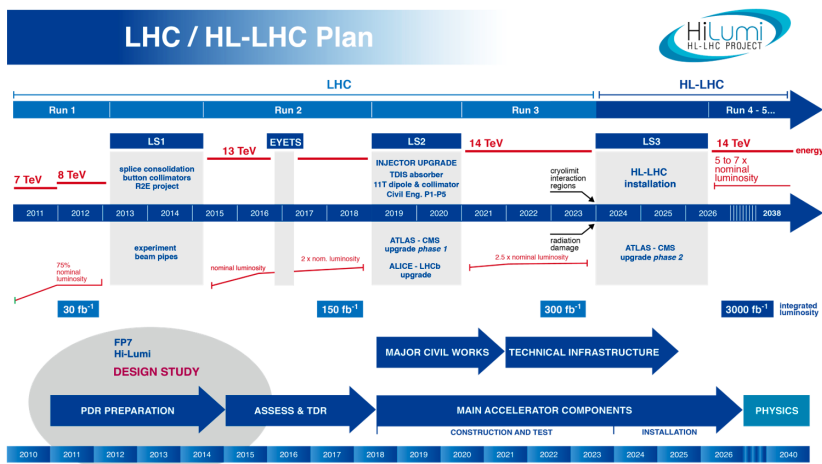


Figure 3.1 – Summary of the LHC timeline for operation and upgrade [50].

At the end of 2018, the LHC was shut-down and for two years it will be upgraded to bring the center-of-mass energy to its design value of 14 TeV and collect 300 fb⁻¹ of data, almost double

the current available statistics of Run2. After 4 years of duty cycle, the High-Luminosity period of LHC (HL-LHC) will start and aims to bring the integrated luminosity to 3000 fb^{-1} , unlocking several studies, mostly related with rare phenomena, which are impossible to perform with the current datasets.

This chapter describes the Barrel Muon Trigger system (Section 3.1), the BI upgrade for the HL-LHC (Section 3.2), and the studies performed in the context of the RPC upgrade. In particular, the goal of this work was the implementation of a new simulation to model the digitization of RPC hits in the BI region (Section 3.3) and, using this new model, trigger efficiency studies were performed in the BI and BM/BO regions (Section 3.4). In the end, summary and final considerations are also reported (Section 3.5).

3.1 ATLAS Barrel Muon Trigger

The muon detector chambers are arranged such that particles from the interaction point traverse three stations of chambers.

The system is subdivided azimuthally into 16 sectors numbered from 1 to 16. The sector number increases in the direction of increasing ϕ with the number 1 corresponding to coordinate $\phi = 0$. The odd sector (called “large sectors”) are located between barrel coils, while, the even sectors (called “small sectors”) are covered by the coils.

The muon spectrometer consists of three large air-core superconducting toroidal magnets (two end-caps and one barrel) providing a field of approximately 0.5 T.

In the barrel, the chambers are arranged in three concentric cylinders around the beam axis called BI (Barrel Inner), BM (Barrel Middle), and BO (Barrel Outer).

The RPC planes are installed in the Middle and Outer stations of the Muon Spectrometer and are mechanically associated with MDT precision chambers (except for some “special” chambers).

Schematic drawings of the present ATLAS MS [51], are shown in Figures 3.2 and 3.3. The MS detector and electronics components have been designed for 10 years of operation at a luminosity of $1 \times 10^{34} \text{ cm}^{-2} \text{ s}^{-1}$, corresponding to an integrated luminosity of 1000 fb^{-1} . Conservative safety factors for radiation tolerance and rate capability were taken into account in the original designs, and components have been tested up to and above levels corresponding to the expected doses and rates predicted by simulations multiplied by the safety factors. After the start of LHC operation, detector hit rates and radiation doses could be measured directly, and the previous simulations have been found to agree with the measurements to within a maximum deviation of about 50%.

Based on this observation, the original safety factors were reduced [10], and as a consequence the original irradiation and high-rate tests have qualified the detectors for longer running and higher rates than originally anticipated.

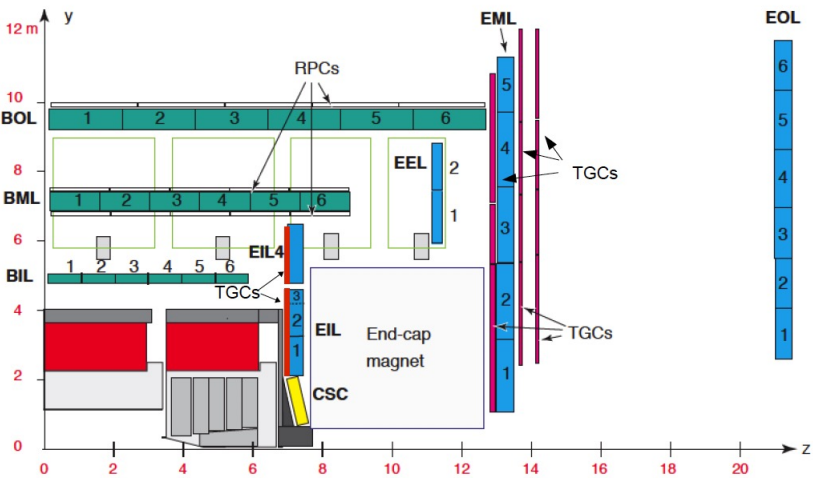
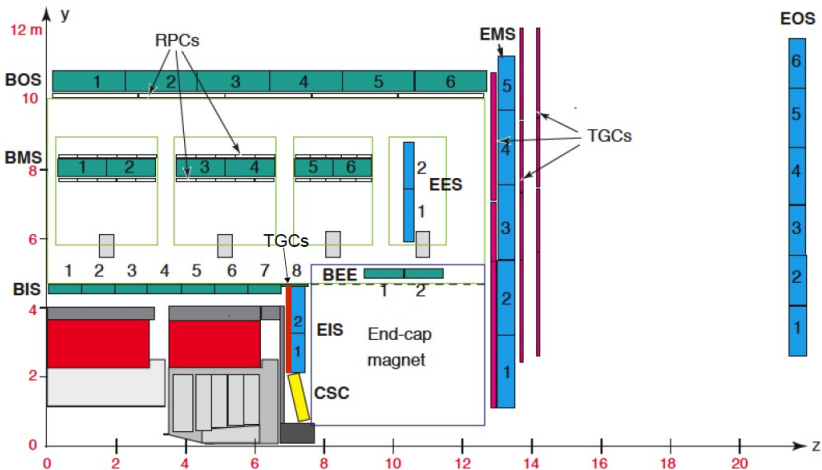


Figure 3.2 – Two R-Z views of the present (Run 1/2) ATLAS muon spectrometer layout. Top: One of the azimuthal sectors that contain the barrel toroid coils (small sector). Bottom: One of the sectors in-between the barrel toroid coils (large sector) [51].

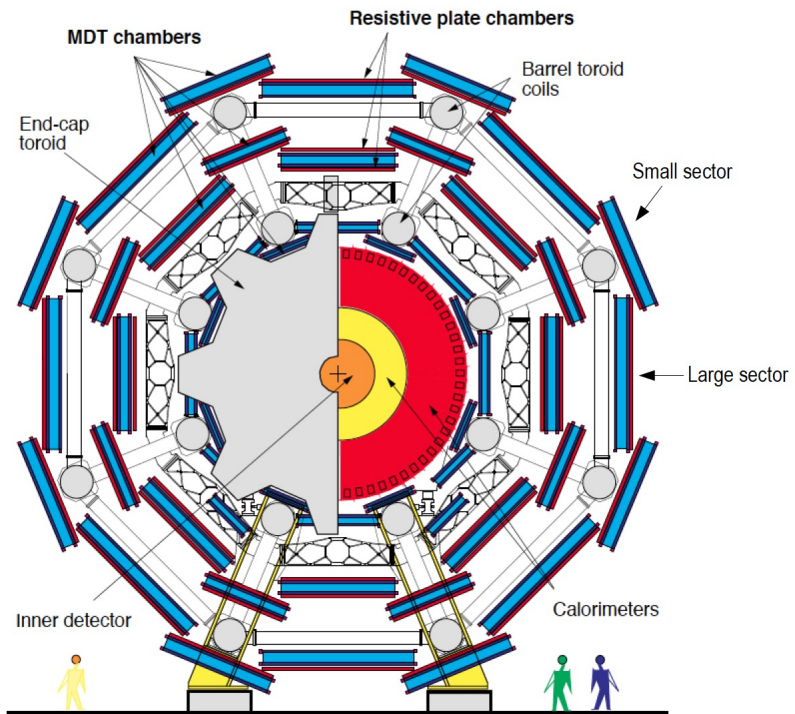


Figure 3.3 – View of the present (Run 1/2) ATLAS muon spectrometer barrel layout in the plane transverse to the beam axis (X-Y plane) [51].

3.2 BI upgrade for Phase-II

In the Phase-I upgrade, foreseen for LS2, the Small Wheels will be replaced by the New Small Wheels (NSW) [52] using small-strip TGC (sTGC) and Micro-Mesh Gaseous Structure (MicroMeGaS or Micromegas) chambers used for both triggering and precision tracking.

At the time of the Phase-II upgrade, there will thus be no CSC chambers any more in the detector, nor will there be the Small Wheel MDT chambers, which are the ones closest to the beam line and exposed to the highest rates. Also in LS2, the BIS7 and BIS8 MDT chambers will be replaced by integrated BIS78 stations of new RPC and small diameter MDT (sMDT) chambers to enhance the trigger coverage in this region [53].

Schematic drawings of the ATLAS MS with the new detectors that will be installed in the Phase-I and Phase-II upgrades are shown in Figure 3.4.

To maintain a high trigger efficiency, new RPC chambers with increased rate capability will be installed on the inner (BI) MDT chambers of the barrel. This addresses a fundamental issue of the present (old) RPC chambers: to ensure their continued operation at the HL-LHC, these chambers will have to be operated at reduced performance (i.e. efficiency), in order to respect the original design limits on currents and integrated charge. This can be achieved by reducing the gas gain through lowering the operating voltages. In the areas of high backgrounds, the gas gain will have to be reduced to such low levels that hit inefficiencies up to 35% will be encountered. This would reduce the trigger efficiency in the barrel region to an unacceptable level if no compensating measures were taken. In addition, due to changes in regulations, the present gas mixture used in ATLAS RPCs may need to be replaced by one with lower global-warming potential (GWP). Unless new gas mixtures are found in time, this too will imply operation of old RPCs at a reduced efficiency. Despite the lower single-hit efficiencies, a high trigger efficiency and purity can be maintained by loosening the requirements on hit coincidences in the old chambers, if at the same time a coincidence with the new BI RPC chambers is introduced. The installation of these chambers will also close most of the acceptance holes of the present barrel muon trigger, which amount to more than 20% of the $\eta - \phi$ coverage for $|\eta| < 1.05$ (see Section 3.4).

Adding new RPC chambers in the barrel is challenging in terms of available space and installation. In the small sectors, the BI RPC chambers can only be installed if the present MDT chambers are replaced by new sMDT chambers with reduced overall thickness so that the sMDT chambers and the new RPCs fit in the same envelope as the original MDT chambers. In the large sectors there is sufficient space available to add the new RPC chambers without replacing the MDTs, if on-detector services are re-arranged.

The retrofitting of selected RPC chambers in the BM and BO layer in the areas of high rate at $|\eta| > 0.8$, namely the BML7 and BOL6 chambers, is a small additional upgrade. The MDT+RPC stations will be temporarily removed from the detector to replace the front-end electronics and the readout panels, so that the chambers can be run at reduced HV without efficiency loss.

In the Section 3.4.1 it will be presented a study performed on the refurbish of BM and BO chambers and the installation of BI chambers in the rail sectors 11 and 15.

The retrofitting can only be done outside the experimental cavern, on the surface, since it requires the disassembly of the RPC chambers. The retrofitting of the BO chambers does not fit into the LS3 schedule because it would interfere with the BI chamber upgrade, and will likely be performed, at least partly, in winter shutdowns after LS3.

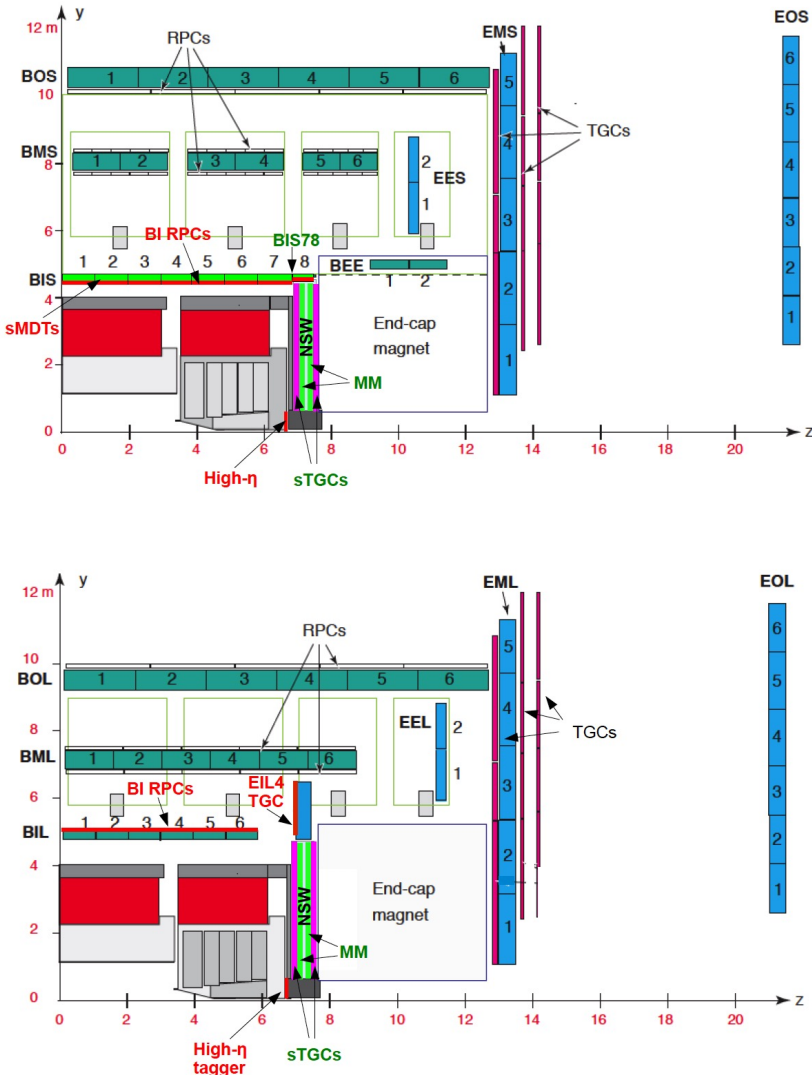


Figure 3.4 – Two R-Z views of the Phase-II ATLAS muon spectrometer layout showing a small sector (top) and a large sector (bottom). The drawings show the new detectors to be added in the Phase-II upgrade, including the addition of the high- η tagger (red text: BI RPC, sMDT, EIL4 TGC, high- η tagger), those to be installed during LS2 (green text: Micromegas and sTGC in the New Small Wheel and BIS78 RPC and sMDT), and those that will remain unchanged from the Run 1 layout (black text) [51].

The main limitations of the RPC system for operation at the HL-LHC are related to the chambers, owing to the more than a factor of seven higher luminosity than the chambers were designed for. The RPC rate capability depends on the total charge delivered per count, which, for the present RPCs, is 30 pC.

As a consequence, the single-gap efficiency will have to be reduced on average by 15%, and by 35% at large η . This efficiency loss will be compensated by installing a new layer of trigger chambers in the BI layer, increasing the overall barrel trigger redundancy.

To operate reliably at the HL-LHC, with high acceptance and efficiency and maintaining the high trigger selectivity of the present system, several upgrades are required for the RPC system:

- A new inner layer of BI RPC chambers will be added to the spectrometer. This will recover most of the current geometrical acceptance holes. The redundancy of the system will be greatly enhanced, so that full trigger efficiency can be maintained even if the old RPCs have to be operated at reduced efficiency, either to limit the effects of ageing or because the use of a different gas mixture is enforced. The BI RPCs will be new-generation RPCs with 1 mm gas gaps and high-sensitivity front-end electronics.
- The trigger and readout electronics (Pad and splitter boxes) have to be replaced in order to make the RPC system compliant with the Phase-II ATLAS trigger and readout scheme. The entire electronics chain, except for the front-end boards, will be replaced. The Pads will be replaced by the new data collector and transmitter (DCT) boards that will send all data off the detector to the counting room USA15 where the trigger and readout logic will be performed.
- In a worst-case scenario for the required reduction of efficiency of the old RPCs, a reduction of the trigger efficiency may still occur even after the BI RPC installation, in the region of $|\eta| > 0.8$. This efficiency loss can be recovered by retrofitting a limited number of BO chambers in that region. The retrofitting comprises replacing the original front-end electronics by the new BI version, and replacing the readout strip panels.

3.2.1 RPC upgrade

The BI system is designed to increase the trigger acceptance and the trigger efficiency, by loosening the requirements on the number of hits in the BM and BO chambers and, at the same time, adding the requirement of a coincidence with the BI layer. Any coincidences of hits in at least three chambers out of four (counting one BI, two BM, and one BO) will be accepted. Two-chamber BI-BO coincidences will be used to cover the remaining acceptance holes. Details of the Phase-II trigger algorithms and their performance are discussed in Section 3.2.2. Figure 3.5 illustrates the recovery of acceptance and efficiency obtained with the Phase-II trigger including the BI RPCs in a worst-case scenario in which the single-hit efficiency of the old RPC is reduced by 15–35% as a function of $|\eta|$, depending on the rate to which each chamber is exposed.

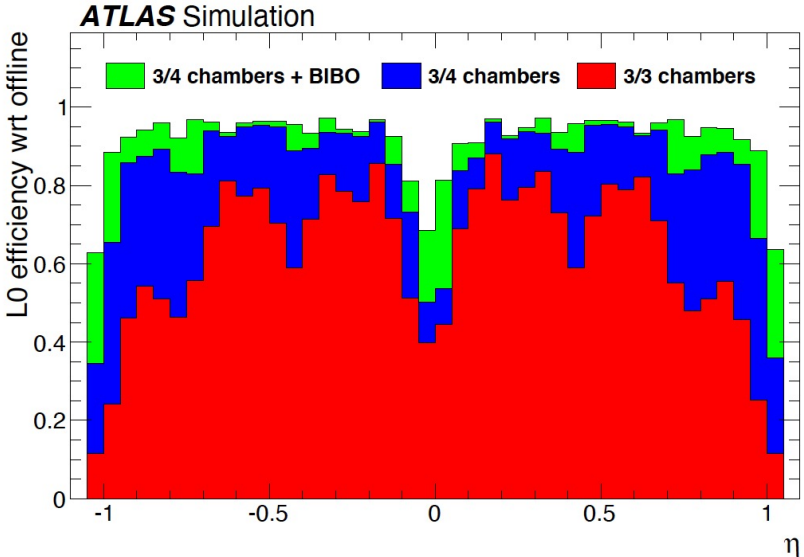


Figure 3.5 – Efficiency times acceptance of the L0 barrel trigger for reconstructed muons with $p_T = 25$ GeV as a function of η , assuming the worst-case scenario [51].

The new BI RPC chambers will have three sensitive gas gaps that are read out independently. A majority logic requiring hits in at least two out of three planes provides high efficiency while suppressing the rate of random coincidences due to uncorrelated hits from photons and neutrons. This is necessary, for instance, to keep the rate of BI-BO coincidences at an acceptable level. A major re-design of the RPC technology started around the year 2010, mainly aiming at a better rate capability and ageing behaviour. The new design is based on a reduced thickness of the gas gaps (from 2 mm to 1 mm) and of the resistive electrodes (from 1.8 mm to 1 mm), and on the use of a new generation of low-noise high-sensitivity amplifiers. Using these amplifiers, full efficiency can be achieved for a lower voltage across the gas gap, thus transferring part of the amplification from the gas avalanche to the electronics. In this way, the RPCs can be operated at a reduced charge per avalanche, reducing the detector current and thus improving rate capability

and ageing. A detail view of the positions of the BI RPCs in ATLAS is shown in Figure 3.6.

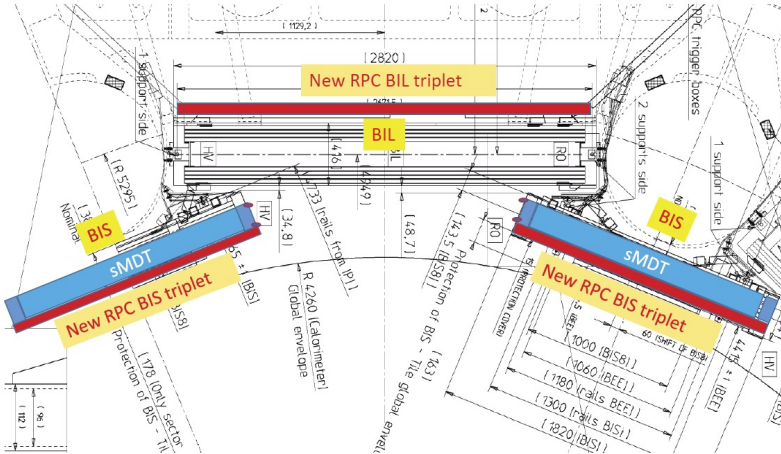


Figure 3.6 – X-Y view of the inner barrel layer, indicating the positions of the BI RPCs (red) and BIS sMDTs (blue) in the small and large sectors [51].

In the small sectors (BIS), due to the tight space limitations, the MDT chambers need to be replaced by new small-diameter MDT (sMDT) chambers with half the tube diameter (15 mm instead of 30 mm) in order to create space for the RPCs on the inside of the sMDT chambers. In the large sectors (BIL), the new RPCs will be installed on the outside of the existing MDTs. The layout of the new BI RPCs leaves the necessary holes and cut-outs for the existing MDT alignment lines and for detector services. It comprises 272 triplet RPC chambers, for a total area of about 470 m². Acceptance studies based on a realistic description of the BI RPC geometry show a geometrical acceptance of the BI RPC chambers of 91% for reconstructed muons with $|\eta| < 1.05$, compared to 95% for the MDT chambers. This results in a barrel trigger acceptance of 96%.

Each detector layer of the triplets is read out on both surfaces by orthogonal strip panels, providing η and ϕ measurements. The compact triplet structure and the use of highly sensitive amplifiers require a complete isolation of individual layers from each other. The choice of strip pitches, 24–26 mm depending on the chamber type, has been constrained by the performance requirements, the strip impedance, and cost considerations. The total number of readout channels is about 8700.

3.2.2 Trigger scheme

All the hits from RPC detectors will be available to the barrel Sector Logic board that uses them to generate barrel trigger candidates. The new BI RPCs increase the geometrical acceptance of the present barrel muon trigger and its robustness against inefficiencies of the old BM and BO RPCs caused by the reduced operating voltages necessary to ensure their longevity.

The RPC trigger will use nine measurement planes, provided by four layers of RPC chambers: one BI triplet (RPC0), two BM doublets (RPC1 and RPC2), and one BO doublet (RPC3).

Figure 3.7 shows the positions of the BI, BM, and BO RPC chambers in a small barrel sector together with the MDT chambers. The acceptance holes in the BM layer, caused by the magnet coils and their supports, are also visible.

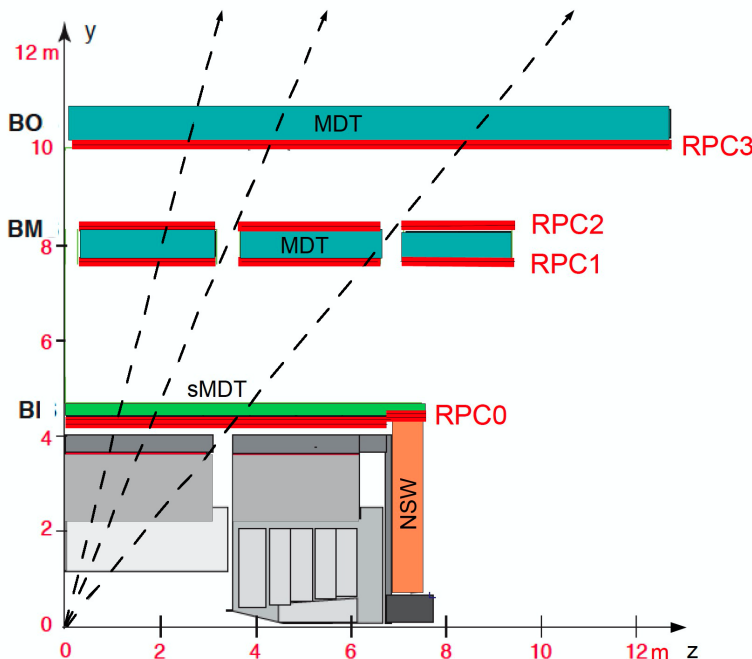


Figure 3.7 – Transverse section of a small sector in the barrel region, showing the four layers of RPC chambers (RPC0,1,2,3), as well as the MDT chambers in the barrel-inner (BI), barrel-middle (BM), and barrel-outer (BO) layers. The three dashed lines represent muon trajectories traversing four, two, and three RPC chambers [51].

To take advantage of the redundancy of detector planes, a trigger algorithm that does not make use of a fixed pivot plane (as in present ATLAS muon trigger) has been developed. This makes it possible to define different trigger coincidence logic schemes.

These schemes (summarised in Table 3.1 and illustrated in Figure 3.8) are based on different requirements on the four layers of RPC chambers:

- 3/3 chambers. Hits in at least three out of four planes of the RPC1+RPC2 chambers and in at least one out of two planes of RPC3. This is equivalent to the present high-pT trigger.
- 3/4 chambers. The previous requirement in a logical OR with the requirement of hits in at least two planes out of three in RPC0 and in at least three planes out of six in RPC1+RPC2+RPC3. In this way, all combinations of three-chamber coincidences (satisfying the above hit requirements) are accepted.
- 3/4 chambers + BI-BO. The previous requirement in a logical OR with the requirement of at least two hits in RPC0 and at least one hit in RPC3. This enhances the trigger coverage in the regions where no BM RPCs are installed due to the mechanical support structure of the toroid coils. The BI-BO coincidence is expected to be prone to accidental coincidences of uncorrelated background hits that are negligible in three-chamber coincidences. In the baseline version of this trigger, BI-BO coincidences are used in the whole barrel region, but can be limited to the BM acceptance gaps, if the muon trigger rate in the barrel gets too high.

Trigger	Requirement
3/3 chambers	$3[\text{RPC1+RPC2}] \text{ AND } 1[\text{RPC3}]$
3/4 chambers	$(3[\text{RPC1+RPC2}] \text{ AND } 1[\text{RPC3}]) \text{ OR } (2[\text{RPC0}] \text{ AND } 3[\text{RPC1+RPC2+RPC3}])$
3/4 ch.+BI&BO	$(3[\text{RPC1+RPC2}] \text{ AND } 1[\text{RPC3}]) \text{ OR } (2[\text{RPC0}] \text{ AND } 3[\text{RPC1+RPC2+RPC3}])$ $\text{OR } (2[\text{RPC0}] \text{ AND } 1[\text{RPC3}])$

Table 3.1 – The hit requirements used in different RPC triggers. The left column shows the short name used in the text. The right column gives the coincidence scheme used for the selection logic. The notation $N[\text{RPC}_i+\text{RPC}_j+\dots]$ indicates a majority requirement of hits in at least N planes out of all the possible planes available in RPC chambers RPC_i , RPC_j, \dots with $i, j, \dots \in \{0, 1, 2, 3\}$.

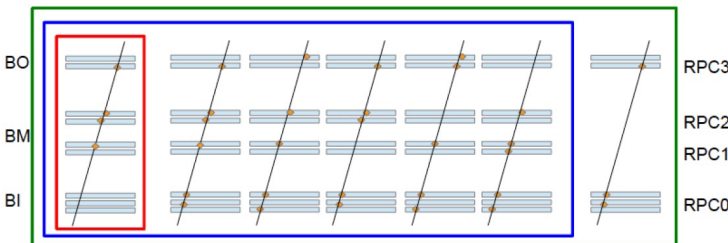


Figure 3.8 – Graphic view of the coincidence scheme used for the selection logic. High-Pt (3/3 chambers) in red, 3/4 chambers in blue, 3/4 chambers+BI&BO in green.

3.3 Hit digitization in the BI region

Since at the present time the new chambers in the BI region are not yet installed, the simulation performed for this work takes into account the presence of hits in the BI RPC chambers exploiting the true hits, recorded by the MDT chambers in the BI region, and treating them as hits of the future RPC chambers.

In this work, it has been used the the common framework `muTrigNt_write` [54] that includes a realistic digitization. This code reproduces the dimensions of the new BI RPC chambers and, given as input the true MDT hits, it checks if the hits are in the geometric acceptance. The code also allows to generate strips, of an arbitrary pitch, in the two orthogonal directions (η and ϕ) and thus to digitize the true MDT hits, recording them as hits with the coordinates reported in the center of the strip. In this way, it is possible to completely simulate the RPC chamber.

The studies presented in this chapter were performed using the official MC sample `mc15_14TeV.422063.ParticleGun_single_mu_Pt50.recon.ESD.e5392_s2988_s3000_r8974` [55], containing 50K events, produced with the ITk (Inner Tracker) simulation and with the layout of Run-I muons, that differs compared to the layout of Run-II muons because the feet and the elevator chambers are missing. This MC sample considers muons reconstructed in $|\eta| < 1.05$ by the off-line reconstruction, using a single-muon MC sample with fixed $p_T = 50$ GeV.

Given the framework described above, the goal of this work was to implement a simulation with a more realistic digitization that would produce:

- cluster size, strip number and the associated coordinates of the strips (Section 3.3.1);
- timing (Section 3.3.2);

3.3.1 The cluster size model

A single discharge in the gas volume can induce a signal in more than one RPC strip (i.e. it causes a so-called *cluster*), which is due to the charge sharing. The number of the RPC strips fired in temporal coincidence is called *cluster size*. The cluster size is a relevant parameter for the RPC detector and it must be strictly monitored to ensure a full trigger efficiency. The cluster size is simulated using a Gaussian charge distribution, with fixed width and centered on the true MDT hit that is induced on the strips [56]. This function is defined as:

$$G(z) = A(z) \cdot \frac{2}{\pi} \int e^{-\frac{\mu-z}{\sigma\sqrt{2}}} \quad (3.1)$$

where the amplitude $A(z)$ is a random distribution having a decreasing exponential distribution $f(A) = e^{-\frac{z}{\tau}}$, with the parameter $\tau = 0.8$, fixed width $\sigma = 16$ mm and μ is the z -coordinate of the hit. When the charge integrated over a strip exceeds a certain threshold (0.2 in this simulation), the strip is switched on.

This is not a strictly physical model but a decreasing exponential is useful to produce the expected tail, in the absence of a more realistic model for amplitudes based on experimental studies. A picture of the model used in this simulation is illustrated in Figure 3.9.

Cluster size is given by the number of strips fired at the same time.

It depends on the absolute value of charge integrated over a strip, but it also depends on the position of the true hit. Originally, the RPC hit is fixed to be at the center of the strip and the true MDT hit belongs to one strip only but in this simulation, it would be possible to have many strips fired at the same time using the relation: $\text{GlobPos}_i = \text{GlobPos}_{i,\text{true}} \pm \text{strip_center}_i$.

The resulting cluster size distribution is in line with the expectations in [51] and shown in Figure 3.10.

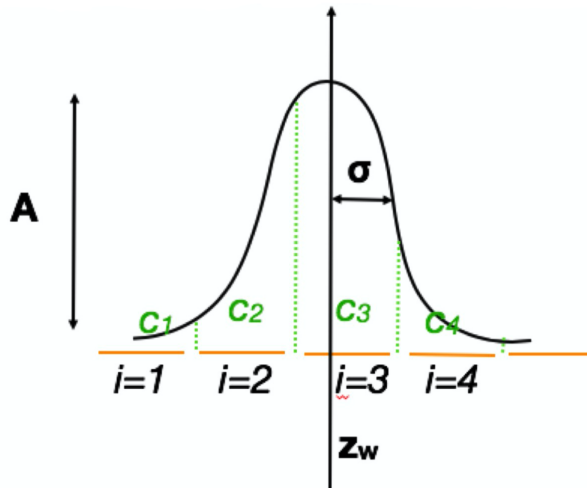


Figure 3.9 – Cluster size model used in the simulation. C_i is the charge integrated over a strip i . Some other parameters are the strip pitch z_w (22 mm), random amplitude A and width σ . When the charge integrated over a strip exceeds a certain threshold, the strip is switched on [56].

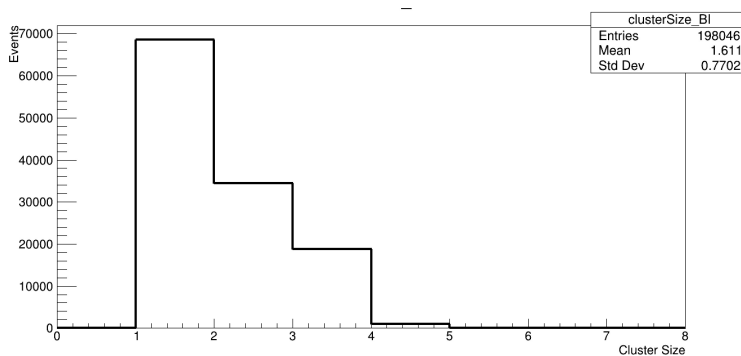
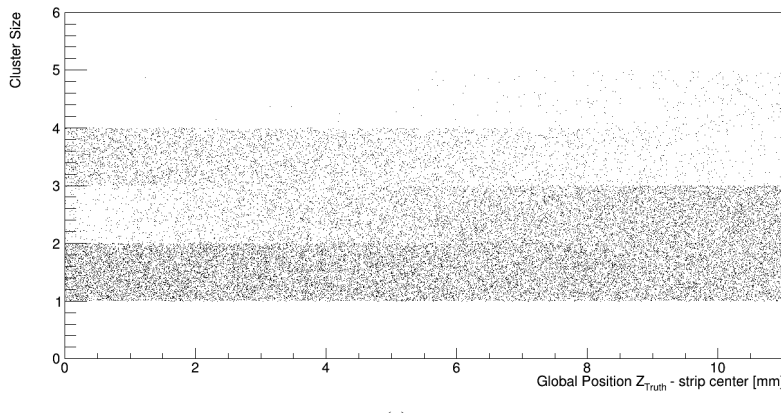


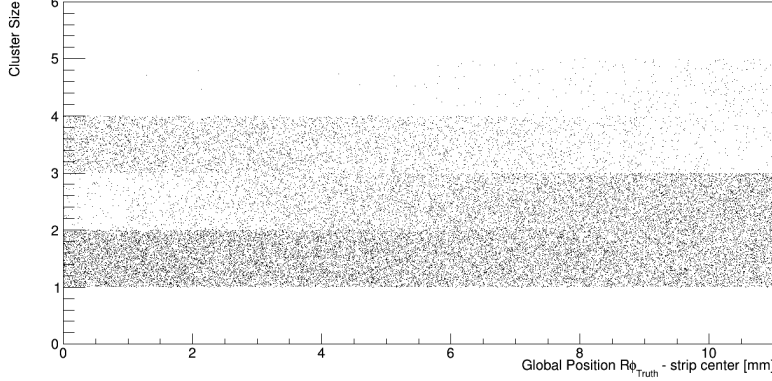
Figure 3.10 – Cluster size distribution obtained with the model and parameters illustrated in this section. The average value is 1.6.

Considering the hit distribution in Figure 3.11(a) for the η layer and Figure 3.11(b) for the ϕ layer, it is possible to see that:

- CS=0 is never possible by definition, one hit corresponds to at least one fired strip;
- CS=1 the hit distribution is uniform, because the integrated charge is less than the fixed threshold;
- CS=2 mostly when the truth hit is far from the strip center and at the strip edge;
- CS=3 mostly when the truth hit is far from the strip edge and at the strip center;
- CS=4 mostly when the truth hit is far from the strip center and at the strip edge.



(a)



(b)

Figure 3.11 – RPC hit distribution GlobPos_i for (a) strips along η and (b) strips along $R\phi$.

Strips in η and ϕ layers are orthogonal to each other and it is possible to see how they are arranged as a function of the Global Position in the BI region of the ATLAS detector.

In particular, in Figure 3.12(a) strips oriented along η are ordered in such a way that the strip number one is the inner strip, while Figure 3.12(b) shows that strips oriented along ϕ are always oriented with increasing ϕ .

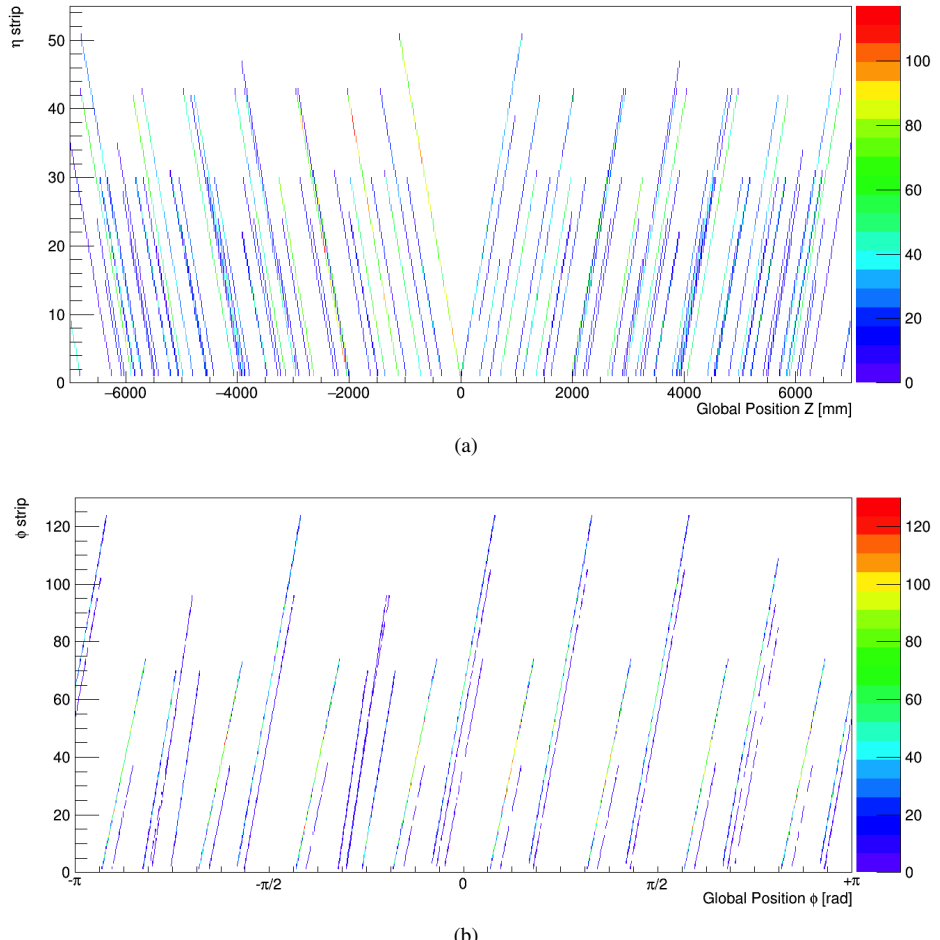


Figure 3.12 – Arrangement of strips in the (a) η layer and (b) ϕ layer as a function of the Global Position in the BI region of the ATLAS detector.

Tables 3.1(a) and 3.1(b) summarises the main chamber parameters of the expected layout for the Phase-II upgrade. Strip and front-end board entries are based on the assumptions of a 20 mm pitch and eight channels per board.

Figure 3.13 shows the number of η and ϕ strips switched on in the simulation. It is possible to verify that the simulation developed for this work follows the requirements of the Phase-II upgrade for BI RPCs to be realistic and reliable as much as possible.

RPC type	BIL-A	BIL-B	BIL-C	BIL-D	BIL-K	BIL-E	BIL-F	BIL-G	BIL-H	BIL-I	BIL-J
# of units	72	2	4	2	2	14	2	8	6	2	2
# of layers	3	3	3	3	3	3	3	3	3	3	3
length in Z (mm)	640	510	365	600	220	640	540	450	310	370	370
width in ϕ (mm)	2750	2750	2750	2750	2750	2380	2380	2300	2100	1850	1700
η strip pitch (mm)	18.4	19.2	19.7	17.2	21.3	18.4	20.4	16.7	16.3	20.0	20.0
ϕ strip pitch (mm)	21.1	21.1	21.1	21.1	21.1	20.8	20.8	21.6	21.4	20.5	20.6
# η strips/layer	32	32	16	32	8	32	24	24	16	16	16
# η strips/unit	96	96	48	96	24	96	72	72	48	48	48
# ϕ strips/layer	128	128	128	128	128	112	112	104	96	88	80
# ϕ strips/unit	408	408	408	408	408	360	360	336	312	288	264
area/layer (m^2)	1.76	1.40	1.00	1.65	0.61	1.52	1.29	1.04	0.65	0.68	0.63
gap area (m^2)	1.61	1.25	0.86	1.50	0.47	1.39	1.15	0.91	0.54	0.58	0.54
Gas volume/layer (l)	4.82	3.76	2.59	4.49	1.41	4.16	3.46	2.73	1.63	1.75	1.61
# FE cards/layer η	4	4	2	4	1	4	3	3	2	2	2
# FE cards/layer ϕ	16	16	16	16	16	14	14	13	12	11	10

RPC type	BIR-A	BIR-B	BIR-C	BIR-D	BIM-A	BIM-B	BIS-A	BIS-B
# of units	4	8	8	4	12	24	16	80
# of layers	3	3	3	3	3	3	3	3
length in Z (mm)	780	916	1104	735	437	495	1096	916
width in ϕ (mm)	2099	1251	819	1260	1536	1536	1820	1820
η strip pitch (mm)	18.3/22.8	21.7	22.0	21.4	16.1/24.2	18.5/27.8	21.8	21.7
ϕ strip pitch (mm)	21.3	21.4	19.2/24.0	21.6	20.6	20.6	20.1	20.1
# η strips/layer	40/32	40	48	32	24/16	24/16	48	40
# η strips/unit	120/96	144	168	96	72	72	168	120
# ϕ strips/layer	96	56	40/32	56	72	72	88	88
# ϕ strips/unit	288	168	120/96	168	216	216	264	264
area/layer (m^2)	1.64	1.15	0.90	0.93	0.67	0.76	2.00	1.67
gap area (m^2)	1.51	1.05	0.82	0.84	0.58	0.67	1.86	1.54
Gas volume/layer (l)	4.52	3.15	2.45	2.51	1.75	2.01	5.59	4.63
# FE cards/layer η	5/4	5	6	4	3/2	3/2	6	5
# FE cards/layer ϕ	12	8	5/4	7	9	9	11	11

Table 3.2 – Main parameters of (a) the BIL RPC chambers and (b) the BIR/BIM/BIS RPC chambers [51].

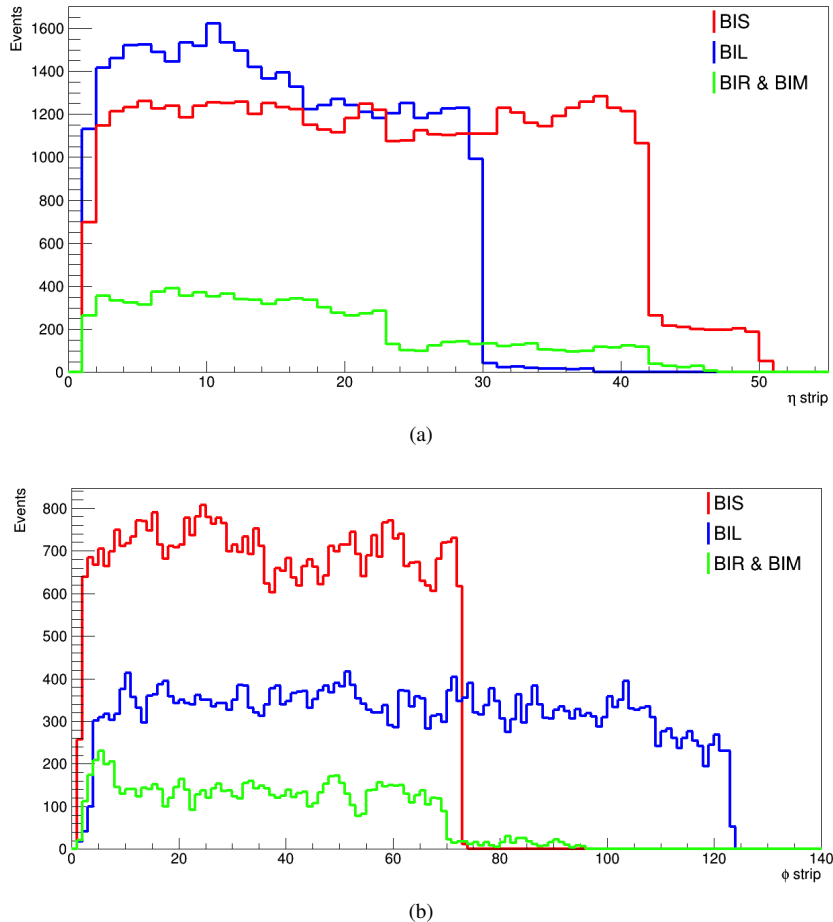


Figure 3.13 – Number of (a) η and (b) ϕ strips switched on for different chambers: BIS in red, BIL in blue, BIR & BIM in green.

3.3.2 Timing

Another important variable is the time taken for the particle to pass through the detector. It is important because it is one of the discriminating variables in the algorithm's selection of hits. Only hits recorded in the bunch crossing event are considered and not all the hits previously recorded. Therefore, all hits outside 25 ns coincidence window around the bunch crossing of interest are excluded.

In order to simulate the new RPCs one has to take into account several effects and apply an appropriate correction and extract a digital readout.

The final formula used to extract the digitized time in which the hit is recorded by the detector is:

$$t_{hit} = \text{int}^1 \left\{ \frac{t_{true} + t_{Gauss} + t_{FE} - t_{cal}}{\Delta t} \right\} \Delta t \quad (3.2)$$

- t_{true} is the true hit recorded by the MDT;
- Δt is the sampling rate (0.3 ns). The final t_{hit} must be a multiple of the sampling rate to have a digitization;
- t_{Gauss} is a Gaussian term that reproduces the fluctuations in the RPC signal (smearing 0.4 ns);
- t_{FE} is the propagation of the signal along the strip to the FE electronics assuming that the signal speed on the layer is 200 mm/ns;
- t_{cal} is the calibration offset. The true hit timing is recorded referring to the time of the collision on the MDT tubes. To report the timing centered around 0, it was necessary to subtract the time of flight of the particle assuming time to be calibrated with prompt muons crossing the center of the strip at $t = 0$.

Figure 3.14 shows the digitized time associated to the RPC hit calculated using the Equation 3.2. The tail of the distribution is given by low p_T muons that produce secondary hits.

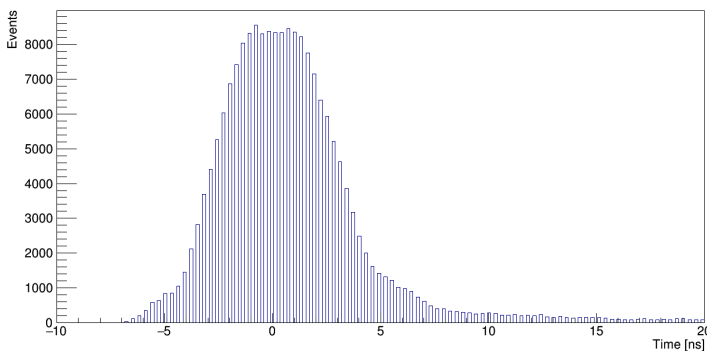


Figure 3.14 – Digitized time associated to the RPC hit. The tail of the distribution is given by low p_T muons that produce secondary hits

¹The int function takes the integer part of a real number.

3.4 L0 barrel trigger efficiency

The performance of the barrel muon trigger was studied using single-muon MC samples with fixed $p_T = 50$ GeV, for a fixed transverse momentum threshold: $p_T > 10$ GeV [57] and with the hit digitization described in the previous sections.

To study the robustness of the trigger against possible efficiency reductions of the old RPCs in the BM and BO layers, the simulation was performed in the so-called "worst-case scenario" that introduces inefficiencies depending on the station type and sector and summarised as Table 3.3. It includes inefficiencies due to a reduction of the high voltage of the BM and BO RPCs such that the expected RPC current is always below the safe operation limit.

Station Name	StationEta							
	1	2	3	4	5	6	7	8
BOL	0.90	0.90	0.82	0.82	0.76	0.74	-	-
BOS/BOG/BOF	0.89	0.90	0.90	0.90	0.89	0.66	0.60	0.60
BML	0.88	0.88	0.88	0.83	0.56	0.56	0.60	-
BMS	0.90	0.90	0.90	0.87	0.81	0.81	-	-

Table 3.3 – Efficiency for each station and sector of the barrel muon trigger in the "worst-case scenario". This scenario includes inefficiencies due to a reduction of the HV of the BM and BO RPC [57].

The trigger efficiency times acceptance for each trigger logic scheme is listed in Table 3.4 and it is defined as the fraction of reconstructed muons that are accepted by the trigger, using the simulation that includes the RPC detector efficiency. The trigger efficiency times acceptance is also presented in Figure 3.15. Adding the new BI RPC layer greatly reduces the dependence of the trigger efficiency on the hit efficiency of the old RPCs.

BM and BO efficiency (%)	Trigger efficiency x acceptance (%)		
	3/3 chambers	3/4 chambers	3/4 chambers + BIBO
WCS	58.78	83.27	91.89

Table 3.4 – Efficiency times acceptance for the L0 barrel trigger for each trigger logic scheme, assuming the worst-case scenario with the hit digitization .

Starting from the WCS scenario, other two studies have been performed on the L0 barrel trigger efficiency using simulations with RPC stations in various operational conditions: the first study is the refurbish of BM and BO chambers (Section 3.4.1) and the second study is about the installation of BI chambers in the rail sectors 11 and 15 (Section 3.4.2).

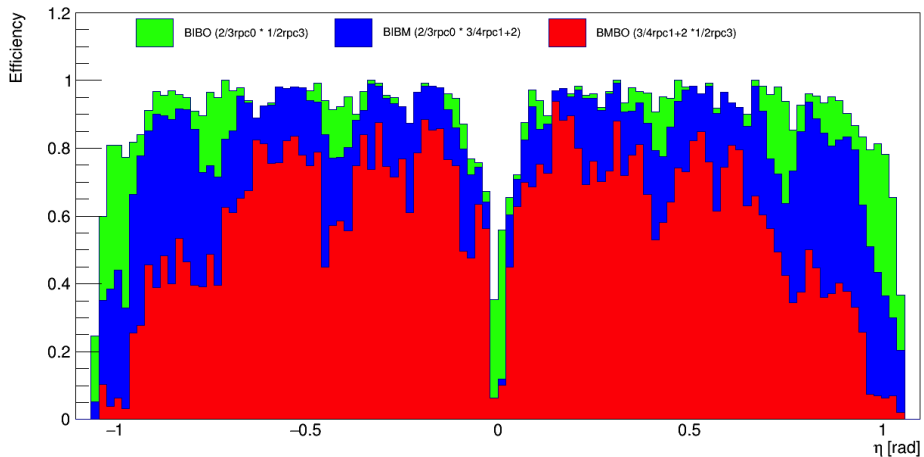


Figure 3.15 – Efficiency times acceptance of the L0 barrel trigger for each trigger logic scheme, assuming the worst-case scenario with the hit digitization.

3.4.1 BM and BO retrofitting

In the Phase-II upgrade of the muon system, most of the readout electronics will be replaced to make it faster and resistant to radiation. An essential step is therefore to understand what would be the impact of the legacy BM/BO chambers with the new electronics.

In this first study, efficiencies of the "worst-case scenario" summarised in Table 3.3, are used, except for the following stations set to 100% efficiency:

1. BML 7,
2. BOL 6,
3. BOS 6,
4. BOL 5.

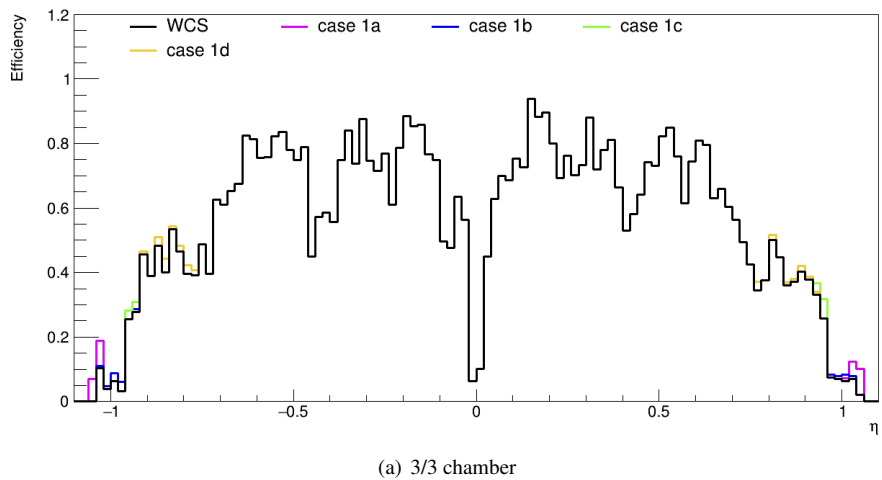
The products of muon trigger efficiency and acceptance for the BM and BO retrofitting are listed in Table 3.5.

The trigger efficiency times acceptance is also presented in Figure 3.16 that compare the "worst-case scenario" with all the variants of the WCS, in which some stations are fixed to 100% efficiency.

In the first analysed case, the most relevant effect on the trigger efficiency times acceptance is on the 3/4 chambers logic scheme, in particular for the Case 1b (BOL 6 100%) the variation is +1.08% compared to the "worst-case scenario".

BM and BO efficiency (%)	Trigger efficiency x acceptance (%)		
	3/3 chambers	3/4 chambers	3/4 chambers + BIBO
WCS	58.78	83.27	91.89
Case 1a (BML 7 100%)	+0.22	+0.26	+0.14
Case 1b (BOL 6 100%)	+0.13	+1.08	+0.53
Case 1c (BOS 6 100%)	+0.16	+0.51	+0.63
Case 1d (BOL 5 100%)	+0.23	+0.82	+0.41

Table 3.5 – Efficiency times acceptance for the L0 barrel trigger for different assumptions on the hit efficiency of the present RPC detectors. The “WCS” row corresponds to the scenario in which the efficiencies are listed in Table 3.3. The other rows correspond to the variants of the WCS, in which the efficiency of some stations are set to 100%. The corresponding results of these variants, are expressed as variations to the WCS [57].



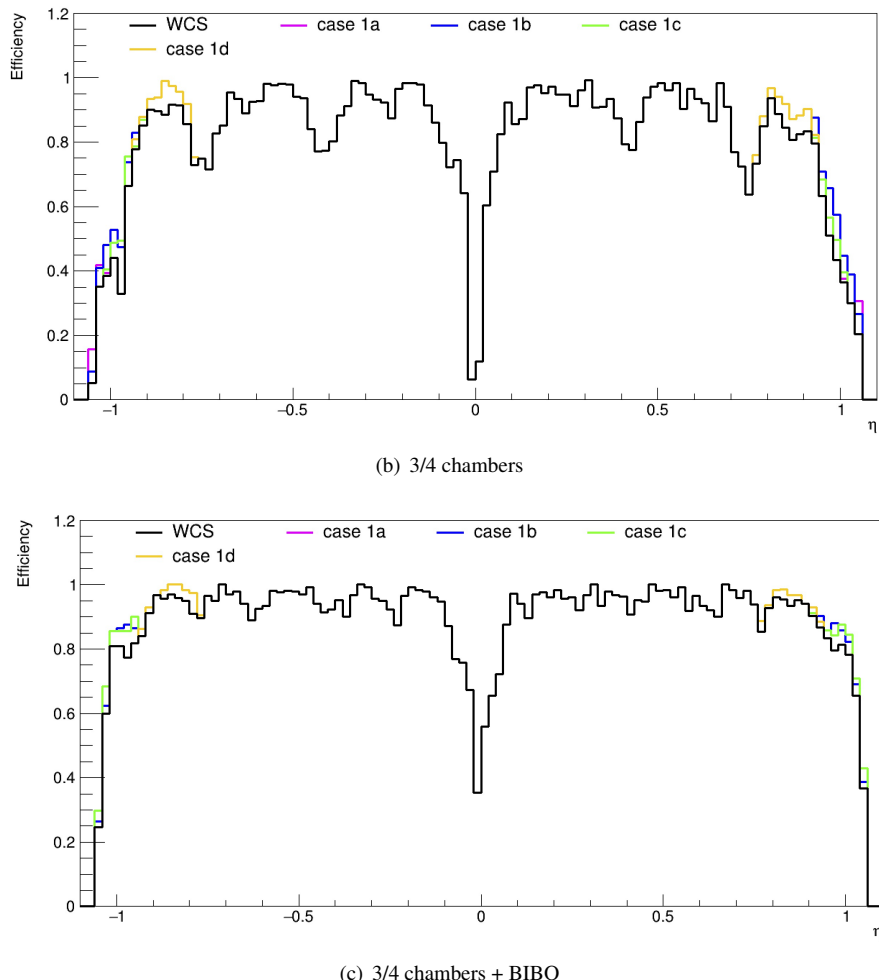


Figure 3.16 – Efficiency times acceptance of the L0 barrel trigger compared to reconstructed muons with $p_T = 50$ GeV as a function of η taking in to account all the variants of the WCS. The histograms show the efficiency of (a) the existing 3/3 chambers trigger, of (b) the 3/4 chambers trigger including the BI layer, and (c) the additional gain from the BI-BO trigger. Efficiency times acceptance is defined as the fraction of reconstructed muons accepted by the trigger, using a simulation that includes the RPC detector efficiency [57].

3.4.2 Dropping BIR and BIM chambers

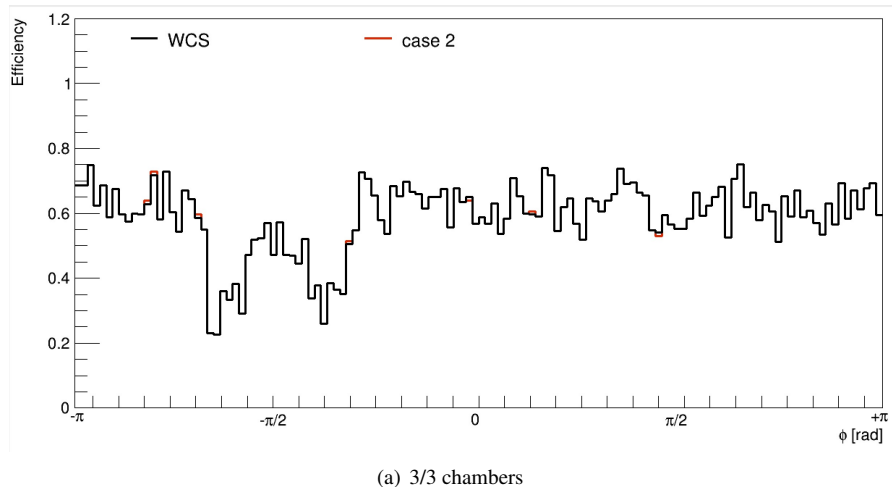
Since the installation of the RPCs in the sectors 11 and 15 seems to be very hard, another special case was performed simulating a scenario in which BIM and BIR RPC are not installed in these sectors.

The products of muon trigger efficiency and acceptance for this second study are listed in Table 3.6.

The results are also presented in Figure 3.17 that compares the "worst-case scenario" with this second case, in which BIM and BIR are turned off. The efficiency distributions show that the absence of BIR and BIM has the most relevant effect on the 3/4 chambers + BIBO logic scheme with a corresponding variation of -3.11%.

BM and BO efficiency (%)	Trigger efficiency x acceptance (%)		
	3/3 chambers	3/4 chambers	3/4 chambers + BIBO
WCS	58.78	83.27	91.89
Case 2 (BIM BIR off)	+0.03	-2.70	-3.11

Table 3.6 – Efficiency times acceptance for the L0 barrel trigger for different assumptions on the hit efficiency of the present RPC detectors. The WCS row corresponds to the scenario in which the efficiencies are listed in Table 3.3. The row "Case 2" corresponds to the case in which the RPCs in the sectors 11-15 (BIM and BIR) are turned off. The corresponding results of the Case 2, are expressed as variations to the WCS [57].



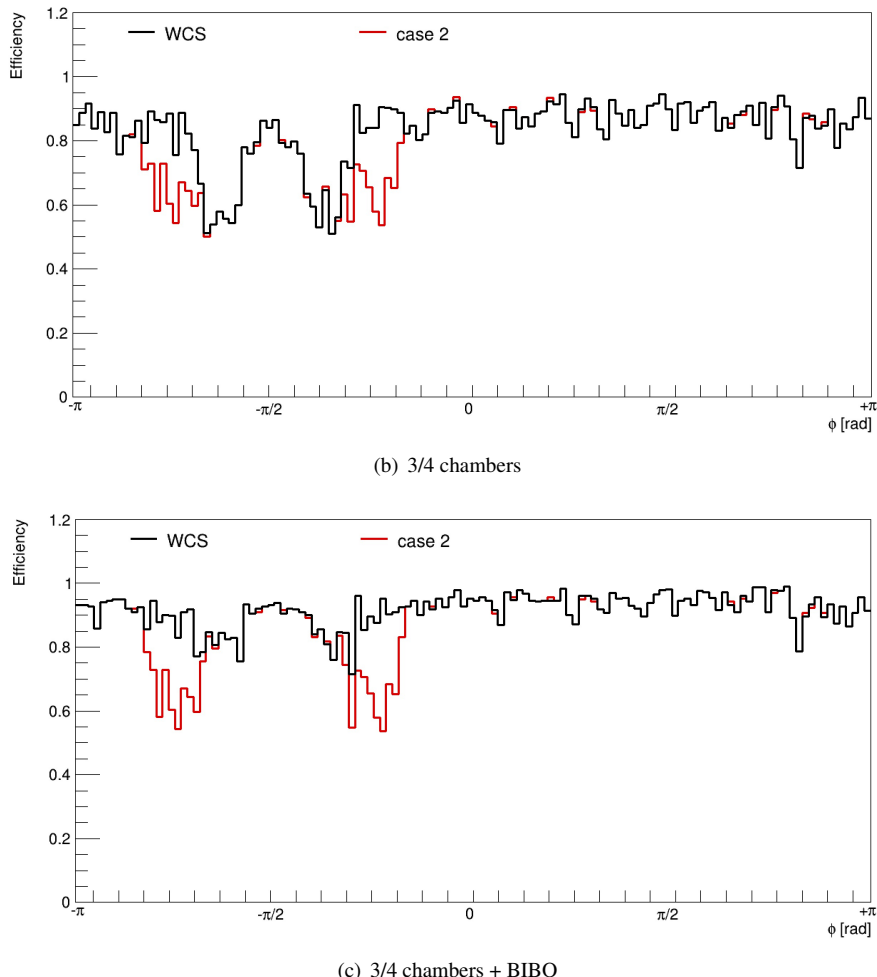


Figure 3.17 – Efficiency times acceptance of the L0 barrel trigger compared to reconstructed muons with $p_T = 50$ GeV as a function of ϕ . The histograms show the efficiency of (a) the existing 3/3 chambers trigger, of (b) the 3/4 chambers trigger including the BI layer, and (c) the additional gain from the BI-BO trigger. Efficiency times acceptance is defined as the fraction of reconstructed muons accepted by the trigger, using a simulation that includes the RPC detector efficiency [57].

3.5 Summary and considerations

The works described in this chapter aimed at a new simulation of the RPC in the BI region. They involved the construction of a model:

- for the definition of the cluster size, which is important for creating a simulation as realistic as possible;
- to define a variable that represents the time taken by the particle to pass through the detector, which is important because it is one of the discriminating variables in the algorithm's selection of hits.

The new developed model results in agreement with the required technical characteristics of the RPCs for Phase-II, described in the Technical Design Report [51].

A more realistic simulation of the RPCs is now available for further studies.

Using this model, L0 barrel trigger efficiency studies were performed in the following two scenarios:

1. the refurbish of BM and BO chambers, to understand what would be the impact of the legacy BM / BO chambers with the new electronics;
2. the drop of BIR and BIM chambers, given that the installation of the RPCs in the sectors 11 and 15 seems to be very hard.

The first scenario gives an estimation of the improvements by replacing the electronics. Moreover, the most significant expected improvement is from BOL6.

The second scenario showed that there is a significant loss of efficiency if the collaboration decides to don't install the RPC in sectors 11 and 15.

These two studies will help plan the work for the Phase-II upgrade.

CHAPTER 4

Data modeling and object reconstruction

Monte Carlo event generators are the indispensable workhorses of particle physics, bridging the gap between theoretical ideas and first-principles calculations on the one hand, and the complex detector signatures on the other hand. In fact, they are mainly used to predict event rates and topologies, simulate possible backgrounds, study detector requirements and study detector imperfections.

The same reconstruction algorithms are used to reconstruct data and all Monte Carlo samples.

4.1 Event simulation

To understand what the final state of any given physics process looks like, *Monte Carlo simulation* (MC) is used to model both the initial and final state of the process of interest, as well as the propagation of particles through the detector.

A typical MC simulated $p - p$ collision can be schematized as in Figure 4.1.

The first step of an event simulation is represented by the extraction of initial-state partons and the evaluation of their momenta using the proton PDFs. Fixed order matrix element (ME) are used to determine the cross section for the hard scatter integrated over the phase space of the final state particles and it also predicts their momenta. The particles produced by the hard scatter then undergo a process of *parton showering* (PS), where the quarks and gluons produce a “shower” of further coloured particles. Gluons are emitted and particles are produced until the energy scale is below 1 GeV, at which point, the *hadronisation* process starts and colorless hadrons are formed. These hadrons then decay into lighter particles.

As well as the original hard scatter, additional interactions between other partons within the proton must be included in a process known as *underlying event*.

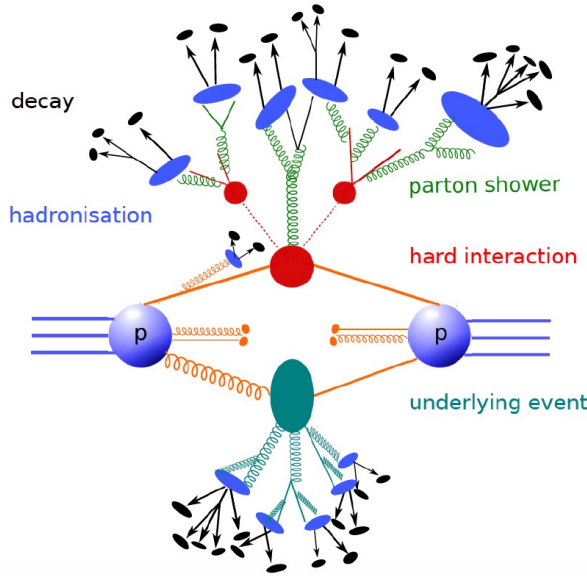


Figure 4.1 – Typical Monte Carlo simulated event with representation of several processes: underlying event, hard scattering, parton shower, hadronisation and decay.

Finally, *pile-up* collisions are also overlaid, which originate from collisions of other protons in the beam. For hadronisation, two main models exist: the string model [58] and the cluster model [59]. In the PYTHIA event generator [60] the string model is used whereas the HERWIG event generator [61] uses the cluster model. The differences in behaviour of these models can be used to assess the uncertainty due to the model chosen.

The output of the MC event generation process is used as an input to a simulation of the ATLAS detector. This simulation describes all of the detector material and geometry, as well as any defects in the material or electrical problems. The simulation is built using the GEANT4 [62] simulation software. The output of the detector simulation is reconstructed in the exact same way as data to allow the two to be compared directly. The simulation of the passage of particles through the detector is very computationally expensive. This is mainly due to simulation of the calorimeters, because it is extremely time-consuming to simulate the particle showers. To speed this up, an approximate simulation, ATLASFAST-II (AFII) [63], is often used. This approximate model simulates the particle showers in the calorimeters using parametrised functions applied to particle energy, rather than carrying out the full shower simulation.

4.2 Object reconstruction

This section describes the main reconstruction and identification criteria applied for each physics objects considered in this analysis (electrons, muons, jets, b -tagged jets and missing transverse momentum). A summary of the object selections is reported in Table 4.1 and acronyms are defined in the following sections.

	p_T	$ \eta $	ID	Isolation	Additional cuts
Electrons	$> 15 \text{ GeV}$	< 2.47	MediumLH	PLVTight	$ d_0^{\text{BL}} \text{ significance} < 5$ $ \Delta z_0^{\text{BL}} \sin \theta < 0.5 \text{ mm}$
Muons	$> 15 \text{ GeV}$	< 2.5	Medium	PLVTight	$ d_0^{\text{BL}} \text{ significance} < 5$ $ \Delta z_0^{\text{BL}} \sin \theta < 0.5 \text{ mm}$
Soft Muons	$> 4 \text{ GeV}$	< 2.5	Tight	–	$ d_0 < 3 \text{ mm}$ $ z_0 \sin \theta < 3 \text{ mm}$ $\Delta R(\mu, \text{jet}) < 0.4$
Jets	$> 25 \text{ GeV}$	< 2.5	PFlow	–	JVT
b -jets	$> 25 \text{ GeV}$	< 2.5	DL1r @77 %	–	–

Table 4.1 – Overview of the requirements applied for selecting objects.

4.2.1 Electrons

Electron candidates are reconstructed from energy clusters in the electromagnetic (EM) calorimeter that match a reconstructed track in the inner detector (ID) [64–67]. The clusters are required to be within the range $|\eta| < 2.47$, excluding the transition region between the barrel and endcap calorimeters at $1.37 < |\eta| < 1.52$. Electron candidates must also satisfy a transverse energy requirement of $E_T > 15 \text{ GeV}$.

Further requirements on the electromagnetic shower shape, calorimeter energy to tracker momentum ratio, and other discriminating variables are combined into a likelihood-based object quality cut (LH), optimised for strong background rejection. All electron candidates in this analysis must pass the MediumLH selection.

Electron tracks are also required to be consistent with the primary vertex of the collision, applying the requirements: $|d_0^{\text{BL}} \text{ significance}| < 5$ and $|\Delta z_0^{\text{BL}} \sin \theta| < 0.5 \text{ mm}$.

Electrons are further required to be isolated, to reject candidates coming from sources other than prompt W or Z boson decays (hadrons faking an electron signature, heavy-flavour decays or photon conversions).

The isolation working point used in this analysis is PLVTight. Correction factors are applied to simulated performance functions to take into account the small differences in reconstruction, identification and isolation efficiencies between data and MC simulation.

4.2.2 Muons

Muon candidates are reconstructed by combining a reconstructed track from the ID with one from the muon spectrometer (MS) [68], and are required to have $p_T > 15 \text{ GeV}$ and $|\eta| < 2.5$.

The different combinations of input information (from ID and MS) leads to four different types of reconstructed muons:

- **Combined muons (CB):** a combined track is formed reconstructing independently tracks in the ID and MS;
- **Segment-tagged muons (ST):** a track in the ID is classified as a muon if, once extrapolated to the MS, it is associated with at least one local track segment in the MDT or CSC chambers;
- **Calorimeter-tagged muons (CT):** classification for ID tracks that are matched to an energy deposit in the calorimeter and it is compatible to a minimum ionising particle;
- **Extrapolated muons (ME):** the reconstructed trajectory of ME muons uses only the MS track and some loose requirement that its origin is the interaction point;

Muons from Z or W boson decays are labelled *prompt* muons whereas those coming from pion or kaon decays are *non-prompt* muons.

This analysis needs the suppression of the contribution from non-prompt muons, therefore requirements are placed on muon candidates.

In CB tracks, the variables commonly used in muon identification are:

- **q/p significance:** defined as the absolute value of the difference between the ratio of the charge and momentum of the muons measured in the ID and MS divided by the sum in quadrature of the corresponding uncertainties;
- ρ' : defined as the absolute value of the difference between the transverse momentum measurements in the ID and the MS divided by the p_T of the combined track;
- χ^2 : normalised χ^2 of the combined track fit.

To reject misidentified muon candidates, primarily originating from pion and kaon decays, several quality requirements can be imposed on the muon candidate.

There are four muon identification working points:

- **Tight Muons:** selected to maximise the purity of muons at the cost of some efficiency. Only CB muons with hits in at least two stations of the MS and satisfying the Medium selection criteria are considered. The reconstruction efficiency for Tight muons in the range $20 < p_T < 100$ GeV is 91.8%.
- **Medium Muons:** this is the default working point used by the ATLAS collaboration. Only CB and ME tracks are used. The CB tracks are required to have 3 hits in at least two MDT layers. The reconstruction efficiency for this working point in the range $20 < p_T < 100$ GeV is 96.1%.
- **Loose Muons:** all CB and ME muons that satisfy the Medium requirement are also included in the Loose selection. It is optimised to maximise the reconstruction efficiency, while still retaining only good quality muon tracks. The reconstruction efficiency for Loose muons in the range $20 < p_T < 100$ GeV is 98.1%.
- **High- p_T Muons:** the selection is optimised for analyses searching for high-mass resonances using muons. CB muons are required to pass the Medium selection and have at least three hits in three MS stations. This selection maximises the momentum resolution for muons with $pT > 100$ GeV

The muon candidates in this analysis must pass the Medium identification definition, already described above. Muon tracks are also required to be consistent with the primary vertex applying the requirements: $|d_0^{\text{BL}} \text{ significance}| < 3$ and $|\Delta z_0^{\text{BL}} \sin \theta| < 0.5 \text{ mm}$.

Muons are further required to be isolated and the isolation working point used in this analysis is PLVTight.

Like for electrons, correction factors are applied to simulated performance functions to account for residual small differences between data and simulation.

4.2.3 Jets

Jets are reconstructed using the particle flow algorithm [69].

All jets considered in this analysis should have a transverse momentum $p_T > 25 \text{ GeV}$ and a pseudo-rapidity of $|\eta| < 2.5$. To suppress jets from in-time pileup, the Jet Vertex Tagger (JVT) discriminant, which is based on a two-dimensional likelihood method, is used [70]. A JVT value of at least 0.59 is required for jets with $p_T < 60 \text{ GeV}$ and $|\eta| < 2.4$, corresponding to an efficiency of 92%.

4.2.4 Soft Muon Tagging

The Soft Muon Tagging (SMT) is a tagging technique for heavy-flavour jets.

It exploits the $b \rightarrow \mu + X$, $b \rightarrow c \rightarrow \mu + X$ and $c \rightarrow \mu + X$ decay chains (with a total BR $\approx 20\%$), by identifying muons reconstructed inside jets. Those muons are referred to as soft muons. Different requirements are applied to select and distinguish muons from leptonic decays of the Z and W bosons (referred to as ‘prompt’ or ‘isolated’ muons in the following) and muons from semi-leptonic heavy-hadron decays (called ‘soft’ or ‘SMT’ muons in the following).

Reconstructed muons with $p_T > 4 \text{ GeV}$ not passing the prompt muon selection can instead be selected as soft muons.

Soft muons are required to pass the Tight quality requirements [71] because this working point has a better rejection of muons coming from pions/kaons with respect to Medium quality requirements. Soft muons are also required to be closer than 0.25 in ΔR within a selected jet.

The closest jet to a soft muon is defined as the ‘SMT’ jet. This value has been optimized looking at the kinematic distributions of $\Delta R(\mu^{\text{soft}}, \text{SMT jet})$, maximizing $S/\sqrt{S+B}$.

Very loose requirements are applied on the impact parameters to remove pathological cases: $|d_0| < 3 \text{ mm}$ and $|z_0 \sin \theta| < 3 \text{ mm}$.

More details on the soft muon tagging are in Ref. [72].

4.2.5 Recurrent Deep-Learning DL1r

In this analysis the DL1r algorithm is used [73, 74]. It is based on a deep feed-forward neural network (NN) trained using Keras [75] with the Theano [76] backend and the Adam optimiser [77]. The DL1 NN has a multidimensional output corresponding to the probabilities for a jet to be a b-jet, a c-jet or a light-flavour jet. The topology of the output consists of a mixture of fully connected hidden and Maxout layers [78]. The input variables to DL1 consist of those used for the previous official algorithm MV2, with the addition of the JETFITTER c-tagging variables described in Ref. [74].

4.2.5.1 *b*-tagged jets

Jets originating from bottom quarks (called *b*-tagged jets) are identified by reconstructing secondary vertices from the tracks associated to the jets and by combining their spatial parameters with life-time related information. In the current analysis the `DL1r` algorithm with the 77% of *b*-quark-tag efficiency operation point is used.

Finally, all *b*-tagged jets considered in this analysis should have a transverse momentum $p_T > 25 \text{ GeV}$ and a pseudo-rapidity of $|\eta| < 2.5$.

4.2.5.2 *c*-tagged jets

The `DL1r` algorithm also allows to construct DL1r_c discriminant that is used for charm-tagging. They are reconstructed jets satisfying $p_T > 25 \text{ GeV}$ and $|\eta| < 2.5$ requirements, and failing the *b*-tagging requirement. This search uses the cut operation point giving the *c*-efficiency of 20% studied and being calibrated in the *tc+MET SUSY* analysis [79].

More details of charm-tagging are given in Chapter C.

4.2.6 Missing transverse momentum

The missing transverse momentum, E_T^{miss} , is a measure of the transverse momentum imbalance, usually due to escaping neutrinos. It is calculated as the magnitude of the negative vector sum of the momenta in the transverse plane of all selected calibrated physics objects in the event [80, 81]. To account for the soft hadronic activity, a soft term is added, built from tracks that are associated to the hard-scatter vertex but are not associated to any of the reconstructed objects. The soft term is included in order to account for low-momentum particles that are not identified among the final state objects [82–84].

It also includes an extra term to account for energy losses due to the detector inefficiencies and resolution leading to the mis-measurement of the true transverse energy of the final interacting objects.

4.2.7 Overlap removal

In order to avoid double counting of single final state objects, like e.g. an isolated electron being reconstructed both as an electron and as a jet with the requirements above, a procedure is followed to remove overlaps between final state objects. This is the sequence of operation that are performed to solve these ambiguities, as implemented by the harmonized option [85] in the `AssociationUtils` [86] package:

- Electron candidates which share a track with a muon candidate are removed.
- If the distance in ΔR between a jet and an electron candidate is $\Delta R < 0.2$, then the jet is dropped. If multiple jets are found with this requirement, only the closest one is dropped.
- If the distance in ΔR between a jet and a baseline electron is $0.4 < \Delta R < 0.2$, then the electron is dropped.
- If the distance in ΔR between a jet and a muon candidate is $\Delta R < 0.4$, then: if the jet has more than 2 associated tracks then the muon is not considered as prompt, otherwise the jet is removed. This procedure does not affect the E_T^{miss} calculation.

No overlap removal is performed on muons used for the Soft Muon Tagging.

CHAPTER 5

Analysis strategy, "Data and Monte Carlo samples"

This chapter presents a search for flavour-changing neutral current top-quark decay $t \rightarrow Zc$. The study uses a data sample from proton–proton collisions at $\sqrt{s} = 13$ TeV recorded in full Run2 (from 2015 to 2018) by the ATLAS experiment, and targets final states with three leptons (either electrons or muons).

I developed most of the analysis, from the event selection up to the extraction of the final results.

5.1 Analysis strategy

In the following, the analysis strategy is described.

Analysis overview The analysis presented in this thesis is a search for flavour-changing neutral current (FCNC) coupling between the top-quark and the Z boson, in proton–proton collisions at $\sqrt{s} = 13$ TeV with the ATLAS detector.

The search is carried out in both single-top quark production and top-quark pair-production events. The analysis targets both events with the production of a Z boson and a single-top quark decaying to a W boson and a b-quark, and events with the production of top-anti-top quark pairs, where one top quark decays to a Z boson and a charm quark and the other top quark decays to a W boson and a b-quark. For both modes (see Figure 5.1), the Z boson decays into two charged leptons (electrons or muons including those coming from leptonic τ -lepton decays) and the W boson from the top quark decays leptonically too. The main difference between the final states of decay and production modes is the presence of one additional jet.

In addition, to increase the sensitivity to FCNC tZc couplings, a charm tagging technique is exploited using the semi-leptonic decays of c-hadrons produced in the FCNC top decay.

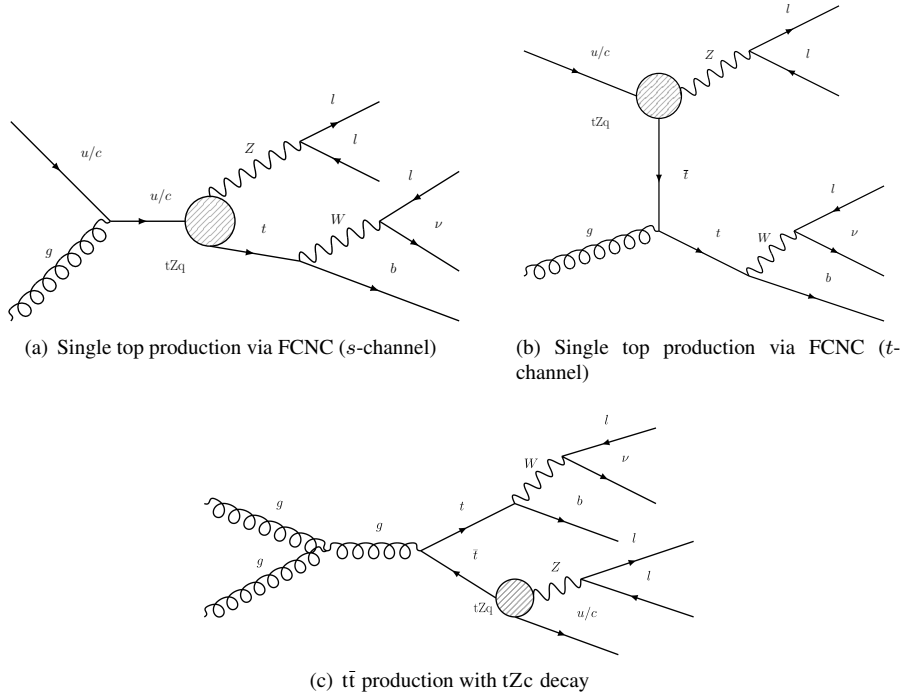


Figure 5.1 – Examples of lowest order Feynman diagrams for single top production via FCNC in (a) the *s*-channel and (b) the *t*-channel. Example of the lowest order Feynman diagrams for (c) $t\bar{t}$ production, with one top-quark decaying through the SM and the other via *tZc* coupling. The vertex labelled as *tZq* corresponds to the coupling responsible for the FCNC interaction.

Dataset Data from proton–proton collisions at $\sqrt{s} = 13$ TeV recorded in full Run2 (from 2015 to 2018) by the ATLAS experiment is used, for a total integrated luminosity of 139 fb^{-1} .

The description of the data and Monte Carlo samples used in the following is shown in Section 5.2.

Signal regions Three Signal Regions (SRs) are defined for the *tZc* coupling extraction, targeting:

- FCNC *tZc* in $t\bar{t}$ decays, vetoing the presence of a c-tagged jet (called SR1*tZc*),
- FCNC *tZc* in single-top production (called SR2*tZc*),
- FCNC *tZc* in $t\bar{t}$ decays (called SR3*tZc*) using either:
 - the SMT technique or
 - the c-tagger DL1*r_c*

The SRs are orthogonal between each other. The main focus of this thesis is the definition of SR3tZc, and the investigation of the best c-tagging technique for this analysis.

The event selection using the SMT technique is reported in Section 6.1.

The event selection using DL1 r_c tagger is reported in Section 6.4, together with the comparison with SMT.

The description of the other SRs selections, used to extract expected limits, is reported in Section 6.5.

Background estimation The main background sources are:

- for SR1tZc, t̄tZ and Diboson (VV)+HF;
- for SR2tZc, VV + HF and Standard Model tZq;
- for SR3tZc, t̄tZ and Diboson (VV)+HF.

All backgrounds are estimated using Monte Carlo samples. They are normalised to the theoretical cross-sections. Various control regions (CRs) are constructed to validate the background normalisations. A total of four CRs is used. The description of the background sources and the CR selections is reported in Section 6.6.

Separation of signal and backgrounds A multivariate analysis is used to improve the discrimination of signal to background events providing SRs with increased $\frac{S}{\sqrt{B}}$.

Gradient Boosted Decision Trees (GBDTs) are trained separately for each SR. The description of the multivariate analysis can be found in Section 6.3.

Fit and limit extraction To extract limits on the FCNC tZc coupling, the output of the GBDT in the SRs are simultaneously fit, together with other distributions in the CRs. The description of the fit and of the extraction of the limits can be found in Chapter 7.

Blinding strategy A blinding strategy is set to reduce any possible bias in the measurement. The prescriptions of the Top Working Group are followed [87].

To make sure that the background sources are correctly described, data is only looked at in regions where the signal contribution is expected to be small, while *pseudo-data*, called *Asimov data* are used in Signal Regions (see Section 7.4).

Unblinded data Data are used both in Signal Regions and in Control Regions (see Section 7.5).

5.2 Data and Monte Carlo samples

This section describes the samples used in this analysis. The detailed lists of data and Monte Carlo (MC) samples can be found in Appendix A, while a description is presented below. The starting point for the analysis are the ROOT [88] ntuples, produced using the common ATLAS software version AnalysisBase-21.2.127, starting from TOPQ1 derivations [89].

The derivations contain a filter that requires at least one lepton (a loose electron or a good combined muon) with a p_T above 20 GeV and $|\eta| \leq 2.5$.

5.2.1 Data sample

The selected data periods were collected during stable beam LHC operations and with the ATLAS detector fully functioning.

The partial integrated luminosities and the Good Run Lists¹ (GRL) used are reported in table 5.1.

Year	Int. lumi. (fb^{-1})	GRL
2015	3.2	data15_13TeV/20170619/physics_25ns_21.0.19.xml
2016	33.0	data16_13TeV/20170605/physics_25ns_21.0.19.xml
2017	44.3	data17_13TeV/20180619/physics_25ns_Trigger017e33prim.xml
2018	58.5	data18_13TeV/20181111/physics_25ns_Trigger017e33prim.xml

Table 5.1 – Integrated luminosity per year.

Events are considered only if they are accepted by at least one of the single-muon or single-electron triggers described in Refs. [90–93] and listed in Table 5.2. The ATLAS trigger system is composed by two levels: the first level (L1) is a hardware trigger implemented in custom-built electronics, while the second level, referred to as high level trigger (HLT), is software based.

Year	Single e	Single μ
2015	HLT_e24_lhmedium_L1EM20VH HLT_e60_lhmedium HLT_e120_lhloose	HLT_mu20_iloose_L1MU15 HLT_mu50
2016–2018	HLT_e26_lhtight_nod0_ivarloose HLT_e60_lhmedium_nod0 HLT_e140_lhloose_nod0	HLT_mu26_ivarmedium HLT_mu50

Table 5.2 – Trigger selections.

The electron triggers select a calorimeter cluster matched to a track. Electrons must then satisfy identification criteria based on a multivariate technique using a likelihood (LH) discriminant.

In 2015, electrons had to satisfy a medium identification and have $E_T > 24 \text{ GeV}$. In 2016–2018, electrons had to satisfy a tight identification together with an isolation criteria and have $E_T > 26 \text{ GeV}$. During the four years, to avoid efficiency losses due to identification and isolation at high p_T , two other triggers were also available, selecting medium electrons with $E_T > 60 \text{ GeV}$ and selecting loose electrons with $E_T > 120 \text{ GeV}$ (140 GeV in 2016–2018).

Muons are triggered on by matching tracks reconstructed in the muon spectrometer and in the inner detector. In 2015, muons had to satisfy a loose isolation requirement and have $p_T > 20 \text{ GeV}$. In 2016–2018, the isolation criterion was tightened and the threshold increased to $p_T > 26 \text{ GeV}$. During the four years, to avoid efficiency losses due to isolation at high p_T , another muon trigger without any isolation requirement was available, selecting muons with $p_T > 50 \text{ GeV}$.

¹The Good Runs List (GRL) is a file that selects good luminosity blocks from within the data runs (spanning 1–2 minutes of data-taking).

5.2.2 Monte Carlo simulated samples

ATLAS Monte Carlo samples for analyses on the 2015–2018 dataset are split into three subsets: mc16a reflects the pile-up conditions of the years 2015 and 2016, mc16d reflects the pile-up conditions of 2017 data, and mc16e reflects the pile-up conditions of 2018 data. Therefore, mc16a samples need to be scaled to 2015+2016 integrated luminosity, mc16d samples need to be scaled to 2017 integrated luminosity, and mc16e samples need to be scaled to the 2018 integrated luminosity.

The generated MC samples containing top-quarks are produced with the top-quark mass, m_t , parameter set to 172.5 GeV and a branching fraction of the top-quark decay to a W boson and a b quark of 1. In all samples, decays into τ leptons are included and if the τ decays leptonically such events are taken into account in the analysis.

In the following, samples used in the analysis are explained in detail, both for the signal and for the background sources.

5.2.2.1 Signal samples

The Monte Carlo simulation samples for the signal were generated at next-to-leading order (NLO) with MADGRAPH5_aMC@NLO [94] interfaced to PYTHIA8 [95] with the A14 tune [96] and the NNPDF2.3LO PDF set. Only decays of the W and Z bosons involving charged leptons were generated at matrix element level ($Z \rightarrow e^+e^-$, $\mu^+\mu^-$, $\tau^+\tau^-$ and $W \rightarrow e\nu, \mu\nu, \tau\nu$). For the matrix element, the PDF set NNPDF3.0NLO is used. The Universal FeynRules Output (UFO) model [97] is used for the computation at NLO in QCD. The top quark FCNC decay is done by TopFCNC model [98, 99]. The TopFCNC UFO model includes the effects of new physics at an energy scale Λ by adding effective terms to the SM lagrangian:

$$\mathcal{L} = \mathcal{L}_{SM} + \mathcal{L}^{eff} = \mathcal{L}_4 + \frac{1}{\Lambda^2} \mathcal{L}_6 + \dots, \quad (5.1)$$

where $\mathcal{L}_4 = \mathcal{L}_{SM}$ and \mathcal{L}_6 contains operators with dimension-six. The rest of the terms contain operators of dimension higher than 6 and will be suppressed due to the associated factors $1/\Lambda^4, \dots$. \mathcal{L}_6 can be written as a linear combination of dimension-six operators O_j :

$$\mathcal{L}_6 = \sum_j C_j O_j, \quad (5.2)$$

with C_j being complex constants and O_j being SM gauge invariant dimension-six operators that contain the fermion doublets and singlets, the gauge field tensors, the Higgs doublet and the covariant derivatives.

Taking into account that both production and decay modes are considered in this analysis, separated samples for each mode and for the tZc (using IC_{ctB} and IC_{ctW}) anomalous coupling were generated. In order to allow the study of the chirality of these couplings, samples with left-handed or right-handed couplings were obtained as well but the latter are not considered in this thesis. Finally, an additional sample for $t\bar{t}$ production was generated including a soft muon filter targeting the charm-tagged signal region requiring a soft-muon with $p_T > 3.25$ GeV, and three hard leptons (either electron or muon) from the leptonic W and Z decay to have $p_T > 20$ GeV.

Therefore, three different signal samples are considered:

- tZ production for tZc left-handed coupling;

- $t\bar{t}$ production for tZc left-handed coupling;
- $t\bar{t}$ production with soft muon filter for tZc left-handed coupling.

For the signal samples with $t\bar{t}$ production, it is considered that one of the top-quarks decays through FCNC to cZ and the other, according to the SM, to Wb .

For the tZ production, a top-quark and a Z boson is generated, where the top-quark decays according to the SM, since the tZq anomalous coupling is assumed in the primary vertex.

The branching ratio is setted to $BR(t \rightarrow Zc) = 2.4 \times 10^{-4}$, constraining

$BR(t \rightarrow bW) = 1 - BR(t \rightarrow Zc)$, which is the observed limit obtained from the previous analysis at a center-of-mass energy of 13 TeV with 36 fb^{-1} [28].

The FCNC $t\bar{t}$ decay signal is normalised using the $t\bar{t}$ cross-section prediction at next-to-next-to-leading order (NNLO) in QCD including the re-summation of next-to-next-to-leading logarithmic (NNLL) soft-gluon terms calculated using TOP++2.0 [100–106]. For proton–proton collisions at a centre-of-mass energy of $\sqrt{s} = 13 \text{ TeV}$, this cross section corresponds to $\sigma(t\bar{t})_{\text{NNLO+NNLL}} = 832 \pm 51 \text{ pb}$ using a top-quark mass of $m_t = 172.5 \text{ GeV}$.

The uncertainties on the cross-section due to PDF and α_s are calculated using the PDF4LHC prescription [107] with the MSTW2008 68% CL NNLO [108, 109], CT10 NNLO [110, 111] and NNPDF2.3 5f FFN [112] PDF sets, and are added in quadrature to the scale uncertainty. The FCNC single-top quark production signal normalisation cross-section is calculated at NLO using the TopFCNC model as implemented in the MADGRAPH5_aMC@NLO .

5.2.2.2 Background samples

Simulated samples are included in the analysis in order to account for all the SM predicted background sources.

$t\bar{t}$ production The production of $t\bar{t}$ events is modelled using the POWHEGBOX [113–116] v2 generator at NLO with the NNPDF3.0NLO [117] parton set of distribution functions (PDF) and the h_{damp} parameter² set to $1.5 m_t$ [118]. The events are interfaced to PYTHIA8.230 [119] to model the parton shower, hadronisation, and underlying event, with parameters set according to the A14 tune [120] and using the NNPDF3.0NLO set of PDFs [112]. The decays of bottom and charm hadrons are performed by EVTGEN v1.6.0 [121]. In the sample used, it is required that both the W bosons from the t quarks decay leptonically.

The impact of the parton shower and hadronisation model is evaluated by comparing the nominal generator setup with a sample produced with the POWHEGBOX [113–116] v2 generator using the NNPDF3.0NLO [117] parton distribution function (PDF). The events are interfaced with HERWIG7.04 [122, 123], using the H7UE set of tuned parameters [123] and the MMHT2014LO PDF set [124]. The decays of bottom and charm hadrons are simulated using the EVTGEN v1.6.0 program [121]. The Var3c A14 tune variation [120], that largely corresponds to the variation of α_s for initial state radiation (ISR) in the A14 tune, is considered as an uncertainty. The impact of final-state-radiation (FSR) is evaluated using PS weights which vary the renormalisation scale for QCD emission in the FSR by a factor of 0.5 and 2.0, respectively. Additionally, the uncertainty

²The h_{damp} parameter is a re-summation damping factor and one of the parameters that controls the matching of Powheg matrix elements to the parton shower and thus effectively regulates the high- p_T radiation against which the $t\bar{t}$ system recoils.

associated to the h_{damp} parameter is evaluated using the alternative sample with the h_{damp} value increased to 3.0 m_t .

$t\bar{t}V$ production

The production of $t\bar{t}V$ events is modelled using the MADGRAPH5_AMC@NLO v2.3.3 [94] generator at NLO with the NNPDF3.0NLO [117] parton distribution function (PDF). The events are interfaced to PYTHIA8.210 [119] using the A14 tune [120] and the NNPDF2.3LO [117] PDF set. The decays of bottom and charm hadrons are simulated using the EVTGEN v1.2.0 program [121].

The uncertainty due to initial-state-radiation (ISR) is estimated by comparing the nominal $t\bar{t}V$ sample with two additional samples, which have the same setting as the nominal one, but with the Var3 up or down variation of the A14 tune. The Var3c A14 tune variation corresponds to the variation of α_s for initial state radiation (ISR) in the A14 tune.

Additional $t\bar{t}V$ samples are produced with the SHERPA 2.2.0 [125] generator at LO accuracy, using the MEPS@LO setup [126, 127] with up to one additional parton for $t\bar{t}\ell\ell$ sample and two additional partons for the others. A dynamic renormalization scale is used and it is defined similarly to that of the nominal $t\bar{t}V$ samples. The CKKW matching scale of the additional emissions is set to 30 GeV. The default SHERPA 2.2.0 parton shower is used along with the NNPDF3.0NNLO [117] PDF set.

tZq production

The production of tZq events is modelled using the MADGRAPH5_AMC@NLO v2.3.3 [94] generator at NLO with NNPDF3.0NLO [117] parton distribution function (PDF). The events are interfaced with PYTHIA8.230 [119] using the A14 tune [120] and the NNPDF2.3LO [117] PDF set.

The uncertainty due to initial-state-radiation (ISR) is estimated by comparing the nominal tZq sample with two additional samples, which have the same setting as the nominal one, but with the Var3 up and down variations of the A14 tune. The predicted cross-section was calculated with MADGRAPH5_aMC@NLO 2.6.0, using the five-flavour scheme with the NNPDF30NLO PDF set and with the renormalization and factorisation scales, μ_R and μ_F , set to

$\mu_R = \mu_F = (m_t + m_Z)/4 = 66$ GeV. The SM tZq cross-section at NLO in QCD, including non-resonant contributions with $m_{\ell^+\ell^-} > 30$ GeV, is 102 fb.

tW production Although having a very low contribution, single top-quark production is also considered. The associated production of top-quarks with W bosons (tW) is modelled using the POWHEGBOX [114–116, 128] v2 generator at NLO in QCD using the five-flavour scheme and the NNPDF3.0NLO set of PDFs [117]. The diagram removal (DR) scheme [129] is used to remove interference and overlap with $t\bar{t}$ production.

The events are interfaced to PYTHIA8.230 [119] using the A14 tune [120] and the NNPDF2.3LO set of PDFs [112]. In the samples used, it is required that both W bosons in the event decay leptonically.

tWZ production

The production of tWZ events is modelled using the MADGRAPH5_AMC@NLO v2.3.3 [94] generator at NLO with NNPDF3.0NLO [117] parton distribution function (PDF). The events are interfaced with PYTHIA8.212 [119] using the A14 tune [120] and the NNPDF2.3LO [117] PDF set. The decays of bottom and charm hadrons are simulated using the EVTGEN v1.2.0 program [121]. In the sample used, it is required that the Z boson decays leptonically.

An additional tWZ sample is used to estimate the uncertainty connected with the description of the interference between $t\bar{t}Z$ and tWZ . The nominal samples is generated with the DR1 scheme, while the alternative sample is generated using the DR2 scheme.

Diboson production The samples simulating WW, WZ and ZZ events with at least two charged leptons are all considered. In the trilepton topology, WZ events are the ones that significantly contribute to the background.

Samples of diboson final states (VV) are simulated with the SHERPA v2.2.1 or v2.2.2 [125] generator depending on the process, including off-shell effects and Higgs-boson contributions, where appropriate. Fully leptonic final states and semi-leptonic final states, where one boson decays leptonically and the other hadronically, are generated using matrix elements at NLO accuracy in QCD for up to one additional parton and at LO accuracy for up to three additional parton emissions. Samples for the loop-induced processes $gg \rightarrow VV$ are generated using LO-accurate matrix elements for up to one additional parton emission for both cases of fully leptonic and semi-leptonic final states. The matrix element calculations are matched and merged with the SHERPA parton shower based on Catani-Seymour dipole [130, 131] using the MEPS@NLO prescription [126, 127, 132, 133]. The virtual QCD correction are provided by the OPENLOOPS library [134, 135]. The NNPDF3.0NNLO set of PDFs is used [117], along with the dedicated set of tuned parton-shower parameters developed by the SHERPA authors.

Electroweak production of diboson in association with two jets ($VVjj$) is simulated with the SHERPA v2.2.2 [125] generator. The LO-accurate matrix elements are matched to a parton shower based on Catani-Seymour dipoles [130, 131] using the MEPS@LO prescription [126, 127, 132, 133].

Samples are generated using the NNPDF3.0NNLO set [117], along with the dedicated set of tuned parton-shower parameters developed by the SHERPA authors.

To assess the uncertainty from the generator, alternative samples are used. The PowhegBox v2 [114–116] generator is used to generate these alternative WW, WZ and ZZ samples [136] processes at NLO-accuracy in QCD. The effect of singly resonant amplitudes as well as the interference effects due to Z/γ^* and identical leptons in the final state is included, where appropriate. Events are interfaced to PYTHIA8.186 [95] for the modelling of the parton shower, hadronisation, and underlying event, with parameters set according to the AZNLO tune [137]. The CT10 PDF set [110] is used for the hard-scattering processes, whereas the CTEQ6L1 PDF set [138] is used for the parton shower. The EVTGEN v1.2.0 program [121] is used to decay bottom and charm hadrons.

Z+jets production The POWHEGBOX v1 MC generator [114–116, 139] is used for the simulation at NLO accuracy of the hard-scattering processes of Z-boson production and decay in the electron, muon, and tau channels. It is interfaced to PYTHIA8.186 [95] for the modelling of the parton shower, hadronisation, and underlying event, with parameters set according to the AZNLO tune [137]. The CT10 PDF set [110] is used for the hard-scattering processes, whereas the CTEQ6L1 PDF set [138] is used for the parton shower. The effect of QED final-state radiation is simulated with Photos++ (v3.52) [140, 141]. The EVTGEN v1.2.0 program [142] is used to decay bottom and charm hadrons.

$t\bar{t}H$ production The production of $t\bar{t}H$ events is modelled using the POWHEGBOX v2 [113–116, 143] generator which provides matrix elements at next-to-leading order (NLO) in the strong

coupling constant α_S in the five-flavour scheme with the NNPDF3.0NLO [117] PDF set. The functional form of the renormalisation and factorisation scale is set to $\sqrt[3]{m_T(t) \cdot m_T(t) \cdot m_T(H)}$. The events are interfaced to PYTHIA8.230 [119] using the A14 tune [120] and the NNPDF2.3LO [117] PDF set. The decays of bottom and charm hadrons are performed by EVTGEN v1.6.0 [142].

Other rare backgrounds The production of triboson (VVV) events is simulated with the SHERPA v2.2.2 [125] generator using factorised gauge boson decays. Matrix elements, accurate at NLO for the inclusive process, and at LO for up to two additional parton emissions, are matched and merged with the SHERPA parton shower based on Catani-Seymour dipole factorisation [130, 131] using the MEPS@NLO prescription [126, 127, 132, 133]. The virtual QCD correction for matrix elements at NLO accuracy are provided by the OPENLOOP library [134, 135]. Samples are generated using the NNPDF3.0NNLO set [117], along with the dedicated set of tuned parton-shower parameters developed by the SHERPA authors.

The production of $t\bar{t}t\bar{t}$ is modelled using the MADGRAPH5_AMC@NLO v2.3.3 [94] generator at NLO with the NNPDF3.1NLO [117] parton distribution function (PDF). The events are interfaced with PYTHIA8.230 [119] using the A14 tune [120] and the NNPDF2.3LO [117] PDF set. The decays of bottom and charm hadrons are simulated using the EVTGEN v1.6.0 program [142]. The other rare top quark processes namely the production of $t\bar{t}WW$ and $t\bar{t}t$ are all modeled using the MADGRAPH5_AMC@NLO generator at LO interfaced with PYTHIA8 using the A14 tune.

CHAPTER 6

Search for FCNC $t \rightarrow Zc$

This chapter presents an important fraction of my work. It is dedicated to the search for FCNC $t \rightarrow Zc$ using the SMT technique, the charm-tagger $DL1r_c$ and the comparison between these two techniques. The design and optimization of the multivariate analysis is part of my work as well, and it is presented in this chapter.

6.1 Event selection and reconstruction

This section describes the event selection for the search for FCNC tZc decay. One of the t -quarks decays following the SM into a W boson and a b -quark (called in the following *SM top*), while the other t -quark (called in the following *FCNC top*) decays into a Z boson and a c -quark that subsequently decays semi-leptonically. This semi-leptonic decay is tagged using the Soft Muon Tagging (SMT) technique.

Only the trileptonic channel is considered, i.e. the Z boson from the FCNC top decays leptonically and the W boson from the SM top decays leptonically. Therefore the final state is characterised by the presence of three leptons, an SMT-jet, a b -tagged jet and missing transverse momentum from the escaping neutrino.

The final states where either the Z or the W bosons decay hadronically are not considered because of the higher backgrounds.

The pre-selection criteria, common to all the Signal Regions used in this work, are the following:

- Exactly three isolated leptons (electrons or muons) are required. These leptons must satisfy the requirements described in Sections 4.2.1 and 4.2.2. At least one lepton must have $p_T > 27\text{ GeV}$ to be above the trigger threshold. The other two leptons must have $p_T > 15\text{ GeV}$. Events with a fourth lepton with $p_T > 15\text{ GeV}$ are vetoed.

- There should be at least one opposite-sign same-flavour lepton pair (OSSF) with an invariant mass in the range $|m_{\ell\ell} - 91.2 \text{ GeV}| < 15 \text{ GeV}$. These two leptons are considered to be the ones coming from the Z boson.
- If more than one lepton pair satisfies these selections, the pair with the invariant mass closest to the mass of the Z boson is considered to be from the Z decay.

6.1.1 Top quarks reconstruction

The next step is the reconstruction of the two top quarks. The signal event has at least two jets with one of them being b-tagged, two top quark (FCNC and SM tops) candidates are reconstructed under the FCNC $t\bar{t}$ decay signal hypothesis. The kinematics of the top-quark candidates can be reconstructed from the corresponding decay particles.

The reconstructed Z boson is assumed to come from the FCNC top decay ($t \rightarrow cZ$), while the b-tagged jet from SM top decay ($t \rightarrow bW$).

In order to reconstruct both top quarks, we need to associate a reconstructed jet to the c-quark from the FCNC top decay, and to reconstruct the W boson from the SM top decay. This can be done by assuming that the lepton not used to reconstruct the Z boson is the one coming from the W boson decay, the missing transverse momentum is the transverse momentum of the neutrino from W boson decay and determining the longitudinal component of the neutrino momentum (p_z^ν) using the minimisation of the following expression for each jet combination:

$$\chi^2_{t\bar{t}} = \frac{(m_{j_a\ell\ell}^{\text{reco}} - m_{t_{\text{FCNC}}})^2}{\sigma_{t_{\text{FCNC}}}^2} + \frac{(m_{j_b\ell_W\nu}^{\text{reco}} - m_{t_{\text{SM}}})^2}{\sigma_{t_{\text{SM}}}^2} + \frac{(m_{\ell_W\nu}^{\text{reco}} - m_W)^2}{\sigma_W^2}, \quad (6.1)$$

where $m_{j_a\ell\ell}^{\text{reco}}$, $m_{j_b\ell_W\nu}^{\text{reco}}$, and $m_{\ell_W\nu}^{\text{reco}}$ are the reconstructed masses of the cZ , bW , and $\ell_W\nu$ systems, respectively. For each jet combination, where any jet can be assigned to j_a , while j_b must correspond to a b-tagged jet, the $\chi^2_{t\bar{t}}$ minimisation gives the most probable value for p_z^ν . From all combinations, the one with the minimum χ^2 is chosen. Since a semi-leptonic decay can be originated from a C-hadron decay but also from a B-hadrons decay (see Section 6.2.1), the SMT-jet can be associated to the FCNC top decay or to the SM top decay, depending on the minimum χ^2 .

When the DL1r_c charm tagger is used (see Section 6.4), the c-tagged jet is assigned to j_a .

In Equation (6.1), the central value for the masses and the widths of the top quarks and W boson are taken from reconstructed simulated FCNC $t\bar{t}$ decay signal events. This is done by matching the true c- and b-quarks in the simulated events to the reconstructed ones, setting the longitudinal momentum of the neutrino to the p_z of the true simulated neutrino and then performing Bukin fits¹ [144] to the masses of the reconstructed top quarks and W boson (more details are in Appendix B). The extracted values are:

- $m_{t_{\text{FCNC}}} = 171.2 \text{ GeV}$, $\sigma_{t_{\text{FCNC}}} = 11.4 \text{ GeV}$;
- $m_{t_{\text{SM}}} = 168.0 \text{ GeV}$, $\sigma_{t_{\text{SM}}} = 23.9 \text{ GeV}$;
- $m_W = 82.6 \text{ GeV}$, $\sigma_W = 16.6 \text{ GeV}$.

¹These fits use a piecewise function with a Gaussian function in the centre and two asymmetric tails. Five parameters determine the overall normalization, the peak position, the width of the core, the asymmetry, the size of the lower tail, and the size of the higher tail. Of these parameters, only the peak position and the width enter the χ^2 .

The SM top quark candidate is reconstructed under the FCNC single-top quark production hypothesis in the events having one or two jets with exactly one being b -tagged, which is assumed to come from the top-quark decay ($t \rightarrow bW$). The most probable value for the longitudinal component of the neutrino momentum for the FCNC single-top quark production is determined using the minimisation of the following expression:

$$\chi^2_{tZ} = \frac{(m_{j_b \ell_W \nu}^{\text{reco}} - m_{t_{\text{SM}}})^2}{\sigma_{t_{\text{SM}}}^2} + \frac{(m_{\ell_W \nu}^{\text{reco}} - m_W)^2}{\sigma_W^2}, \quad (6.2)$$

where $m_{j_b \ell_W \nu}^{\text{reco}}$ and $m_{\ell_W \nu}^{\text{reco}}$ are the reconstructed masses of the bW and $\ell_W \nu$ systems, respectively. In Equation (6.2), the central value for the masses and the widths of the top quark and W boson are the same as in Equation (6.1), therefore, in the events with two jets, the four-momentum of SM top-quark candidate reconstructed under the FCNC single-top quark production signal hypothesis is the same as the one reconstructed under the FCNC $t\bar{t}$ decay signal hypothesis. Moreover, the first term (the FCNC top) in Equation (6.1) is a constant term in the minimisation of χ^2 , therefore it does not affect the extraction of the longitudinal component of the neutrino momentum.

6.1.2 Main sources of background

A variety of background sources are considered. These include SM processes with three leptons in the final state as the FCNC $t\bar{t}$ (Zc) process (such as VV or the associated production of $t\bar{t}$ with a Z boson), as well as events in which at least one of the leptons in the final state is *fake* (either a jet misidentified as a lepton or a non-prompt lepton). The estimation of the various sources of background relies on MC simulations while for the $t\bar{t}$ fake-lepton background the shapes are taken from MC events but the normalisation is extracted from data.

The $t\bar{t}Z$ process enters the event selection because of the presence in the final state of a SM top quark and of a Z boson. The only difference w.r.t the signal topology, for the semi-leptonic $t\bar{t}$ decay, is the presence of additional jets in the event.

The diboson background (mainly WZ and ZZ) enters the selection because of the presence of three leptons and of additional jets emitted, that can come from heavy quarks. The diboson background is split into $VV + HF$ (heavy flavour) and $VV + LF$ (light flavour) based on the type of jets associated: if one of the associated jets originated from a b -quark or a c -quark then it is considered as $VV + HF$, otherwise it is considered as $VV + LF$. The jet type is determined in simulations using the `jet_truthflav` variable. This variable, provided by the flavour tagging group, defines a cone of $\Delta R < 0.3$ associated with each jet. If a b -hadron with $p_T > 5 \text{ GeV}$ is found within this cone the jet is identified as a b -jet. If no b -hadrons are found, the algorithm searches for c -hadrons, then τ leptons. If none of these identifiers are found the jet is labelled as a light jet.

In the following sections, some other backgrounds are grouped as follows:

- $t\bar{t}Z + tWZ$;
- $t\bar{t}W + t\bar{t}H$;
- $t\bar{t} + Wt$, backgrounds with fake leptons;
- *Other fakes* which contains backgrounds with fake leptons as well ($Z + \text{jets}$, VV (2l), $t\bar{t}Z$ (2l)) but categorized in a different group as explained in Section 7.2;
- *Other* which contains minor backgrounds ($t\bar{t}t$, VVV , $t\bar{t}WW$ etc.).

6.2 Signal Region with SMT requirement

The Signal region considered in this chapter is called SR3tZc and it has the following requirements in addition to the cuts described previously:

- At least two jets satisfying the requirements described in Section 4.2.3.
- Zero, one or two b-jets satisfying the requirements in Section 4.2.5.1.
- The selected soft muon must be opposite-sign with the lepton coming from W boson also satisfying the requirements described in Section 4.2.4 .
- At least one SMT jet described in Section 4.2.4. For each event that contains at least one soft muon, the SMT-jet must be assigned to the FCNC top or the SM top, depending on the χ^2 in Equation (6.1).
- No requirements on the masses of both the FCNC and the SM top-quark candidates are applied.

These selections are summarized in Table 6.1.

The event yields for each b-jet multiplicity and the total event yields are shown in Table 6.2. Even though the selection with exactly one b-jet is the purest, events containing zero and two b-jets are also considered in order to have the largest possible signal acceptance and then work on the separation of signal from background, as described in Section 6.3.

Figures 6.1 and 6.2 show the distributions of some kinematic variables for events selected in the SR3 region for the tZc coupling extraction selection (SR3tZc). As it can be noticed, the main background sources are $t\bar{t}Z$ and $VV + HF$. In the next section these two backgrounds will be investigated more in detail exploiting the information carried by the soft muon decay chain.

SR3tZc using SMT
Exactly 3 leptons with $ \eta < 2.5$ and $p_T(\ell_1) > 27 \text{ GeV}$, $p_T(\ell_2) > 15 \text{ GeV}$, $p_T(\ell_3) > 15 \text{ GeV}$ ≥ 1 OSSF pair, with $ m_{\ell\ell} - 91.2 \text{ GeV} < 15 \text{ GeV}$ ≥ 2 jets with $ \eta < 2.5$ ≤ 2 b-jets $\text{OS}(\mu^{soft}, \ell_W)$ ≥ 1 SMT jet

Table 6.1 – Overview of the requirements applied to select events in the Signal Region with SMT.

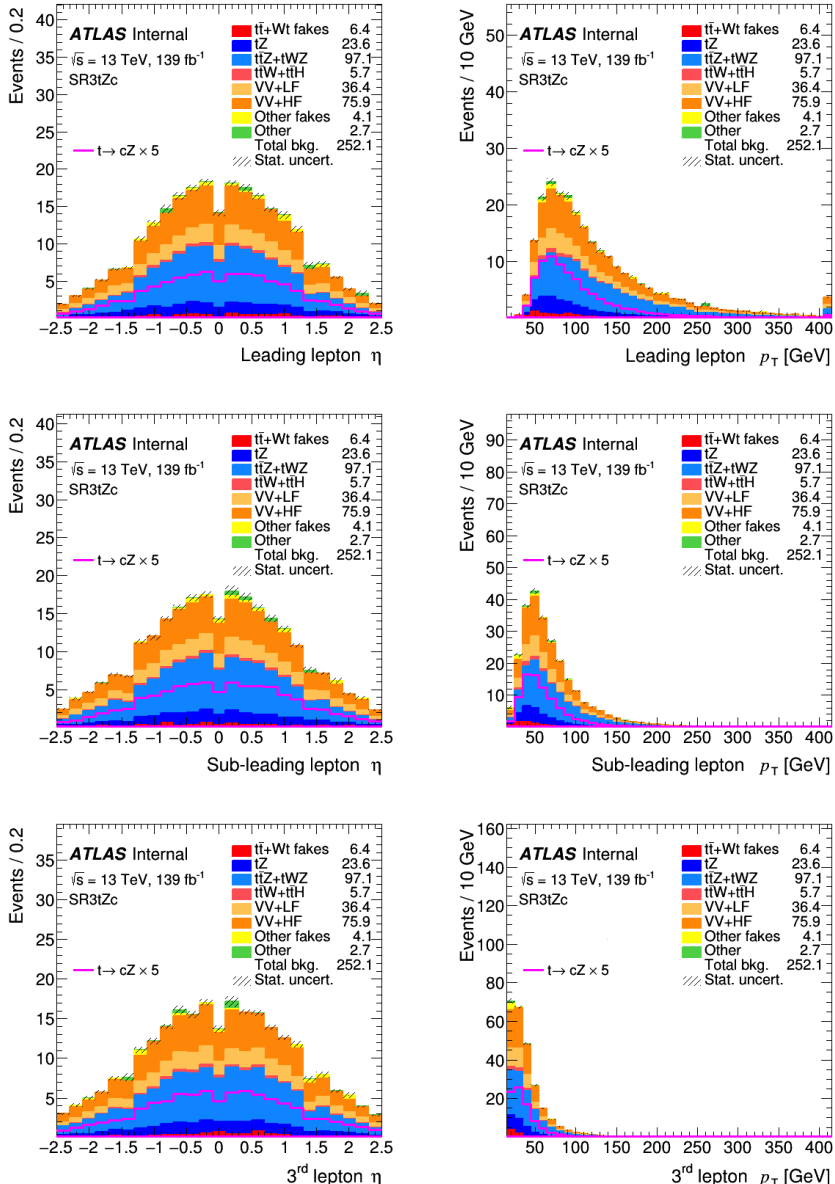


Figure 6.1 – Pre-fit distributions of kinematic variables of leptons for events selected in the SR3tZc region. Number of signal events are normalised to the current observed branching ratio limits and scaled by factor 5. The uncertainty band includes only the statistical uncertainty. These distributions are blinded, following the blinding strategy.

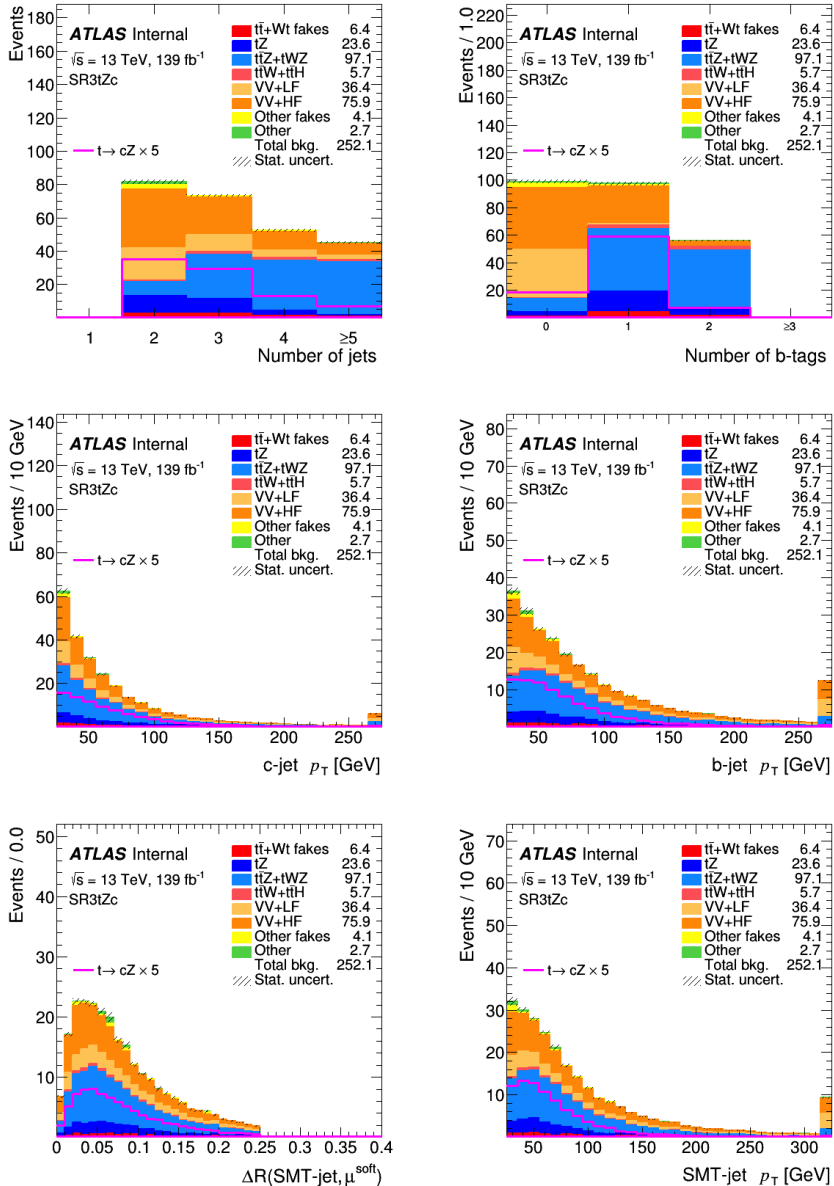


Figure 6.2 – Pre-fit distributions of kinematic variables of jets for events selected in the SR3tZc region. Number of signal events are normalised to the current observed branching ratio limits and scaled by factor 5. The uncertainty band includes only the statistical uncertainty. These distributions are blinded, following the blinding strategy.

Sample	Number of b -jets			Total yield
	=0	=1	=2	
ZZ+LF	15.40 ± 0.24	0.41 ± 0.04	0.00 ± 0.00	15.81 ± 0.25
ZZ+HF	4.64 ± 0.12	5.15 ± 0.13	0.83 ± 0.03	10.63 ± 0.18
WZ+LF	20.13 ± 0.36	0.45 ± 0.06	0.01 ± 0.01	20.59 ± 0.37
WZ+HF	40.24 ± 0.51	21.92 ± 0.38	3.10 ± 0.12	65.27 ± 0.65
VV (2l)	0.05 ± 0.08	0.09 ± 0.04	0.00 ± 0.00	0.15 ± 0.09
tWZ	1.87 ± 0.19	7.80 ± 0.40	3.59 ± 0.26	13.26 ± 0.51
t tW	0.23 ± 0.04	1.28 ± 0.10	1.04 ± 0.09	2.55 ± 0.14
t tZ (2l)	0.00 ± 0.00	0.02 ± 0.02	0.00 ± 0.00	0.02 ± 0.02
t tZ	7.69 ± 0.20	37.81 ± 0.45	38.35 ± 0.46	83.85 ± 0.67
Wt	0 ± 0.00	0.27 ± 0.19	0.00 ± 0.00	0.27 ± 0.19
tZ	8 ± 0.15	14.85 ± 0.30	5.60 ± 0.16	23.63 ± 0.37
t t	0.91 ± 0.19	3.97 ± 0.39	1.29 ± 0.22	6.17 ± 0.48
Z+jets	2.85 ± 0.80	1.07 ± 0.65	0.20 ± 0.20	4.12 ± 1.05
4 tops	0.01 ± 0.00	0.05 ± 0.01	0.15 ± 0.01	0.20 ± 0.01
3 tops	0.00 ± 0.00	0.01 ± 0.00	0.02 ± 0.00	0.03 ± 0.00
VVV	37 ± 0.02	0.11 ± 0.01	0.01 ± 0.00	0.49 ± 0.03
VH	5 ± 0.64	0.80 ± 0.57	0.00 ± 0.00	1.76 ± 0.86
t tH	0.24 ± 0.02	1.37 ± 0.04	1.51 ± 0.04	3.12 ± 0.05
t tWW	0.01 ± 0.01	0.09 ± 0.03	0.13 ± 0.03	0.23 ± 0.05
Total bkg.	98.79 ± 1.29	97.53 ± 1.25	55.82 ± 0.64	252.14 ± 1.91
FCNC t $t(cZ)$	3.44 ± 0.02	10.65 ± 0.04	1.40 ± 0.02	15.49 ± 0.05
FCNC (c)tZ	0.31 ± 0.02	1.34 ± 0.03	0.10 ± 0.01	1.74 ± 0.04

Table 6.2 – Event yields for each b -jet multiplicity and total event yields for the SR3tZc selection.

6.2.1 Reconstruction of the soft muon decay chain

In $t\bar{t}$ events, a soft muon in jets can be originated by various sources. In MC simulation, truth information can be used to determine the origin of the soft muon and the truth flavour of the SMT-jet that contains the soft muon. Therefore it is possible to reconstruct the chain of ancestors which in the end produces the soft muon. Four categories of events can be identified:

- muons originating from the decay chain of a b -quark produced by a $t \rightarrow bW$ decay if the hadron and the b -quark are spatially matched within $\Delta R < 0.4$. Events with muons from $b \rightarrow \mu$, $b \rightarrow c \rightarrow \mu$ and $b \rightarrow \tau \rightarrow \mu$, are included in this category;
- muons originating from the decay chain of a c -quark produced by a $t \rightarrow Zc$ decay if the hadron and the c -quark are spatially matched within $\Delta R < 0.4$. Events with muons from $c \rightarrow \mu$ and $c \rightarrow \tau \rightarrow \mu$, are included in this category;
- muons which are either produced by light hadrons coming from a top-quark decay ($t \rightarrow Wb$ or $t \rightarrow Zc$) or muons coming from the decay in flight of light hadrons, mostly pions and kaons. These muons can be also categorised as ‘fake-SMT’;
- muons that are effectively prompt leptons from a W or Z boson decay, failing the prompt lepton selection cuts, being close to a jet and therefore entering the soft muon selection criteria, referred to as prompt $\rightarrow \mu$.

According to the categories described above, Table 6.3 shows the composition for the FCNC t $t(cZ)$ signal. Soft muons mostly come from B-hadrons ($\sim 60\%$) and C-hadrons ($\sim 40\%$) decays.

Table 6.4 and Table 6.5 show the composition for the main backgrounds, $t\bar{t}Z$ and $VV + HF$ respectively. For $t\bar{t}Z$ the main contributions come from B-hadrons ($\sim 80\%$) as expected by the $t\bar{t}Z$ topology. For $VV + HF$ the main contributions come from C-hadrons ($\sim 60\%$), mostly $WZ + c\bar{c}$.

FCNC $t\bar{t}(cZ)$	
Total number of events = 15.49	
Chain	Fractions [%]
b $\rightarrow \mu$	44.57
b $\rightarrow c \rightarrow \mu$	10.68
b $\rightarrow \tau \rightarrow \mu$	2.61
c $\rightarrow \mu$	40.11
c $\rightarrow \tau \rightarrow \mu$	1.55
light $\rightarrow \mu$	0.48
prompt $\rightarrow \mu$	0.00

Table 6.3 – Reconstructed chain of ancestors that produces the soft muon for the FCNC $t\bar{t}(cZ)$ signal.

$t\bar{t}Z$	
Total number of events = 83.85	
Chain	Fractions [%]
b $\rightarrow \mu$	42.24
b $\rightarrow c \rightarrow \mu$	31.82
b $\rightarrow \tau \rightarrow \mu$	3.01
c $\rightarrow \mu$	12.95
c $\rightarrow \tau \rightarrow \mu$	0.14
light $\rightarrow \mu$	7.32
prompt $\rightarrow \mu$	2.52

Table 6.4 – Reconstructed chain of ancestors that produces the soft muon for the $t\bar{t}Z$ background.

$VV + HF$	
Total number of events = 75.90	
Chain	Fractions [%]
b $\rightarrow \mu$	6.60
b $\rightarrow c \rightarrow \mu$	9.23
b $\rightarrow \tau \rightarrow \mu$	0.80
c $\rightarrow \mu$	57.46
c $\rightarrow \tau \rightarrow \mu$	0.60
light $\rightarrow \mu$	10.83
prompt $\rightarrow \mu$	4.48

Table 6.5 – Reconstructed chain of ancestors that produces the soft muon for the $VV + HF$ background.

6.3 Separation of signal from background events

Given the selection requirements in Table 6.1, a multivariate analysis (MVA) technique is used to have a better separation of the signal from the background and to increase the value of $\frac{S}{\sqrt{S+B}}$. The Gradient Boosted Decision Trees (GBDT) method with TMVA software package [145, 146] is exploited in this study. The output of this algorithm (called GBDT score) is correlated with $\frac{S}{\sqrt{S+B}}$ and it is in the range between -1 and 1. The most signal-like events have scores near 1 while the most background-like events have scores near -1. The GBDTs are trained separately in each signal regions as described below. The SR3tZc is defined targeting the FCNC tZc coupling in $t\bar{t}$ decay events using the soft muon tagging, therefore the MVA discriminant, D_3 , is built using a GBDT trained with FCNC tZc $t\bar{t}$ decay events against all backgrounds.

6.3.1 Input variables

A set of variables as the GBDT input is used to train and test the GBDT method on the events in SR3tZc. Those variables are listed in Table 6.6, ordered by the separation value, defined by, as in [146]:

$$\langle s^2 \rangle = \frac{1}{2} \int \frac{[p_s(y) - p_b(y)]^2}{p_s(y) + p_b(y)} dy$$

where $p_s(y)$ and $p_b(y)$ are the signal and background PDFs of the classifier y . The separation is 0 (1) for identical (non-overlapping) signal and background shapes.

The set of input variables presented in this section has been constructed and optimized based on separation values, correlations and impact on the BDT performance. The details of the optimization procedure are documented in Appendix D. The distributions of input variables in the Signal Region are presented in Figure 6.3.

Variable	$\langle s^2 \rangle$	Definition
$m_{b\ell\nu}$	0.1717	SM top-quark candidate mass
$N b\, jets$	0.08218	Number of b-jets tagged with DL1r
$m_{q\ell\ell}$	0.07019	FCNC top-quark candidate mass
$\frac{\mu_{soft}\, IDp_T}{SMT\, jet\, Sump_T\, Trk}$	0.03357	Ratio between the soft muon ID pT and pT sum of tracks
$\Delta R(\ell, Z)$	0.03141	ΔR between W boson lepton and Z boson candidates
$\Delta R(t_{SM}, t_{FCNC})$	0.02508	ΔR between SM and FCNC top-quark candidates
$\Delta R(\mu^{soft}, Z)$	0.006596	ΔR between soft muon and Z boson candidates

Table 6.6 – Set of variables used in the training of the GBDT in SR3tZc to build the D_3 discriminant. Variables are ordered by the separation $\langle s^2 \rangle$ value.

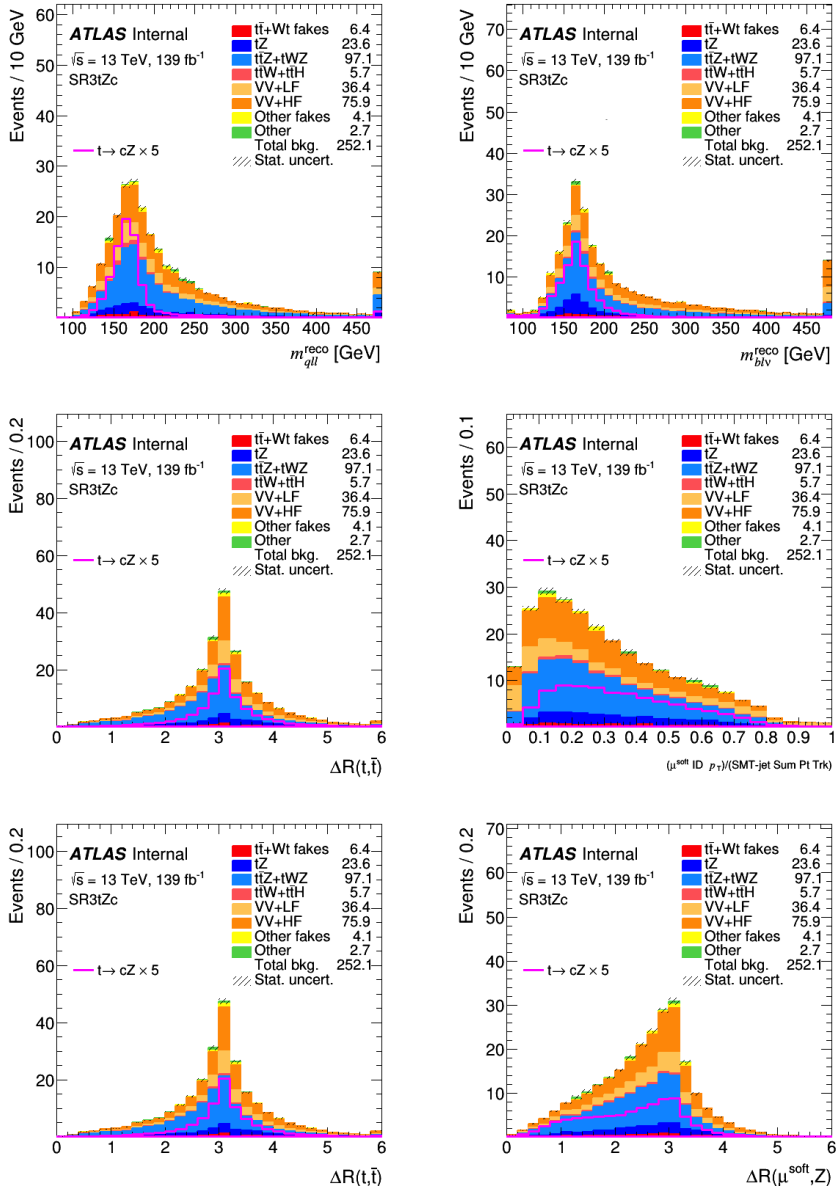


Figure 6.3 – Pre-fit distributions of the input variables used in the training of the GBDT in SR3tZc to build the D_3 discriminant. Number of signal events are normalised to the current observed branching ratio limits and scaled by factor 5. The uncertainty band includes only the statistical uncertainty. These distributions are blinded, following the blinding strategy.

6.3.2 GBDT training and evaluation

In order to train the GBDT algorithm and have a reliable model with a good performance, it is better to use as much statistics as possible from the available signal and background MC samples. On the other hand, to check the performance and validate the model, the trained GBDT model must be applied on a test sample (events that are not used in the training phase) that has sufficiently large statistics. Therefore, a *k-Fold Cross-Validation* method is exploited, where $k=5$, so that the 80 % of available MC statistics is used for the training while 20 % for the testing, as described below. All samples, including MC systematics samples and data (currently only in CRs), are divided into five approximately equal size groups using pseudo-random numbers. All events in each group have assigned the same integer pseudo-random number from 1 to 5 so that five equivalent GBDT models are trained using four groups of nominal MC samples to test the stability of the training. Each training uses different combination of four groups out of five. The remaining one group is used as a test sample. Each of five GBDTs is evaluated on events with the assigned pseudo-random number that is not assigned to the training events of that GBDT.

Table 6.7 shows the values for configuration options of the BDT method. They are chosen to counteract overtraining and have an optimal performance.

Option	Value for D_3
NTrees	800
MinNodeSize	2%
BoostType	Grad
Shrinkage	0.05
UseBaggedBoost	True
BaggedSampleFraction	0.6
nCuts	200
MaxDepth	2
NegWeightTreatment	IgnoreNegWeightsInTraining

Table 6.7 – Used values for configuration options of the TMVA method BDT [146].

6.3.3 GBDT performance and overtraining checks

An important step to validate the GBDT training is the *overtraining* check, needed to verify if there is disagreement between the output from the training sample and the test sample and therefore to verify its stability. In fact, overtraining leads to a seeming increase in the classification performance over the objectively achievable one, if measured on the training sample, and to an effective performance decrease when measured with an independent test sample. A convenient way to detect overtraining and to measure its impact is therefore to compare the performance results between training and test samples. Figure 6.4 present the Receiver Operating Characteristic (ROC) curves for each GBDT output score in the signal region, while Figures 6.5 and 6.6 show the GBDT output score distributions for signal and background samples, comparing results between training and test samples. No significant overtraining is detected. The five GBDT output scores used to built discriminant variables are compared in Figure 6.7. The results of the five GBDTs are in agreement within the statistical uncertainties indicating the good stability of the trained

GBDTs.

Input variables importance for each GBDT are presented in Table 6.8. The importance is evaluated as the total separation gain that this variable had in the decision trees (weighted by the number of events). It is normalized to all variables together, which have an importance of 1. For most of the variables, the spread of importance values across the five GBDTs is below 3%, indicating again a good stability of the trained GBDTs.

Variable	GBDT #1	GBDT #2	GBDT #3	GBDT #4	GBDT #5
$m_{q\ell\ell}$	0.1807	0.1758	0.1795	0.1799	0.1767
$\Delta R(\mu^{soft}, Z)$	0.1613	0.1597	0.1603	0.1555	0.1616
$\Delta R(t_{SM}, t_{FCNC})$	0.161	0.1635	0.1598	0.1634	0.1635
$m_{b\ell\nu}$	0.1536	0.1566	0.1565	0.1642	0.1478
$\Delta R(\ell, Z)$	0.1359	0.1433	0.1399	0.1378	0.1446
$\frac{\mu^{soft} ID p_T}{SMT \text{ jet } Sump_T Trk}$	0.1216	0.1179	0.122	0.1203	0.1216
$N b \text{ jets}$	0.08582	0.08308	0.08205	0.07875	0.08431

Table 6.8 – Input variables importance in each GBDT used to build the D_3 discriminant.

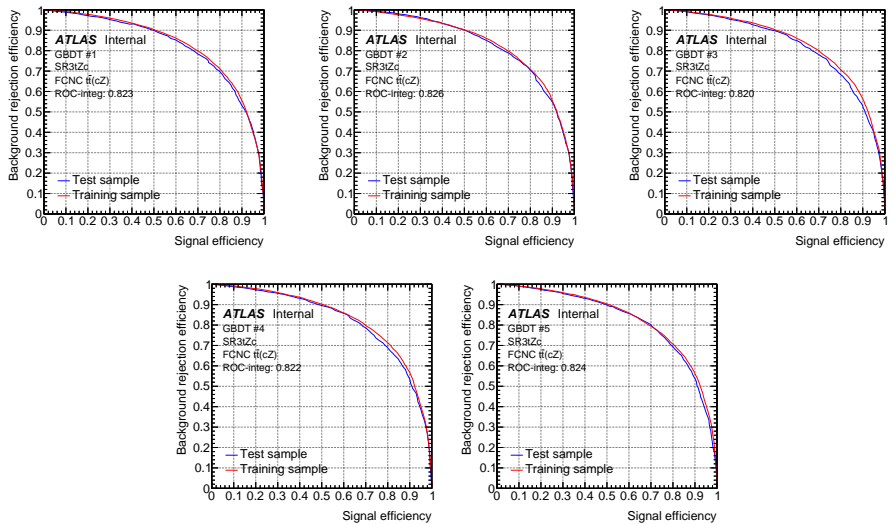


Figure 6.4 – The ROC curves for each of five GBDTs trained in SR3tZc to build the D_3 discriminant. Comparing results between training and test samples.

6. SEARCH FOR FCNC $t \rightarrow Zc$

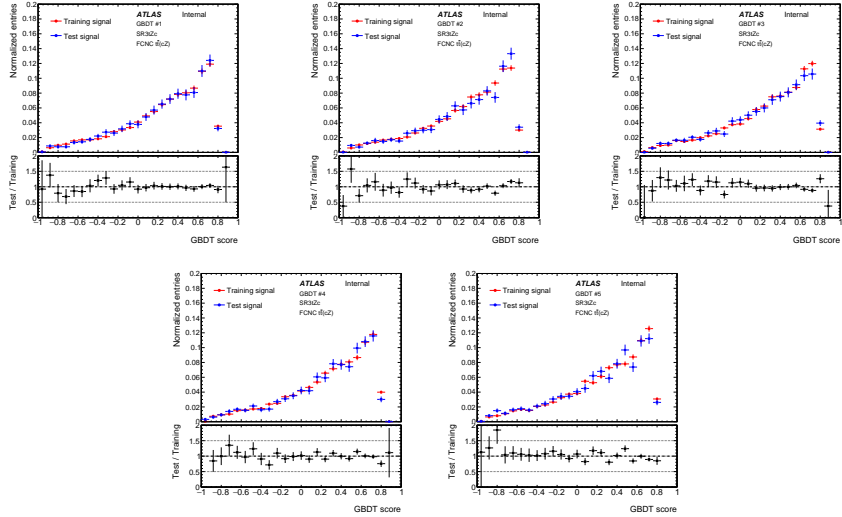


Figure 6.5 – The FCNC tZc $t\bar{t}$ decay signal GBDT output score distributions for each of the five GBDTs trained in SR3tZc to build the D_3 discriminant. Comparing results between training and test samples.

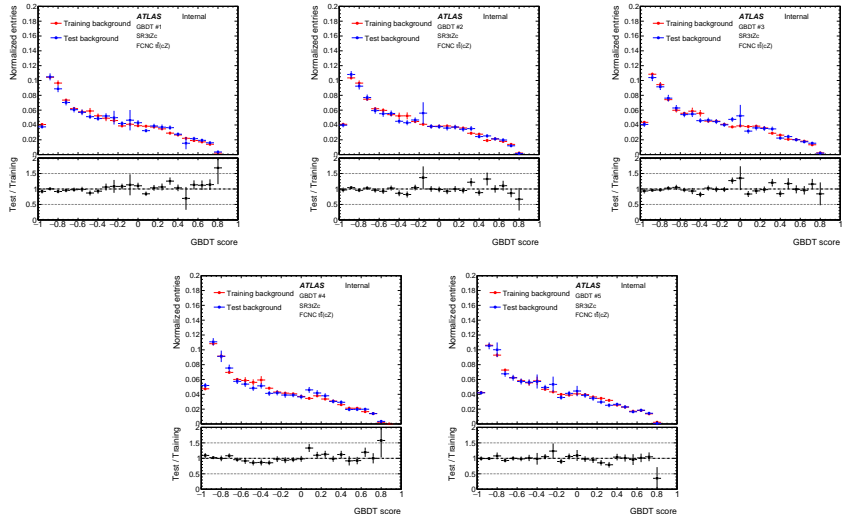


Figure 6.6 – The background GBDT output score distributions for each of the five GBDTs trained in SR3tZc to build the D_3 discriminant. Comparing results between training and test samples.

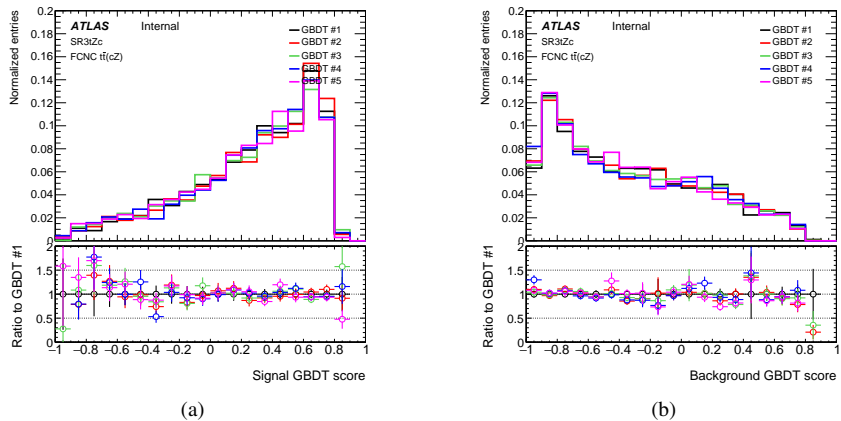


Figure 6.7 – The GBDT output score distributions for (a) signal events and (b) background events, in the test samples. The five trained GBDTs are compared in the signal region.

6.4 The alternative selection using the c-tagger DL1r_c

The c-tagger DL1r_c (see Section 4.2.5.2) has been investigated for SR3tZc as an alternative to SMT, already discussed in Section 6.2. The requirements for this selection are the following:

- At least two jets satisfying the requirements described in Section 4.2.3.
- Exactly one b-jet satisfying the requirements in Section 4.2.5.1.
- At least one c-jets satisfying the requirements described in Section 4.2.5.2.
- No requirements on the masses of both the FCNC and the SM top-quark candidates are applied.

This selection is summarized in Table 6.9 together with the selection using SMT for comparison. Kinematic distributions are presented in Section E.3.

Common selections	
Exactly 3 leptons with $ \eta < 2.5$ and $p_T(\ell_1) > 27 \text{ GeV}$, $p_T(\ell_2) > 15 \text{ GeV}$, $p_T(\ell_3) > 15 \text{ GeV}$ ≥ 1 OSSF pair, with $ m_{\ell\ell} - 91.2 \text{ GeV} < 15 \text{ GeV}$ ≥ 2 jets with $ \eta < 2.5$	
SR3tZc using SMT	SR3tZc using DL1r _c
≤ 2 b-tagged jets	=1 b-jet
OS(μ^{soft}, ℓ_W)	–
≥ 1 SMT jet	–
–	≥ 1 c-tagged jet

Table 6.9 – Overview of the requirements applied to select events in the Signal Region with DL1r_c

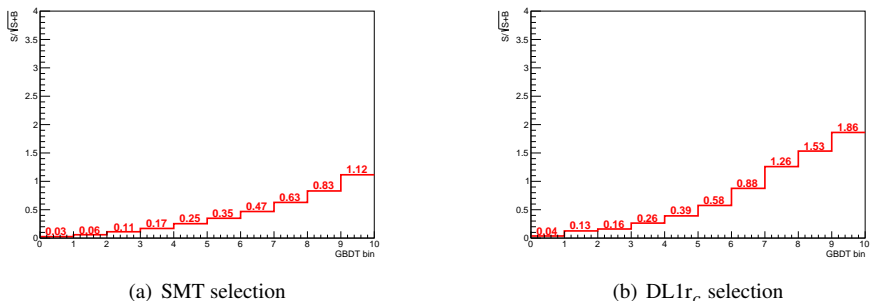
The event yields for this selection are shown in Table 6.10.

Comparing the two event yields in Table 6.2 with Table 6.10 it is possible to see that using DL1r_c the number of signal events is significantly larger than using SMT since the semi-leptonic decay of heavy hadrons is limited by the branching ratio (20%). To increase the signal acceptance in the SMT selection, not only events containing exactly one b-jet, but also events containing zero or two b-jets have been considered. However, taking into account the SMT selection with only one b-jet, it is also possible to see that SMT has a better discrimination of backgrounds mainly due to a better light-jet rejection.

To choose the best c-tagger for this analysis, one can compare the values of $\frac{S}{\sqrt{S+B}}$ for each bin of the GBDT discriminant, as it can be seen in Table 6.11 for the SMT selection, in Table 6.12 for DL1r_c selection, and Figure 6.8. A new GBDT training has been performed for the DL1r_c selection. The GBDT output for SMT was already presented in Section 6.3, while for DL1r_c it will be presented in Section 6.7 together with the discriminants for all the other Signal Regions defined. For the DL1r_c selection, in the last three bins of the GBDT discriminant, there are 12.3 events of signal and 9.3 events of background which corresponds to more signal events and 10% background events of the whole SR3tZc with SMT.

The GBDT output for SMT was already presented in Section 6.3, while for DL1r_c it will be presented in Section 6.7 together with the discriminants for all the other Signal Regions defined.

Sample	Total yield
ZZ+LF	0.71 ± 0.07
ZZ+HF	5.31 ± 0.13
WZ+LF	2.18 ± 0.12
WZ+HF	25.02 ± 0.39
VV (2l)	0.05 ± 0.04
tWZ	12.39 ± 0.49
$t\bar{t}W$	2.04 ± 0.12
$t\bar{t}Z$ (2l)	0.02 ± 0.02
$t\bar{t}Z$	69.49 ± 0.61
Wt	0.00 ± 0.00
tZ	13.82 ± 0.28
$t\bar{t}$	3.66 ± 0.37
Z+jets	1.32 ± 0.58
4 tops	0.09 ± 0.01
3 tops	0.02 ± 0.00
VVV	0.22 ± 0.02
VH	0.00 ± 0.00
$t\bar{t}H$	2.63 ± 0.05
$t\bar{t}WW$	0.16 ± 0.04
Total bkg.	139.13 ± 1.17
FCNC $t\bar{t}(cZ)$	21.94 ± 0.39
FCNC (c)tZ	1.21 ± 0.03

Table 6.10 – Total event yields for the SR3tZc selection using the c-tagger DL1r_c.**Figure 6.8** – Values of $\frac{S}{\sqrt{S+B}}$ for each bin of the GBDT discriminant (a) for the SMT selection and (b) for the DL1r_c selection.

Sample	Bin 6	Bin 7	Bin 8	Bin 9	Bin 10
Others	0.46 ± 0.42	0.91 ± 0.63	0.04 ± 0.05	0.02 ± 0.05	0.00 ± 0.05
$Z + \text{jets}$	0.18 ± 0.17	0.00 ± 0.17	0.26 ± 0.23	0.40 ± 0.28	0.21 ± 0.36
$t\bar{t} + tW$	1.07 ± 0.28	0.61 ± 0.24	0.43 ± 0.23	0.59 ± 0.22	0.16 ± 0.21
tZq	2.80 ± 0.13	2.08 ± 0.12	2.10 ± 0.11	1.48 ± 0.10	1.03 ± 0.08
$VV + \text{HF}$	6.11 ± 0.19	4.65 ± 0.20	2.85 ± 0.14	1.70 ± 0.11	0.82 ± 0.09
$VV + \text{LF}$	2.67 ± 0.13	1.56 ± 0.10	0.62 ± 0.07	0.15 ± 0.04	0.06 ± 0.01
$t\bar{t}H + t\bar{t}W$	0.55 ± 0.05	0.40 ± 0.04	0.25 ± 0.04	0.15 ± 0.03	0.06 ± 0.02
$t\bar{t}Z + tWZ$	7.83 ± 0.23	6.43 ± 0.21	4.65 ± 0.18	3.12 ± 0.15	1.62 ± 0.12
Total bkg	21.67 ± 0.63	16.65 ± 0.77	11.21 ± 0.43	7.60 ± 0.42	3.97 ± 0.45
Signal	1.69 ± 0.03	2.02 ± 0.03	2.31 ± 0.03	2.66 ± 0.03	2.93 ± 0.03
S/B	0.08	0.12	0.21	0.35	0.74
$S/\sqrt{S+B}$	0.35	0.47	0.63	0.83	1.12

Table 6.11 – Values of $\frac{S}{\sqrt{S+B}}$ for the last five bins of the GBDT discriminant for the SMT selection.

Sample	Bin 6	Bin 7	Bin 8	Bin 9	Bin 10
Others	0.03 ± 0.03	0.01 ± 0.03	0.02 ± 0.03	0.00 ± 0.03	0.00 ± 0.03
$Z + \text{jets}$	0.36 ± 0.29	0.06 ± 0.07	0.00 ± 0.07	0.21 ± 0.24	0.00 ± 0.07
$t\bar{t} + tW$	0.64 ± 0.15	0.17 ± 0.08	0.16 ± 0.08	0.14 ± 0.07	0.17 ± 0.09
tZq	1.80 ± 0.10	1.37 ± 0.08	0.76 ± 0.06	0.46 ± 0.04	0.27 ± 0.03
$VV + \text{HF}$	2.51 ± 0.13	1.86 ± 0.12	0.97 ± 0.07	0.53 ± 0.06	0.19 ± 0.03
$VV + \text{LF}$	0.25 ± 0.04	0.24 ± 0.05	0.08 ± 0.02	0.06 ± 0.03	0.00 ± 0.00
$t\bar{t}H + t\bar{t}W$	0.36 ± 0.04	0.37 ± 0.04	0.30 ± 0.03	0.17 ± 0.03	0.10 ± 0.02
$t\bar{t}Z + tWZ$	6.77 ± 0.22	4.53 ± 0.18	2.60 ± 0.14	1.38 ± 0.09	0.66 ± 0.07
Total bkg	12.74 ± 0.43	8.60 ± 0.26	4.88 ± 0.20	2.97 ± 0.28	1.40 ± 0.14
Signal	2.23 ± 0.12	2.98 ± 0.14	3.69 ± 0.16	4.07 ± 0.16	4.54 ± 0.17
S/B	0.17	0.35	0.76	1.37	3.24
$S/\sqrt{S+B}$	0.58	0.88	1.26	1.53	1.86

Table 6.12 – Values of $\frac{S}{\sqrt{S+B}}$ for the last five bins of the GBDT discriminant for the DL1 r_c selection.

6.5 Additional Signal Regions

The previous sections described the event selection targeting the FCNC $t\bar{t}$ decay process using a charm-tagger. Without the use of a charm-tagger, two addition selections can be investigated: FCNC $t\bar{t}$ decays and FCNC single top production.

The pre-selection criteria, common to all the Signal Regions used in this work have already been discussed in Section 6.1. In this section, the topology of the final states of the signal in the Signal Regions are described. For SR3tZc, the selection using DL1 r_c and presented in Section 6.4, is using henceforth. There are two more channels that remain to present.

The first selection is FCNC tZc in $t\bar{t}$ decays, where one of the t-quarks decays following the SM into a W boson and a b-quark (called in the following *SM top*), while the other t-quark (called in the following *FCNC top*) decays into a Z boson and a c-quark. Only the trileptonic channel is considered, i.e. when the Z boson from the FCNC top decays leptonically and the W boson from the SM top decays leptonically. Therefore the final state is characterised by the presence of three leptons, a c-jet, a b-tagged jet and missing transverse momentum from the escaping neutrino. The final state of this channel was already presented in Section 6.1 with the exception that no SMT or c-tagged jet is required.

The second selection is FCNC tZc in single-top production, where the production of a single top-quark proceeds through an FCNC interaction. The t-quark is produced in association with a Z boson. Also in this case, only the trileptonic channel is considered. Therefore the final state is characterised by the presence of three leptons, a b-tagged jet and missing transverse momentum from the escaping neutrino.

6.5.1 SR1tZc selections

The SR1tZc has the following additional requirements:

- At least two jets satisfying the requirements described in Section 4.2.3.
- Exactly one b-jet satisfying the requirements described in Section 4.2.5.1.
- The mass of the FCNC top-quark candidate, m_t^{FCNC} , must be within $2\sigma^{FCNC}$ from 172.5 GeV, while no requirement on the mass of the SM top-quark candidate, m_t^{SM} , is applied.
- A veto is applied on the events where there is a c-tagged jet, described in Section 4.2.5.2.

Kinematic plots are presented in Appendix E.1.

6.5.2 SR2tZc selections

The SR2tZc has the following additional requirements:

- Exactly one or two jets satisfying the requirements described in Section 4.2.3.
- Exactly one b-jet satisfying the requirements described in Section 4.2.5.1.

- The lepton not used to reconstruct the Z boson is assumed to be the one coming from the W boson. The transverse mass is calculated using the momentum of the lepton associated with the W boson, E_T^{miss} and azimuthal angle, ϕ , between them: $m_T(\ell_W, \nu) = \sqrt{2p_T^\ell E_T^{\text{miss}} (1 - \cos \Delta\phi)}$. Events are required to have $m_T(\ell_W, \nu) > 40 \text{ GeV}$.
- For events with exactly one jet, no requirement is applied on the masses of the FCNC and SM top-quark candidates. For events with exactly two jets, the mass of the FCNC top-quark candidate, m_t^{FCNC} , must be outside $2\sigma^{\text{FCNC}}$ from 172.5 GeV, while the mass of the SM top-quark candidate, m_t^{SM} , must be within $2\sigma^{\text{SM}}$ from 172.5 GeV. The requirement on m_t^{FCNC} makes this region orthogonal to SR1.
- A veto is applied on the events where there is a c-tagged jet, described in Section 4.2.5.2.

Kinematic plots are presented in Appendix E.2.

6.5.3 Orthogonality between Signal Regions

The SRs are orthogonal between each other. The orthogonality is assured by selecting events with different jet multiplicities, by selecting or vetoing the presence of c-tagged jet and selecting different mass windows using the reference value for the top mass of 172.5 GeV. The mass windows applied are much larger than the difference between 172.5 GeV and the mass values extracted in Appendix B and used in the χ^2 calculation (see Equations (6.1) and (6.2)). Therefore, changing the mass value would not have a significant effect on the number of events in the SRs. Moreover, it is better to keep the mass window larger as possible to have a high signal sensitivity. This can be verified in Table 6.13 where an overview of the requirements applied to select events in the Signal Regions is presented.

Common selections			
Exactly 3 leptons with $ \eta < 2.5$ and $p_T(\ell_1) > 27 \text{ GeV}, p_T(\ell_2) > 15 \text{ GeV}, p_T(\ell_3) > 15 \text{ GeV}$ ≥ 1 OSSF pair, with $ m_{\ell\ell} - 91.2 \text{ GeV} < 15 \text{ GeV}$			
SR1tZc	SR2tZc	SR3tZc	
≥ 2 jets with $ \eta < 2.5$ $= 1$ b-jet $-$ $= 0$ c-tagged jet $ m_t^{\text{FCNC}} - 172.5 \text{ GeV} < 2\sigma^{\text{FCNC}}$ $-$	$= 1$ jet with $ \eta < 2.5$ $= 1$ b-jet $m_T(\ell_W, \nu) > 40 \text{ GeV}$ $-$ $ m_t^{\text{SM}} - 172.5 \text{ GeV} < 2\sigma^{\text{SM}}$ $-$	$= 2$ jets with $ \eta < 2.5$ $= 1$ b-jet $m_T(\ell_W, \nu) > 40 \text{ GeV}$ $= 0$ c-tagged jet $ m_t^{\text{FCNC}} - 172.5 \text{ GeV} > 2\sigma^{\text{FCNC}}$ $ m_t^{\text{SM}} - 172.5 \text{ GeV} < 2\sigma^{\text{SM}}$ $-$	≥ 2 jets with $ \eta < 2.5$ $= 1$ b-jet $-$ ≥ 1 c-tagged jet $-$

Table 6.13 – Overview of the requirements applied to select events in the Signal Regions.

6.5.4 Event yields in the Signal Regions

Event yields in the SRs for the tZc coupling extraction are reported in Table 6.14. The SR1 and SR2 have been presented before (in Section 6.5.1 and Section 6.5.2 respectively), while for SR3, as demonstrated in Section 6.4, the selection using the charm-tagger DL1 r_c w.r.t. SMT, provided the best $\frac{S}{\sqrt{S+B}}$ ratio for this analysis and then it is exploited in the following. As it can be noticed, the main background sources are:

- for SR1tZc, $t\bar{t}Z$ and $VV + HF$;
- for SR2tZc, $VV + HF$ and Standard Model tZq ;
- for SR3tZc, $t\bar{t}Z$ and $VV + HF$.

	SR1tZc	SR2tZc	SR3tZc
$t\bar{t}Z$	137.9 ± 0.9	24.11 ± 0.31	69.5 ± 0.6
tWZ	30.6 ± 0.8	9.4 ± 0.4	12.4 ± 0.5
$t\bar{t}W$	5.78 ± 0.22	3.33 ± 0.15	2.04 ± 0.12
$t\bar{t}H$	6.10 ± 0.08	0.881 ± 0.023	2.63 ± 0.05
$VV + LF$	28.2 ± 0.5	34.8 ± 1.5	2.89 ± 0.14
$VV + HF$	142.7 ± 1.0	155.9 ± 2.2	30.3 ± 0.4
tZq	46.5 ± 0.6	110.0 ± 0.7	13.82 ± 0.28
$t\bar{t}$	20.0 ± 0.9	31.5 ± 1.1	3.7 ± 0.4
W t	0.7 ± 0.4	0.8 ± 0.4	< 0.001
Z + jets	9.9 ± 1.6	11.8 ± 1.9	1.3 ± 0.6
VH	1.2 ± 1.2	3.2 ± 1.2	< 0.001
$t\bar{t}WW$	0.39 ± 0.06	0.027 ± 0.016	0.16 ± 0.04
VVV	0.704 ± 0.032	0.590 ± 0.034	0.220 ± 0.016
4 tops	0.151 ± 0.011	0.0030 ± 0.0012	0.092 ± 0.010
3 tops	0.0220 ± 0.0029	0.0011 ± 0.0010	0.0155 ± 0.0025
$t\bar{t}Z$ (2l)	0.046 ± 0.034	0.009 ± 0.029	0.02 ± 0.05
VV (2l)	0.49 ± 0.12	0.30 ± 0.11	0.05 ± 0.07
Total background	431.4 ± 2.7	387 ± 4	139.1 ± 1.2
FCNC $t\bar{t}$ (cZ)	57.3 ± 0.6	17.67 ± 0.33	21.9 ± 0.4
FCNC (c)tZ	3.24 ± 0.06	11.81 ± 0.10	1.205 ± 0.033

Table 6.14 – Event yields in the SRs for the tZc coupling extraction. The error includes only the statistical uncertainty.

As expected, SR1 has the greater fraction of FCNC $t\bar{t}$ (cZ) events because it is designed to target the decay signal topology, while SR2 has the greater fraction of FCNC (c)tZ events because it is designed to target the FCNC single top production.

The signal yield in SR3 is affected by the DL1 r_c c-efficiency (20%), as discussed in Section 4.2.5.2 but it also has the best background rejection. However, SR1 cannot distinguish between $t \rightarrow Zu$ and $t \rightarrow Zc$ as no c-tagger is not used in this region and the choice of the jet coming from the FCNC top decay is led by the χ^2 minimization.

6.6 Background estimation

A variety of background sources are considered and already discussed in Section 6.1.2.

In order to improve the modelling of the main background processes, Control Regions (CRs) are used in the fit to extract the normalisation of some relevant background sources.

Several CRs are defined:

- $t\bar{t}$ CR is designed to control the minor $t\bar{t}$ background. As previously mentioned, this background enters the selection because of the presence of a mis-reconstructed lepton, i.e. a fake lepton. Since this background is small, the decision was taken to evaluate it using MC simulations. Nevertheless, the normalisation is taken from data because these events are considered fakes for this analysis..
- $t\bar{t}Z$ CR is designed to control the $t\bar{t}Z$ background. It is constructed by requiring the presence of more jets with respect to the jet multiplicity required in the SRs.
- Side-band CRs are designed to contain a mixture of the main background sources ($t\bar{t}Z$ and diboson). They are constructed reversing the SR cuts on the top masses.

6.6.1 Control Regions definition

In the following, the event selection in the CRs is described.

Table 6.15 summarises the selection cuts in the various CRs.

$t\bar{t}$ CR selections The $t\bar{t}$ CR is defined by requiring that there is at least one pair of opposite-sign but different-flavour leptons in the event. No cut on the invariant mass of the opposite-sign leptons is applied. Concerning the jet multiplicity, there should be at least one jet in the event, of which exactly one should be b-tagged. Kinematic plots are presented in Appendix F.1.

$t\bar{t}Z$ CR selections The $t\bar{t}Z$ CR is defined by requiring the presence of at least four jets of which exactly two b-tagged. Also the cut on the transverse mass of the W boson is softened to 30 GeV. To be orthogonal with SR3tZc, also a veto on the presence of a c-jet is required. Kinematic plots are presented in Appendix F.2.

Side-band CR1 selections The mass side-band CR1 is defined by requiring the presence of at least two jets and of exactly one b-tagged jet. The mass of the FCNC top-quark candidate, m_t^{FCNC} , must be outside $2\sigma^{FCNC}$ from 172.5 GeV, the mass of the SM top-quark candidate, m_t^{SM} , must be also outside $2\sigma^{SM}$ from 172.5 GeV. In addition, a veto on the presence of a c-jet is required. Kinematic plots are presented in Appendix F.3.

Side-band CR2 selections The mass side-band CR2 is defined by requiring the presence of exactly one or two jets and of exactly one b-tagged jet. Events are required to have $m_T(\ell_W, \nu) > 40$ GeV.

The mass of the SM top-quark candidate, m_t^{SM} , must be also outside $2\sigma^{SM}$ from 172.5 GeV. Kinematic plots are presented in Appendix F.4.

Common selections			
Exactly 3 leptons with $ \eta < 2.5$ and $p_T(\ell_1) > 27 \text{ GeV}, p_T(\ell_2) > 15 \text{ GeV}, p_T(\ell_3) > 15 \text{ GeV}$			
$t\bar{t}$ CR	$t\bar{t}Z$ CR	Side-band CR1	Side-band CR2
≥ 1 OS pair, no OSSF	≥ 1 OSSF pair with $ m_{e\ell} - 91.2 \text{ GeV} < 15 \text{ GeV}$ $m_T(\ell_w, \nu) > 30 \text{ GeV}$ ≥ 4 jet with $ \eta < 2.5$ $= 2$ b-jet	≥ 1 OSSF pair with $ m_{e\ell} - 91.2 \text{ GeV} < 15 \text{ GeV}$ $m_T(\ell_w, \nu) > 40 \text{ GeV}$ ≥ 2 jet with $ \eta < 2.5$ $= 1$ b-jet	≥ 1 OSSF pair with $ m_{e\ell} - 91.2 \text{ GeV} < 15 \text{ GeV}$ $m_T(\ell_w, \nu) > 40 \text{ GeV}$ $= 1$ jet with $ \eta < 2.5$ $= 1$ b-jet
≥ 1 jet with $ \eta < 2.5$ $= 1$ b-jet	—	$= 0$ c-jet	—
—	—	$ m_t^{\text{FCNC}} - 172.5 \text{ GeV} > 2\sigma^{\text{FCNC}}$	—
—	—	$ m_t^{\text{SM}} - 172.5 \text{ GeV} > 2\sigma^{\text{SM}}$	$ m_t^{\text{SM}} - 172.5 \text{ GeV} > 2\sigma^{\text{SM}}$
—	—	—	—

Table 6.15 – Overview of the requirements applied to select events in the control regions.

6.6.2 Event yields in the Control Regions

Event yields in the CRs are shown in Table 6.16. As it can be noticed, the signal contribution in the various CRs is small. Every Control Region is enriched of the correspondent background.

	Side-band CR1	Side-band CR2	$t\bar{t}Z$ CR	$t\bar{t}$ CR
$t\bar{t}Z + tWZ$	88 ± 12	9.1 ± 2.1	164 ± 22	14.8 ± 1.9
$t\bar{t}W$	4.3 ± 0.7	2.5 ± 0.5	2.3 ± 0.5	27 ± 4
$t\bar{t}H$	2.3 ± 0.4	0.36 ± 0.07	5.4 ± 0.9	13.8 ± 2.1
$VV + LF$	25 ± 15	18 ± 7	0.20 ± 0.22	0.40 ± 0.21
$VV + HF$	130 ± 80	69 ± 28	13 ± 11	2.3 ± 1.4
tZq	20 ± 4	9.9 ± 1.7	14.6 ± 2.9	0.90 ± 0.15
$t\bar{t} + Wt$	10 ± 4	9.1 ± 2.7	3.0 ± 1.2	102 ± 24
Other fakes	3 ± 5	10 ± 11	0.00 ± 0.06	0.12 ± 0.14
Other	2.2 ± 1.6	0.8 ± 2.6	1.1 ± 0.5	2.9 ± 1.5
Total background	280 ± 80	130 ± 32	203 ± 27	164 ± 25
Data	331	169	197	156
Data / Bkg.	1.18 ± 0.35	1.30 ± 0.34	0.97 ± 0.14	0.95 ± 0.16

Table 6.16 – Event yields in the CRs for the tZc coupling extraction. The error includes both statistical and systematic uncertainties.

6.7 Separation of signal from background events using DL1r_c

Three different GBDTs are trained separately in each signal region. In this section only the GBDT for SR3tZc will be presented because directly related to the work of this thesis.

The SR3tZc is defined targeting the FCNC tZc coupling in $t\bar{t}$ decay events using the charm tagger DL1r_c , therefore the MVA discriminant for this coupling, D_3 , is built using the GBDT trained with the FCNC tZc $t\bar{t}$ decay events against backgrounds.

The procedure is not different from that described in Section 6.3 and only the final results will be presented. The final set of variables used to train and test the GBDT method on the events in SR3tZc is in Table 6.17, ordered by the separation value.

The five GBDT output scores used to built discriminant variables are compared in Figure 6.9.

Variable	$\langle s^2 \rangle$	Definition
$m_{b\ell\nu}$	0.1329	SM top-quark candidate mass
p_T^q	0.07402	u/c -quark candidate transverse momentum
N_{jets}	0.0575	Jet multiplicity
$m_{q\ell\ell}$	0.04343	FCNC top-quark candidate mass
$\Delta R(t_{\text{SM}}, t_{\text{FCNC}})$	0.03822	ΔR between SM and FCNC top-quark candidates
$\Delta R(c, Z)$	0.0359	ΔR between c -quark and Z boson candidates
$\Delta R(\ell, Z)$	0.02417	ΔR between W boson lepton and Z boson candidates

Table 6.17 – Variables used in the training of the GBDT in SR3tZc to built the D_3 discriminant used in tZc coupling search. Variables are ordered by the separation $\langle s^2 \rangle$ value, already defined in Section 6.3.1.

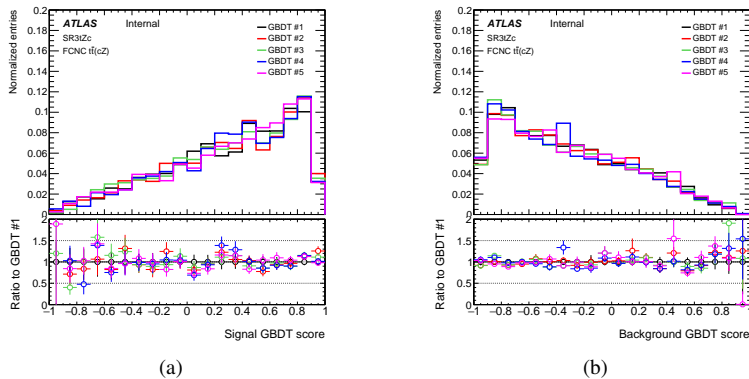


Figure 6.9 – The GBDT output score distributions for (a) signal events and (b) background events, in the test samples. The five trained GBDTs are compared in each signal region.

CHAPTER 7

Extraction of the limit on the branching ratio $t \rightarrow Zc$

In this section the statistical analysis for the extraction of the limit on the branching ratio $t \rightarrow Zc$ is presented. In Section 7.1 a discussion on the systematic uncertainties included in this study is reported. In Section 7.2 the fit strategy for the tZc coupling is presented. In Section 7.3 a summary of how the fit is performed is reported. In Section 7.6 the results of the fit for the tZc coupling extraction is described.

7.1 Systematic uncertainties

Many sources of systematic uncertainties are considered in the search for FCNC tZc interaction and all of them will be reported in this section. Systematic uncertainties that cause variations on the signal acceptance, the background rates, and the shape of the distributions that are fed to the fit are considered. They are evaluated following the common prescriptions and the standard ATLAS procedures. Systematics uncertainties from various sources are considered for the normalisation and shape of the individual backgrounds.

7.1.1 Sources of systematic uncertainties

Systematic uncertainties due to residual differences between data and Monte Carlo simulations, for jet, electron and muon reconstruction after calibration, as well as uncertainties on the calibration scale factors are propagated to the event yields and observables.

- **Lepton reconstruction**

The mis-modelling of muon (electron) trigger, reconstruction, identification and isolation efficiencies in simulation is corrected by introducing scale factors derived from measured efficiencies in data. The decays of $Z \rightarrow \mu^+ \mu^-$ ($Z \rightarrow e^+ e^-$) are used to obtain scale

factors as functions of the lepton kinematics. The uncertainties are evaluated by varying the lepton and signal selections and from the uncertainties in the backgrounds evaluations. For the SMT muons it was proved that the scale factors obtained for isolated muons are valid also for muons inside jets [72].

- **Lepton momentum scale and resolution**

The $Z \rightarrow ll$ process is used to measure the lepton momentum scale and resolution. Calibration factors and associated uncertainties are derived to match the simulation to observed distributions in collision data. The effect of momentum scale uncertainties is evaluated by repeating the event selection after varying the lepton momentum up by 1σ and down by 1σ . For the momentum resolution uncertainties, the event selection is repeated by smearing the lepton momentum [147].

- **Jet energy scale**

The jet energy scale (JES) was derived using information from test-beam data, LHC collision data and simulation. The JES calibration consists of several steps that account for detector problems, jet reconstruction algorithms, jet fragmentation models, dense data-taking environment from high pile-up conditions and response difference between data and MC simulation. The fractional uncertainty decreases with the p_T of the reconstructed jet and is rather stable in η . The JES uncertainty has various components according to the factors it accounts for and the different steps used to compute it. The jet calibration procedure is described in Ref. [148]. The sources of the JES uncertainties with different effective number of parameters are: BJES response, detector, mixed, modelling, statistical, eta intercalibration, flavour composition, pile-up and relative non-closure.

- **Jet energy resolution**

The impact of the uncertainty on the jet energy resolution (JER) is evaluated by smearing the jet energy in the MC samples.

- **Jet vertex tagger**

The uncertainty for the JVT requirement is also applied.

- **Missing transverse momentum**

Uncertainties of the soft-track component are derived from the level of agreement between data and MC simulation of the p_T balance between the hard and soft E_T^{miss} components. Three different uncertainties are considered: an offset along the p_T (hard) axis, as well as the smearing resolution along and perpendicular to the p_T (hard) axis.

- **b -tagging efficiency**

The b -tagging efficiencies and mis-tag rate for the taggers have been measured in data using the same methods as described in [149, 150]. The number of NP used for the b -tagging data/MC scale factors is evaluated separately for b , c and light-flavour quark jets in the MC samples.

- **c -tagging efficiency**

Since an official calibration is not available yet, the c -tagging efficiencies are not considered in this analysis. Nevertheless, assuming a flat 20% variation on the related scale factor, the final expected limit will be degraded by almost 5%.

Systematic uncertainties on template shapes from MC modelling of various background sources are estimated by comparing different generators and varying parameters for the event generation.

- **Signal**

Renormalization and factorization scale uncertainties are considered for the signal, following the latest prescriptions. In particular, the μ_r and μ_f variations are included and the envelope of the variations is added (called *Signal μ_r and μ_f*).

- **$t\bar{t}$**

The effect of changing the parton shower for the generation of $t\bar{t}$ events is included and the difference between PYTHIA8 and HERWIG 7 parton shower is added as $t\bar{t}$ parton showering uncertainty (called *$t\bar{t} PS$*).

Scale, radiation and tune systematics are also included, following the latest prescriptions. In particular, the μ_r and μ_f variations are included and the envelope of the variations is added (called *$t\bar{t} \mu_r$ and μ_f*). The A14 tune variations are added (called *$t\bar{t} A14$ tune (ISR)*). Finally the FSR is varied (called *$t\bar{t} FSR$*).

The systematic uncertainties related to the parton distribution functions are taken into account for the $t\bar{t}$ background (called *$t\bar{t} PDF$*).

Additionally, the uncertainty associated to the h_{damp}^1 parameter is evaluated (NP called *$t\bar{t} hdamp$*) using the alternative sample with the h_{damp} value increased to $3.0 m_t$.

Last but not least, an uncertainty is added to take into account the differences in the photon conversion and b-hadron fractions in the signal regions with respect to the $t\bar{t}$ control region where the $t\bar{t}$ background is controlled. This uncertainty is obtained by taking the maximum difference in the fractions between the regions (13% for b-hadron and 50% for photon conversions) and it's applied to the relevant fraction. The two uncertainties are called *$t\bar{t}$ non-prompt lep. (photon conv.)* and *$t\bar{t}$ non-prompt lep. (b-decay)*.

- **$t\bar{t}Z$**

The effect of changing the MC generator for $t\bar{t}Z$ events was investigated and the difference between MADGRAPH5_aMC@NLO and SHERPA prediction is included as $t\bar{t}Z$ generator systematic uncertainty (called *$t\bar{t} Z Generator$*).

A scale uncertainty systematic is also included, following the latest prescriptions. In particular, the μ_r and μ_f variations are included and the envelope of the variations is added (called *$t\bar{t} Z \mu_r$ and μ_f*). Additionally, the effects of QCD radiation for this sample are also taken into account through samples for different A14 tune variations (called *$t\bar{t} Z QCD$*).

- **tWZ**

The effect of changing the diagram removal scheme used for the generation of tWZ events was investigated and the difference between the two diagram removal predictions is included as tWZ generator systematic uncertainty (called *$t W Z DR$*).

¹The h_{damp} factor is the model parameter that controls ME/Parton Shower matching and effectively regulates the high- p_T radiation.

- **tZq**

The differences of using different A14 tune variations are accounted and considered in the fit (called $tZ QCD$).

- **Diboson**

The effect of changing the MC generator for diboson events was also investigated and the difference between SHERPA and POWHEG-Box prediction is included as diboson generator uncertainty. This uncertainty is split into two components: light- and heavy-flavour (called $VV + LF Generator$ and $VV + HF Generator$) using truth information.

An uncertainty depending on the jet multiplicity is also included for the diboson samples with the separation by light- and heavy-flavour as well. Therefore, an uncertainty of 25 % (called $VV + LFN Jet$ and similarly for $VV + HF$) is added in quadrature per jet in each jet multiplicity resulting into 5 NP ($= 1, = 2, = 3, = 4, \geq 5$ jets). This uncertainty is also known as *Berends scaling*

- **MC statistics**

The uncertainty due to the limited size of the various MC samples is also included.

The uncertainties on the background rate uncertainties are summarised in table 7.1 and described in the following:

- **$t\bar{t}$**

For the $t\bar{t}$ process, an uncertainty of 5.5 % on the normalisation is applied. Since this analysis targets final states with three prompt leptons (see Table 6.13), the $t\bar{t}$ process is a fake background. Therefore a normalisation factor is added to the fit as a free-floating parameter to better control the event rate.

- **$t\bar{t}V$**

For $t\bar{t}Z$ and $t\bar{t}W$ backgrounds, the uncertainty on the normalisation is taken from [151], where a 12 % theory uncertainty is quoted.

- **tWZ**

For the tWZ background, an uncertainty of 30 % is applied to the normalisation [152].

- **tZq**

For the tZq process, an uncertainty of 14 % on the normalisation is applied following the recent results from the tZq observation [153].

- **Diboson**

For diboson background, the normalization uncertainty is taken from ATLAS results [154]. The uncertainties applied are 20 % for the light diboson component and 30 % for the heavy diboson component.

- **$Z + jets$**

Concerning the $Z + jets$ processes, an uncertainty on the normalisation is applied with a value of 100 % allowing the constraint of this value by the fit.

- **$t\bar{t}H$**

Normalisation uncertainty of 15 % is applied on the $t\bar{t}H$ background [155].

Process	Uncertainty
t̄t	5.5 %
t̄tV	12 %
tWZ	30 %
tZq	14 %
VV + LF	20 %
VV + HF	30 %
Z + jets	100 %
t̄H	15 %
Other ($t\bar{t}t, t\bar{t}t\bar{t}, VVV, VH$ and $t\bar{t}WW$)	50 %

Table 7.1 – Uncertainties on the normalisation of all background processes.

- **Other background processes** A conservative overall normalization uncertainty of 50 % is applied on the remaining minor backgrounds ($t\bar{t}t, t\bar{t}t\bar{t}, VVV, VH$ and $t\bar{t}WW$). These background components are typically well below of 1 % in the SRs.

The uncertainty in the combined 2015–2018 integrated luminosity is 1.7 %. It is derived, following a methodology similar to that detailed in Ref. [156], from the calibration of the luminosity scale using $x - y$ beam-separation scans.

The uncertainty of the pile-up reweighting in simulated samples is included.

7.1.2 Acceptance and shape uncertainties

The systematic uncertainties discussed above cause variations on the signal acceptance, the background rates, and the shape of the distributions that are fed to the fit. We denote the relative variation of the acceptance of process j due to a systematic source i α_{ij+} and α_{ij-} for a positive or negative variation of the systematic uncertainty.

The MC statistics is related to the statistical uncertainty in each bin of the distributions that are used in the fit, so it can change the shape of the distributions. For all other systematics listed, rate and shape differences are taken into account.

7.1.2.1 Symmetrization of shape uncertainties

For the shape uncertainties included in the fit, the templates are symmetrised by taking half the difference between the up and down variation around the nominal template. For the bins where both the initial up and down variations are on the same side from the nominal, the largest variation is symmetrically assigned for the final templates.

Concerning all systematic uncertainties containing up and down systematic variations, these are symmetrised by $(\alpha_{ij-} + \alpha_{ij+})/2 = \alpha_{ij-} = \alpha_{ij+}$. For the systematic uncertainties with one sided systematics, these are symmetrised by defining $\alpha_{ij-} = \alpha_{ij+}$.

7.1.2.2 Smoothing and Pruning

Some fluctuations in individual bins can be caused by the low statistics shape systematic uncertainties. A smoothing of systematic shape uncertainties is performed using the default smoothing algorithm available through the `TRExFitter` package to average adjacent bins to remove statistical fluctuations.

Different levels of pruning are applied for shape and normalisation. A value of 1% and 0.5% were used for normalisation and shape, respectively.

7.2 Fit strategy

In order to extract the tZc coupling, a binned maximum likelihood $L(\mu, \theta)$ fit is performed using the MC templates for both signal and background predictions. The $L(\mu, \theta)$ is constructed as a product of Poisson probability terms over all bins in each considered distribution, and Gaussian constraint terms for θ , a set of nuisance parameters that parametrize effects of systematic uncertainties on the signal and background expectations.

The software framework used for performing the fit is `TRExFitter` [157]. This combines the functionalities of `Roofit` [158] and `RooStats` [159] and is designed to build probability density functions that are automatically fit to data and interpreted with statistical tests. The likelihood function comprises histogram bins from both SRs and CRs.

Regions The regions included in the fit, as well as the distributions that are fitted together, are summarised in Table 7.2. The definitions of the various regions are shown in Table 6.13 for the SRs and in Table 6.15 for the CRs. Some regions are used to control the overall normalisation of various backgrounds.

tZc coupling extraction	
Region	Distribution
SR1 tZc	D_1
SR2 tZc	D_2^c
SR3 tZc	D_3
Side-band CR1 tZc	D_1
Side-band CR2	D_2^c
$t\bar{t}Z$ CR	Leading lepton p_T
$t\bar{t}$ CR	Leading lepton p_T

Table 7.2 – Overview of the regions included in the fits.

Inputs The inputs to the fit consist of binned distributions, including the signal and all background sources. Additionally, for each MC sample, separate templates that take into account the systematic variations discussed in Section 7.1 are created and included in the fit.

POI The global likelihood function describing the agreement between data and prediction as a function of the parameter of interest (POI) and the set of nuisance parameters describing the effect of the corresponding systematic uncertainty sources is constructed and fitted. The POI is the signal strength parameter, μ , a multiplicative factor for the number of signal events normalised to a reference branching ratio $BR_{\text{ref}}(t \rightarrow Zc) = 0.024\%$. The relationship between μ and the corresponding $BR(t \rightarrow Zc)$ is

$$\mu = \frac{BR(t \rightarrow Zc)(1 - BR(t \rightarrow Zc))}{BR_{\text{ref}}(t \rightarrow Zc)(1 - BR_{\text{ref}}(t \rightarrow Zc))} \quad (7.1)$$

Systematic uncertainty NPs The impact of the systematic uncertainties on the extracted μ is estimated as follows.

A nuisance parameter (NP) is associated to each systematic uncertainty. These NPs have a central value and an associated pre-fit uncertainty. The fit is able to change the central value of the NPs (called *pull*) and the uncertainty on the NP can change (this is called *constraint* if the uncertainty becomes smaller), to better describe the data. To understand the impact of the NPs on the extracted μ , the following procedure is used: several fits are performed, each fit separately for each NP, changing the central value of each NP up and down by the pre-fit (post-fit) $\pm 1\sigma$ uncertainties, fixing it to that value and performing the fit to μ . The difference between this μ and the one extracted from the standard fit, $\Delta\mu$, is the pre-fit (post-fit) impact on μ . The values of $\Delta\mu$ are shown in the so called ranking plot that helps to understand the size of the effect that the uncertainty has on the signal strength.

Statistical uncertainty NPs The same procedure is applied to the so called γ parameters, which represent the background statistical uncertainty in each bin of the input distributions. There is therefore one gamma parameter per bin of each input distribution.

Background treatment in the fit The $t\bar{t}Z$ and tWZ backgrounds are merged in one template as well as $t\bar{t}$ and Wt . Two templates are included in the fit for diboson process that correspond to the heavy and light components ($VV + HF$ and $VV + LF$). Separate templates are used for the remaining background sources. Since this analysis targets final states with three prompt leptons (see Table 6.13), the $t\bar{t}$ and the Wt processes are a fake background. Therefore the normalisation of $t\bar{t} + Wt$ background is free floating in the fit meaning that an unconstrained NP is associated to the corresponding template, namely $\mu_{t\bar{t}+Wt}$. All other backgrounds have pre-fit normalizations with uncertainties (see Section 7.1.1).

7.3 Summary of fits

For the extraction of the tZc coupling, the following fits are presented:

Background-only fit in CRs: in this fit only CRs are used. Data are used. The signal templates are not included in the fit. This fit is used to estimate the preliminary background.

Signal+Background fit in SR+CRs with pseudo-data: in this fit both SRs and CRs are used. Data are used in the CRs. In the SRs, pseudo-data are constructed using post-fit background normalisations from the B-only fit in CRs. In the following, this dataset is called 'realistic Asimov'. This fit is used to extract the expected upper limit.

Signal+Background fit in SR+CRs with data: in this fit both SRs and CRs are used. Data are used in both SRs and CRs. This fit is used to extract the tZc coupling, therefore the observed and the expected upper limit.

These fits are summarised in the following table:

Setup	Fit	SRs	CRs	Template	Reference
1	B-only in CRs	–	data	B	Appendix G
2	S+B in SRs+CRs with realistic Asimov	realistic Asimov from Setup 1	data	S+B	Section 7.4
3	S+B in SRs+CRs with data	data	data	S+B	Section 7.5

Table 7.3 – Overview of the fits for the extraction of the tZc coupling.

7.4 Signal + Background fit in SRs+CRs with realistic Asimov data

To extract the expected sensitivity, an SRs+CRs S+B fit is performed. Data in used in CRs while in SRs an Asimov dataset is used, constructed using the background normalisations found in Appendix G.

Plots and tables shown in this section are the following:

- The value of the post-fit normalisation parameters of the free floating background is shown in Figure 7.1.
- The list of the systematic shapes that are dropped from the fit for each sample and for each region is shown in fig. 7.2.
- The pull distributions of the all nuisance parameters can be seen in Figures 7.3 and 7.4 and Figure 7.5.
- The correlation matrix of the nuisance parameters is shown in Figure 7.6.
- The ranking of the nuisance parameters is shown in Figure 7.7.
- Event yields pre- and post-fit are shown in Tables 7.4 and 7.5.

- Pre-fit and post-fit distributions of the fitted distributions in the various regions are shown in Figures 7.8 to 7.11.

As expected, the behaviour of the fit with the realistic Asimov dataset provides similar results to those of the B-only fit in the CRs (Appendix G). In fact, normalisation factors (Figure 7.1) and NPs pulls and constrains (Figures 7.3 and 7.4) are very similar since in the CRs the expected signal is negligible and in the SRs the Asimov data are used. The signal strength μ is expected to be zero for the same reason. The fake normalization factor $\mu_{\bar{t}t+W_t}$ is compatible with unity.

The most pulled NPs (e.g. $t\bar{t}$ FSR and $VV + HF$ Berends scaling for events with 1 jet) are not among the highest ranked NPs (Figure 7.7). Slightly pulled NPs (e.g. $t\bar{t}Z$ normalization, Other fakes norm. and $VV + HF$ generator) have a small post-fit impact on the signal strength, around 2%, as can be seen again in Figure 7.7. Moreover, none of the systematic uncertainties has a post-fit impact on the signal strength parameter greater than 3%.

Concerning the correlations between NPs (Figure 7.6), some strong correlations between diboson related NPs are present, as expected. This is also true for the $t\bar{t}$ normalization and some $t\bar{t}$ modeling NPs. Event yields pre- and post-fit, shown in Tables 7.4 and 7.5 and distributions in Figures 7.8 to 7.11 show a good agreement between the observed data and MC predictions in Control and Signal Regions.

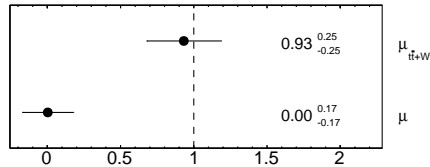


Figure 7.1 – Normalisation factors for the S+B tZc fit in SRs+CRs with realistic Asimov.

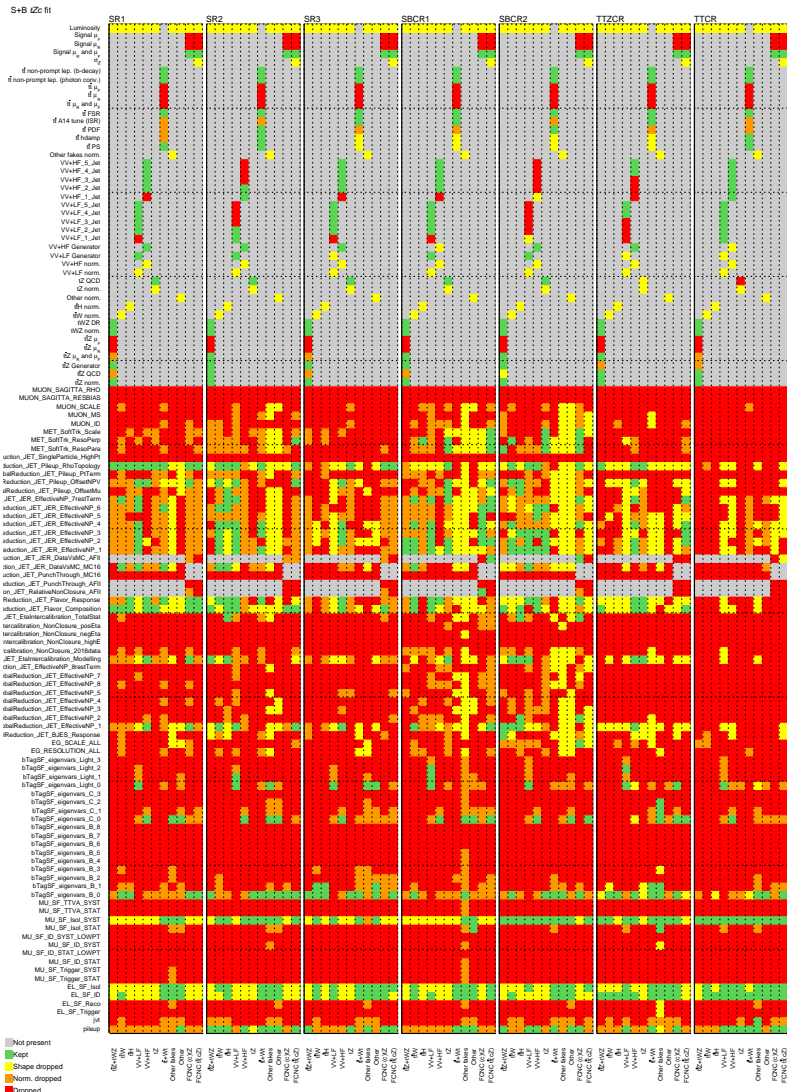


Figure 7.2 – Pruning of the nuisance parameters for the S+B tZc fit in SRs+CRs with realistic Asimov.

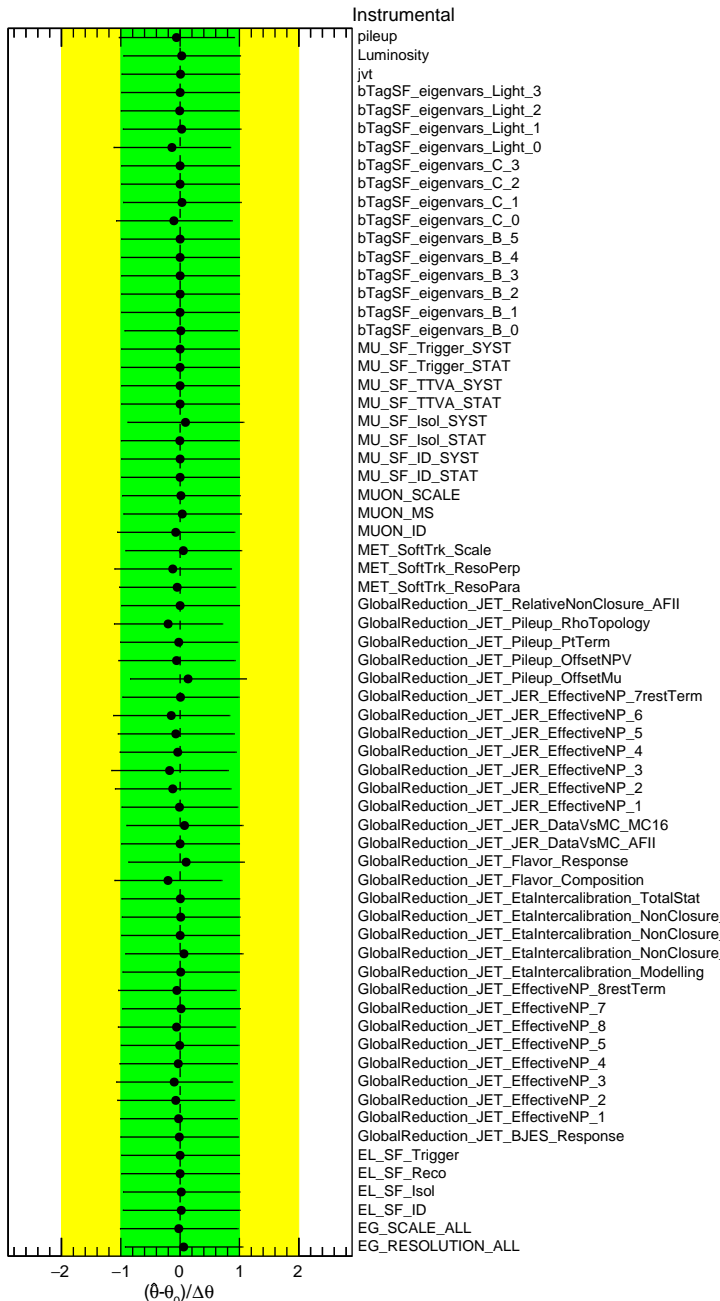


Figure 7.3 – Pulls and constraints of the instrumental nuisance parameters for the S+B tZc fit in SRs+CRs with realistic Asimov.

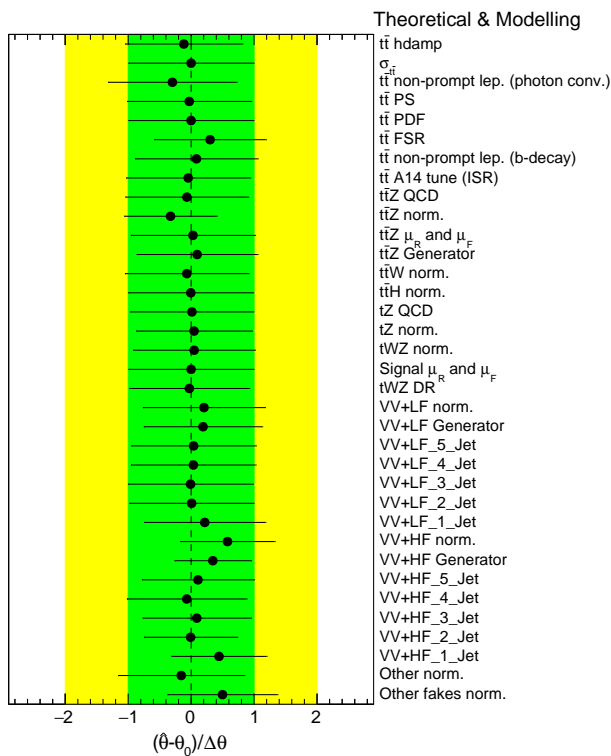
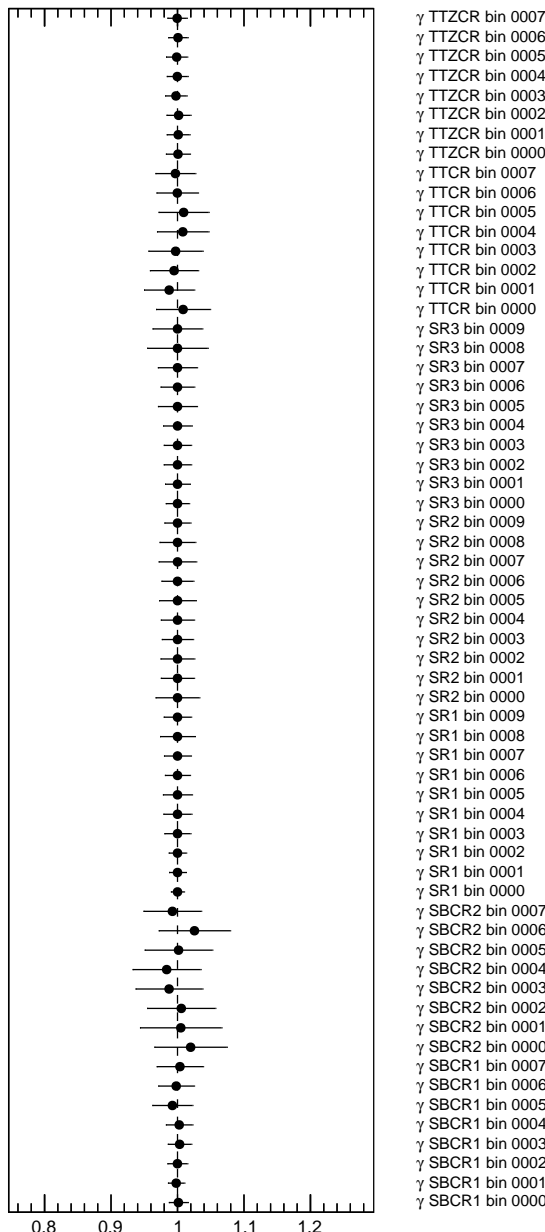


Figure 7.4 – Pulls and constraints of the theoretical and modeling nuisance parameters for the S+B tZc fit in SRs+CRs with realistic Asimov.

**Figure 7.5 –** Gamma parameters for the S+B tZc fit in SRs+CRs with realistic Asimov.

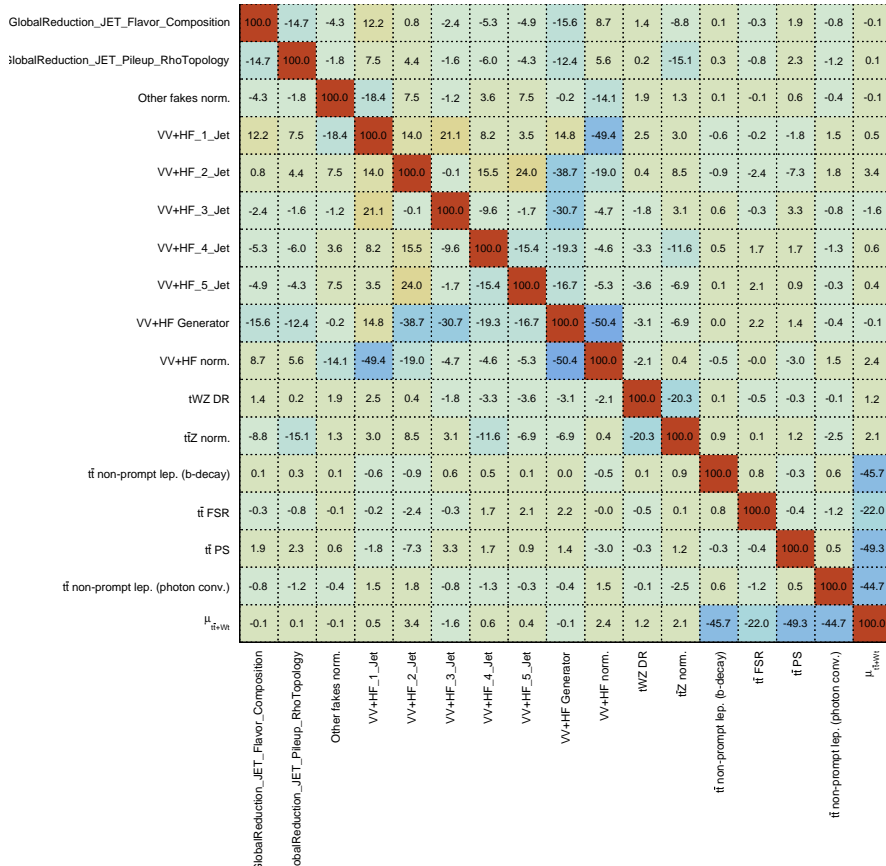


Figure 7.6 – Correlation matrix of the nuisance parameters for the $S+B$ $t \rightarrow Zc$ fit in SRs+CRs with realistic Asimov.

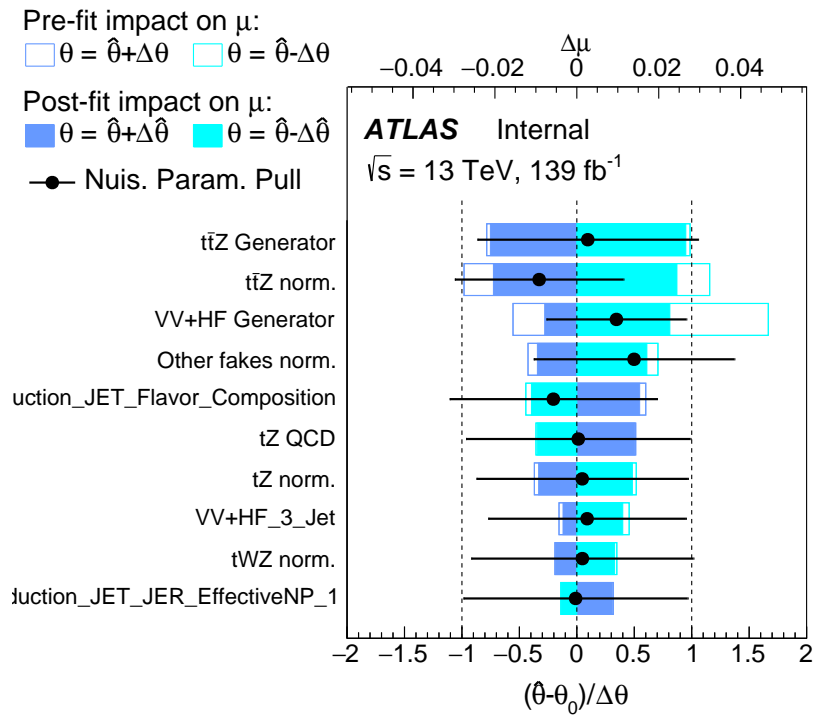


Figure 7.7 – Ranking of the nuisance parameters for the S+B tZc fit in SRs+CRs with realistic Asimov.

7. EXTRACTION OF THE LIMIT ON THE BRANCHING RATIO $t \rightarrow Zc$

	SR1	SR2	SR3	Side-band CR1	Side-band CR2	$t\bar{t}Z$ CR	$t\bar{t}$ CR
$t\bar{t}Z + tWZ$	168 ± 22	33 ± 7	82 ± 11	88 ± 12	9.1 ± 2.1	164 ± 22	14.8 ± 1.9
$t\bar{t}W$	5.8 ± 1.0	3.3 ± 0.6	2.04 ± 0.35	4.3 ± 0.7	2.5 ± 0.5	2.3 ± 0.5	27 ± 4
$t\bar{t}H$	6.1 ± 1.0	0.88 ± 0.18	2.6 ± 0.4	2.3 ± 0.4	0.36 ± 0.07	5.4 ± 0.9	13.8 ± 2.1
$VV + LF$	28 ± 17	35 ± 13	2.9 ± 2.0	25 ± 15	18 ± 7	0.20 ± 0.22	0.40 ± 0.21
$VV + HF$	140 ± 100	160 ± 70	30 ± 22	130 ± 80	69 ± 28	13 ± 11	2.3 ± 1.4
tZq	47 ± 7	110 ± 18	13.8 ± 2.3	20 ± 4	9.9 ± 1.7	14.6 ± 2.9	0.90 ± 0.15
$t\bar{t} + Wt$	21 ± 4	32 ± 11	3.7 ± 1.0	10 ± 4	9.1 ± 2.7	3.0 ± 1.2	102 ± 24
Other fakes	10 ± 11	12 ± 12	1.4 ± 1.6	3 ± 5	10 ± 11	0.00 ± 0.06	0.12 ± 0.14
Other	2.5 ± 1.5	3.8 ± 2.8	0.48 ± 0.25	2.2 ± 1.6	0.8 ± 2.6	1.1 ± 0.5	2.9 ± 1.5
FCNC (c) Z	3.24 ± 0.26	11.8 ± 0.6	1.21 ± 0.09	1.06 ± 0.12	0.83 ± 0.09	0.24 ± 0.04	0.083 ± 0.012
FCNC $t\bar{t}$ (cZ)	57 ± 5	17.7 ± 1.9	21.9 ± 1.6	4.2 ± 0.6	1.9 ± 0.4	3.7 ± 0.5	0.37 ± 0.07
Total background	430 ± 110	390 ± 80	139 ± 25	280 ± 80	130 ± 32	203 ± 27	164 ± 25
Data	488	452	150	331	169	197	156
Data / Bkg.	1.13 ± 0.28	1.17 ± 0.24	1.08 ± 0.21	1.18 ± 0.35	1.30 ± 0.34	0.97 ± 0.14	0.95 ± 0.16

Table 7.4 – Pre-fit event yields in the S+B tZc fit in SRs+CRs with realistic Asimov. The error includes both statistical and systematic uncertainties.

	SR1 tZc	SR2 tZc	SR3 tZc	Side-band CR1	Side-band CR2	$t\bar{t}Z$ CR	$t\bar{t}$ CR
$t\bar{t}Z + tWZ$	163 ± 14	$.34 \pm 6$	79 ± 7	85 ± 9	9.3 ± 1.9	157 ± 13	14.4 ± 1.3
$t\bar{t}W$	5.7 ± 0.9	3.4 ± 0.6	2.01 ± 0.32	4.2 ± 0.7	2.5 ± 0.5	2.2 ± 0.4	26 ± 4
$t\bar{t}H$	6.1 ± 0.9	0.90 ± 0.17	2.6 ± 0.4	2.3 ± 0.4	0.37 ± 0.07	5.3 ± 0.8	13.8 ± 2.1
$VV + LF$	32 ± 18	39 ± 14	3.3 ± 2.1	29 ± 16	21 ± 8	0.24 ± 0.23	0.40 ± 0.18
$VV + HF$	198 ± 32	212 ± 29	43 ± 7	172 ± 25	94 ± 16	18 ± 6	3.3 ± 0.5
tZq	46 ± 7	112 ± 16	13.9 ± 2.1	19.6 ± 3.3	10.1 ± 1.6	14.4 ± 2.5	0.91 ± 0.12
$t\bar{t} + Wt$	18 ± 4	30 ± 7	3.2 ± 0.7	9.5 ± 2.8	8.6 ± 1.7	2.5 ± 0.8	95 ± 13
Other fakes	15 ± 11	17 ± 13	2.1 ± 1.7	5 ± 5	18 ± 15	0.005 ± 0.009	0.18 ± 0.13
Other	2.2 ± 1.2	3.7 ± 2.5	0.44 ± 0.23	1.8 ± 1.2	0.2 ± 0.8	1.0 ± 0.5	2.7 ± 1.4
FCNC (c) Z	0.0 ± 0.6	0.0 ± 2.1	0.00 ± 0.21	0.00 ± 0.18	0.00 ± 0.15	0.00 ± 0.04	0.000 ± 0.014
FCNC $t\bar{t}$ (cZ)	0 ± 10	0.1 ± 3.1	0 ± 4	0.0 ± 0.7	0.01 ± 0.33	0.0 ± 0.6	0.00 ± 0.06
Total background	487 ± 21	452 ± 20	150 ± 7	328 ± 17	165 ± 13	201 ± 12	157 ± 12
Data	488	452	150	331	169	197	156
Data / Bkg.	1.00 ± 0.04	1.00 ± 0.04	1.00 ± 0.05	1.01 ± 0.05	1.02 ± 0.08	0.98 ± 0.06	0.99 ± 0.08

Table 7.5 – Post-fit event yields in the S+B tZc fit in SRs+CRs with realistic Asimov. The error includes both statistical and systematic uncertainties.

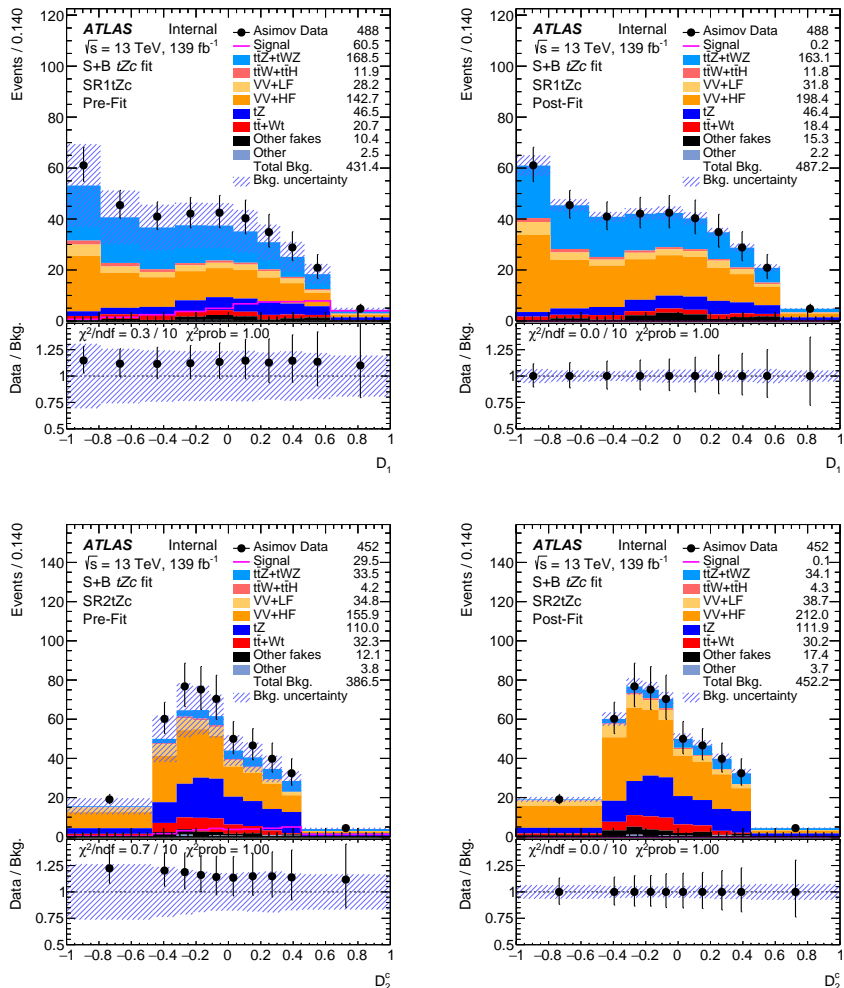


Figure 7.8 – Pre-fit (left) and post-fit (right) BDTG output distributions in SR1 and SR2 for the S+B tZc fit in SRs+CRs with realistic Asimov. The uncertainty band includes both statistical and systematic uncertainties.

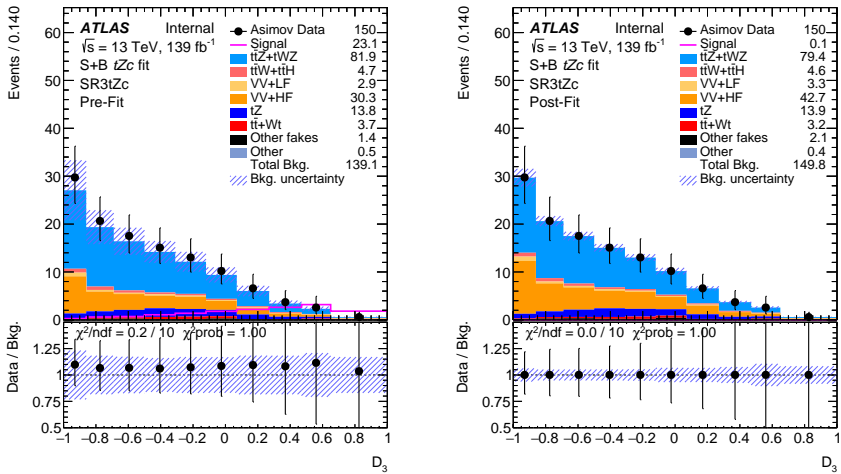


Figure 7.9 – Pre-fit (left) and post-fit (right) leading lepton p_T distributions in SR3 for the S+B tZc fit in SRs+CRs with realistic Asimov. The uncertainty band includes both statistical and systematic uncertainties.

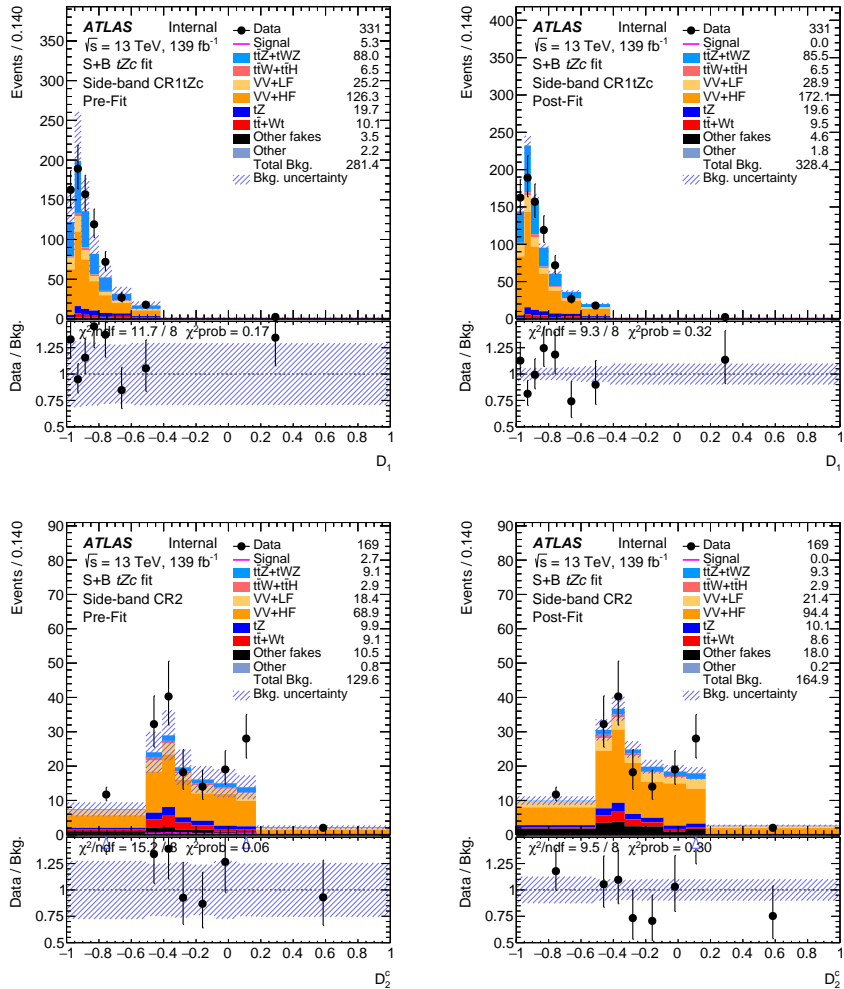


Figure 7.10 – Pre-fit (left) and post-fit (right) BDTG output distributions in the side-band CRs for the S+B tZc fit in SRs+CRs with realistic Asimov. The uncertainty band includes both statistical and systematic uncertainties.

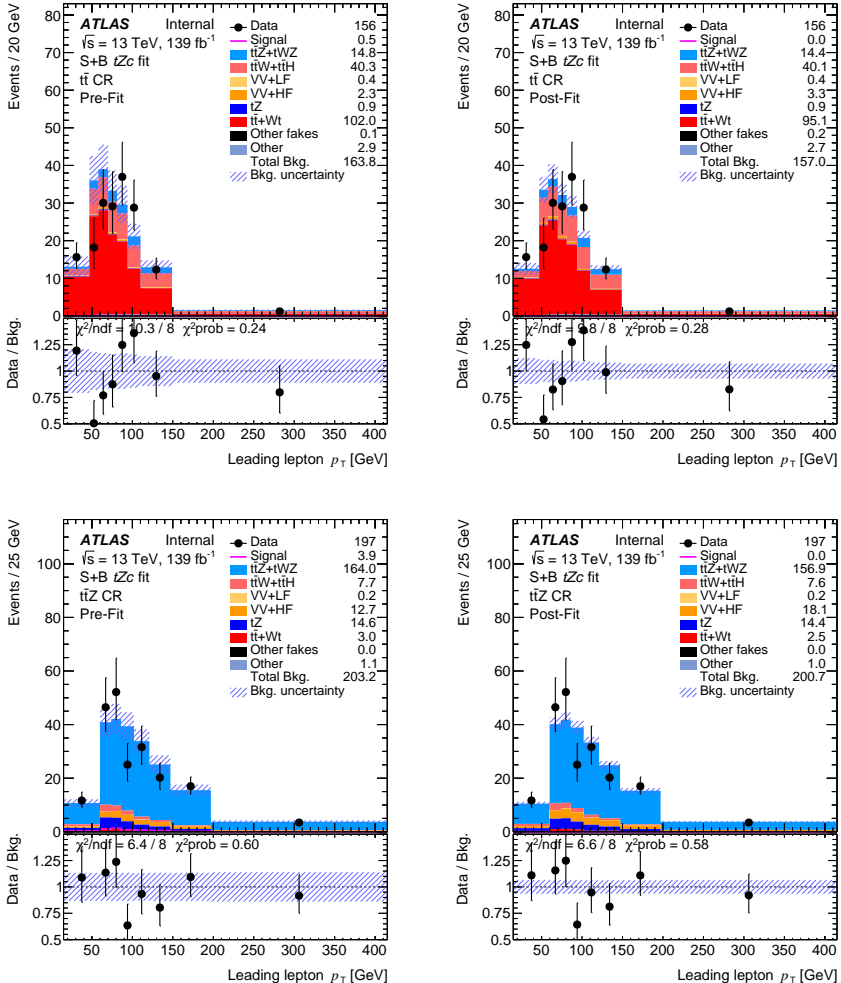


Figure 7.11 – Pre-fit (left) and post-fit (right) leading lepton p_T distributions in the $t\bar{t}$ and $t\bar{t}Z$ CRs for the S+B tZc fit in SRs+CRs with realistic Asimov. The uncertainty band includes both statistical and systematic uncertainties.

7.5 S+B fit in SRs+CRs with unblinded data

In this section, results with unblinded data are presented. The combined fit has been performed in the background control and signal regions with data under the signal+background hypothesis. This test statistic is used to measure the compatibility of the observed data with the signal+background hypothesis and to make statistical inferences about μ , such as upper limits using the CL_s method [160, 161]. Plots and tables shown in this section are the following:

- The value of the post-fit normalisation parameter of the free floating background is shown in Figure 7.12.
- The list of the systematic shapes that are dropped from the fit for each sample and for each region is shown in fig. 7.13.
- The pull distributions of the all nuisance parameters can be seen in Figures 7.14 and 7.15 and Figure 7.16.
- The correlation matrix of the nuisance parameters is shown in Figure 7.17.
- The ranking of the nuisance parameters is shown in ??.
- Event yields pre- and post-fit are shown in Tables 7.6 and 7.7.
- Pre-fit and post-fit distributions of the fitted distributions in the various regions are shown in Figures 7.18 to 7.21.

The fake normalization factor $\mu_{t\bar{t}+Wt}$ (Figure 7.12) is compatible with unity and the signal strength μ is compatible with zero within the uncertainties.

Results are similar to what was found with blinded Signal Regions (Section 7.4).

The value of the fitted nuisance parameters (Figures 7.14 and 7.15) are within their prior uncertainties, meaning that the data are well modelled with the MC predictions within the uncertainties. Concerning the correlations between NPs (Figure 7.17), some strong correlations between diboson related NPs are present, as expected. This is also true for the $t\bar{t}$ normalisation and some $t\bar{t}$ modeling NPs. None of the systematic uncertainties has a post-fit impact on the signal strength parameter greater than 4% as can be seen again in Figure 7.7.

Event yields pre- and post-fit, shown in Tables 7.6 and 7.7 and distributions in Figures 7.18 to 7.21 show a good agreement between the observed data and MC predictions in Control and Signal Regions. No evidence for the FCNC $t \rightarrow Zc$ signal is found.

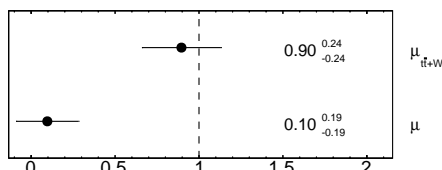


Figure 7.12 – Normalisation factors for the S+B tZc fit in SRs+CRs with data.

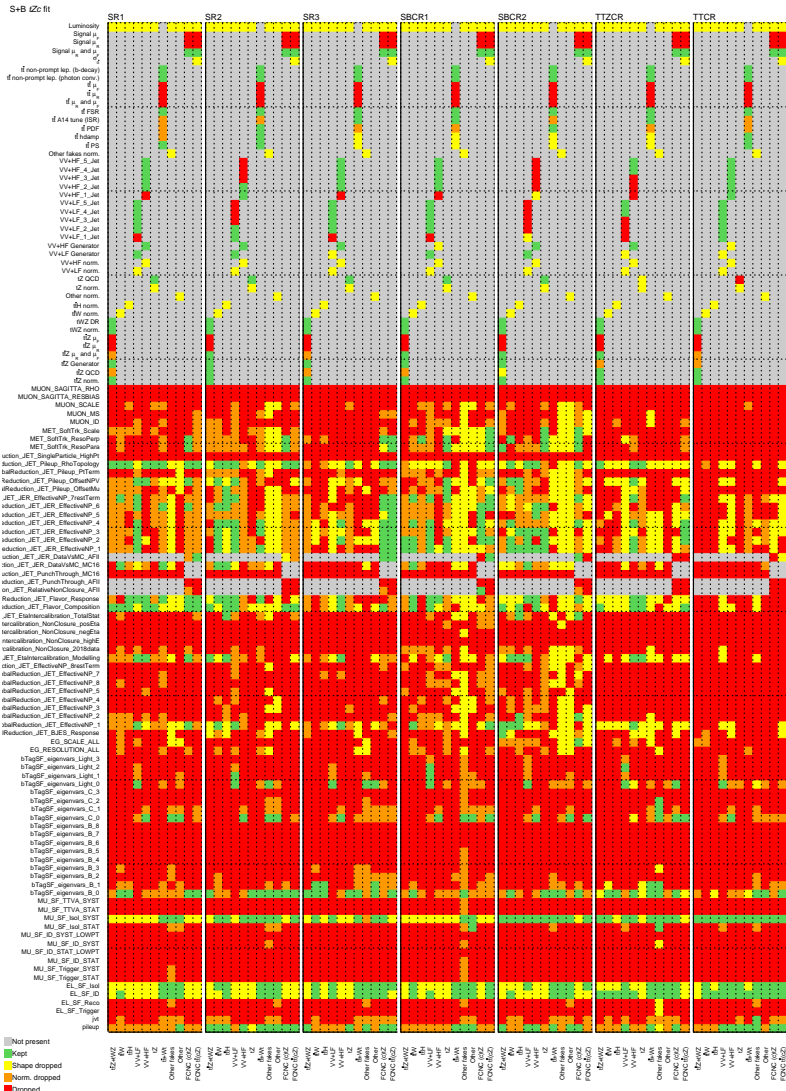


Figure 7.13 – Pruning of the nuisance parameters for the S+B tZc fit in SRs+CRs with data.

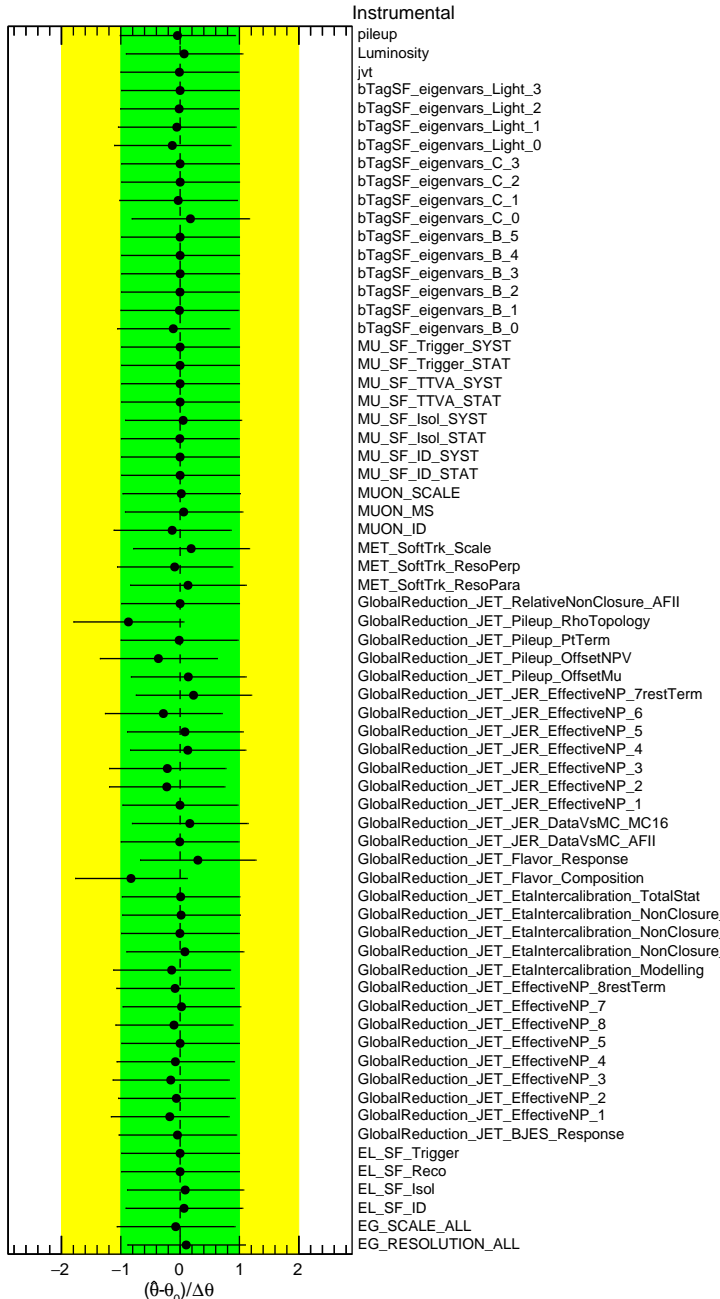


Figure 7.14 – Pulls and constraints of the instrumental nuisance parameters for the S+B tZc fit in SRs+CRs with data.

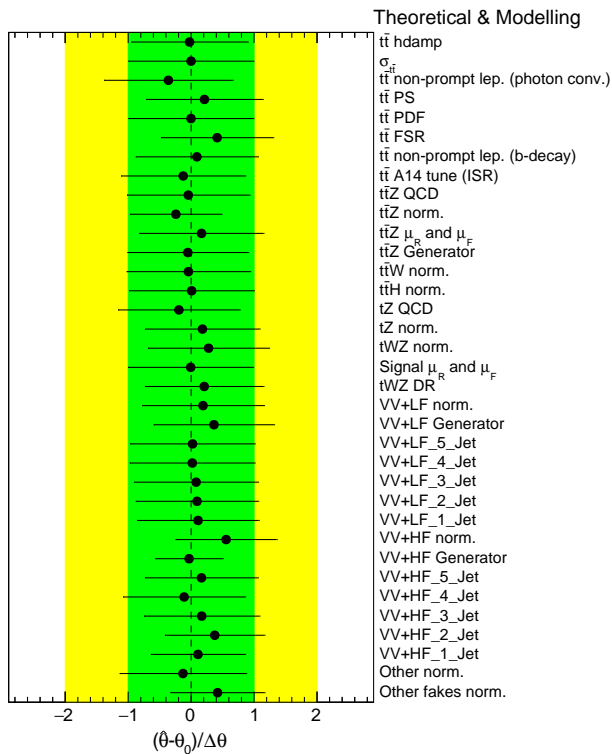


Figure 7.15 – Pulls and constraints of the theoretical and modeling nuisance parameters for the S+B tZc fit in SRs+CRs with data.

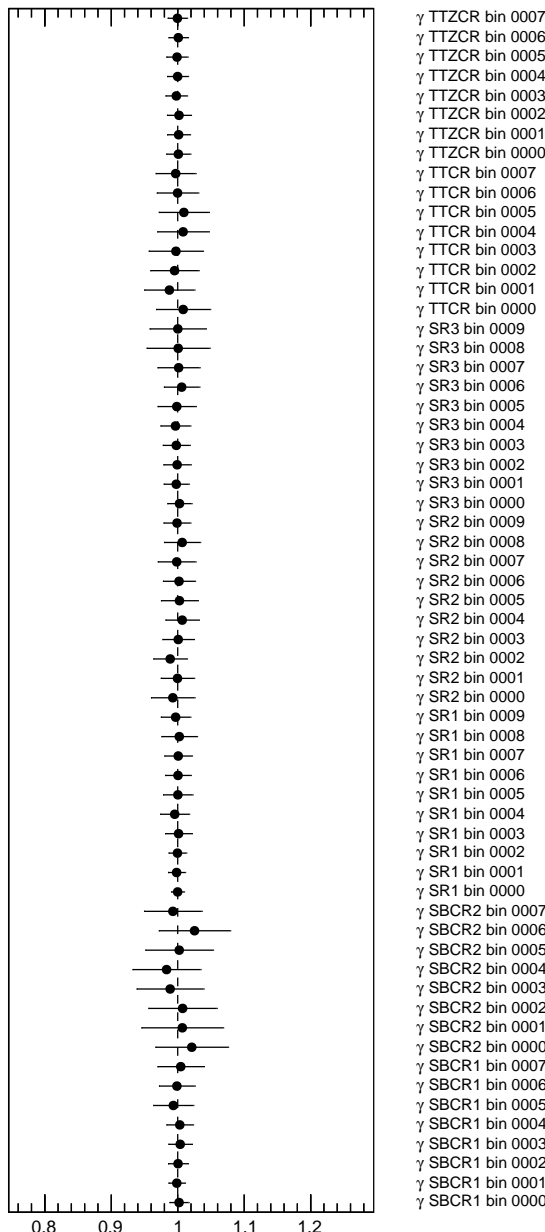


Figure 7.16 – Gamma parameters for the S+B tZc fit in SRs+CRs with data.

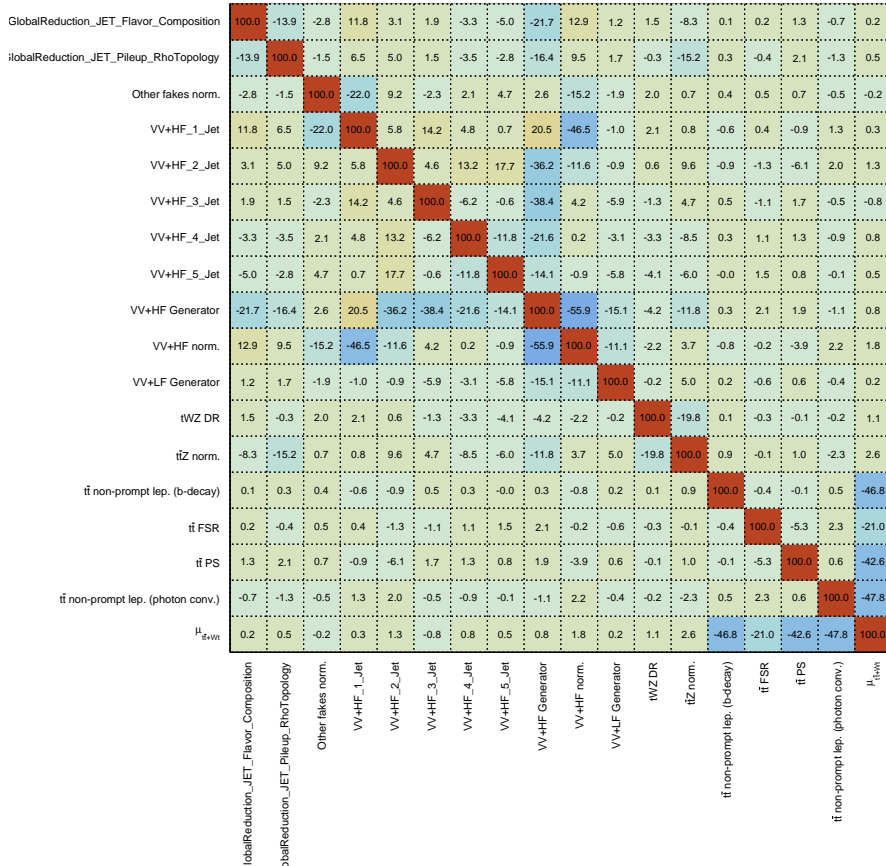


Figure 7.17 – Correlation matrix of the nuisance parameters for the S+B $t \rightarrow Zc$ fit in SRs+CRs with data.

	SR1	SR2	SR3	Side-band CR1	Side-band CR2	t̄Z CR	t̄ CR
t̄Z +tWZ	168 ± 22	33 ± 7	82 ± 11	88 ± 12	9.1 ± 2.1	164 ± 22	14.8 ± 1.9
t̄W	5.8 ± 1.0	3.3 ± 0.6	2.04 ± 0.35	4.3 ± 0.7	2.5 ± 0.5	2.3 ± 0.5	27 ± 4
t̄H	6.1 ± 1.0	0.88 ± 0.18	2.6 ± 0.4	2.3 ± 0.4	0.36 ± 0.07	5.4 ± 0.9	13.8 ± 2.1
V V + LF	28 ± 17	35 ± 13	2.9 ± 2.0	25 ± 15	18 ± 7	0.20 ± 0.22	0.40 ± 0.21
V V + HF	140 ± 100	160 ± 70	30 ± 22	130 ± 80	69 ± 28	13 ± 11	2.3 ± 1.4
tZq	47 ± 7	110 ± 18	13.8 ± 2.3	20 ± 4	9.9 ± 1.7	14.6 ± 2.9	0.90 ± 0.15
t̄ +Wt	21 ± 4	32 ± 11	3.7 ± 1.0	10 ± 4	9.1 ± 2.7	3.0 ± 1.2	102 ± 24
Other fakes	10 ± 11	12 ± 12	1.4 ± 1.6	3 ± 5	10 ± 11	0.00 ± 0.06	0.12 ± 0.14
Other	2.5 ± 1.5	3.8 ± 2.8	0.48 ± 0.25	2.2 ± 1.6	0.8 ± 2.6	1.1 ± 0.5	2.9 ± 1.5
FCNC (c)Z	3.27 ± 0.29	11.7 ± 0.8	1.13 ± 0.26	1.06 ± 0.12	0.83 ± 0.09	0.24 ± 0.04	0.083 ± 0.012
FCNC t̄ (cZ)	57 ± 5	17.7 ± 1.9	22.3 ± 2.2	4.2 ± 0.6	1.9 ± 0.4	3.7 ± 0.5	0.37 ± 0.07
Total background	430 ± 110	390 ± 80	139 ± 25	280 ± 80	130 ± 32	203 ± 27	164 ± 25
Data	433	443	143	331	169	197	156
Data / Bkg.	1.00 ± 0.25	1.15 ± 0.24	1.03 ± 0.20	1.18 ± 0.35	1.30 ± 0.34	0.97 ± 0.14	0.95 ± 0.16

Table 7.6 – Pre-fit event yields in the S+B tZc fit in SRs+CRs with data. The error includes both statistical and systematic uncertainties.

	SR1	SR2	SR3	Side-band CR1	Side-band CR2	t̄Z CR	t̄ CR
t̄Z +tWZ	164 ± 14	38 ± 7	81 ± 7	90 ± 9	10.2 ± 2.1	155 ± 13	14.9 ± 1.4
t̄W	5.6 ± 0.9	3.6 ± 0.6	2.03 ± 0.32	4.0 ± 0.6	2.7 ± 0.5	2.1 ± 0.4	27 ± 4
t̄H	5.9 ± 0.9	1.01 ± 0.20	2.6 ± 0.4	2.3 ± 0.4	0.42 ± 0.08	5.2 ± 0.8	13.9 ± 2.1
V V + LF	32 ± 18	37 ± 14	3.4 ± 2.2	31 ± 17	21 ± 8	0.21 ± 0.20	0.37 ± 0.17
V V + HF	160 ± 28	191 ± 29	35 ± 6	150 ± 24	85 ± 17	13 ± 5	2.7 ± 0.5
tZq	46 ± 6	119 ± 17	14.2 ± 2.1	20.0 ± 3.4	10.7 ± 1.6	14.0 ± 2.4	0.94 ± 0.12
t̄ +Wt	16.9 ± 3.1	33 ± 7	3.0 ± 0.6	9.9 ± 3.0	9.0 ± 1.7	2.2 ± 0.7	94 ± 13
Other fakes	13 ± 8	15 ± 10	2.0 ± 1.3	4 ± 5	22 ± 16	0.005 ± 0.008	0.16 ± 0.10
Other	1.9 ± 1.0	3.3 ± 2.2	0.44 ± 0.23	1.8 ± 1.3	0.4 ± 1.5	1.0 ± 0.5	2.7 ± 1.4
FCNC (c)Z	0.3 ± 0.6	1.2 ± 2.2	0.11 ± 0.21	0.09 ± 0.18	0.08 ± 0.16	0.02 ± 0.04	0.008 ± 0.015
FCNC t̄ (cZ)	5 ± 10	2 ± 4	2 ± 4	0.4 ± 0.8	0.2 ± 0.4	0.3 ± 0.6	0.03 ± 0.07
Total background	446 ± 18	441 ± 20	143 ± 7	313 ± 16	162 ± 13	193 ± 12	156 ± 12
Data	433	443	143	331	169	197	156
Data / Bkg.	0.97 ± 0.04	1.00 ± 0.05	1.00 ± 0.05	1.06 ± 0.05	1.04 ± 0.08	1.02 ± 0.06	1.00 ± 0.08

Table 7.7 – Post-fit event yields in the S+BtZc fit in SRs+CRs with data. The error includes both statistical and systematic uncertainties.

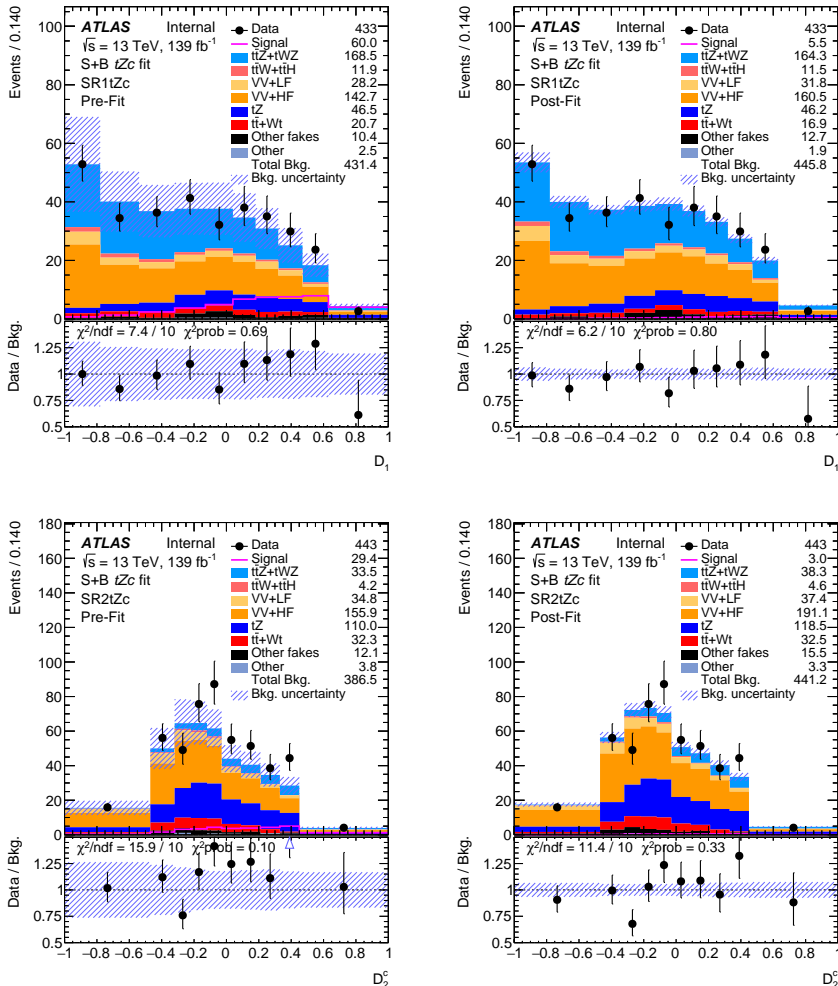


Figure 7.18 – Pre-fit (left) and post-fit (right) BDTG output distributions in SR1 and SR2 for the S+B $t\bar{Z}c$ fit in SRs+CRs with data. The uncertainty band includes both statistical and systematic uncertainties.

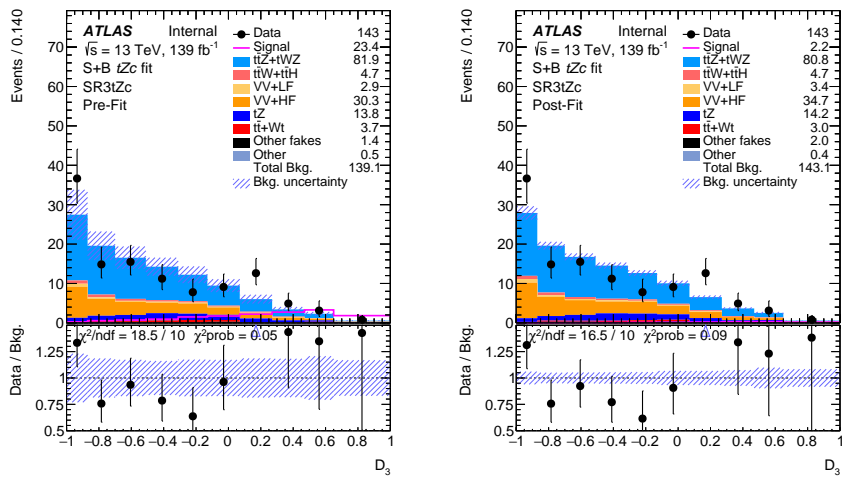


Figure 7.19 – Pre-fit (left) and post-fit (right) leading lepton p_T distributions in SR3 for the S+B tZc fit in SRs+CRs with data. The uncertainty band includes both statistical and systematic uncertainties.

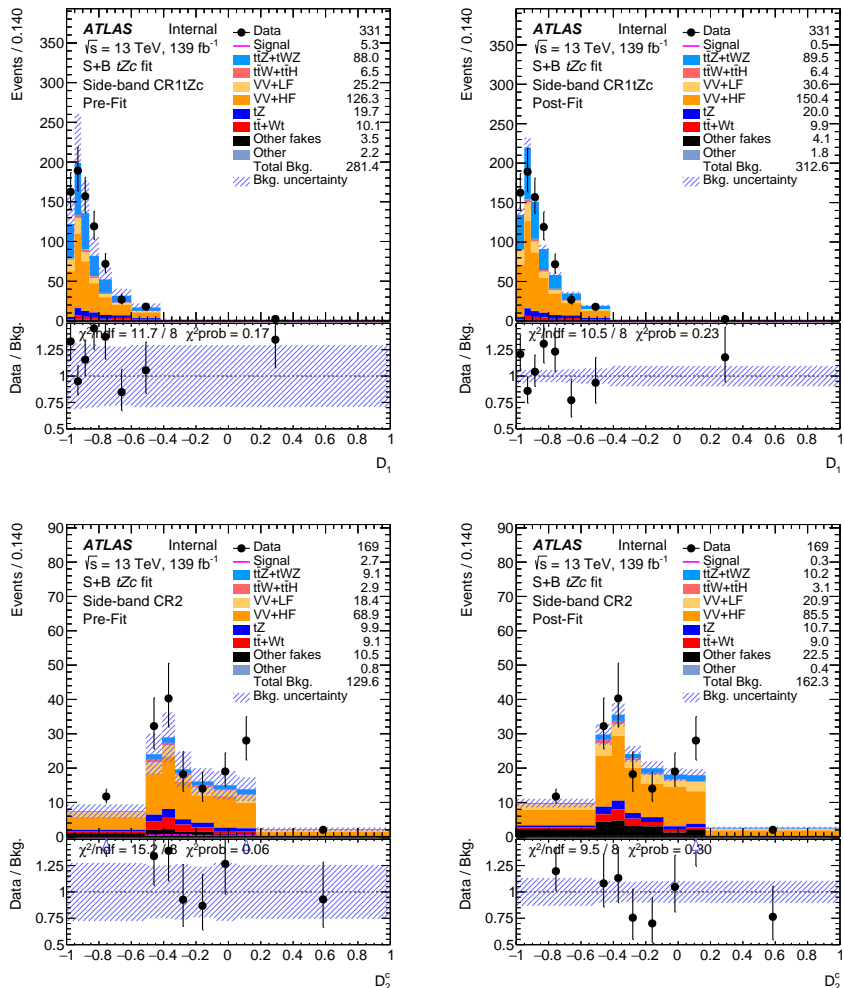


Figure 7.20 – Pre-fit (left) and post-fit (right) BDTG output distributions in the side-band CRs for the S+B tZc fit in SRs+CRs with data. The uncertainty band includes both statistical and systematic uncertainties.

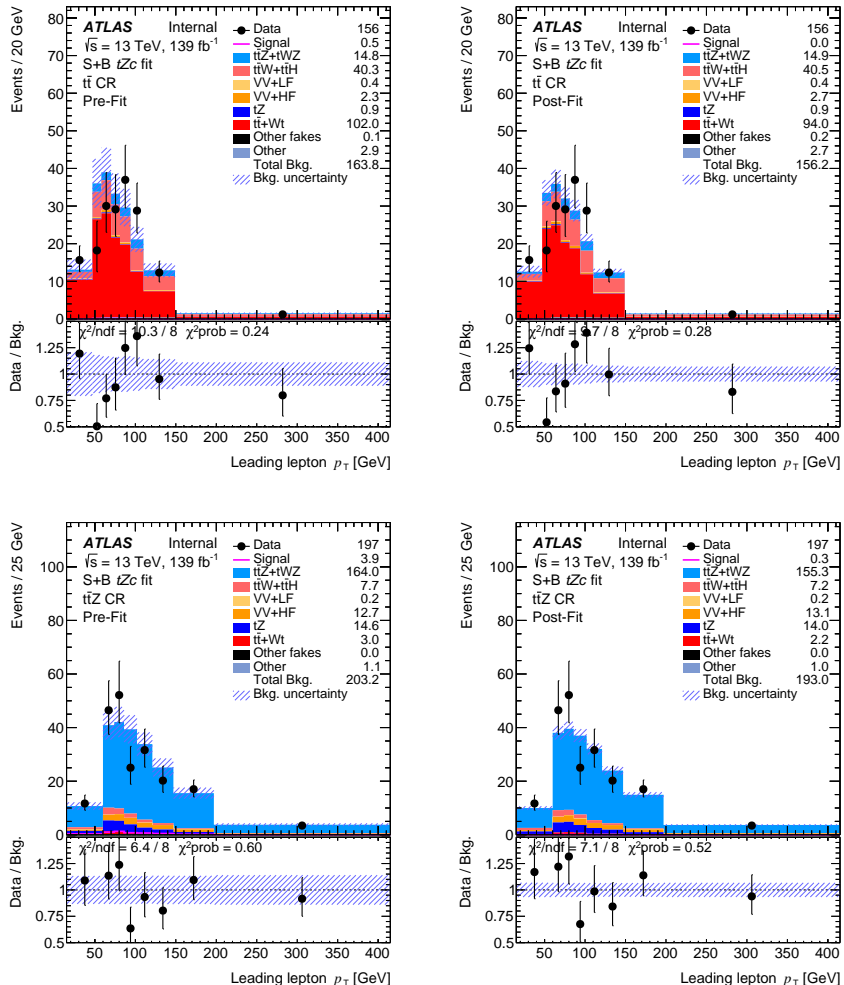


Figure 7.21 – Pre-fit (left) and post-fit (right) leading lepton p_T distributions in the $t\bar{t}$ and $t\bar{t}Z$ CRs for the S+B $t\bar{t}Z$ fit in SRs+CRs with data. The uncertainty band includes both statistical and systematic uncertainties.

7.6 Results

Blinded data From the likelihood fit described in this chapter, namely the signal+background fit in SRs+CRs with the realistic Asimov datasets in Section 7.4, expected upper limits can be computed with the CL_s method [160, 161] with the expected 95% confidence level (CL) limit on the branching ratio $BR(t \rightarrow Zc)$.

Table 7.8 shows the expected limits on $BR(t \rightarrow Zc)$ extracted for various selections:

- without the use of any c-tagger ('Baseline'),
- using SMT, presented in Chapter H,
- using $DL1r_c$.

The improvement over baseline obtained using SMT is around 3%, while using $DL1r_c$ is around 10%.

Expected limits on $BR(t \rightarrow Zc) [\times 10^{-5}]$		
Baseline	Using SMT	Using $DL1r_c$
10.7	10.4	9.6

Table 7.8 – Expected limits on the branching ratios of $t \rightarrow Zc$. Results using $DL1r_c$, SMT and none of them are reported to estimate the impact of these techniques on the analysis.

The expected limits, using $DL1r_c$, together with statistical only limits and the expected limits from the previous ATLAS analysis [28], are reported in Table I.3.

The overall impact of systematics on the expected limit is 22%.

The expected upper limit from the previous analysis is improved by a factor of 3.3 for the tZc coupling.

Limits	$-1\sigma [\times 10^{-5}]$	Expected $[\times 10^{-5}]$	$+1\sigma [\times 10^{-5}]$
$BR(t \rightarrow Zc)$ [28]	22	32	46
$BR(t \rightarrow Zc)$ (stat. only)	5.3	7.4	10.5
$BR(t \rightarrow Zc)$	6.9	9.6	13.8

Table 7.9 – Expected upper limits on the branching ratios of $t \rightarrow Zc$. Expected upper limit from [28] is also included for reference.

Unblinded data From the likelihood fit described in Section 7.5 under the Signal+Background hypothesis, no evidence for the FCNC $t \rightarrow Zc$ signal is found but a good agreement between data and Standard Model is observed. The results obtained under the Background-only hypothesis shows similar results (see Appendix I). In the absence of signal, the 95% CL upper limit is set on $BR(t \rightarrow Zc)$. Figure 7.22 shows the observed and expected CL_s as a function of $BR(t \rightarrow Zc)$. The observed limit is $BR(t \rightarrow Zc) < 11.8 \times 10^{-5}$, inside the $\pm 1\sigma$ band of the expected limit: $BR(t \rightarrow Zc) < 9.5 \times 10^{-5}$. The observed upper limit is improved by a factor of 2, while the expected upper limit is improved by a factor of 3.4 compared to the previous analysis.

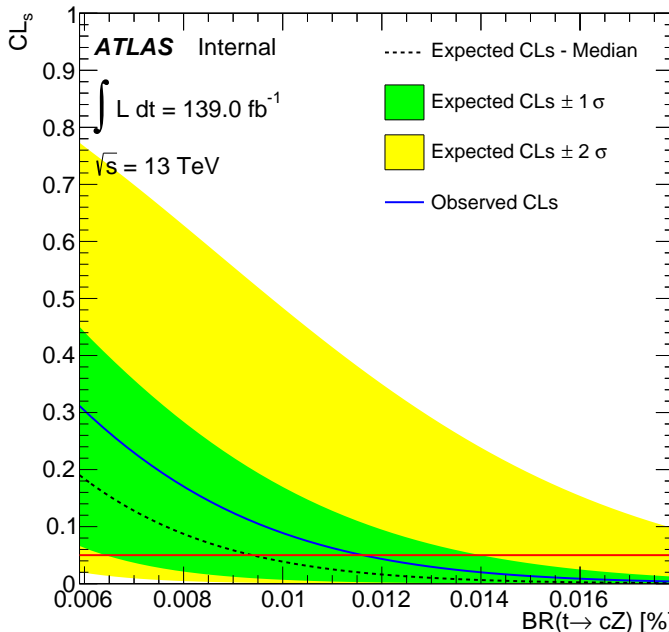


Figure 7.22 – CL_s vs $\text{BR}(t \rightarrow Zc)$ plot. The median expected CL_s under the Signal+Background hypothesis (black dashed line) is displayed along with the ± 1 and ± 2 standard deviations bands (green and yellow, respectively). The solid red line at $\text{CL}_s = 0.05$ denotes the threshold below which the hypothesis is excluded at 95% CL.

$\text{BR}(t \rightarrow Zc) [\times 10^{-5}]$	
Observed [28]	24
Observed	11.8
Expected -1σ	6.9
Expected	9.5
Expected $+1\sigma$	13.8

Table 7.10 – Observed and expected 95% CL upper limits on the FCNC $t \rightarrow Zc$ branching ratio. The expected central value is shown together with the $\pm 1\sigma$ bands. Observed upper limit from [28] is also included for reference.

Conclusions

In this thesis, the search for flavour-changing neutral-current process $t \rightarrow Zc$ using pp collision data recorded by the ATLAS detector at the LHC has been presented. The data were recorded at a center-of-mass energy of 13 TeV and correspond to the full Run-2 dataset with an integrated luminosity of 139 fb^{-1} .

The analysis searches for $t\bar{t}$ events where one top quark decays through the $t \rightarrow Zc$ channel and the other through the dominant Standard Model mode $t \rightarrow Wb$ with fully leptonic final state, where the Z boson decays into charged leptons and leptonic W boson decays are considered as signal. The FCNC process of production of a single top-quark in association with a Z boson is also considered.

Two different techniques to identify the c -jet have been tested to improve the final expected upper limits and to provide explicit charm identification in case of positive signal.

The first technique is the Soft Muon Tagging technique, for the tagging of heavy-flavour jets. It exploits the $b \rightarrow \mu + X$, $b \rightarrow c \rightarrow \mu + X$ and $c \rightarrow \mu + X$ decay chains (with a total $\text{BR} \approx 20\%$), by identifying muons reconstructed inside jets.

The second technique is the DL1r_c discriminant that is used for charm-tagging. It is based on a deep feed-forward neural network (NN) and recently developed by the ATLAS collaboration.

In order to extract the limit on tZc couplings, a multivariate analysis has been used and a binned maximum likelihood fit is performed on the Boosted Decision Tree (BDT) output, using the Monte Carlo templates for both signal and background predictions.

There is good agreement between the data and the Monte Carlo expectations, and the overall impact of systematics on the expected limit is 22%.

The estimated improvement using SMT is around 2%, while the improvement using DL1r_c is around 10% compared with a scenario where none of the two techniques has been used.

When data are unblinded also in the Signal Regions, a good agreement between data and Standard Model predictions is observed, and no evidence of a signal is found. The 95% CL observed (expected) upper limit on the $t \rightarrow Zc$ branching ratio is:

$$\text{BR}(t \rightarrow Zc) = 11.8 \times 10^{-5} (9.5 \times 10^{-5}),$$

improving the previous ATLAS results by a factor of 2 (3.4).

APPENDIX A

Monte Carlo samples

This appendix summarises the MC datasets used in this analysis.

Table A.1 shows the nominal signal samples produced in fast simulation, for mc16a, mc16d and mc16e.

Table A.2 shows the nominal background samples produced in full simulation, for mc16a, mc16d and mc16e.

Table A.3 shows the samples used for systematic uncertainty evaluation, which are produced in fast simulation, for mc16a, mc16d and mc16e.

MC samples are normalised using the cross-sections and k-factors from the XSection-MC16-13TeV.data¹ file taken from the TopDataPreparation² on 22.06.2020.

In this file, the tZq SM cross-section is increased by 15% according to the theoretical calculations update [162].

Signal samples

mc16_13TeV.412143.aMcAtNloPythia8EvtGen_TopFCNC_ctZLH_tt_3l.deriv.DAOD_TOPQ1.e7718_a875_r9364/r10201/r10724_p3956
mc16_13TeV.412141.aMcAtNloPythia8EvtGen_TopFCNC_ctZLH_tZ_3l.deriv.DAOD_TOPQ1.e7718_a875_r9364/r10201/r10724_p3956
mc16_13TeV.412146.aMcAtNloPythia8EvtGen_TopFCNC_ctZLH_tt_3l_SMTFilter.deriv.DAOD_TOPQ1.e7718_a875_r9364/r10201/r10724_p3956

Table A.1 – Overview of the signal simulated samples (Fast Simulation).

¹<https://gitlab.cern.ch/adurglis/tqZAnalysis/-/blob/master/share/XSection-MC16-13TeV.data>

²[/cvmfs/atlas.cern.ch/repo/sw/database/GroupData/dev/AnalysisTop/TopDataPreparation/](https://cvmfs.atlas.cern.ch/repo/sw/database/GroupData/dev/AnalysisTop/TopDataPreparation/)

A. MONTE CARLO SAMPLES

t̄tV

mc16_13TeV.410155.aMcAtNloPythia8EvtGen_MEN30NNLO_A14N23LO_ttW.deriv.DAOD_TOPQ1.e5070_s3126_r9364/r10201/r10724_p4166
 mc16_13TeV.410218.aMcAtNloPythia8EvtGen_MEN30NNLO_A14N23LO_ttee.deriv.DAOD_TOPQ1.e5070_s3126_r9364/r10201/r10724_p4166
 mc16_13TeV.410219.aMcAtNloPythia8EvtGen_MEN30NNLO_A14N23LO_ttumu.muriv.DAOD_TOPQ1.e5070_s3126_r9364/r10201/r10724_p4166
 mc16_13TeV.410220.aMcAtNloPythia8EvtGen_MEN30NNLO_A14N23LO_tttautau.deriv.DAOD_TOPQ1.e5070_s3126_r9364/r10201/r10724_p4166
 mc16_13TeV.410156.aMcAtNloPythia8EvtGen_MEN30NNLO_A14N23LO_ttZnumu.deriv.DAOD_TOPQ1.e5070_s3126_r9364/r10201/r10724_p4166
 mc16_13TeV.410157.aMcAtNloPythia8EvtGen_MEN30NNLO_A14N23LO_ttZqq.deriv.DAOD_TOPQ1.e5070_s3126_r9364/r10201/r10724_p4166

Diboson

mc16_13TeV.345705.Sherpa_222_NNPDF30NNLO_gglIII_0M4I130.deriv.DAOD_TOPQ1.e6213_s3126_r9364/r10201/r10724_p4164
 mc16_13TeV.345706.Sherpa_222_NNPDF30NNLO_gglIII_130M4I1.deriv.DAOD_TOPQ1.e6213_s3126_r9364/r10201/r10724_p4164
 mc16_13TeV.364283.Sherpa_222_NNPDF30NNLO_IIIll_6W6W.deriv.DAOD_TOPQ1.e6055_s3126_r9364/r10201/r10724_p4029
 mc16_13TeV.364284.Sherpa_222_NNPDF30NNLO_IIIll_llvjj_EW6W.deriv.DAOD_TOPQ1.e6055_s3126_r9364/r10201/r10724_p4164
 mc16_13TeV.364250.Sherpa_222_NNPDF30NNLO_III_lll.deriv.DAOD_TOPQ1.e5894_s3126_r9364/r10201/r10724_p4164
 mc16_13TeV.364253.Sherpa_222_NNPDF30NNLO_III_llv.deriv.DAOD_TOPQ1.e5916_s3126_r9364/r10201/r10724_p4164
 mc16_13TeV.364254.Sherpa_222_NNPDF30NNLO_III_llvv.deriv.DAOD_TOPQ1.e5916_s3126_r9364/r10201/r10724_p4029
 mc16_13TeV.345723.Sherpa_222_NNPDF30NNLO_gglvvZZ.deriv.DAOD_TOPQ1.e6213_s3126_r9364/r10201/r10724_p4029
 mc16_13TeV.363356.Sherpa_221_NNPDF30NNLO_ZqqZll.deriv.DAOD_TOPQ1.e5525_s3126_r9364/r10201/r10724_p4029
 mc16_13TeV.363358.Sherpa_221_NNPDF30NNLO_WqqZll.deriv.DAOD_TOPQ1.e5525_s3126_r9364/r10201/r10724_p4164

tqZ SM

mc16_13TeV.412063.aMcAtNloPythia8EvtGen_tlq_NNPDF30_nf4_A14.deriv.DAOD_TOPQ1.e7054_s3126_r9364/r10201/r10724_p4062

tWZ

mc16_13TeV.410408.aMcAtNloPythia8EvtGen_tWZ_Ztoll_minDR1.deriv.DAOD_TOPQ1.e6423_s3126_r9364/r10201/r10724_p4174

tH

mc16_13TeV.346345.PhPy8EG_A14NNPDF23_NNPDF30ME_ttH125_dilep.deriv.DAOD_TOPQ1.e7148_s3126_r9364/r10201/r10724_p4031
 mc16_13TeV.346344.PhPy8EG_A14NNPDF23_NNPDF30ME_ttH125_semilep.deriv.DAOD_TOPQ1.e7148_s3126_r9364/r10201/r10724_p4031
 mc16_13TeV.346343.PhPy8EG_A14NNPDF23_NNPDF30ME_ttH125_allhad.deriv.DAOD_TOPQ1.e7148_s3126_r9364/r10201/r10724_p4031

tt

mc16_13TeV.410472.PhPy8EG_A14_ttbar_hdamp258p75_dil.deriv.DAOD_TOPQ1.e6348_s3126_r9364/r10201/r10724_p4166

tW

mc16_13TeV.410648.PowhegPythia8EvtGen_A14_Wt_DR_dilepton_top.deriv.DAOD_TOPQ1.e6615_s3126_r9364/r10201/r10724_p4031
 mc16_13TeV.410649.PowhegPythia8EvtGen_A14_Wt_DR_dilepton_antitop.deriv.DAOD_TOPQ1.e6615_s3126_r9364/r10201/r10724_p4031

Z+jets

mc16_13TeV.361106.PowhegPythia8EvtGen_AZNLOCTEQ6L1_Zee.deriv.DAOD_TOPQ1.e3601_s3126_r9364/r10201/r10724_p4029
 mc16_13TeV.361107.PowhegPythia8EvtGen_AZNLOCTEQ6L1_Zmmumu.deriv.DAOD_TOPQ1.e3601_s3126_r9364/r10201/r10724_p4029
 mc16_13TeV.361108.PowhegPythia8EvtGen_AZNLOCTEQ6L1_Ztautau.deriv.DAOD_TOPQ1.e3601_s3126_r9364/r10201/r10724_p4029

Four tops

mc16_13TeV.412043.aMcAtNloPythia8EvtGen_A14NNPDF31_SM4topsNLO.deriv.DAOD_TOPQ1.e7101_a875_r9364/r10201/r10724_p4031

Three tops

mc16_13TeV.304014.MadGraphPythia8EvtGen_A14NNPDF23_3top_SM.deriv.DAOD_TOPQ1.e4324_s3126_r9364/r10201/r10724_p4166

VH

mc16_13TeV.342284.Pythia8EvtGen_A14NNPDF23LO_WH125_inc.deriv.DAOD_TOPQ1.e4246_s3126_r9364/r10201/r10724_p4164

mc16_13TeV.342285.Pythia8EvtGen_A14NNPDF23LO_ZH125_inc.deriv.DAOD_TOPQ1.e4246_s3126_r9364/r10201/r10724_p4172

ttWW

mc16_13TeV.410081.MadGraphPythia8EvtGen_A14NNPDF23_ttbarWW.deriv.DAOD_TOPQ1.e4111_s3126_r9364/r10201/r10724_p4166

Triboson

mc16_13TeV.364242.Sherpa_222_NNPDF30NNLO_WWW_3l3v_EW6.deriv.DAOD_TOPQ1.e5887_s3126_r9364/r10201/r10724_p4164
 mc16_13TeV.364243.Sherpa_222_NNPDF30NNLO_WWZ_4l2v_EW6.deriv.DAOD_TOPQ1.e5887_s3126_r9364/r10201/r10724_p4164
 mc16_13TeV.364245.Sherpa_222_NNPDF30NNLO_WZZ_5l1v_EW6.deriv.DAOD_TOPQ1.e5887_s3126_r9364/r10201/r10724_p4164
 mc16_13TeV.364246.Sherpa_222_NNPDF30NNLO_WZZ_3l3v_EW6.deriv.DAOD_TOPQ1.e5887_s3126_r9364/r10201/r10724_p4164
 mc16_13TeV.364247.Sherpa_222_NNPDF30NNLO_WZZ_6l0v_EW6.deriv.DAOD_TOPQ1.e5887_s3126_r9364/r10201/r10724_p4164
 mc16_13TeV.364248.Sherpa_222_NNPDF30NNLO_WZZ_4l2v_EW6.deriv.DAOD_TOPQ1.e5887_s3126_r9364/r10201/r10724_p4164

Table A.2 – Overview of the background simulated samples.

t̄tZ Generator systematicsmc16_13TeV.410142.Sherpa_NNPDF30NNLO_ttll_mll5.deriv.DAOD_TOPQ1.e4686_s3126_r9364/r10201/r10724_p4031

t̄tZ A14 variation

mc16_13TeV.410370.aMcAtNloPythia8EvtGen_MEN30NLO_A14Var3UpN23LO_ttee.deriv.DAOD_TOPQ1.e6113_s3126_r9364/r10201/r10724_p4062
mc16_13TeV.410371.aMcAtNloPythia8EvtGen_MEN30NLO_A14Var3DownN23LO_ttee.deriv.DAOD_TOPQ1.e6113_s3126_r9364/r10201/r10724_p4062
mc16_13TeV.410372.aMcAtNloPythia8EvtGen_MEN30NLO_A14Var3UpN23LO_ttmumu.deriv.DAOD_TOPQ1.e6125_s3126_r9364/r10201/r10724_p4062
mc16_13TeV.410373.aMcAtNloPythia8EvtGen_MEN30NLO_A14Var3DownN23LO_ttmumu.deriv.DAOD_TOPQ1.e6113_s3126_r9364/r10201/r10724_p4062
mc16_13TeV.410374.aMcAtNloPythia8EvtGen_MEN30NLO_A14Var3UpN23LO_tttautau.deriv.DAOD_TOPQ1.e6113_s3126_r9364/r10201/r10724_p4062
mc16_13TeV.410375.aMcAtNloPythia8EvtGen_MEN30NLO_A14Var3DownN23LO_tttautau.deriv.DAOD_TOPQ1.e6113_s3126_r9364/r10201/r10724_p4062

Diboson Generator systematicsmc16_13TeV.361601.PowhegPy8EG_CT10nloME_AZNLOCTEQ6L1_WZl1ll_mll4.deriv.DAOD_TOPQ1.e4475_s3126_r9364/r10201/r10724_p4060

mc16_13TeV.361603.PowhegPy8EG_CT10nloME_AZNLOCTEQ6L1_ZZl1ll_mll4.deriv.DAOD_TOPQ1.e4475_s3126_r9364/r10201/r10724_p4060

t̄Z SM A14 variationmc16_13TeV.412064.aMcAtNloPythia8EvtGen_llq_NNPDF30_nf4_A14.deriv.DAOD_TOPQ1.e7054_a875_r9364/r10201/r10724_p4062

mc16_13TeV.412065.aMcAtNloPythia8EvtGen_llq_NNPDF30_nf4_A14.deriv.DAOD_TOPQ1.e7054_a875_r9364/r10201/r10724_p4062

tWZ Diagram Removal systematicsmc16_13TeV.412119.aMcAtNloPythia8EvtGen_tWZ_Ztoll_DR2.deriv.DAOD_TOPQ1.e7518_s3126_r9364/r10201/r10724_p4166

t̄t Parton Shower systematicsmc16_13TeV.411234.PowhegHerwig7EvtGen_tt_hdamp258p75_713_dil.deriv.DAOD_TOPQ1.e7580_a875_r9364/r10201/r10724_p4031

t̄t hdamp variationmc16_13TeV.410482.PhPy8EG_A14_ttbar_hdamp517p5_dil.deriv.DAOD_TOPQ1.e6454_a875_r9364/r10201/r10724_p4031

Table A.3 – List of systematics MC samples.

APPENDIX B

Mass Resolution

The signal events are reconstructed using a χ^2 minimisation as it is described in Section 6.1. The central value for the masses and the widths in eq. (6.1) are taken from the simulated FCNC $t\bar{t}$ decay signal samples. The values are extracted from the Bukin fits [144] to the masses of the top quarks and W boson reconstructed by matching the true generated q - and b -quarks to the reconstructed jets within the $\Delta R < 0.4$, assuming the missing transverse momentum to be the neutrino transverse momentum, and setting the longitudinal momentum of the neutrino to the p_z of the true generated particle. These represent the optimal resolution of the reconstructed t-quarks and W boson masses in the FCNC $t\bar{t}$ decay signal events. These fits are shown in fig. B.1 along with the mean values and standard deviations.

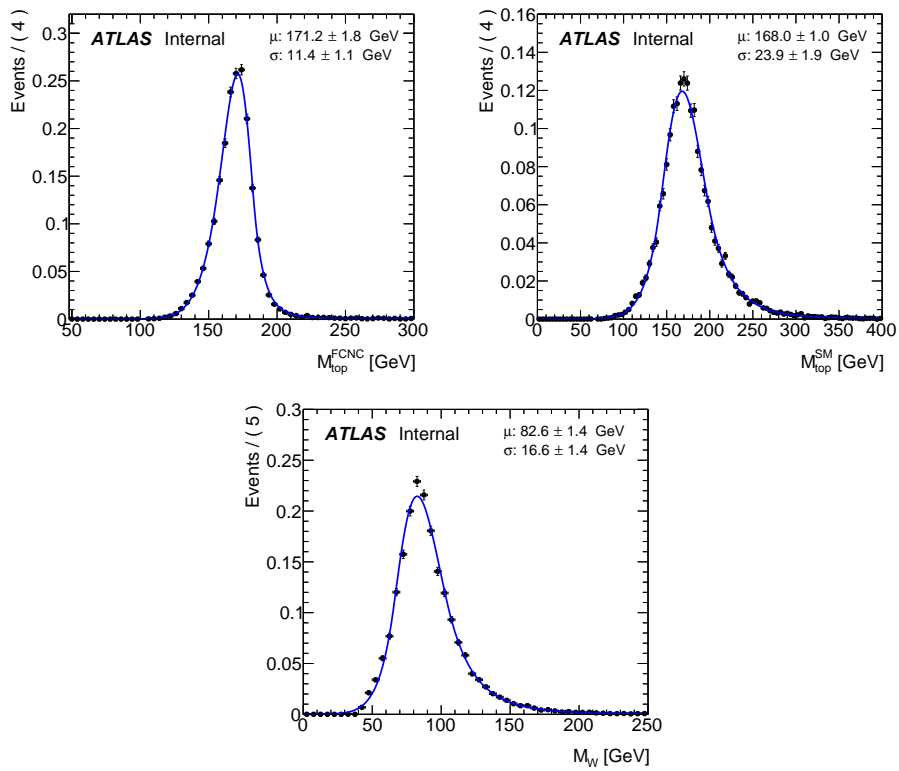


Figure B.1

APPENDIX C

Charm tagging using DL1r

The DL1r tagger gives the probability a jet is a b -jet, p_b , c -jet, p_c , or light jet, p_{light} . Using these probabilities the discriminant variable can be constructed to discriminate a jet of type i from jets of types j and k :

$$\text{DL1r}_i = \ln \frac{p_i}{f_j \cdot p_j + (1 - f_j) \cdot p_k}, \quad (\text{C.1})$$

where the f_j parameter controls whether jets of type i are to be primarily discriminated from jets of type j or type k . In the specific case of c -tagging the discriminant becomes:

$$\text{DL1r}_c = \ln \frac{p_c}{f_b \cdot p_b + (1 - f_b) \cdot p_{light}}. \quad (\text{C.2})$$

A value of DL1r_c must be chosen to cut on to decide whether a jet is a tagged as a c -jet or not. Therefore, there are two parameters which must be chosen, the value of f_b and the cut value, to have an optimal performance.

In order to determine the best values for f_b and DL1r_c cut, events are selected using the SR1 selection described in Section 6.5, excluding the FCNC top mass requirement. So, the selection is: 3 leptons, Z boson mass window, at least 2 jets with exactly one being b -tagged. Then, several values for f_b and DL1r_c cut were considered and for each of them events are split into two categories, c -tagged events ($=1$ c -tag) and c -tag veto events. The c -tagging is applied on jets that fail the b -tagging requirement. For each combination of f_b and DL1r_c cut values, the S/\sqrt{B} values were calculated in both c -tagged and c -tag veto events. The optimal values for f_b and DL1r_c cut would be the ones that give highest value of S/\sqrt{B} combined in quadrature from c -tagged and c -tag veto events. Figure C.1 presents the S/\sqrt{B} values for different f_b and DL1r_c cut values in c -tagged and c -tag veto events, while combined S/\sqrt{B} values are presented in fig. C.2. As the fig. C.2 suggests, the optimal c -tagging working point (WP) would be at 0.6 for f_b and 1.84 for DL1r_c cut, which gives highest value of 3.42 for combined S/\sqrt{B} . However, the optimal c -tagging working point must be calibrated, which is not trivial. Alternatively, the c -tagging working point ($f_b = 0.28$, DL1r_c cut= 1.32) being calibrated in the $t\bar{c}$ +MET SUSY analysis [79]

is used in this analysis.

Chapter C summarises the performance of the considered c -tagging working points.

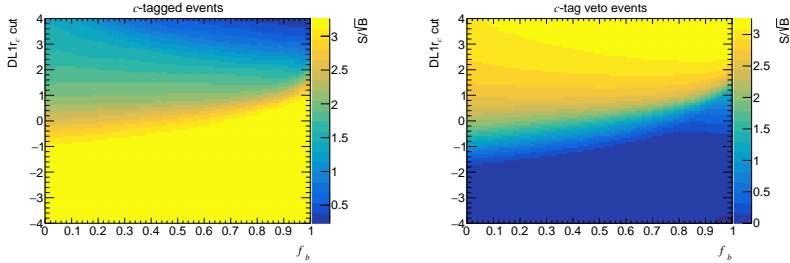


Figure C.1 – The S/\sqrt{B} values for different f_b and $\text{DL1}r_c$ cut values in c -tagged (left) and c -tag veto (right) events.

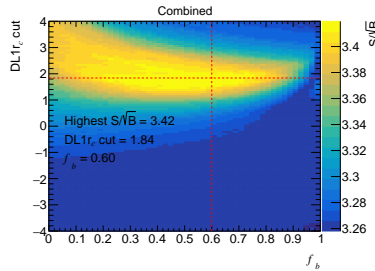


Figure C.2 – The S/\sqrt{B} values combined in quadrature from c -tagged and c -tag veto events for different f_b and $\text{DL1}r_c$ cut values. The vertical and horizontal dashed lines indicate the f_b and $\text{DL1}r_c$ cut values which give highest S/\sqrt{B} value.

	$f_b = 0.28$	$\text{DL1}r_c$ cut	S/\sqrt{B}	$\text{BR}(t \rightarrow Zc)$ limit
Optimal WP	0.6	1.84	3.42	9.5×10^{-5}
$tc+MET$ SUSY WP	0.28	1.32	3.39	9.7×10^{-5}

Table C.1 – Combined S/\sqrt{B} values from c -tagged and c -tag veto events, with optimal c -tagging working point and with the one used in $tc+MET$ analysis [79]. Extracted expected $\text{BR}(t \rightarrow Zc)$ limits are also shown.

APPENDIX D

BDT optimization

This section describes the study of input variables and hyper-parameters optimisation for the BDT discriminants presented in Section 6.3.

The k -fold cross-validation method with $k = 5$ is used to define the final set of input variables and determine the optimal values for BDT hyper-parameters. The total set of MC events is split into 5 folds with approximately equal sizes, using the pseudo-random numbers. Four of folds are used as a training set, and the remaining one as a validation set. Separate BDT is trained and evaluated for each fold considered as the validation fold. The performance across the validation folds is averaged to estimate the expected performance of the BDT with the considered input variables and hyper-parameters.

Many input variables are considered to train the BDT, then the ones that do not have significant impact on the BDT performance are removed since they could introduce instability in the BDT output when considering systematic uncertainties. The strategy is to remove variables that have relatively low values of separation and strong correlations with other variables, without significant loss of the BDT performance. Table D.1 shows the values for configuration options of the BDT method used for this study. They are chosen to counteract overtraining.

Option	Value for D_3
NTrees	800
MinNodeSize	2%
BoostType	Grad
Shrinkage	0.05
UseBaggedBoost	True
BaggedSampleFraction	0.6
nCuts	200
MaxDepth	2
NegWeightTreatment	IgnoreNegWeightsInTraining

Table D.1 – Used values for configuration options of the TMVA method Boosted Decision Trees [146].

D.1 Input variables

The initial (full) set of input variables considered for the D_3 discriminant in SR3 are presented in Table D.2. It includes invariant mass of the reconstructed objects as well as transverse momentum, pseudorapidity, ΔR between them in (η, ϕ) plane and other variables related to soft muons. Separation values are presented in the same table. Input variables that have separation value below 0.02 are removed and correlations among the remaining variables can be seen in Figure D.1. The χ^2_{tt} and $m_{\ell\nu}$ variables have high correlation with $m_{q\ell\ell}$ and $m_{b\ell\nu}$, respectively, and lower separation value, so that they are removed as well as $\frac{\mu^{soft} topoetcone40}{\mu^{soft} ID p_T}$ which is highly correlated

with $\frac{\mu^{soft} ID p_T}{SMT jet Sum p_T Trk}$ and having lower separation value. Also $\Delta R(q, Z)$ and p_T^b are removed since it is highly correlated with $m_{q\ell\ell}$ and lower separation value.

The final set of input variables are presented in Table D.3.

With the full set of input variables, the BDT output score distributions in each fold for the signal and background samples are presented in Figure D.2 and Figure D.3, respectively, while for the final (reduced) set of input variables – in Figure D.4 and Figure D.5.

The ROC integral, averaged over the validation folds, for the BDT trained with the full set of input variables is 0.8595 with RMS of 0.0030, while for the BDT with final set of input variables: 0.8207 with RMS of 0.0037. Figure D.6 shows the $S_{\text{eff}}/\sqrt{B_{\text{eff}}}$ value averaged over the validation folds as a function of the cut on the BDT output score, with full set and final set of input variables. The maximum value of $S_{\text{eff}}/\sqrt{B_{\text{eff}}}$ is 2.263 with RMS of 3.881 for the full set of input variables, while 1.539 with RMS of 0.037 for the final set of input variables.

Results show that after the selection of some variables, the BDT performance is more stable, at the price of loosing $\sim 5\%$ of separation power as can be seen comparing the ROC integrals.

Variable	$\langle s^2 \rangle$	Definition
$m_{b\ell\nu}$	0.1717	SM top-quark candidate mass
$N b\, jets$	0.08218	Number of b-jets tagged with DL1r
$m_{q\ell\ell}$	0.07019	FCNC top-quark candidate mass
$m_{\ell\nu}$	0.05106	W boson candidate mass
$\frac{\mu^{soft} ID p_T}{SMT\,jet\,Sum p_T\,Trk}$	0.03357	Ratio between the soft muon ID pT and pT sum of tracks
$\Delta R(\ell, Z)$	0.03141	ΔR between W boson lepton and Z boson candidates
$\chi^2_{t\bar{t}}$	0.02737	χ^2 from the kinematic fit under the $t\bar{t}$ decay signal hypothesis
$\Delta R(q, Z)$	0.0262	ΔR between c -quark and Z boson candidates
$\frac{\mu^{soft}\, topoetcone40}{\mu^{soft}\, ID\, p_T}$	0.02614	Ratio between the soft muon topoetcone40 and soft muon pT
p_T^b	0.02566	b -quark candidate transverse momentum
$\Delta R(t_{SM}, t_{FCNC})$	0.02508	ΔR between SM and FCNC top-quark candidates
$\Delta R(SMT, nearestJet)$	0.02286	ΔR between SMT-jet and its nearest jet
$N\, jets$	0.01499	Number of jets
$SMT\,jet\,Num\,Trk$	0.01495	SMT-jet Number of tracks
$p_T^{\ell 1}$	0.01319	Leading lepton p_T
$\frac{\mu^{soft}\, EnergyLoss}{\mu^{soft}\, p_T}$	0.01308	Ratio between the soft muon energy loss and soft muon pT
p_T^q	0.01258	c -quark candidate transverse momentum
$SMT\,jet\,Trk\,Width$	0.01165	SMT-jet track width
$\Delta R(b, Z)$	0.01037	ΔR between b -quark and Z boson candidates
p_T^Z	0.00812	Z boson candidate transverse momentum
$\frac{\mu^{soft}\, topoetcone40}{SMT\,jet\,p_T}$	0.0075	Ratio between the soft muon topoetcone40 and SMT-jet pT
$SMT\,jet\,EMF$	0.006978	SMT-jet Electromagnetic Fraction
$\Delta R(\mu^{soft}, Z)$	0.006596	ΔR between soft muon and Z boson candidates
$p_T^{\ell 2}$	0.006018	Sub-leading lepton p_T
$SMT\,jet\,Width$	0.005493	SMT-jet width
η^b	0.004975	b -quark candidate pseudorapidity
η^q	0.004738	c -quark candidate pseudorapidity
p_T^W	0.003908	W boson candidate transverse momentum
$p_T^{\ell 3}$	0.00314	Third lepton p_T
$\eta^{\ell 1}$	0.002857	Leading lepton η
$\eta^{\ell 2}$	0.001557	Sub-leading lepton η
$\eta^{\ell 3}$	0.001484	Third lepton η
$SMT\,jet\,Charge$	0.0004037	SMT-jet charge

Table D.2 – Initial (full) set of input variables considered in the training of the GBDT in SR3 to built the D_3 discriminant for tZc couplings search. Variables are ordered by the separation $\langle s^2 \rangle$ value.

Variable	$\langle s^2 \rangle$	Definition
$m_{b\ell\nu}$	0.1717	SM top-quark candidate mass
$N b\, jets$	0.08218	Number of b-jets tagged with DL1r
$m_{q\ell\ell}$	0.07019	FCNC top-quark candidate mass
$\frac{\mu^{soft}\, ID p_T}{SMT\,jet\,Sum p_T\,Trk}$	0.03357	Ratio between the soft muon ID pT and pT sum of tracks
$\Delta R(\ell, Z)$	0.03141	ΔR between W boson lepton and Z boson candidates
$\Delta R(t_{SM}, t_{FCNC})$	0.02508	ΔR between SM and FCNC top-quark candidates
$\Delta R(\mu^{soft}, Z)$	0.006596	ΔR between soft muon and Z boson candidates

Table D.3 – Final set of input variables considered in the training of the GBDT in SR3 to built the D_3 discriminant. Variables are ordered by the separation $\langle s^2 \rangle$ value.

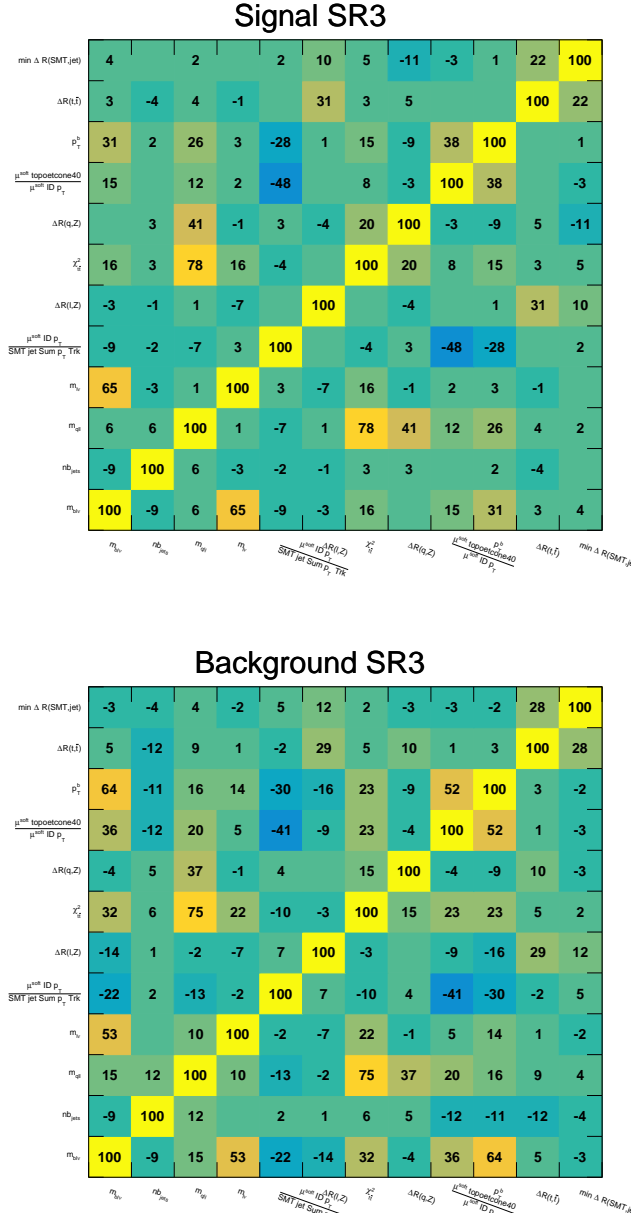


Figure D.1 – Correlation matrix of the input variables from signal (top) and background (bottom) samples considered in the training of the GBDT in SR3 to built the D_3 discriminant for tZc coupling search.

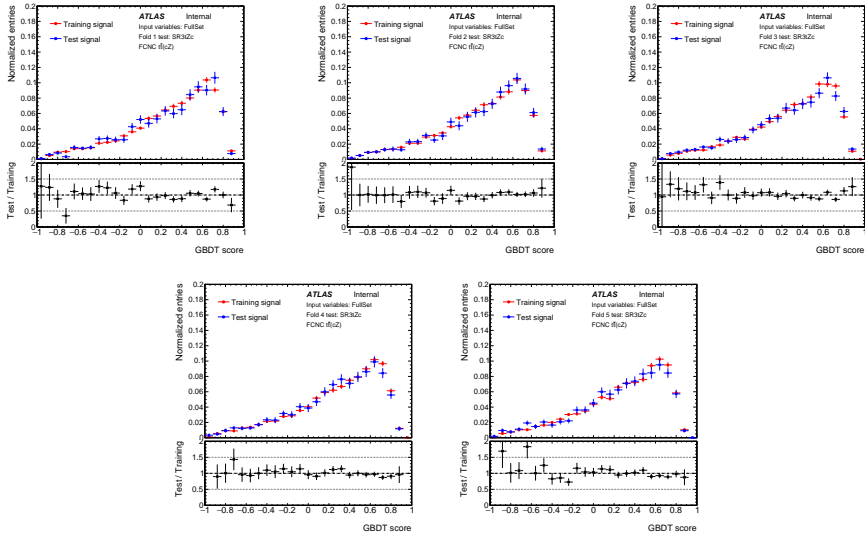


Figure D.2 – The FCNC $t\bar{t}$ decay signal GBDT output score distribution for each of five GBDTs trained in SR3 for the D_3 discriminant. Initial (full) set of input variables is used in the training. Comparing results between training and test samples.

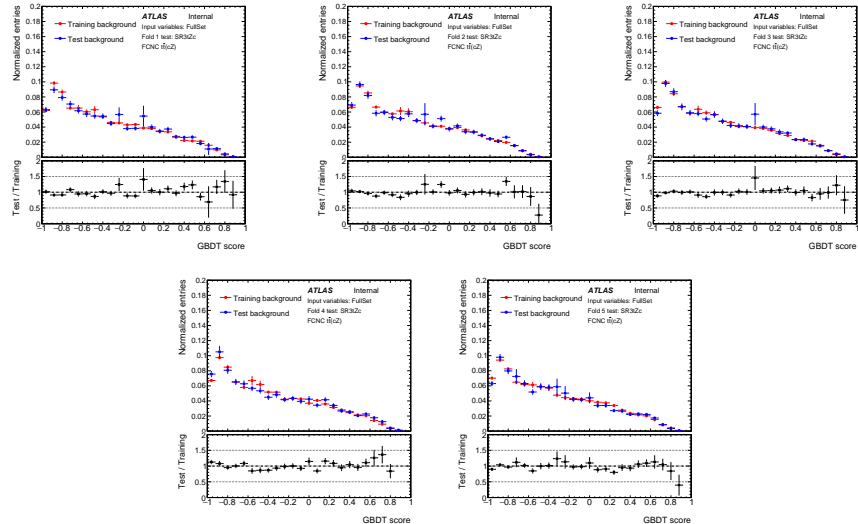


Figure D.3 – The background GBDT output score distribution for each of five GBDTs trained in SR3 for the D_3 discriminant. Initial (full) set of input variables is used in the training. Comparing results between training and test samples.

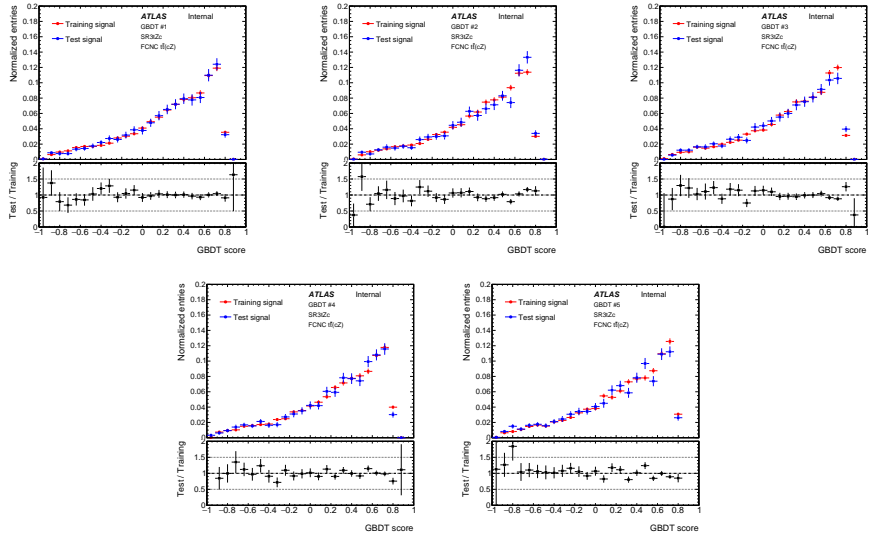


Figure D.4 – The FCNC $t\bar{t}$ decay signal GBDT output score distribution for each of five GBDTs trained in SR3 for the D_3 discriminant. Final set of input variables is used in the training. Comparing results between training and test samples.

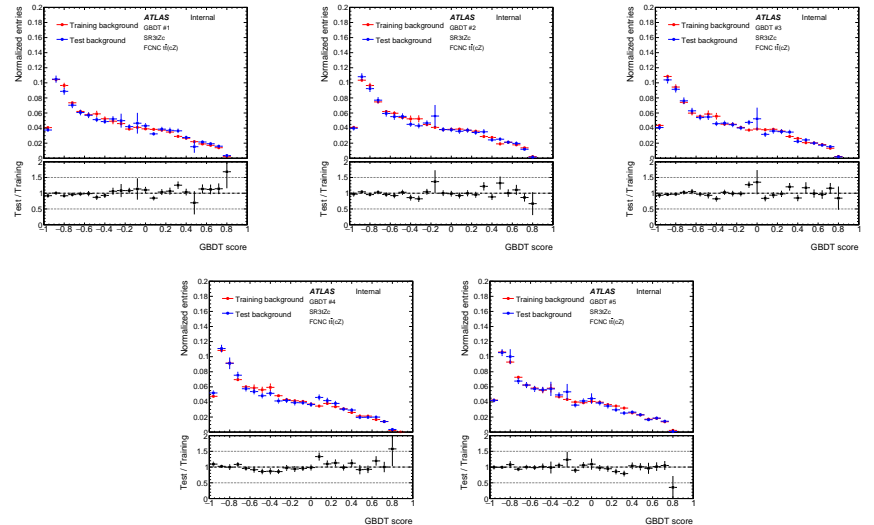


Figure D.5 – The background GBDT output score distribution for each of five GBDTs trained in SR3 for the D_3 discriminant. Final set of input variables is used in the training. Comparing results between training and test samples.

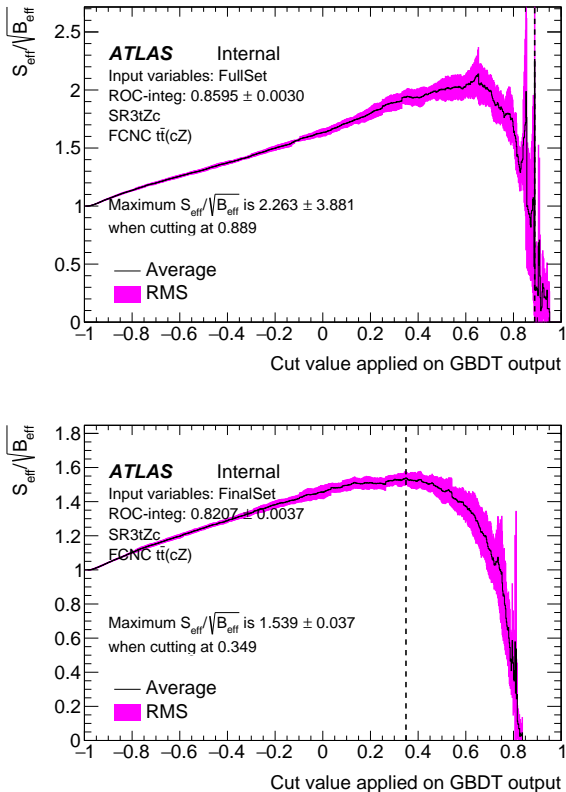


Figure D.6 – The $S_{\text{eff}}/\sqrt{B_{\text{eff}}}$ value averaged over the validation folds as a function of the cut on the BDT output score with full set (up) and final set (down) of input variables in the SR3.

D.2 Hyper-parameters optimisation

Once the final set of input variables are defined, the BDT hyper-parameters optimisation is performed. The following BDT paremeters [146] and values are considered with total of 144 combination: NTrees=[400,600,800,1000], minNodSize=[2.0,4.0,6.0], shrinkage=[0.025,0.05,0.1], maxDepth=[1,2,4]. Figure D.7 presents the maximum value of $S_{\text{eff}}/\sqrt{B_{\text{eff}}}$ by cutting the BDT output score, and the ROC integral, averaged over the validation folds, as a function of BDT hyper-parameters combination.

The difference between highest and lowest values of ROC integral with the different BDT hyper-parameters combinations is $\sim 2\%$. These result indicate that the BDT performance is stable and not much can be improved with the hyper-parameters.

The average ROC integral (0.8207 with RMS of 0.0037) obtained with the reference BDT parameters (see table D.1) is almost identical to the highest value of ROC integral (0.8255 with RMS of 0.0028) obtained from the hyper-parameters optimisation.

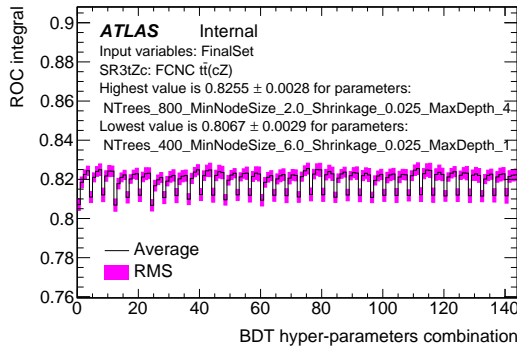


Figure D.7 – ROC integral, averaged over the validation folds, as a function of BDT hyper-parameters combination in the SR3. The highest and lowest values of $S_{\text{eff}}/\sqrt{B_{\text{eff}}}$ and ROC integral are presented on the plots as well as the corresponding BDT parameters values.

APPENDIX E

Kinematic distributions in the Signal Regions

This appendix shows some kinematic distributions in the Signal Regions:

- SR1tZc (Section [E.1](#));
- SR2tZc (Section [E.2](#));
- SR3tZc using DL1r_c (Section [E.3](#));

E.1 SR1tZc

Figures E.1 and E.2 show the distributions of kinematic variables for events selected in the SR1tZc.

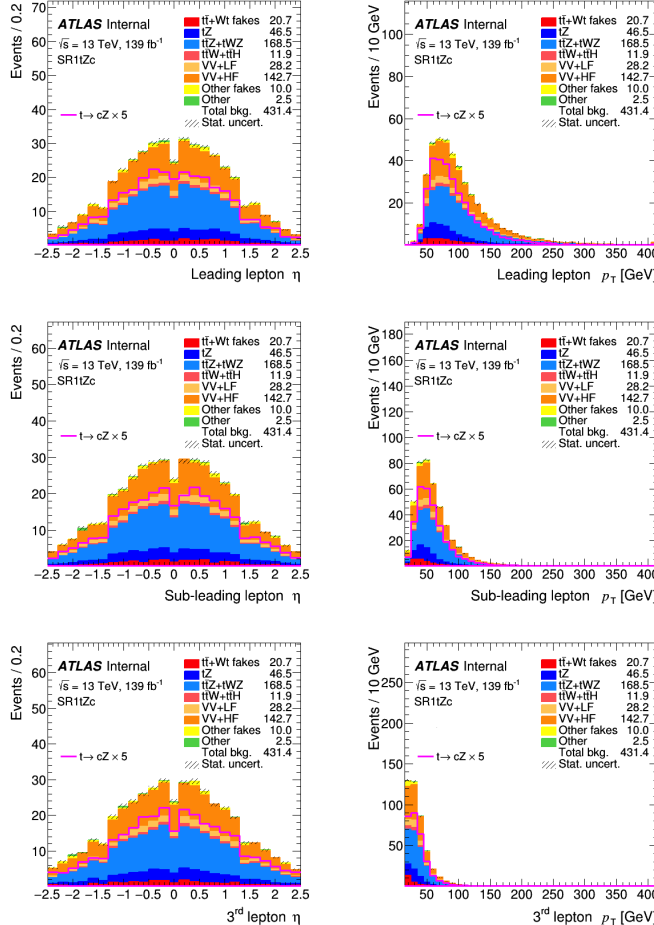


Figure E.1 – Pre-fit distributions of kinematic variables of leptons for events selected in the SR1tZc. The uncertainty band includes only the statistical uncertainty. These distributions are blinded, following the blinding strategy.

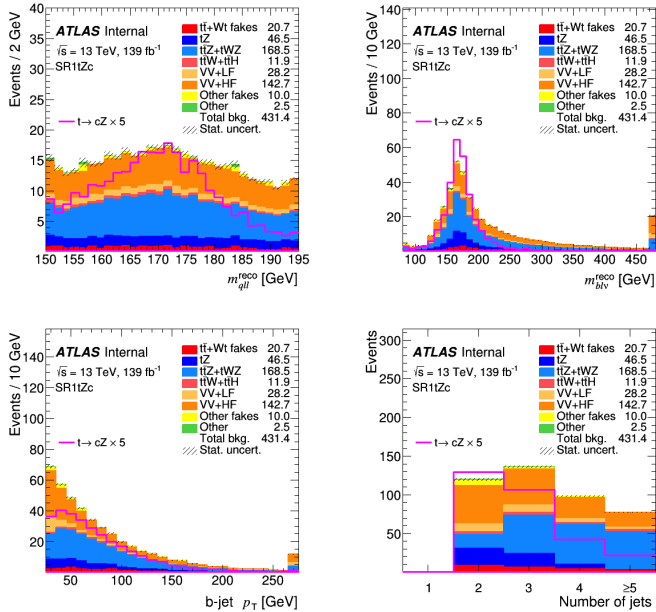


Figure E.2 – Pre-fit distributions of kinematic variables of jets for events selected in the SR1tZc. The uncertainty band includes only the statistical uncertainty. These distributions are blinded, following the blinding strategy.

E.2 SR2tZc

Figures E.3 and E.4 show the distributions of kinematic variables for events selected in the SR1tZc.

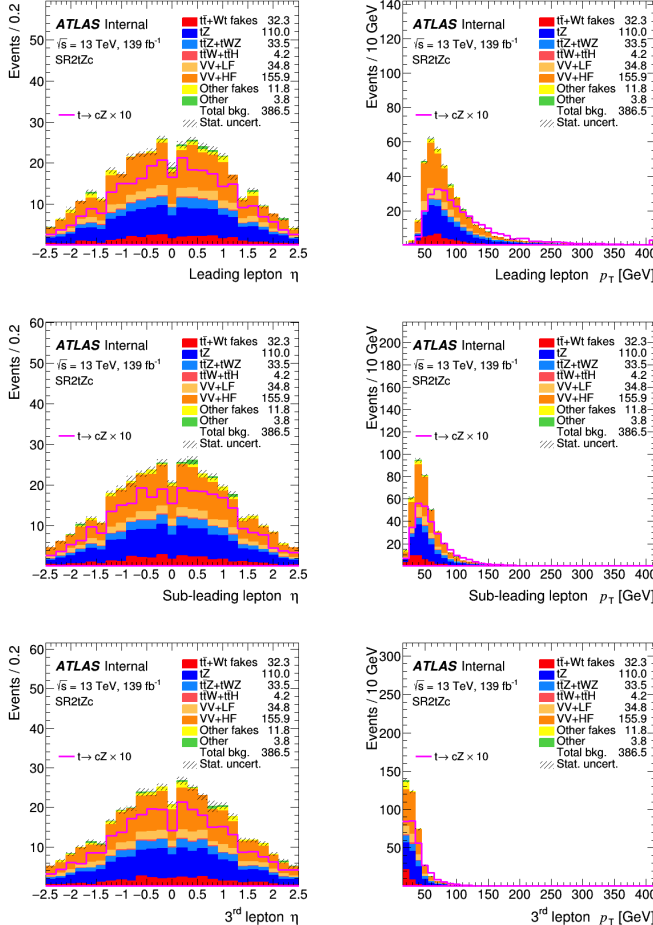


Figure E.3 – Pre-fit distributions of kinematic variables of leptons for events selected in the SR2tZc. The uncertainty band includes only the statistical uncertainty. These distributions are blinded, following the blinding strategy.

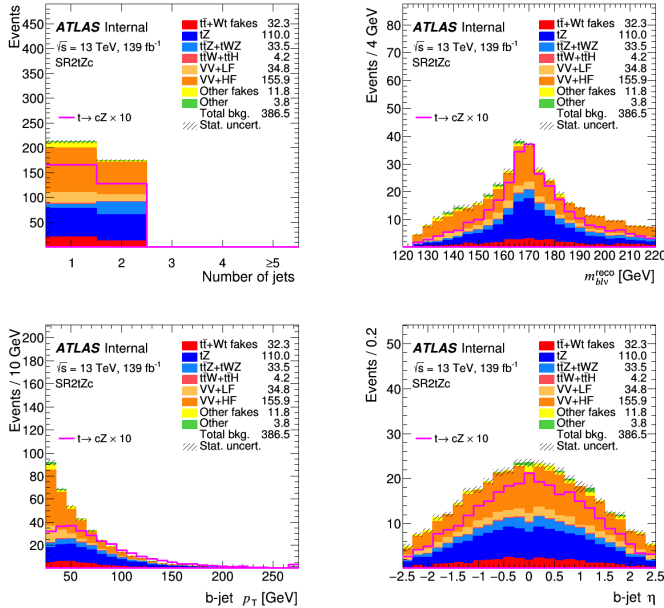


Figure E.4 – Pre-fit distributions of kinematic variables of jets for events selected in the SR2tZc. The uncertainty band includes only the statistical uncertainty. These distributions are blinded, following the blinding strategy.

E.3 SR3tZc

Figures E.5 and E.6 show the distributions of kinematic variables for events selected in the SR3tZc.

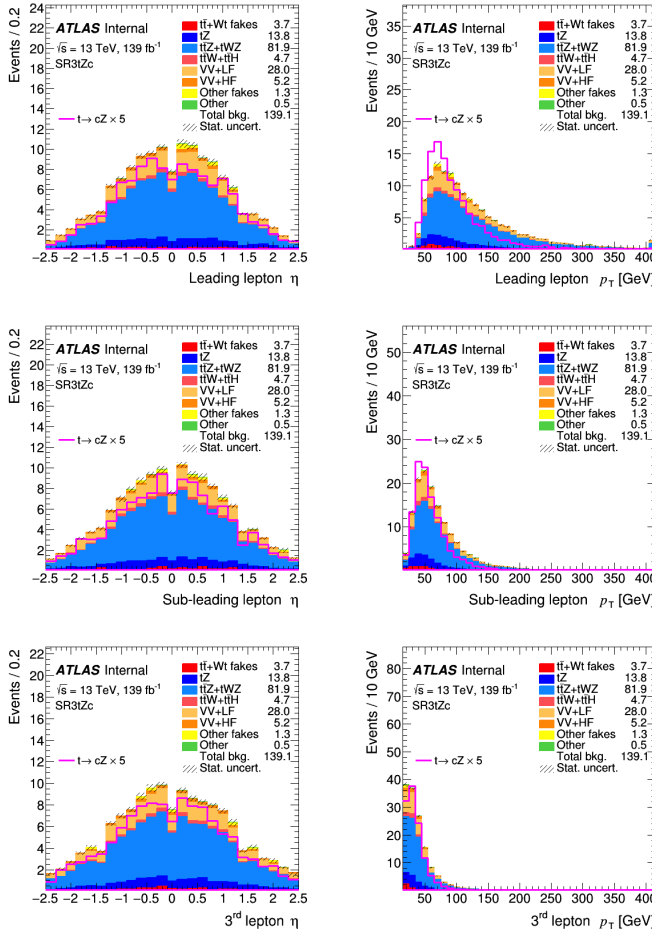


Figure E.5 – Pre-fit distributions of kinematic variables of leptons for events selected in the SR3tZc. The uncertainty band includes only the statistical uncertainty. These distributions are blinded, following the blinding strategy.

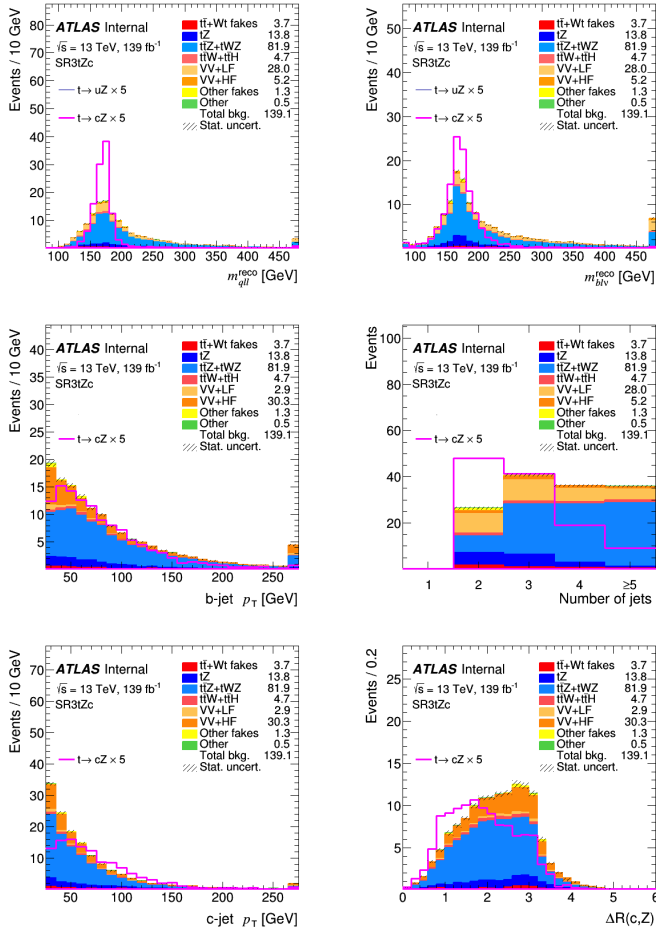


Figure E.6 – Pre-fit distributions of kinematic variables of jets for events selected in the SR3tZc. The uncertainty band includes only the statistical uncertainty. These distributions are blinded, following the blinding strategy.

APPENDIX F

Kinematic distributions in the Control Regions

This appendix shows some kinematic distributions in the Control Regions:

- $t\bar{t}$ CR (Section [F.1](#));
- $t\bar{t}Z$ CR (Section [F.2](#));
- Side-band CR1 (Section [F.3](#));
- Side-band CR2 (Section [F.4](#));

F.1 $t\bar{t}$ CR

Figures F.1 and F.2 show the distributions of kinematic variables for events selected in the $t\bar{t}$ CR region.

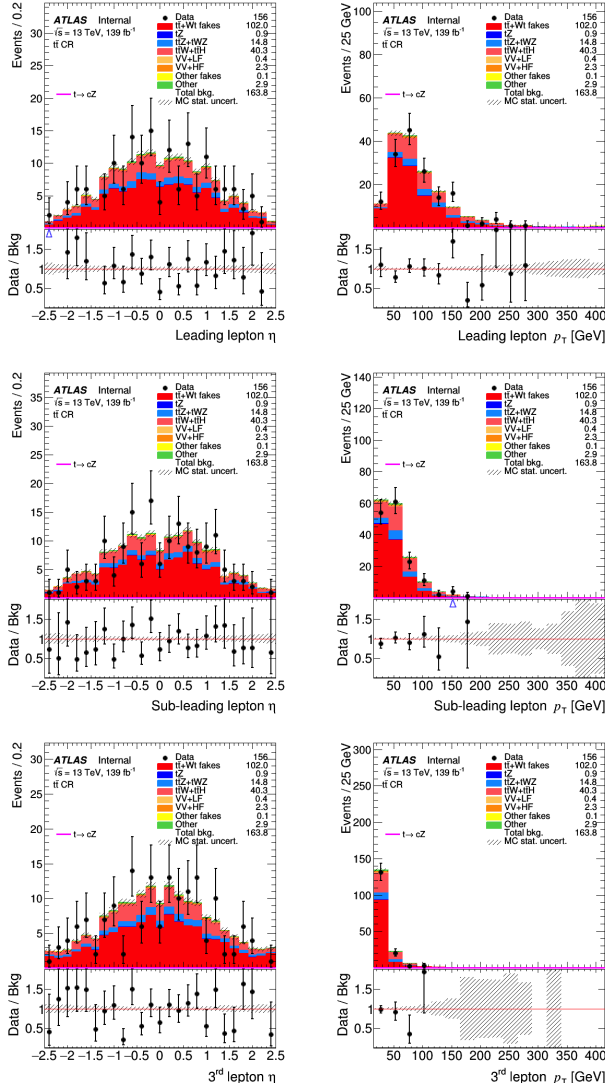


Figure F.1 – Pre-fit distributions of kinematic variables of leptons for events selected in the $t\bar{t}$ CR. The uncertainty band includes only the statistical uncertainty.

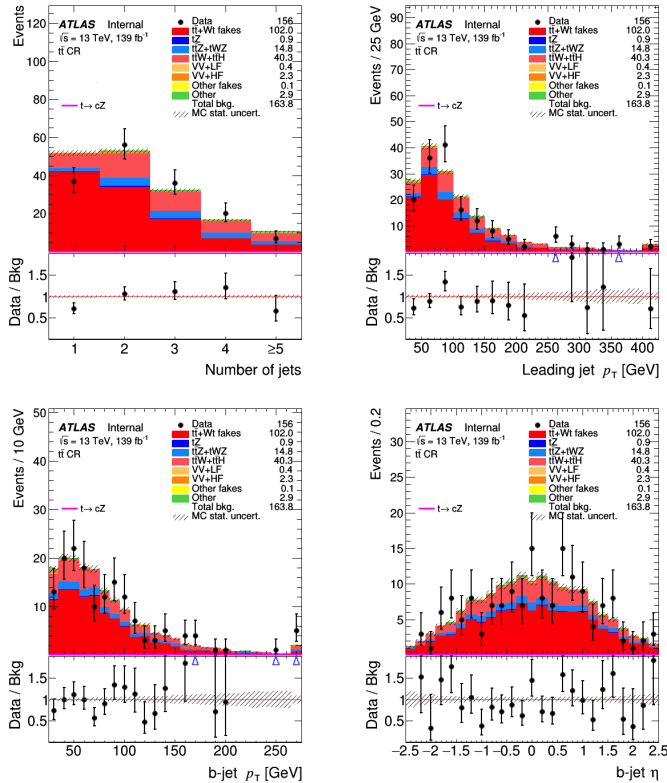


Figure F.2 – Pre-fit distributions of kinematic variables of jets for events selected in the $t\bar{t}$ CR. The uncertainty band includes only the statistical uncertainty.

F.2 $t\bar{t}Z$ CR

Figures F.3 and F.4 show the distributions of kinematic variables for events selected in the $t\bar{t}Z$ CR region.

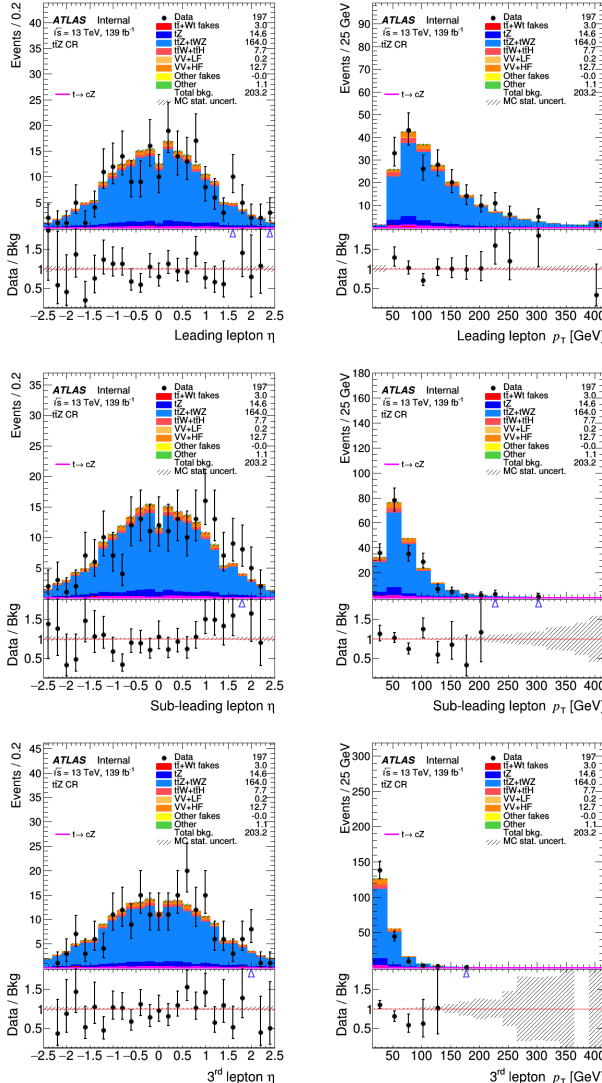


Figure F.3 – Pre-fit distributions of kinematic variables of leptons for events selected in the $t\bar{t}Z$ CR. The uncertainty band includes only the statistical uncertainty.

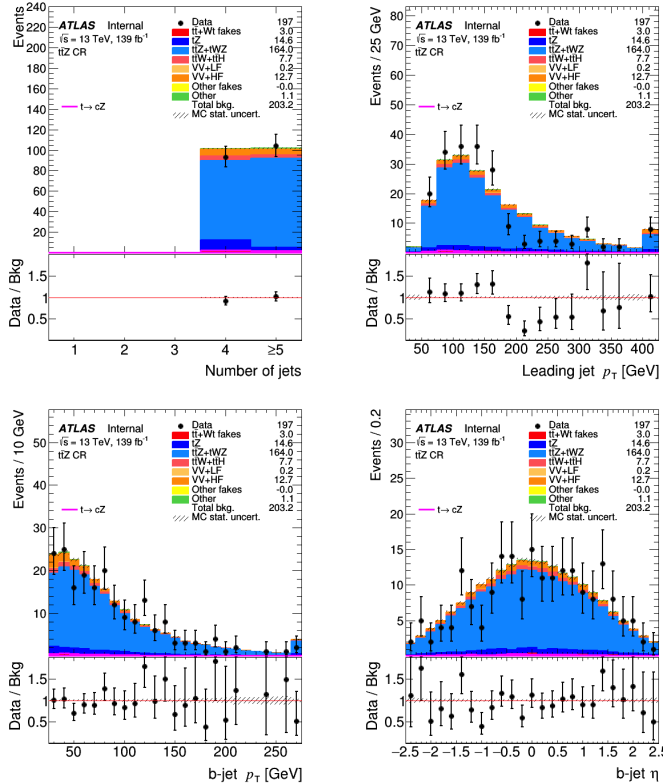


Figure F.4 – Pre-fit distributions of kinematic variables of jets for events selected in the $t\bar{t}Z$ CR. The uncertainty band includes only the statistical uncertainty.

F.3 Side-band CR1

Figures F.5 and F.6 show the distributions of kinematic variables for events selected in the side-band CR1 region.

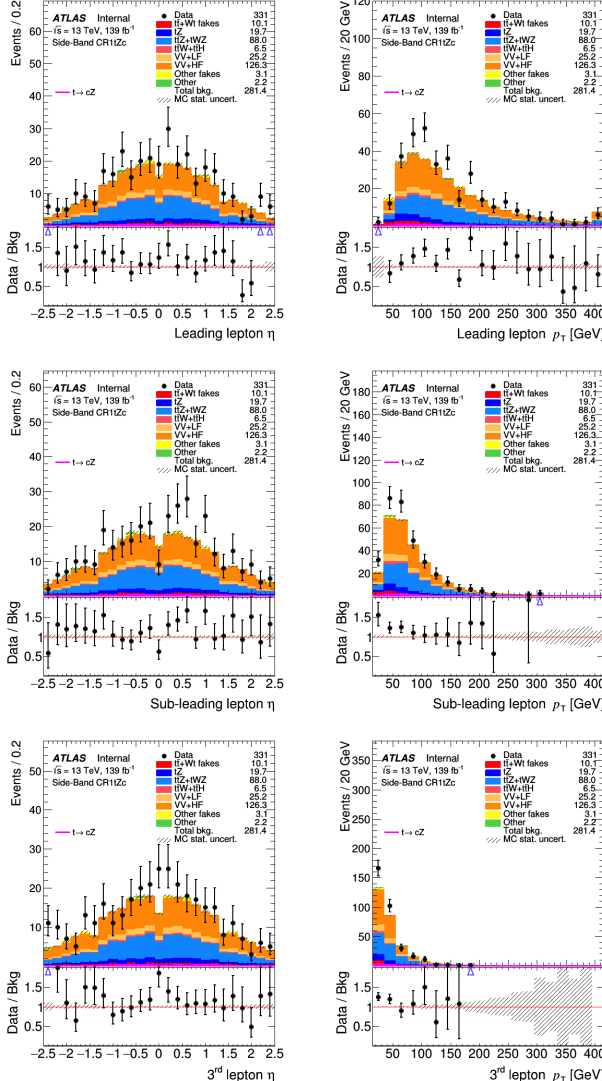


Figure F.5 – Pre-fit distributions of kinematic variables of leptons for events selected in the side-band CR1 region. The uncertainty band includes only the statistical uncertainty.

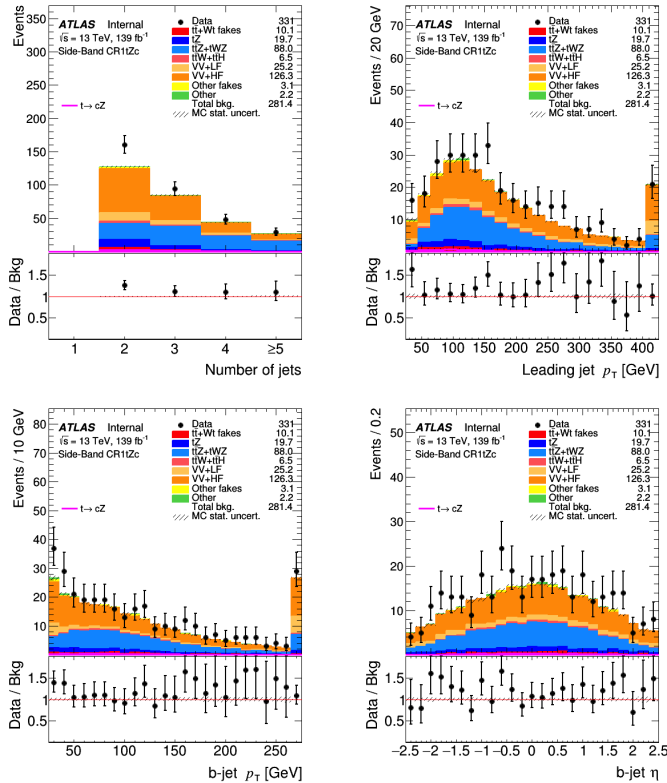


Figure F.6 – Pre-fit distributions of kinematic variables of jets for events selected in the side-band CR1 region. The uncertainty band includes only the statistical uncertainty.

F.4 Side-band CR2

Figures F.7 and F.8 show the distributions of kinematic variables for events selected in the side-band CR2 region.

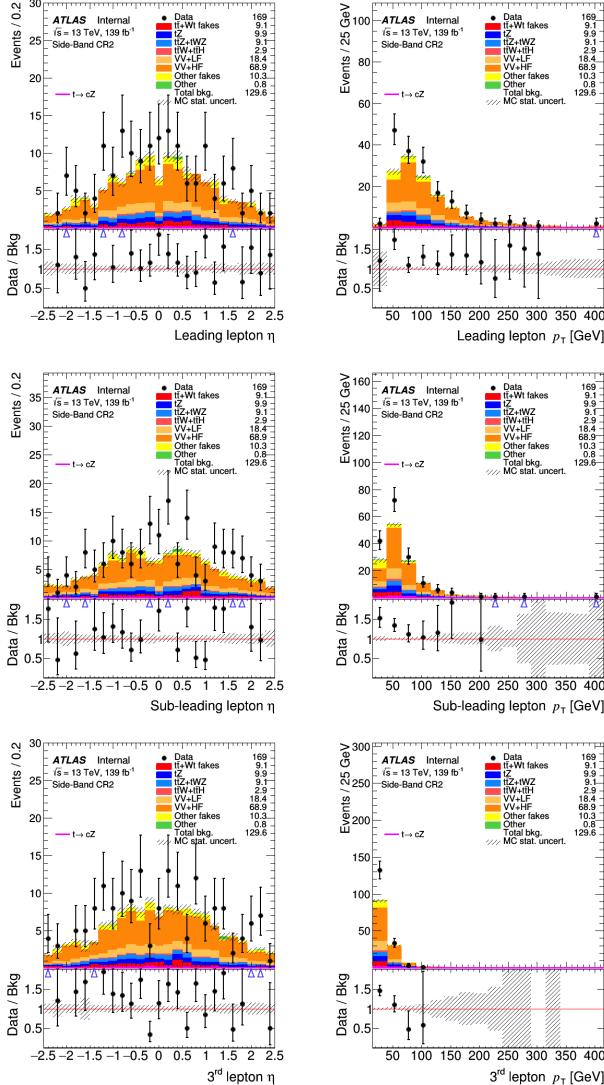


Figure F.7 – Pre-fit distributions of kinematic variables of leptons for events selected in the side-band CR2 region. The uncertainty band includes only the statistical uncertainty.

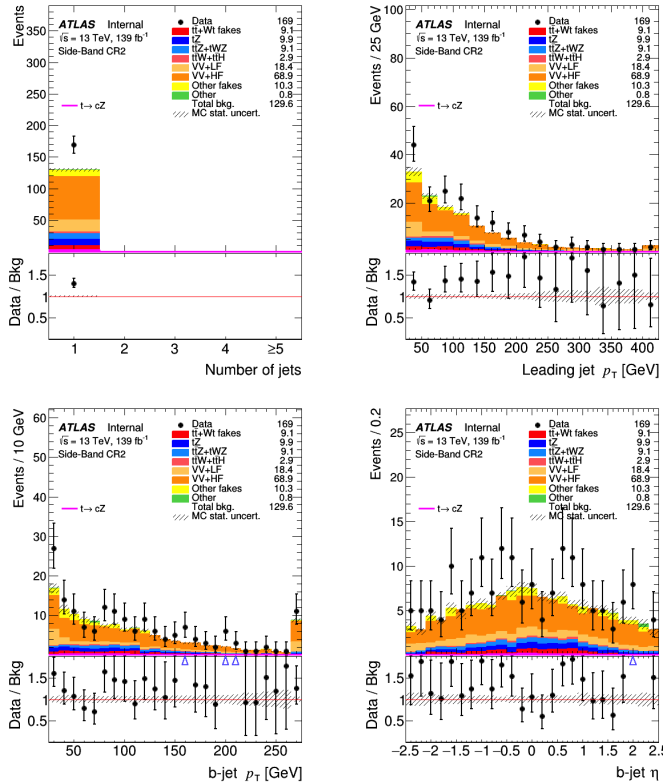


Figure F.8 – Pre-fit distributions of kinematic variables of jets for events selected in the side-band CR2 region. The uncertainty band includes only the statistical uncertainty.

APPENDIX G

Background only fit in CRs

To check the background modeling and extract realistic background normalisations, a CRs-only background-only fit using real data in CRs is performed.

A summary of plots shown in the following:

- The value of the post-fit normalisation parameters of the free floating background is shown in fig. G.1.
- The list of the systematic shapes that are dropped from the fit for each sample and for each region is shown in Figure G.2.
- The pull distributions of the all nuisance parameters can be seen in Figures G.3 and G.4 and Figure G.5.
- Event yields pre- and post-fit are shown in Tables G.1 and G.2.
- Pre-fit and post-fit distributions of the fitted distributions in the various regions are shown in Figures G.6 and G.7.

As shown in fig. G.1, the $t\bar{t}$ scale factor is 0.93 ± 0.25 , compatible with unity. The pull distributions show that the $VV + HF$ normalisation is pulled up (fig. G.4), driven by the prediction being lower than data in the side-band CRs (tables G.1 and G.2). Since this fit uses real data in CRs, some pulls and constraints of the NPs are expected. For the NPs for the instrumental uncertainties, no significant pulls nor constraints are present (fig. G.3), while some NPs for the modeling uncertainties can be seen (fig. G.4), in particular for the $t\bar{t}$ and diboson backgrounds. After the fit, there is an overall good agreement between data and the prediction, as it can be seen in the post-fit event yields (table G.2) and in the distribution of the fitted variables in the CRs (figs. G.6 and G.7).

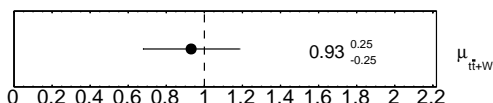


Figure G.1 – Normalisation factors for the B-only tZc fit in CRs.

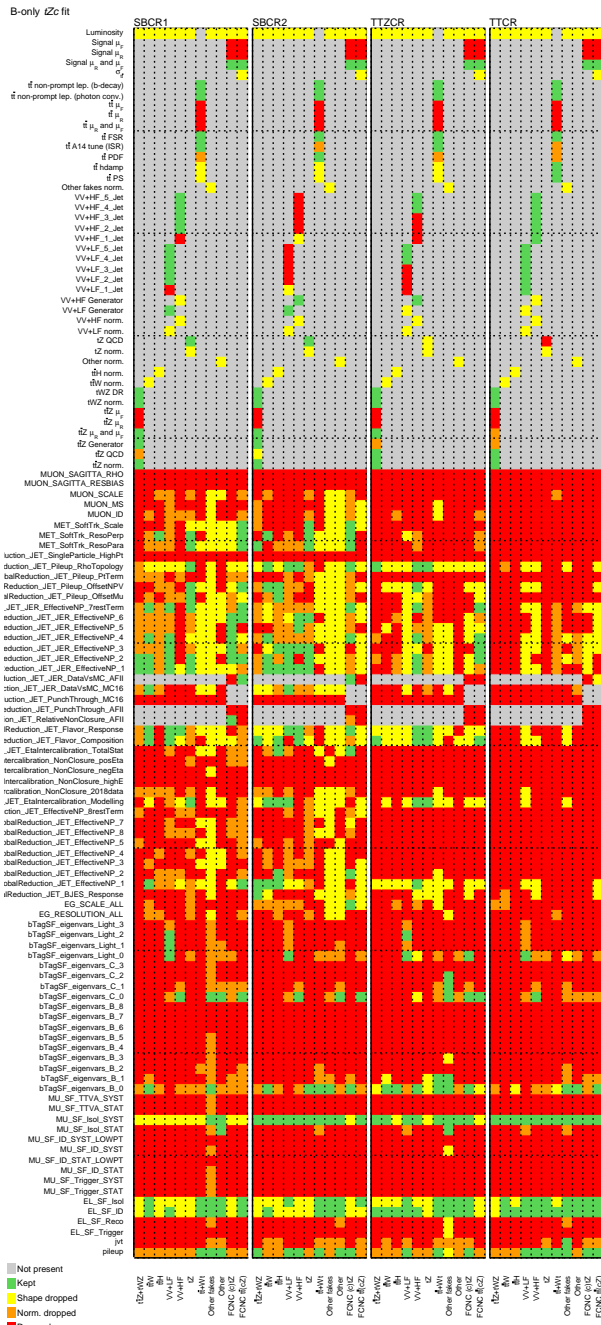


Figure G.2 – Pruning of the nuisance parameters for the B-only tZc fit in CRs.

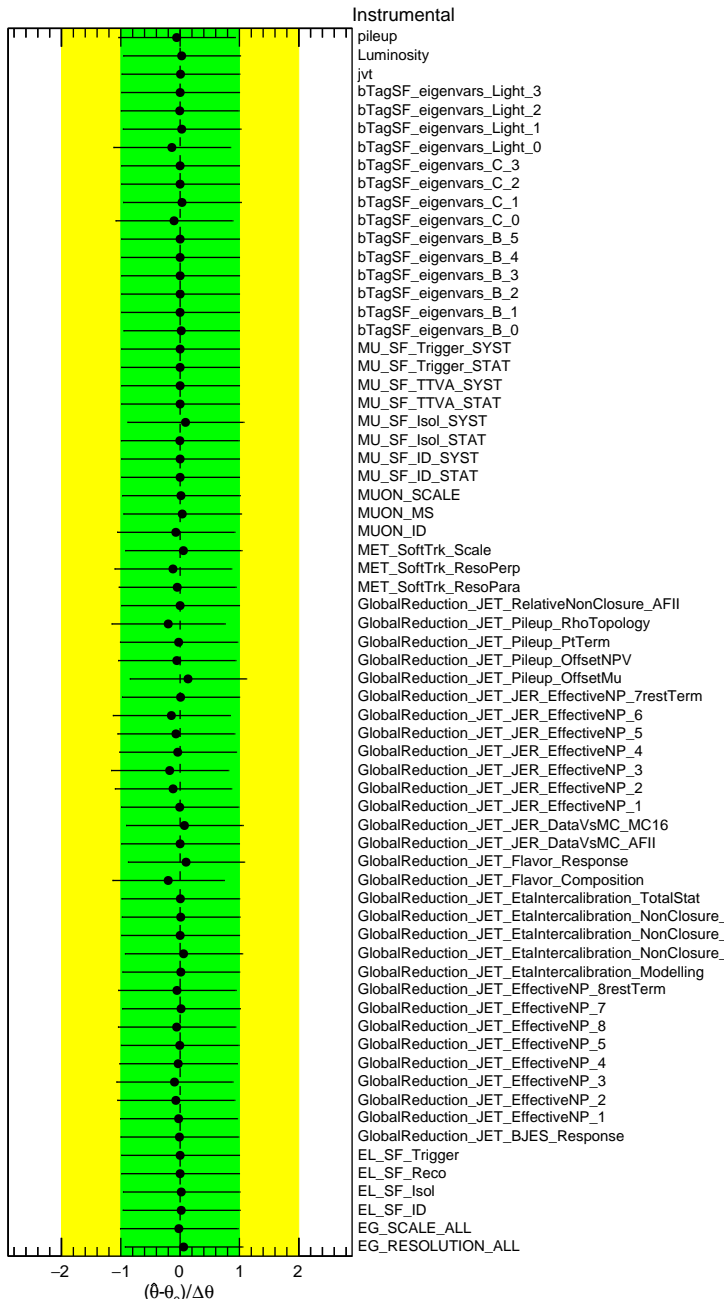


Figure G.3 – Pulls and constraints of the instrumental nuisance parameters for the B-only tZc fit in CRs.

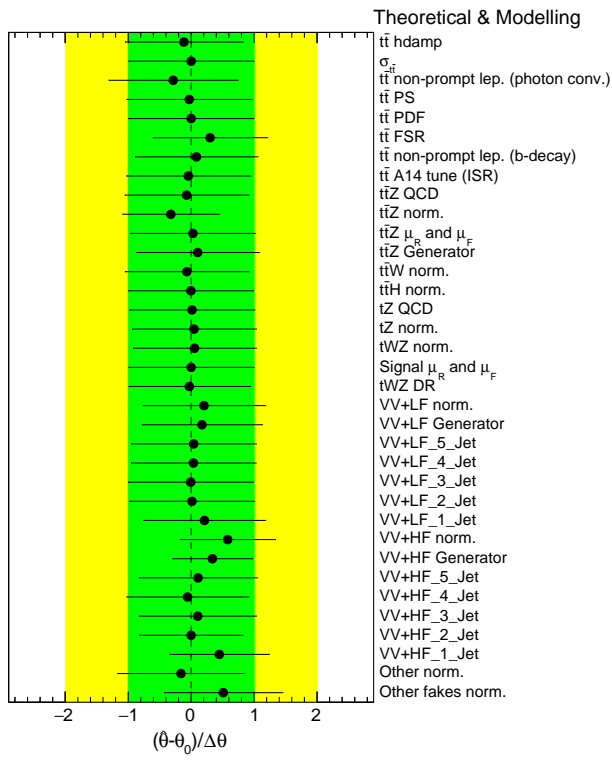


Figure G.4 – Pulls and constraints of the theoretical and modeling nuisance parameters for the B-only tZc fit in CRs.

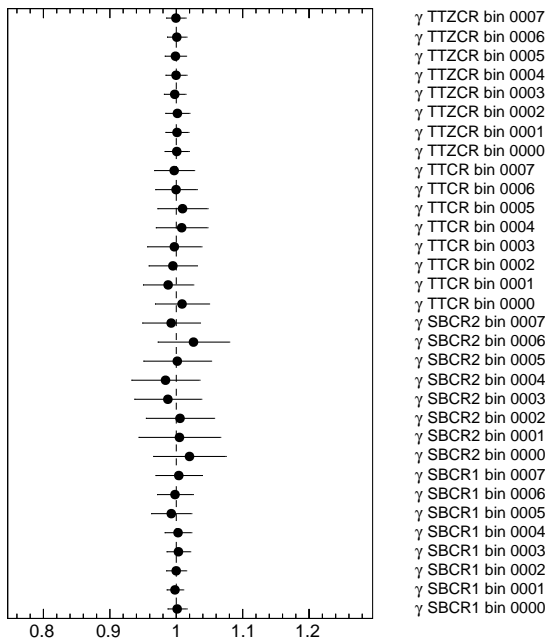


Figure G.5 – Gamma parameters for the B-only tZc fit in CRs.

	Side-band CR1	Side-band CR2	$t\bar{t}Z$ CR	$t\bar{t}$ CR
$t\bar{t}Z + tWZ$	88 ± 12	9.1 ± 2.1	164 ± 22	14.8 ± 1.9
$t\bar{t}W$	4.3 ± 0.7	2.5 ± 0.5	2.3 ± 0.5	27 ± 4
$t\bar{t}H$	2.3 ± 0.4	0.36 ± 0.07	5.4 ± 0.9	13.8 ± 2.1
$VV + LF$	25 ± 15	18 ± 7	0.20 ± 0.22	0.40 ± 0.21
$VV + HF$	130 ± 80	69 ± 28	13 ± 11	2.3 ± 1.4
tZq	20 ± 4	9.9 ± 1.7	14.6 ± 2.9	0.90 ± 0.15
$t\bar{t} + Wt$	10 ± 4	9.1 ± 2.7	3.0 ± 1.2	102 ± 24
Other fakes	3 ± 5	10 ± 11	0.00 ± 0.06	0.12 ± 0.14
Other	2.2 ± 1.6	0.8 ± 2.6	1.1 ± 0.5	2.9 ± 1.5
Total background	280 ± 80	130 ± 32	203 ± 27	164 ± 25
Data	331	169	197	156
Data / Bkg.	1.18 ± 0.35	1.30 ± 0.34	0.97 ± 0.14	0.95 ± 0.16

Table G.1 – Pre-fit event yields in the CRs for the B-only fit for the tZc coupling extraction. The error includes both statistical and systematic uncertainties.

	Side-band CR1	Side-band CR2	$t\bar{t}Z$ CR	$t\bar{t}$ CR
$t\bar{t}Z + tWZ$	86 ± 10	9.3 ± 2.1	157 ± 13	14.4 ± 1.4
$t\bar{t}W$	4.2 ± 0.7	2.5 ± 0.5	2.2 ± 0.4	26 ± 4
$t\bar{t}H$	2.3 ± 0.4	0.37 ± 0.07	5.3 ± 0.8	13.8 ± 2.1
$VV + LF$	29 ± 16	21 ± 8	0.23 ± 0.23	0.40 ± 0.19
$VV + HF$	172 ± 28	94 ± 18	18 ± 7	3.3 ± 0.6
tZq	20 ± 4	10.1 ± 1.7	14.4 ± 2.7	0.91 ± 0.13
$t\bar{t} + Wt$	9.4 ± 2.9	8.6 ± 1.7	2.5 ± 0.8	95 ± 13
Other fakes	5 ± 5	18 ± 16	0.006 ± 0.009	0.18 ± 0.15
Other	1.8 ± 1.2	0.3 ± 0.9	1.0 ± 0.5	2.7 ± 1.4
Total background	329 ± 20	165 ± 14	201 ± 13	157 ± 12
Data	331	169	197	156
Data / Bkg.	1.01 ± 0.06	1.02 ± 0.09	0.98 ± 0.06	0.99 ± 0.08

Table G.2 – Post-fit event yields in the CRs for the B-only fit for the tZc coupling extraction. The error includes both statistical and systematic uncertainties.

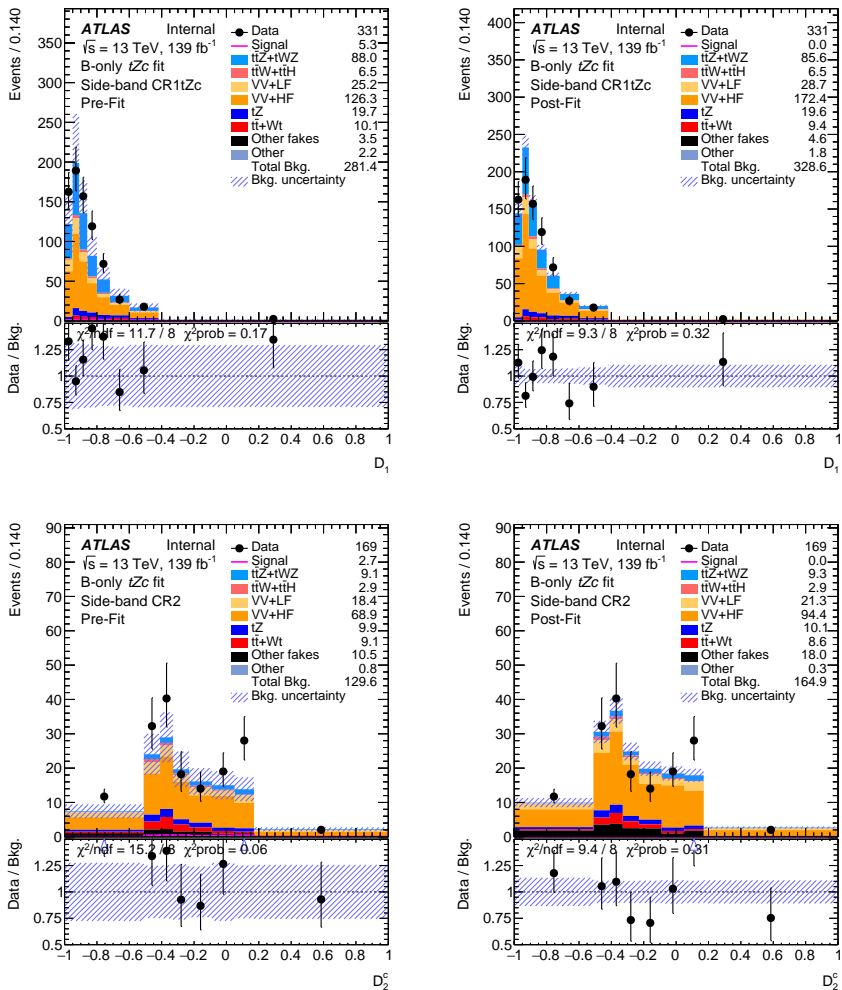


Figure G.6 – Pre-fit (left) and post-fit (right) BDTG output distributions in the side-band CRs for the B-only tZc fit in CRs. The uncertainty band includes both statistical and systematic uncertainties.

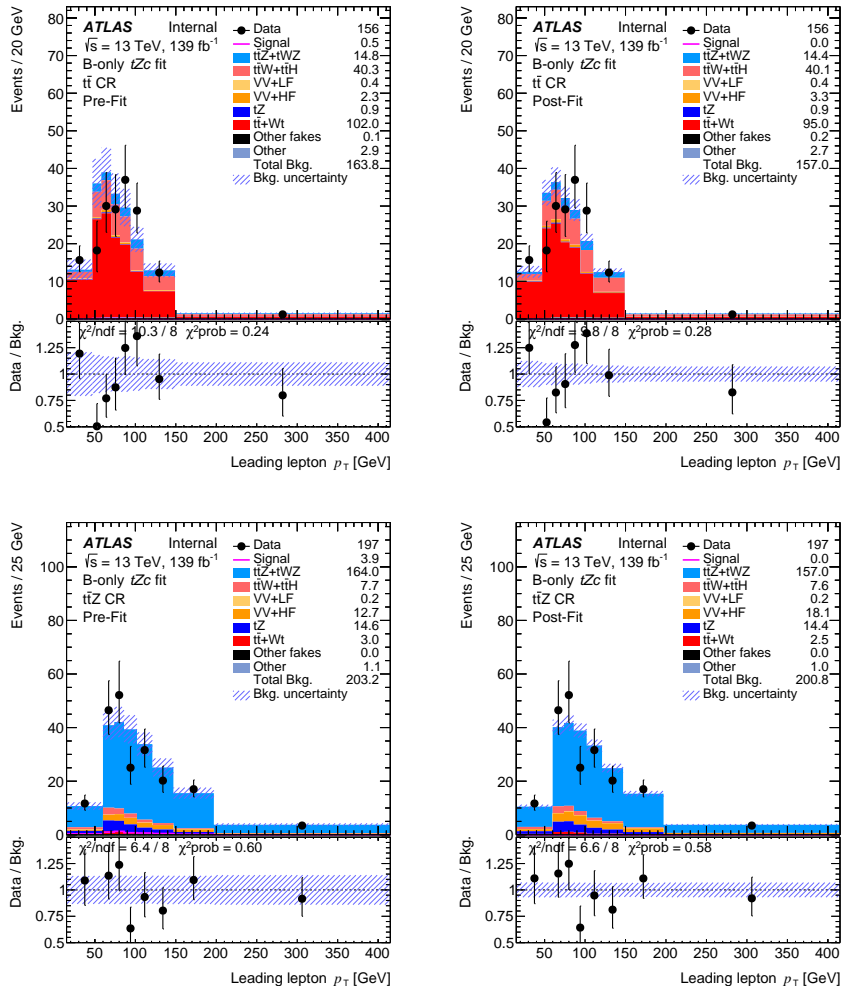


Figure G.7 – Pre-fit (left) and post-fit (right) leading lepton p_T distributions in the $t\bar{t}$ and tZ CRs for the B-only tZ fit in CRs. The uncertainty band includes both statistical and systematic uncertainties.

Signal + Background fit in SRs+CRs using SMT

To extract the expected sensitivity, an SRs+CRs S+B fit is performed. Real data is used in CRs while in SRs an Asimov dataset is used, constructed using the background normalisations as done in Appendix G for the selection using DL1r_c .

A summary of plots and tables shown in this section are the following:

- The value of the post-fit normalisation parameters of the free floating background is shown in Figure H.1.
- The list of the systematic shapes that are dropped from the fit for each sample and for each region is shown in Figure H.2.
- The pull distributions of the all nuisance parameters can be seen in Figures H.3 and H.4 and Figure H.5.
- The correlation matrix of the nuisance parameters is shown in Figure H.6.
- The ranking of the nuisance parameters is shown in Figure H.7.
- Event yields pre- and post-fit are shown in Tables H.1 and H.2.
- Pre-fit and post-fit distributions of the fitted distributions in the various regions are shown in Figures H.8 to H.11.
- Expected limits on the branching ratios of $t \rightarrow Zc$ shown in Table H.3.

Normalisation factors (fig. H.1) and NP pulls and constrains (Figures H.3 and H.4) are very similar. None of the systematic uncertainties has a post-fit impact on the signal strength parameter greater than 4%. Concerning the correlations between NPs (Figure H.6), some strong correlations between diboson related NPs are present, as expected. This is also true for the $t\bar{t}$ normalisation and some $t\bar{t}$ modeling NPs.

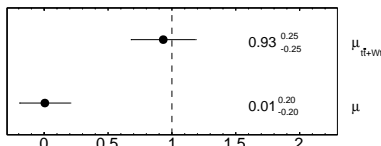


Figure H.1 – Normalisation factors for the S+B tZc fit in SRs+CRs with realistic Asimov.

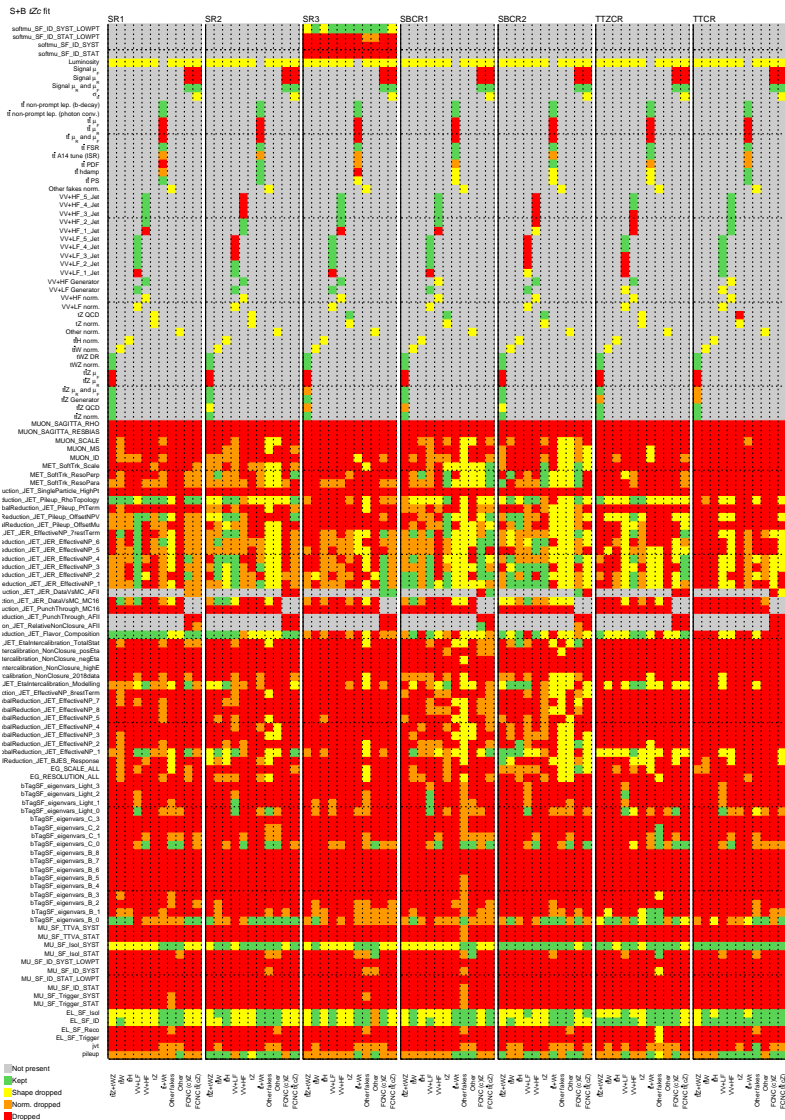


Figure H.2 – Pruning of the nuisance parameters for the S+B tZc fit in SRs+CRs with realistic Asimov.

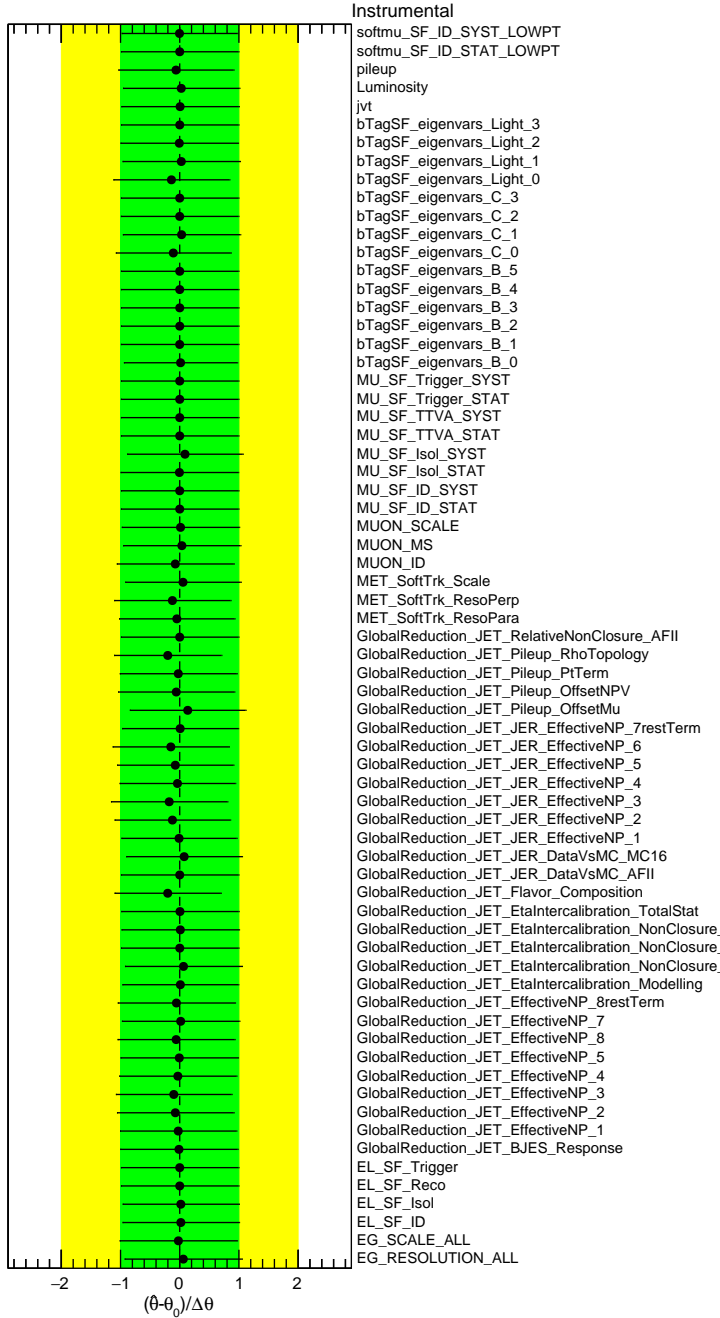


Figure H.3 – Pulls and constraints of the instrumental nuisance parameters for the S+B tZc fit in SRs+CRs with realistic Asimov.

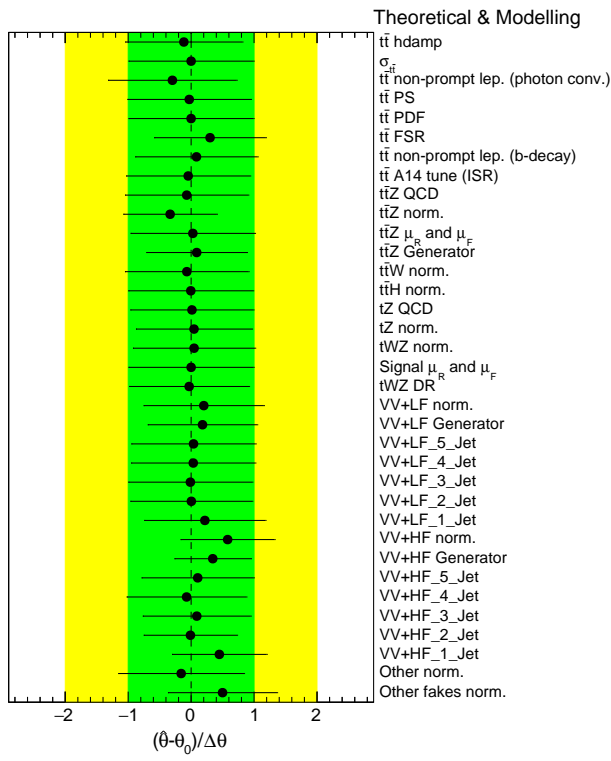


Figure H.4 – Pulls and constraints of the theoretical and modeling nuisance parameters for the S+B tZc fit in SRs+CRs with realistic Asimov.

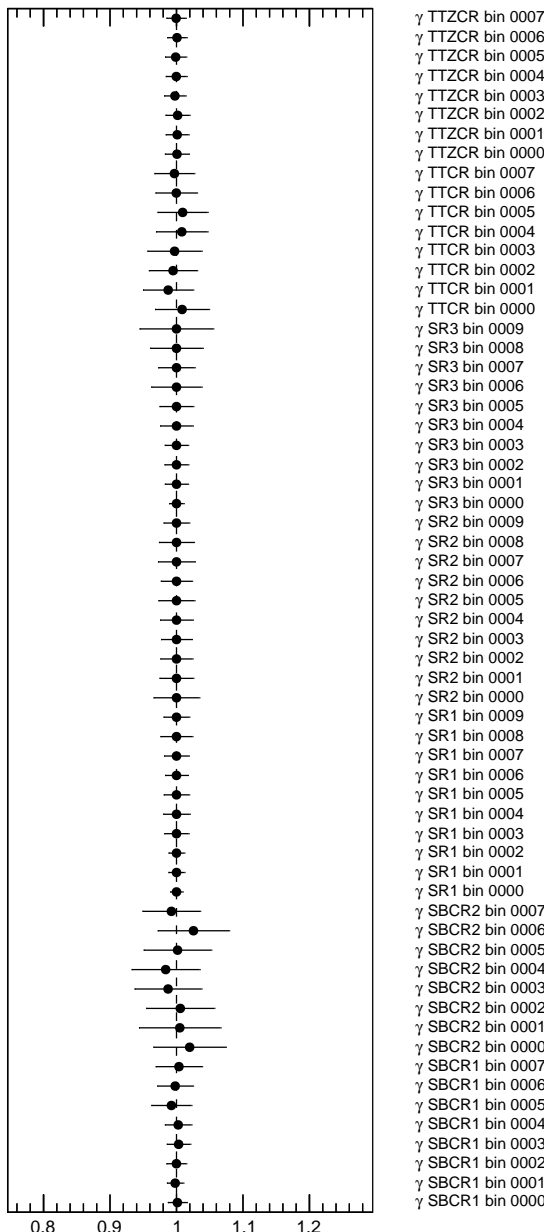


Figure H.5 – Gamma parameters for the S+B tZc fit in SRs+CRs with realistic Asimov.

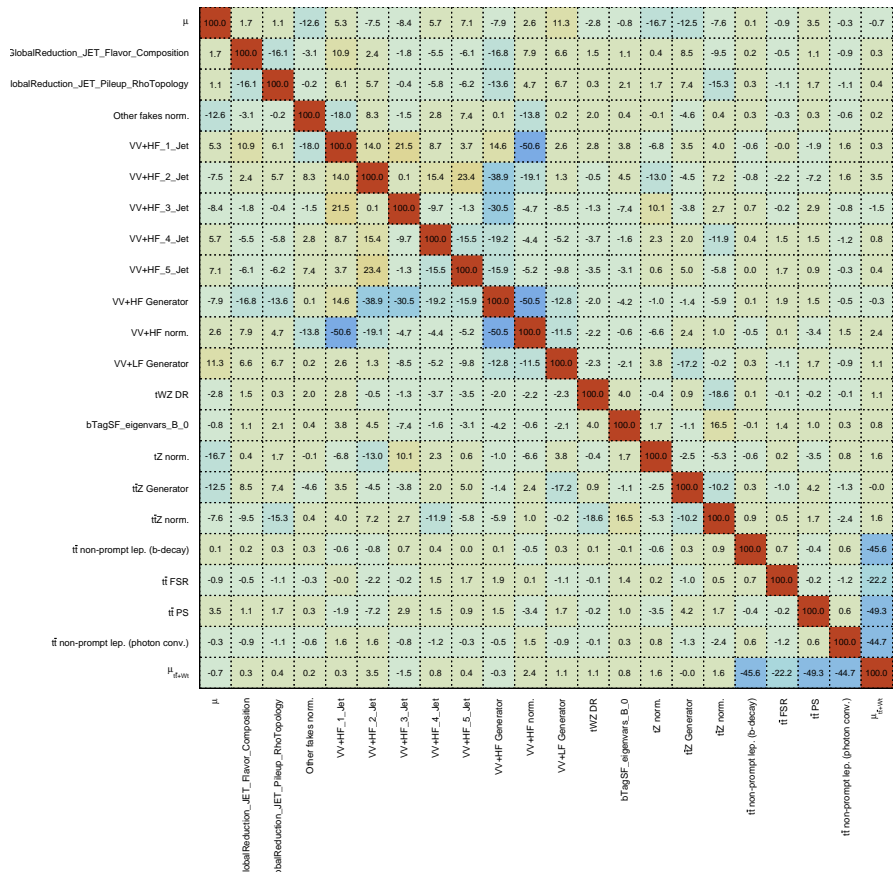


Figure H.6 – Correlation matrix of the nuisance parameters for the S+B tZc fit in SRs+CRs with realistic Asimov.

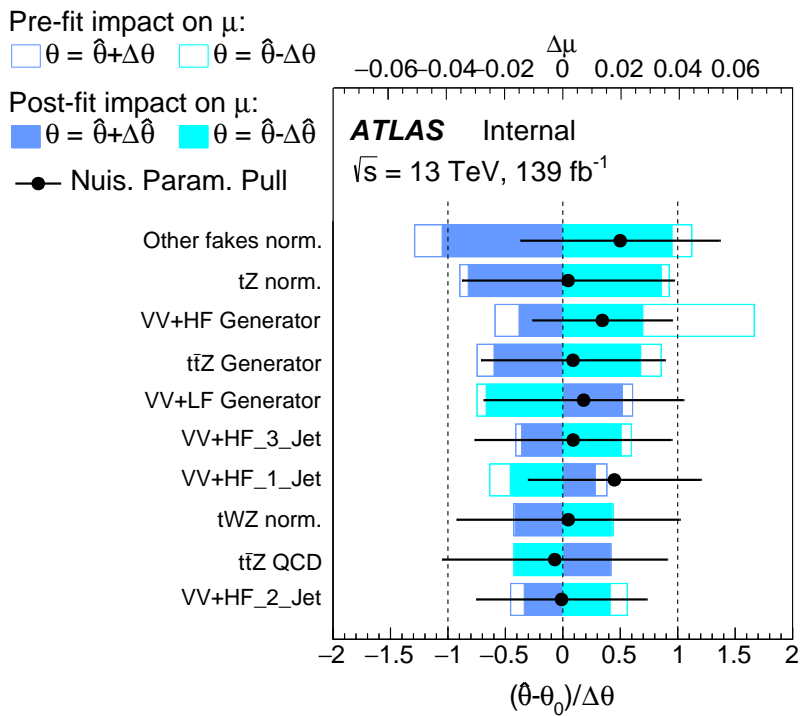


Figure H.7 – Ranking of the nuisance parameters for the S+B tZc fit in SRs+CRs with realistic Asimov.

	SR1tZc	SR2tZc	SR3tZc	Side-band CR1	Side-band CR2	t̄Z CR	t̄ CR
t̄Z +tWZ	200 ± 26	36 ± 7	97 ± 22	88 ± 12	9.1 ± 2.1	164 ± 22	14.8 ± 1.9
t̄W	6.5 ± 1.1	3.5 ± 0.6	2.5 ± 0.4	4.3 ± 0.7	2.5 ± 0.5	2.3 ± 0.4	27 ± 4
t̄H	7.4 ± 1.2	0.93 ± 0.18	3.1 ± 0.5	2.3 ± 0.4	0.36 ± 0.07	5.4 ± 0.9	13.8 ± 2.1
V V + LF	29 ± 18	35 ± 13	36 ± 20	25 ± 15	18 ± 7	0.20 ± 0.22	0.40 ± 0.20
V V + HF	150 ± 110	160 ± 70	80 ± 50	130 ± 80	69 ± 28	13 ± 11	2.3 ± 1.4
tZq	50 ± 8	112 ± 18	24 ± 4	20 ± 4	9.9 ± 1.7	14.6 ± 2.9	0.90 ± 0.15
t̄ +Wt	22 ± 5	33 ± 12	6.4 ± 1.7	10 ± 4	9.1 ± 2.7	3.0 ± 1.2	102 ± 24
Other fakes	11 ± 12	12 ± 12	4 ± 4	3 ± 5	10 ± 11	0.00 ± 0.06	0.12 ± 0.14
Other	2.6 ± 1.5	3.8 ± 2.8	2.7 ± 1.7	2.2 ± 1.6	0.8 ± 2.6	1.1 ± 0.5	2.9 ± 1.5
FCNC (c)Z	3.50 ± 0.27	12.0 ± 0.6	1.7 ± 1.4	1.06 ± 0.12	0.83 ± 0.09	0.24 ± 0.04	0.083 ± 0.012
FCNC t̄ (cZ)	73 ± 6	18.1 ± 1.9	15 ± 10	4.2 ± 0.6	1.9 ± 0.4	3.7 ± 0.5	0.37 ± 0.07
Total background	480 ± 110	390 ± 80	250 ± 60	280 ± 80	130 ± 32	203 ± 27	164 ± 25
Data	542	460	286	331	169	197	156
Data / Bkg.	1.13 ± 0.27	1.17 ± 0.24	1.14 ± 0.27	1.18 ± 0.35	1.30 ± 0.34	0.97 ± 0.14	0.95 ± 0.16

Table H.1 – Pre-fit event yields in the S+B tZc fit in SRs+CRs with realistic Asimov. The error includes both statistical and systematic uncertainties.

	SR1tZc	SR2tZc	SR3tZc	Side-band CR1	Side-band CR2	t̄Z CR	t̄ CR
t̄Z +tWZ	193 ± 17	36 ± 6	95 ± 15	85 ± 9	9.2 ± 1.7	157 ± 13	14.4 ± 1.4
t̄W	6.5 ± 1.0	3.6 ± 0.6	2.5 ± 0.4	4.2 ± 0.7	2.5 ± 0.5	2.3 ± 0.4	26 ± 4
t̄H	7.4 ± 1.1	0.95 ± 0.18	3.1 ± 0.5	2.3 ± 0.4	0.37 ± 0.07	5.3 ± 0.8	13.8 ± 2.1
V V + LF	33 ± 17	39 ± 13	41 ± 19	29 ± 14	21 ± 8	0.24 ± 0.22	0.40 ± 0.18
V V + HF	213 ± 35	215 ± 29	105 ± 16	172 ± 25	94 ± 16	18 ± 6	3.3 ± 0.5
tZq	50 ± 7	114 ± 16	23.8 ± 3.5	19.6 ± 3.3	10.1 ± 1.6	14.4 ± 2.5	0.91 ± 0.12
t̄ +Wt	19.7 ± 3.4	31 ± 7	5.9 ± 1.3	9.4 ± 2.8	8.6 ± 1.7	2.5 ± 0.8	95 ± 13
Other fakes	17 ± 12	17 ± 13	6 ± 5	5 ± 5	18 ± 14	0.005 ± 0.009	0.18 ± 0.13
Other	2.4 ± 1.3	3.7 ± 2.5	2.4 ± 1.3	1.8 ± 1.2	0.2 ± 0.8	1.0 ± 0.5	2.7 ± 1.4
FCNC (c)Z	0.0 ± 0.7	0.1 ± 2.4	0.01 ± 0.34	0.01 ± 0.21	0.00 ± 0.17	0.00 ± 0.05	0.000 ± 0.016
FCNC t̄ (cZ)	0 ± 15	0 ± 4	0.1 ± 3.0	0.0 ± 0.8	0.0 ± 0.4	0.0 ± 0.7	0.00 ± 0.07
Total background	541 ± 24	460 ± 21	286 ± 15	328 ± 16	165 ± 13	201 ± 12	157 ± 12
Data	542	460	286	331	169	197	156
Data / Bkg.	1.00 ± 0.04	1.00 ± 0.05	1.00 ± 0.05	1.01 ± 0.05	1.03 ± 0.08	0.98 ± 0.06	0.99 ± 0.08

Table H.2 – Post-fit event yields in the S+B tZc fit in SRs+CRs with realistic Asimov. The error includes both statistical and systematic uncertainties.

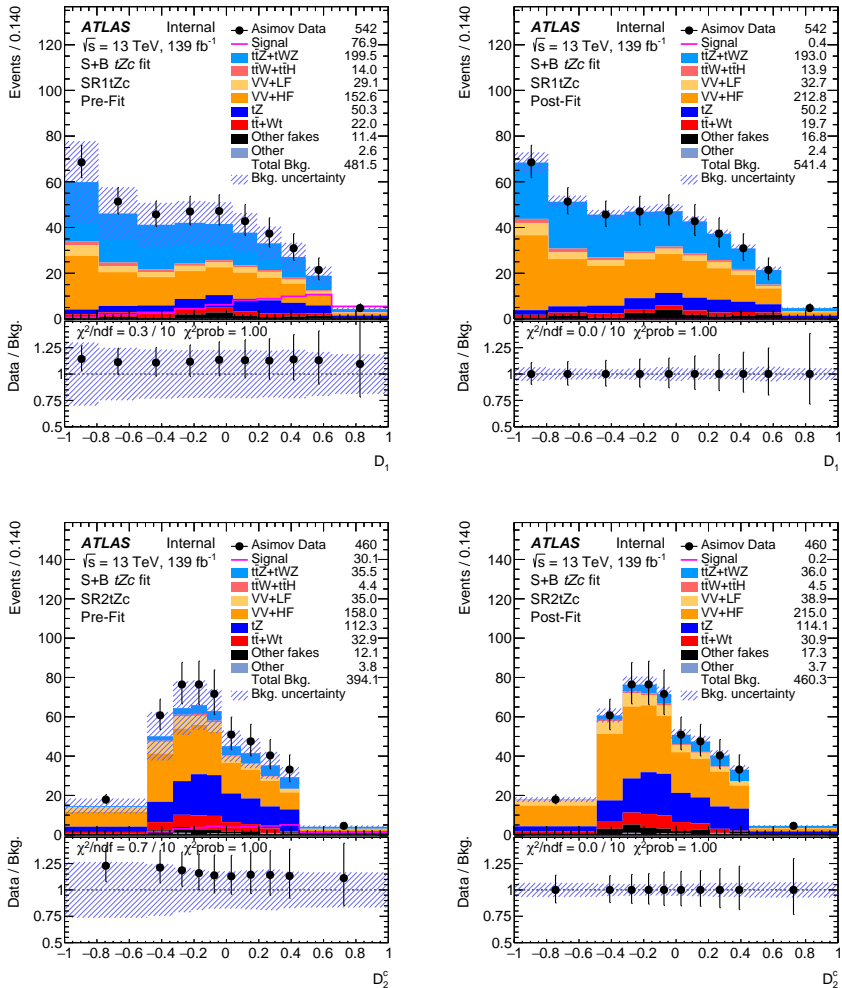


Figure H.8 – Pre-fit (left) and post-fit (right) BDTG output distributions in SR1 and SR2 for the S+B tZc fit in SRs+CRs with realistic Asimov. The uncertainty band includes both statistical and systematic uncertainties.

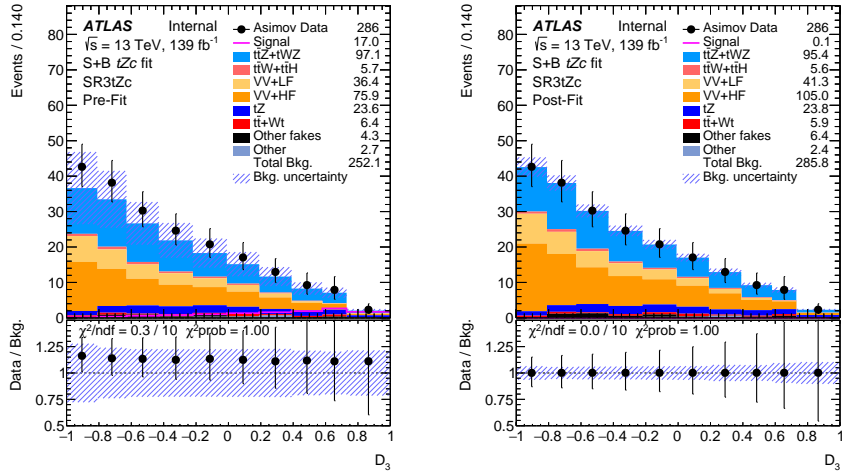


Figure H.9 – Pre-fit (left) and post-fit (right) leading lepton p_T distributions in SR3 for the S+B tZc fit in SRs+CRs with realistic Asimov. The uncertainty band includes both statistical and systematic uncertainties.

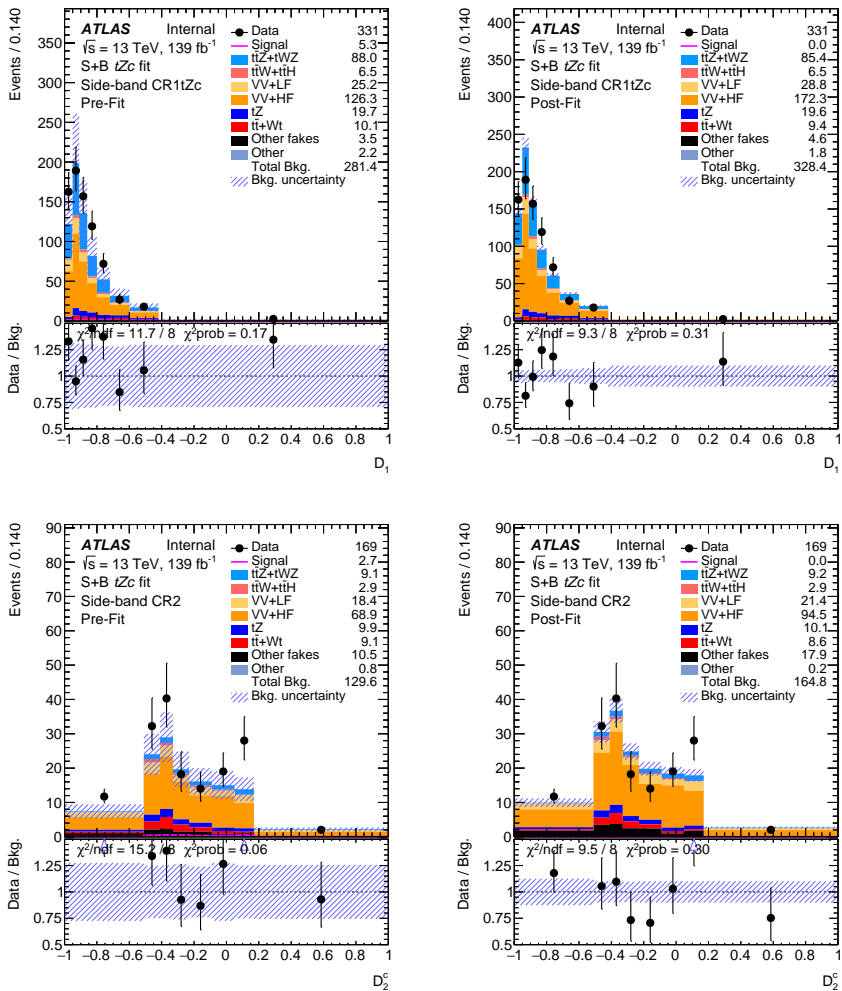


Figure H.10 – Pre-fit (left) and post-fit (right) BDTG output distributions in the side-band CRs for the S+B tZc fit in SRs+CRs with realistic Asimov. The uncertainty band includes both statistical and systematic uncertainties.

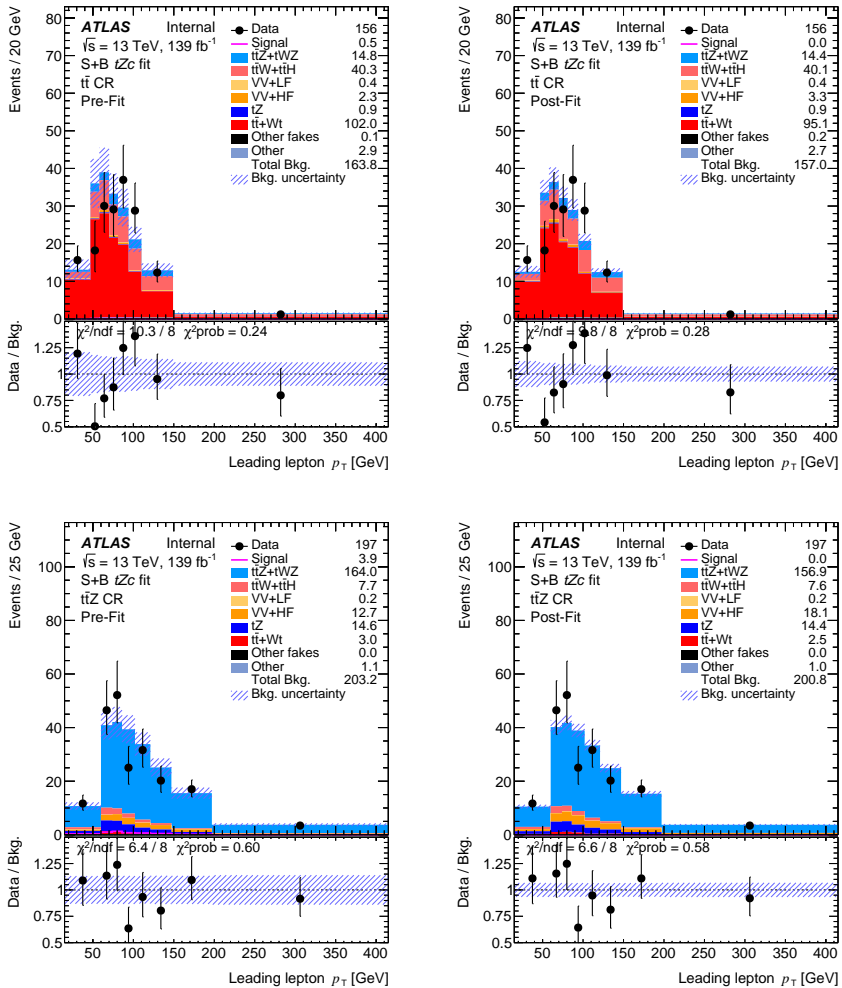


Figure H.11 – Pre-fit (left) and post-fit (right) leading lepton p_T distributions in the $t\bar{t}$ and $t\bar{t}Z$ CRs for the S+B $t\bar{t}Z$ fit in SRs+CRs with realistic Asimov. The uncertainty band includes both statistical and systematic uncertainties.

The expected limits, together with statistical only limits and the expected limits from the previous ATLAS analysis [28], are reported in Table H.3.

The overall impact of systematics on the expected limit is 24%.

The limit from the previous analysis is improved by a factor of 3.1 for the tZc coupling.

Limits	-1σ	Expected	$+1\sigma$
BR $t \rightarrow Zc$ [28]	2.2×10^{-4}	3.2×10^{-4}	4.6×10^{-4}
BR $t \rightarrow Zc$ (stat. only)	5.7×10^{-5}	7.9×10^{-5}	10.9×10^{-5}
BR $t \rightarrow Zc$	7.4×10^{-5}	10.4×10^{-5}	14.8×10^{-5}

Table H.3 – Expected limits on the branching ratios of $t \rightarrow Zc$ using SMT. Expected limit from [28] is also included for reference.

Background-only fit in SRs+CRs with unblinded data

The combined fit has been performed in the background control and signal regions with data under the Background-only hypothesis.

Plots and tables shown in this section are the following:

- The value of the post-fit normalisation parameter of the free floating background is shown in Figure I.1.
- The list of the systematic shapes that are dropped from the fit for each sample and for each region is shown in fig. I.2.
- The pull distributions of the all nuisance parameters can be seen in Figures I.3 and I.4 and Figure I.5.
- The correlation matrix of the nuisance parameters is shown in Figure I.6.
- Event yields pre- and post-fit are shown in Tables I.1 and I.2.
- Pre-fit and post-fit distributions of the fitted distributions in the various regions are shown in Figures I.7 to I.10.

The fake normalization factor $\mu_{t\bar{t}+Wt}$ (Figure I.1) is compatible with unity.

The value of the fitted nuisance parameters (Figures I.3 and I.4) are within their prior uncertainties, meaning that the data are well modelled with the MC predictions within the uncertainties. Concerning the correlations between NPs (Figure I.6), some strong correlations between diboson related NPs are present, as expected. This is also true for the $t\bar{t}$ normalisation and some $t\bar{t}$ modeling NPs. Event yields pre- and post-fit, shown in Tables I.1 and I.2 and distributions in Figures I.7 to I.10 show a good agreement between the observed data and MC predictions in Control and Signal Regions. No evidence for the FCNC $t \rightarrow Zc$ signal is found.

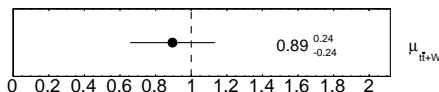


Figure I.1 – Normalisation factors for the B-only tZc fit in SRs+CRs with data.

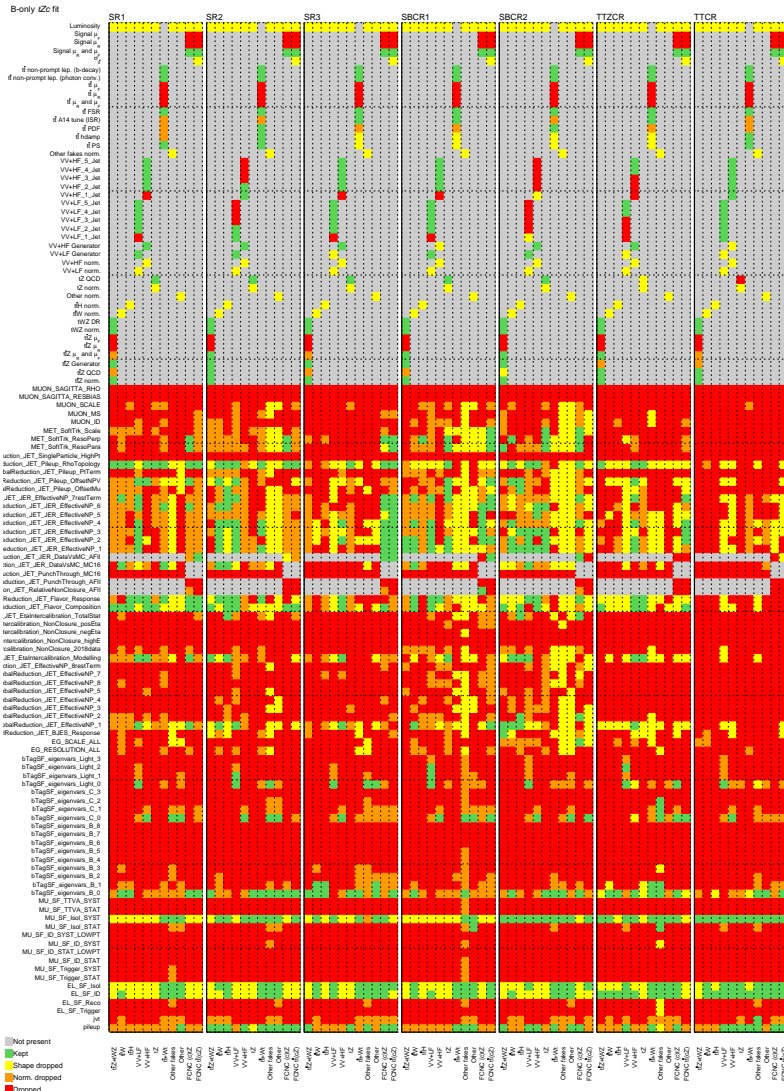


Figure I.2 – Pruning of the nuisance parameters for the B-only fit in SRs+CRs with data.

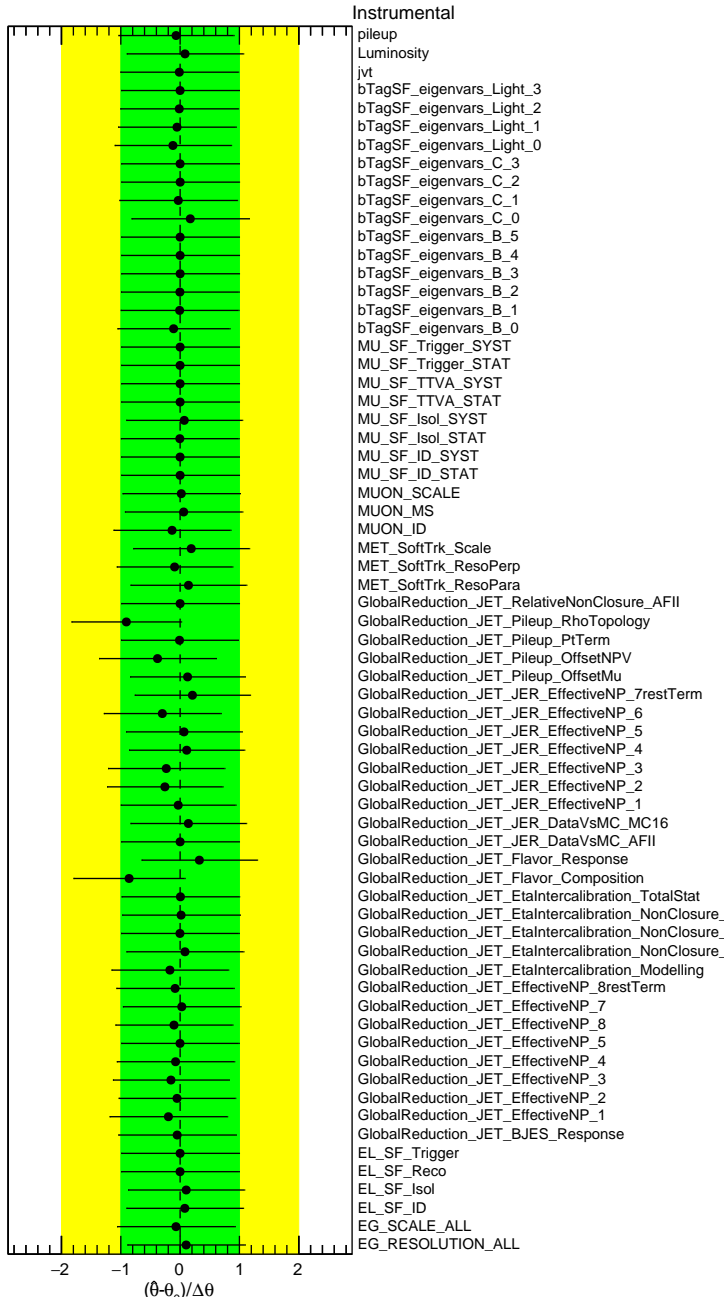


Figure I.3 – Pulls and constraints of the instrumental nuisance parameters for the B-only tZc fit in SRs+CRs with data.

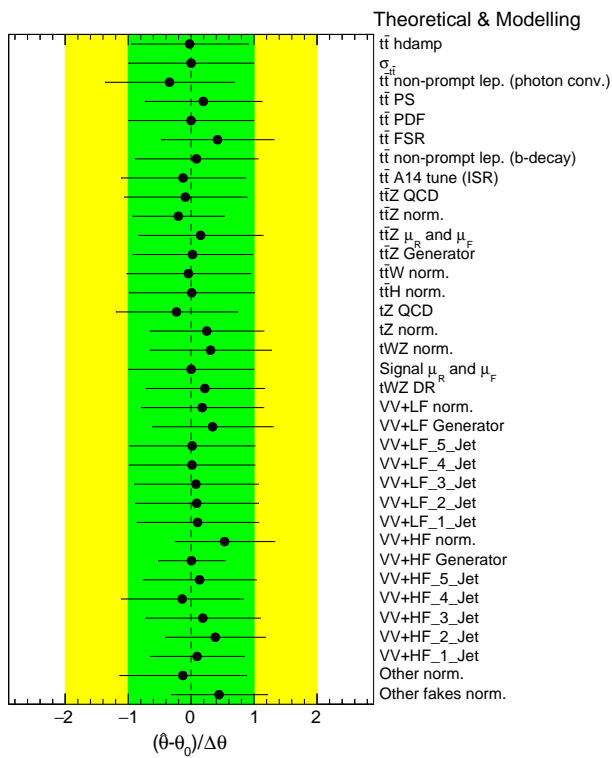


Figure I.4 – Pulls and constraints of the theoretical and modeling nuisance parameters for the B-only tZc fit in SRs+CRs with data.

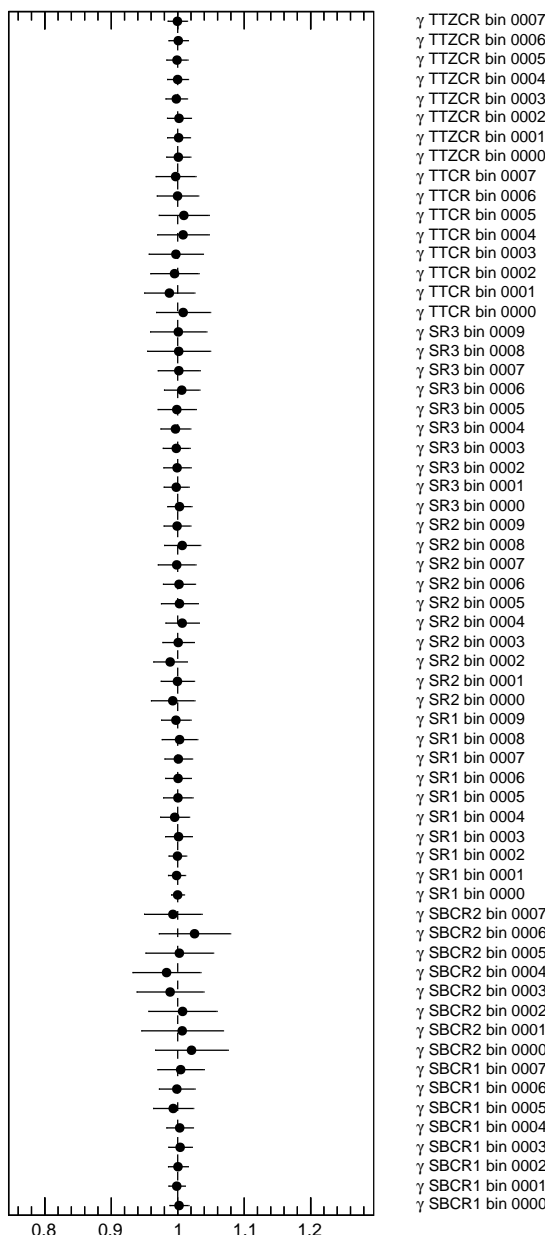


Figure I.5 – Gamma parameters for the B-only tZc fit in SRs+CRs with data.

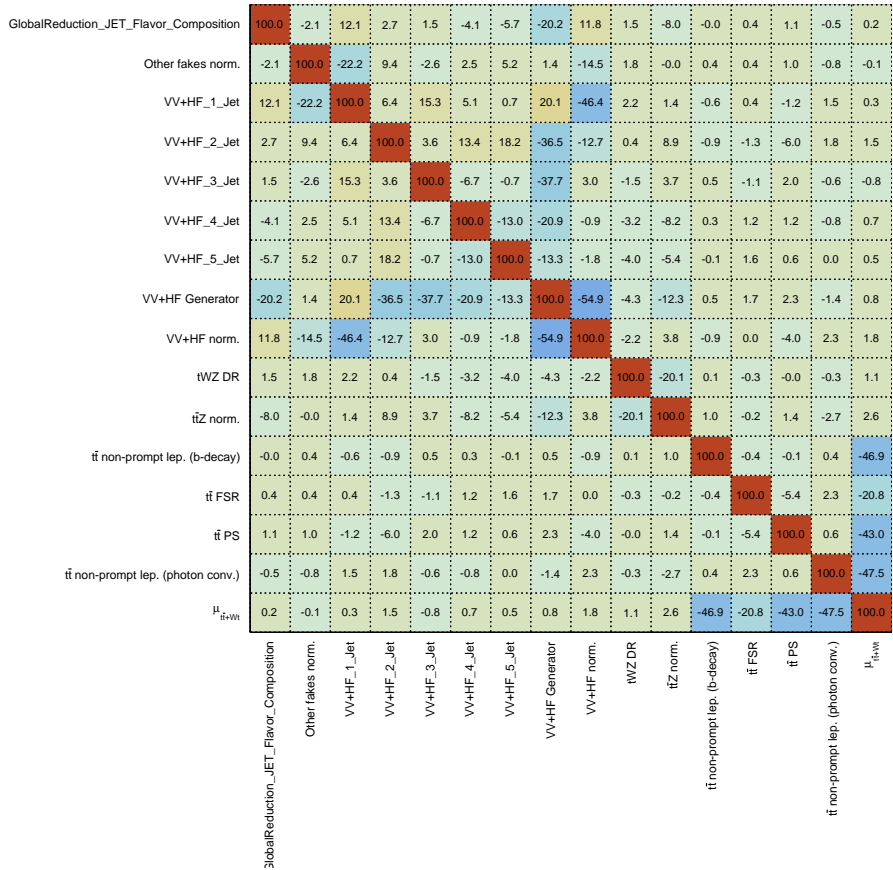


Figure I.6 – Correlation matrix of the nuisance parameters for the B-only tZc fit in SRS+CRS with data.

	SR1	SR2	SR3	Side-band CR1	Side-band CR2	t̄Z CR	t̄t CR
t̄Z +tWZ	168 ± 22	33 ± 7	82 ± 11	88 ± 12	9.1 ± 2.1	164 ± 22	14.8 ± 1.9
t̄tW	5.8 ± 1.0	3.3 ± 0.6	2.04 ± 0.35	4.3 ± 0.7	2.5 ± 0.5	2.3 ± 0.5	27 ± 4
t̄tH	6.1 ± 1.0	0.88 ± 0.18	2.6 ± 0.4	2.3 ± 0.4	0.36 ± 0.07	5.4 ± 0.9	13.8 ± 2.1
V V + LF	28 ± 17	35 ± 13	2.9 ± 2.0	25 ± 15	18 ± 7	0.20 ± 0.22	0.40 ± 0.21
V V + HF	140 ± 100	160 ± 70	30 ± 22	130 ± 80	69 ± 28	13 ± 11	2.3 ± 1.4
tZq	47 ± 7	110 ± 18	13.8 ± 2.3	20 ± 4	9.9 ± 1.7	14.6 ± 2.9	0.90 ± 0.15
t̄t +Wt	21 ± 4	32 ± 11	3.7 ± 1.0	10 ± 4	9.1 ± 2.7	3.0 ± 1.2	102 ± 24
Other fakes	10 ± 11	12 ± 12	1.4 ± 1.6	3 ± 5	10 ± 11	0.00 ± 0.06	0.12 ± 0.14
Other	2.5 ± 1.5	3.8 ± 2.8	0.48 ± 0.25	2.2 ± 1.6	0.8 ± 2.6	1.1 ± 0.5	2.9 ± 1.5
Total background	430 ± 110	390 ± 80	139 ± 25	280 ± 80	130 ± 32	203 ± 27	164 ± 25
Data	433	443	143	331	169	197	156
Data / Bkg.	1.00 ± 0.25	1.15 ± 0.24	1.03 ± 0.20	1.18 ± 0.35	1.30 ± 0.34	0.97 ± 0.14	0.95 ± 0.16

Table I.1 – Pre-fit event yields in the B-only tZc fit in SRs+CRs with data. The error includes both statistical and systematic uncertainties.

	SR1	SR2	SR3	Side-band CR1	Side-band CR2	t̄Z CR	t̄t CR
t̄Z +tWZ	166 ± 14	39 ± 7	82 ± 7	90 ± 9	10.5 ± 2.1	156 ± 13	15.0 ± 1.4
t̄tW	5.6 ± 0.9	3.6 ± 0.6	2.03 ± 0.32	4.0 ± 0.6	2.7 ± 0.5	2.0 ± 0.4	27 ± 4
t̄tH	5.9 ± 0.9	1.02 ± 0.20	2.6 ± 0.4	2.3 ± 0.4	0.42 ± 0.08	5.1 ± 0.8	14.0 ± 2.1
V V + LF	31 ± 18	37 ± 13	3.3 ± 2.1	30 ± 17	21 ± 8	0.20 ± 0.19	0.36 ± 0.17
V V + HF	162 ± 28	192 ± 29	35 ± 6	152 ± 24	85 ± 16	13 ± 5	2.7 ± 0.5
tZq	47 ± 6	120 ± 17	14.4 ± 2.1	20.2 ± 3.4	10.8 ± 1.6	14.2 ± 2.4	0.95 ± 0.12
t̄t +Wt	16.9 ± 3.1	32 ± 7	3.0 ± 0.6	10.0 ± 3.0	9.0 ± 1.7	2.2 ± 0.7	94 ± 13
Other fakes	13 ± 8	16 ± 10	2.0 ± 1.4	4 ± 4	23 ± 16	0.005 ± 0.008	0.17 ± 0.11
Other	1.9 ± 1.0	3.3 ± 2.2	0.44 ± 0.23	1.8 ± 1.2	0.3 ± 1.2	1.0 ± 0.5	2.7 ± 1.4
Total background	449 ± 17	444 ± 19	144 ± 6	315 ± 16	163 ± 13	194 ± 12	156 ± 12
Data	433	443	143	331	169	197	156
Data / Bkg.	0.96 ± 0.04	1.00 ± 0.04	0.99 ± 0.04	1.05 ± 0.05	1.04 ± 0.09	1.02 ± 0.06	1.00 ± 0.08

Table I.2 – Post-fit event yields in the B-only tZc fit in SRs+CRs with data. The error includes both statistical and systematic uncertainties.

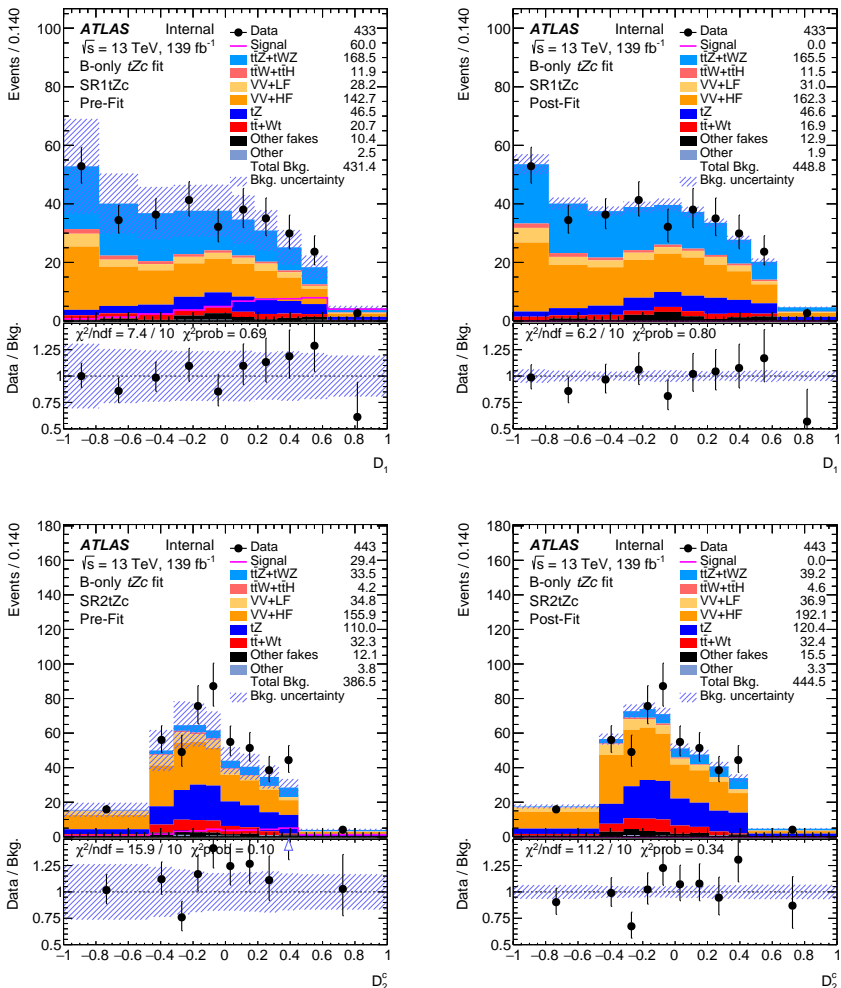


Figure I.7 – Pre-fit (left) and post-fit (right) BDTG output distributions in SR1 and SR2 for the B-only tZc fit in SRS+CRs with data. The uncertainty band includes both statistical and systematic uncertainties.

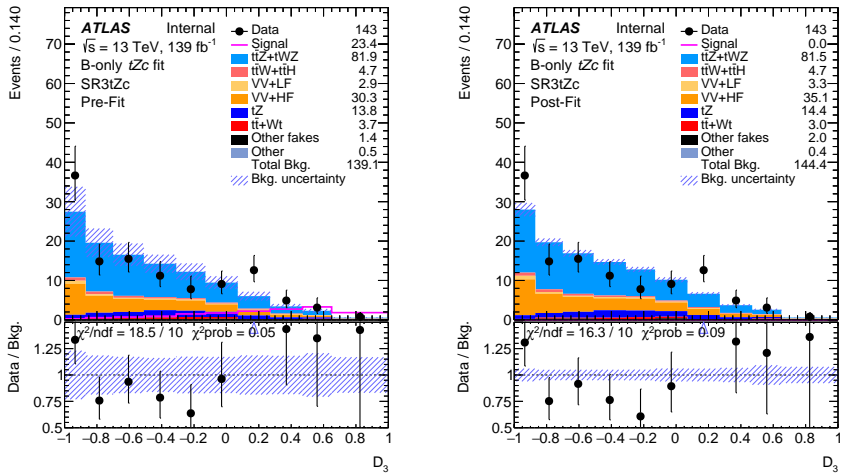


Figure I.8 – Pre-fit (left) and post-fit (right) leading lepton p_T distributions in SR3 for the B-only tZc fit in SRs+CRs with data. The uncertainty band includes both statistical and systematic uncertainties.

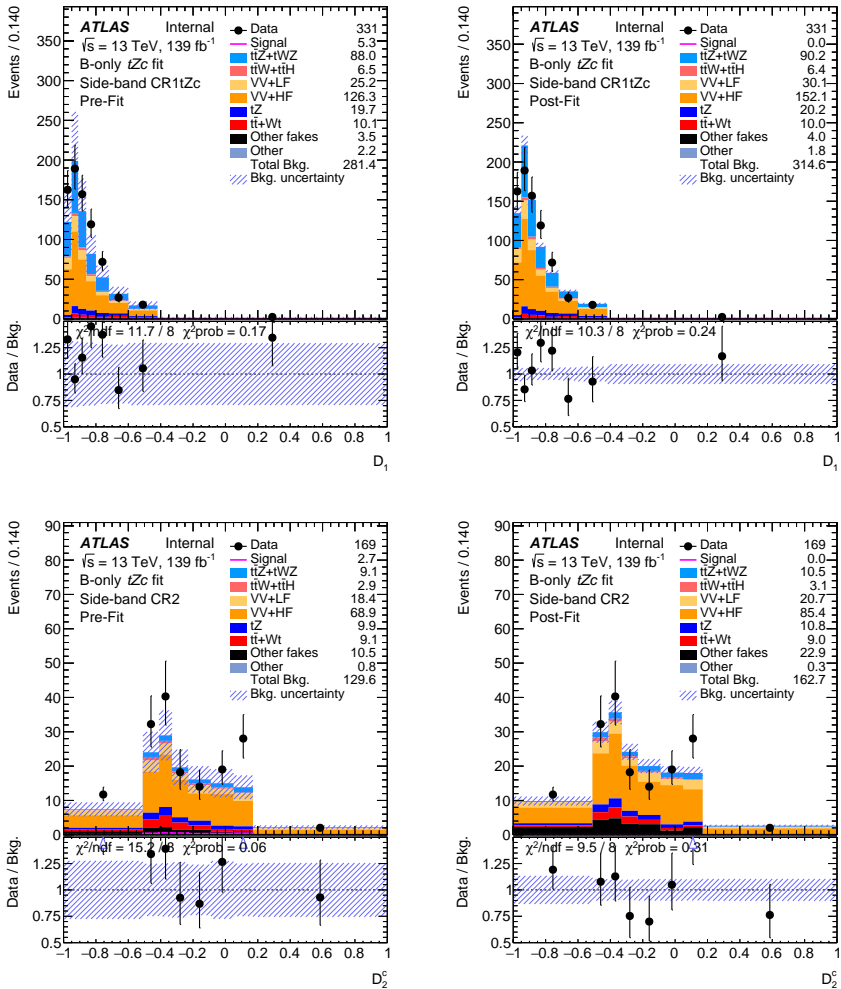


Figure I.9 – Pre-fit (left) and post-fit (right) BDTG output distributions in the side-band CRs for the B-only tZc fit in SRS+CRs with data. The uncertainty band includes both statistical and systematic uncertainties.

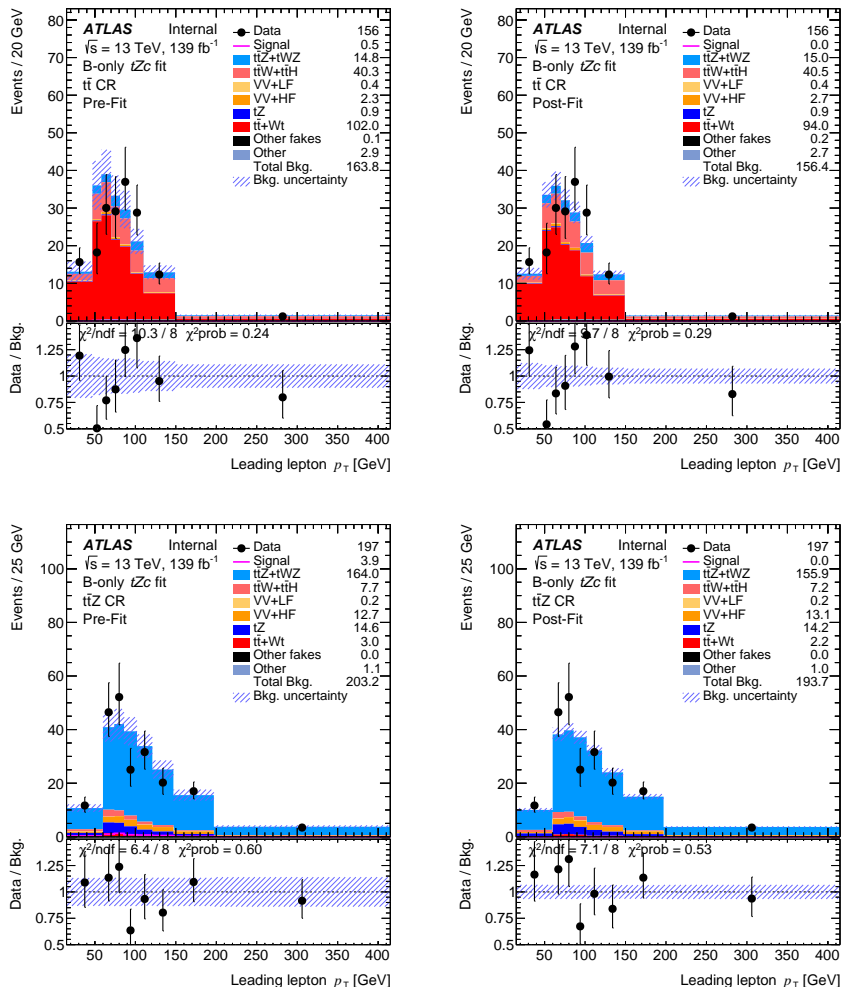


Figure I.10 – Pre-fit (left) and post-fit (right) leading lepton p_T distributions in the $t\bar{t}$ and $t\bar{t}Z$ CRs for the B-only tZc fit in SRs+CRs with data. The uncertainty band includes both statistical and systematic uncertainties.

From the likelihood fit under the Background-only hypothesis no evidence for the FCNC $t \rightarrow Zc$ signal is found but a good agreement between data and Standard Model is observed. In the absence of signal, the 95% CL upper limit is set on $\text{BR}(t \rightarrow Zc)$.

Figure I.11 shows the observed and expected CL_s as a function of $\text{BR}(t \rightarrow Zc)$.

The observed limit is $\text{BR}(t \rightarrow Zc) < 11.8 \times 10^{-5}$, inside the $\pm 1\sigma$ band of the expected limit: $\text{BR}(t \rightarrow Zc) < 9.5 \times 10^{-5}$.

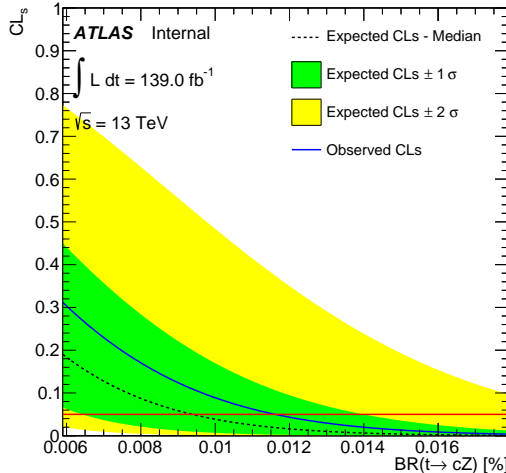


Figure I.11 – CL_s vs $\text{BR}(t \rightarrow Zc)$ plot. The median expected CL_s under the Background-only hypothesis (black dashed line) is displayed along with the ± 1 and ± 2 standard deviations bands (green and yellow, respectively). The solid red line at $\text{CL}_s = 0.05$ denotes the threshold below which the hypothesis is excluded at 95% CL.

BR ($t \rightarrow Zc$) [$\times 10^{-5}$]	
Observed	11.8
Expected -1σ	6.9
Expected	9.5
Expected $+1\sigma$	13.8

Table I.3 – Observed and expected 95% CL upper limits on the FCNC $t \rightarrow Zc$ branching ratio. The expected central value is shown together with the $\pm 1\sigma$ bands.

References

- [1] E. Fermi, *Il Nuovo Cimento* (1934) **11**, 1 (2008).
- [2] F. L. Wilson, *Am.J.Phys* **36**, 1150 (1968).
- [3] C. S. Wu, E. Ambler, R. W. Hayward, D. D. Hoppes, and R. P. Hudson, *Phys. Rev.* **105**, 1413 (1957).
- [4] P. Renton, *Electroweak Interactions: An Introduction to the Physics of Quarks and Leptons* (1990).
- [5] S. L. Glashow, J. Iliopoulos, and L. Maiani, *Phys. Rev. D* **2**, 1285 (1970).
- [6] J. Aguilar-Saavedra, “Top flavour-changing neutral interactions: theoretical expectations and experimental detection,” (2004), arXiv:hep-ph/0409342 [hep-ph].
- [7] N. Cabibbo, *Meeting of the Italian School of Physics and Weak Interactions Bologna, Italy, April 26-28, 1984*, *Phys. Rev. Lett.* **10**, 531 (1963).
- [8] M. Kobayashi and T. Maskawa, *Progress of Theoretical Physics* **49**, 652 (1973).
- [9] Z. Ligeti, *Int. J. Mod. Phys. A* **20**, 5105 (2005), arXiv:hep-ph/0408267 [hep-ph].
- [10] F. Abe *et al.* (CDF Collaboration), *Phys. Rev. Lett.* **74**, 2626 (1995).
- [11] S. Abachi *et al.* (D0 Collaboration), *Phys. Rev. Lett.* **74**, 2632 (1995).
- [12] R. Aaij *et al.* (LHCb Collaboration), *Phys. Rev. Lett.* **115**, 112001 (2015).
- [13] M. Tanabashi *et al.* (Particle Data Group), *Phys. Rev. D* **98**, 030001 (2018).
- [14] W. Bernreuther, *J. Phys. G* **35**, 083001 (2008), arXiv:0805.1333 [hep-ph].
- [15] D0 Collaboration website, “[Useful Diagrams of Top Signals and Backgrounds](#),” .
- [16] C. Patrignani *et al.* (ParticleDataGroup), *Phys. Rev. D* **98**, 030001. 1898 p (2018).
- [17] V. D. Barger, M. S. Berger, and R. J. N. Phillips, *Phys. Rev. D* **52**, 1663 (1995), arXiv:hep-ph/9503204 [hep-ph].

- [18] D. Atwood, L. Reina, and A. Soni, *Phys. Rev. D* **55**, 3156 (1997).
- [19] J. J. Cao, G. Eilam, M. Frank, K. Hikasa, G. L. Liu, I. Turan, and J. M. Yang, *Phys. Rev. D* **75**, 075021 (2007).
- [20] J. M. Yang, B.-L. Young, and X. Zhang, *Phys. Rev. D* **58**, 055001 (1998).
- [21] K. Agashe, G. Perez, and A. Soni, *Phys. Rev. D* **75**, 015002 (2007).
- [22] A. Heister *et al.* (ALEPH), *Phys. Lett. B* **543**, 173 (2002), arXiv:hep-ex/0206070 [hep-ex].
- [23] J. Abdallah *et al.* (DELPHI), *Phys. Lett. B* **590**, 21 (2004), arXiv:hep-ex/0404014 [hep-ex].
- [24] G. Abbiendi *et al.* (OPAL), *Phys. Lett. B* **521**, 181 (2001), arXiv:hep-ex/0110009 [hep-ex].
- [25] P. Achard *et al.* (L3), *Phys. Lett. B* **549**, 290 (2002), arXiv:hep-ex/0210041 [hep-ex].
- [26] H. Abramowicz *et al.* (ZEUS), *Phys. Lett. B* **708**, 27 (2012), arXiv:1111.3901 [hep-ex].
- [27] D0 Collaboration (D0), *Phys. Lett. B* **701**, 313 (2011), arXiv:1103.4574 [hep-ex].
- [28] ATLAS Collaboration, *JHEP* **07**, 176 (2018), arXiv:1803.09923 [hep-ex].
- [29] CMS Collaboration (CMS), *Phys. Rev. Lett.* **112**, 171802 (2014), arXiv:1312.4194 [hep-ex].
- [30] CMS Collaboration, *JHEP* **07**, 003 (2017), arXiv:1702.01404 [hep-ex].
- [31] M. Barros *et al.*, *Eur. Phys. J. Plus* **135**, 339 (2020).
- [32] G. Aad *et al.* (ATLAS), *Phys. Lett. B* **716**, 1 (2012), arXiv:1207.7214 [hep-ex].
- [33] F. Zwicky, *General Relativity and Gravitation* **41**, 207 (2009).
- [34] N. Aghanim *et al.* (Planck), (2018), arXiv:1807.06209 [astro-ph.CO].
- [35] J. A. Aguilar-Saavedra, *Acta Phys. Polon. B* **35**, 2695 (2004), arXiv:hep-ph/0409342 [hep-ph].
- [36] J. A. Aguilar-Saavedra, *Phys. Rev. D* **67**, 035003 (2003), arXiv:hep-ph/0210112 [hep-ph].
- [37] P. Hung, Y.-X. Lin, C. S. Nugroho, and T.-C. Yuan, *Nuclear Physics B* **927**, 166 (2018).
- [38] K. Agashe *et al.* (Top Quark Working Group) (2013) arXiv:1311.2028 [hep-ph].
- [39] Z. Maki, M. Nakagawa, and S. Sakata, *Prog. Theor. Phys.* **28**, 870 (1962).
- [40] G. C. Branco, P. M. Ferreira, L. Lavoura, M. N. Rebelo, M. Sher, and J. P. Silva, *Phys. Rept.* **516**, 1 (2012), arXiv:1106.0034 [hep-ph].
- [41] G. Couture, C. Hamzaoui, and H. König, *Phys. Rev. D* **52**, 1713 (1995).
- [42] L. Evans and P. Bryant, *Journal of Instrumentation* **3**, S08001 (2008).
- [43] E. Mobs, “The CERN accelerator complex - August 2018. Complexe des accélérateurs du CERN,”.
- [44] “LHC public plots,” *ATLAS Twiki*.
- [45] G. Aad *et al.* (ATLAS), *JINST* **3**, S08003 (2008).
- [46] The ATLAS collaboration, *ATLAS magnet system: Technical Design Report* (1997).

- [47] The ATLAS collaboration, *ATLAS liquid argon calorimeter: Technical Design Report* (1996).
- [48] The ATLAS collaboration, *ATLAS muon spectrometer : Technical Design Report* (1997).
- [49] The ATLAS collaboration, *ATLAS high-level trigger, data acquisition and controls: Technical Design Report* (2003).
- [50] “LHC upgrades and operation,” CERN Website.
- [51] *Technical Design Report for the Phase-II Upgrade of the ATLAS Muon Spectrometer*, Tech. Rep. CERN-LHCC-2017-017. ATLAS-TDR-026 (CERN, Geneva, 2017).
- [52] T. Kawamoto, S. Vlachos, L. Pontecorvo, J. Dubbert, G. Mikenberg, P. Iengo, C. Dallapiccola, C. Amelung, L. Levinson, R. Richter, and D. Leilouch, *New Small Wheel Technical Design Report*, Tech. Rep. CERN-LHCC-2013-006. ATLAS-TDR-020 (2013) aTLAS New Small Wheel Technical Design Report.
- [53] G. Aielli, C. Amelung, D. Boscherini, R. Cardarelli, M. Corradi, L. Han, V. Izzo, O. Kortner, H. Kroha, D. Levin, L. Massa, L. Paolozzi, R. Santonico, and R. Vari (ATLAS Collaboration), *The ATLAS BIS78 Project*, Tech. Rep. ATL-MUON-INT-2016-002 (CERN, Geneva, 2016).
- [54] ATLAS Collaboration (ATLAS), *muTrigNt_write code*, Tech. Rep.
- [55] ATLAS Collaboration (ATLAS), *Muon Upgrade Studies Twiki*, Tech. Rep.
- [56] L.Marcoccia, *Phase II Upgrade : High-eta tagger + RPC (Muon Week)*, Tech. Rep. (2018).
- [57] L. Marcoccia, *Efficiency studies on emulated RPC for the Phase-II Upgrade of the ATLAS Muon Spectrometer*, Tech. Rep. ATL-COM-MUON-2019-060 (CERN, Geneva, 2019).
- [58] B. Andersson, G. Gustafson, G. Ingelman, and T. Sjöstrand, *Physics Reports* **97**, 31 (1983).
- [59] G. Marchesini and B. Webber, *Nuclear Physics B* **238**, 1 (1984).
- [60] T. Sjöstrand, S. Mrenna, and P. Skands, *Journal of High Energy Physics* **2006**, 026 (2006).
- [61] M. Bähr, S. Gieseke, M. A. Gigg, D. Grellscheid, K. Hamilton, O. Latunde-Dada, S. Plätzer, P. Richardson, M. H. Seymour, A. Sherstnev, and B. R. Webber, *The European Physical Journal C* **58**, 639 (2008).
- [62] S. Agostinelli *et al.* (GEANT4), *Nucl. Instrum. Meth. A* **506**, 250 (2003).
- [63] E. Richter-Was, D. Froidevaux, and L. Poggioli, *ATLFAST 2.0 a fast simulation package for ATLAS*, Tech. Rep. ATL-PHYS-98-131 (CERN, Geneva, 1998).
- [64] ATLAS Collaboration, “Electron identification measurements in ATLAS using $\sqrt{s} = 13$ TeV data with 50 ns bunch spacing,” ATL-PHYS-PUB-2015-041 (2015).
- [65] ATLAS Collaboration, “Electron and photon energy calibration with the ATLAS detector using data collected in 2015 at $\sqrt{s} = 13$ TeV,” ATL-PHYS-PUB-2016-015 (2016).
- [66] ATLAS Collaboration, “Electron efficiency measurements with the ATLAS detector using the 2015 LHC proton–proton collision data,” ATLAS-CONF-2016-024 (2016).
- [67] ATLAS Collaboration, *Eur. Phys. J. C* **79**, 639 (2019), arXiv:1902.04655 [hep-ex].
- [68] ATLAS Collaboration, *Eur. Phys. J. C* **76**, 292 (2016), arXiv:1603.05598 [hep-ex].
- [69] ATLAS Collaboration, *Eur. Phys. J. C* **77**, 466 (2017), arXiv:1703.10485 [hep-ex].

- [70] ATLAS Collaboration, “Tagging and suppression of pileup jets with the ATLAS detector,” ATLAS-CONF-2014-018 (2014).
- [71] *Muon Combined Performance in Run 2 (25 ns runs)*, Tech. Rep. ATL-COM-MUON-2015-093 (Geneva, 2015).
- [72] *Calibration of the Soft Muon Tagger in Run-2 data*, Tech. Rep. ATL-COM-PHYS-2017-1110 (CERN, Geneva, 2017) updates to be expected.
- [73] *Optimisation and performance studies of the ATLAS b-tagging algorithms for the 2017-18 LHC run*, Tech. Rep. ATL-PHYS-PUB-2017-013 (CERN, Geneva, 2017).
- [74] G. Aad *et al.* (ATLAS), *Eur. Phys. J. C* **79**, 970 (2019), arXiv:1907.05120 [hep-ex].
- [75] F. Chollet *et al.*, “Keras,” <https://keras.io>.
- [76] T. T. D. Team *et al.*, “Theano: A python framework for fast computation of mathematical expressions,” (2016), arXiv:1605.02688 [cs.SC].
- [77] D. P. Kingma and J. Ba, “Adam: A method for stochastic optimization,” (2017), arXiv:1412.6980 [cs.LG].
- [78] I. J. Goodfellow, D. Warde-Farley, M. Mirza, A. Courville, and Y. Bengio, “Maxout networks,” (2013), arXiv:1302.4389 [stat.ML].
- [79] ATLAS Collaboration, “tc+MET: charm tagger definition.”
- [80] G. Aad *et al.* (ATLAS), *Eur. Phys. J. C* **77**, 241 (2017), arXiv:1609.09324 [hep-ex].
- [81] A. Collaboration, *The European Physical Journal C* **77**, 241 (2017).
- [82] ATLAS Collaboration, *Eur. Phys. J. C* **72**, 1844 (2012), arXiv:1108.5602 [hep-ex].
- [83] ATLAS Collaboration, *Eur. Phys. J. C* **77**, 241 (2017), arXiv:1609.09324 [hep-ex].
- [84] ATLAS Collaboration, “Performance of missing transverse momentum reconstruction with the ATLAS detector in the first proton–proton collisions at $\sqrt{s} = 13$ TeV,” ATL-PHYS-PUB-2015-027 (2015).
- [85] D. Adams *et al.*, *Recommendations of the Physics Objects and Analysis Harmonisation Study Groups 2014*, Tech. Rep. ATL-PHYS-INT-2014-018 (CERN, Geneva, 2014).
- [86] “Associationutils,” <https://svnweb.cern.ch>.
- [87] TopWG Blinding Guidelines, “<https://twiki.cern.ch>,” .
- [88] I. Antcheva *et al.*, *Comput. Phys. Commun.* **180**, 2499 (2009), arXiv:1508.07749 [physics.data-an].
- [89] TOPQ derivations, “<https://twiki.cern.ch>,” .
- [90] ATLAS Collaboration, *Eur. Phys. J. C* **77**, 317 (2017), arXiv:1611.09661 [hep-ex].
- [91] ATLAS Collaboration, “2015 start-up trigger menu and initial performance assessment of the ATLAS trigger using Run-2 data,” ATL-DAQ-PUB-2016-001 (2016).
- [92] ATLAS Collaboration, “Trigger Menu in 2016,” ATL-DAQ-PUB-2017-001 (2017).
- [93] ATLAS Collaboration, “Trigger Menu in 2017,” ATL-DAQ-PUB-2018-002 (2018).

- [94] J. Alwall, R. Frederix, S. Frixione, V. Hirschi, F. Maltoni, O. Mattelaer, H. S. Shao, T. Stelzer, P. Torrielli, and M. Zaro, *JHEP* **07**, 079 (2014), arXiv:1405.0301 [hep-ph].
- [95] T. Sjostrand, S. Mrenna, and P. Z. Skands, *Comput. Phys. Commun.* **178**, 852 (2008), arXiv:0710.3820 [hep-ph].
- [96] P. Z. Skands, *Phys. Rev.* **D82**, 074018 (2010), arXiv:1005.3457 [hep-ph].
- [97] A. Alloul, N. D. Christensen, C. Degrande, C. Duhr, and B. Fuks, *Comput. Phys. Commun.* **185**, 2250 (2014), arXiv:1310.1921 [hep-ph].
- [98] C. Degrande, F. Maltoni, J. Wang, and C. Zhang, *Phys. Rev.* **D91**, 034024 (2015), arXiv:1412.5594 [hep-ph].
- [99] G. Durieux, F. Maltoni, and C. Zhang, *Phys. Rev.* **D91**, 074017 (2015), arXiv:1412.7166 [hep-ph].
- [100] M. Beneke, P. Falgari, S. Klein, and C. Schwinn, *Nucl. Phys. B* **855**, 695 (2012), arXiv:1109.1536 [hep-ph].
- [101] M. Cacciari, M. Czakon, M. Mangano, A. Mitov, and P. Nason, *Phys. Lett. B* **710**, 612 (2012), arXiv:1111.5869 [hep-ph].
- [102] P. Bärnreuther, M. Czakon, and A. Mitov, *Phys. Rev. Lett.* **109**, 132001 (2012), arXiv:1204.5201 [hep-ph].
- [103] M. Czakon and A. Mitov, *JHEP* **12**, 054 (2012), arXiv:1207.0236 [hep-ph].
- [104] M. Czakon and A. Mitov, *JHEP* **01**, 080 (2013), arXiv:1210.6832 [hep-ph].
- [105] M. Czakon, P. Fiedler, and A. Mitov, *Phys. Rev. Lett.* **110**, 252004 (2013), arXiv:1303.6254 [hep-ph].
- [106] M. Czakon and A. Mitov, *Comput. Phys. Commun.* **185**, 2930 (2014), arXiv:1112.5675 [hep-ph].
- [107] M. Botje *et al.*, (2011), arXiv:1101.0538 [hep-ph].
- [108] A. D. Martin, W. J. Stirling, R. S. Thorne, and G. Watt, *Eur. Phys. J. C* **63**, 189 (2009), arXiv:0901.0002 [hep-ph].
- [109] A. D. Martin, W. Stirling, R. Thorne, and G. Watt, *Eur. Phys. J. C* **64**, 653 (2009), arXiv:0905.3531 [hep-ph].
- [110] H.-L. Lai, M. Guzzi, J. Huston, Z. Li, P. M. Nadolsky, *et al.*, *Phys. Rev.* **D82**, 074024 (2010), arXiv:1007.2241 [hep-ph].
- [111] J. Gao, M. Guzzi, J. Huston, H.-L. Lai, Z. Li, *et al.*, *Phys. Rev. D* **89**, 033009 (2014), arXiv:1302.6246 [hep-ph].
- [112] R. D. Ball *et al.*, *Nucl. Phys. B* **867**, 244 (2013), arXiv:1207.1303 [hep-ph].
- [113] S. Frixione, P. Nason, and G. Ridolfi, *JHEP* **09**, 126 (2007), arXiv:0707.3088 [hep-ph].
- [114] P. Nason, *JHEP* **11**, 040 (2004), arXiv:hep-ph/0409146.
- [115] S. Frixione, P. Nason, and C. Oleari, *JHEP* **0711**, 070 (2007), arXiv:0709.2092 [hep-ph].
- [116] S. Alioli, P. Nason, C. Oleari, and E. Re, *JHEP* **06**, 043 (2010), arXiv:1002.2581 [hep-ph].
- [117] NNPDF Collaboration, R.D. Ball et al. (NNPDF), *JHEP* **04**, 040 (2015), arXiv:1410.8849 [hep-ph].

- [118] ATLAS Collaboration, “Studies on top-quark Monte Carlo modelling for Top2016,” ATL-PHYS-PUB-2016-020 (2016).
- [119] T. Sjöstrand, S. Ask, J. R. Christiansen, R. Corke, N. Desai, P. Ilten, S. Mrenna, S. Prestel, C. O. Rasmussen, and P. Z. Skands, *Comput. Phys. Commun.* **191**, 159 (2015), arXiv:1410.3012 [hep-ph].
- [120] ATLAS Collaboration, “ATLAS Pythia 8 tunes to 7 TeV data,” ATL-PHYS-PUB-2014-021 (2014).
- [121] D. J. Lange, *Nucl. Instrum. Meth. A* **462**, 152 (2001).
- [122] M. Bahr *et al.*, *Eur. Phys. J. C* **58**, 639 (2008), arXiv:0803.0883 [hep-ph].
- [123] J. Bellm *et al.*, *Eur. Phys. J. C* **76**, 196 (2016), arXiv:1512.01178 [hep-ph].
- [124] L. Harland-Lang, A. Martin, P. Motylinski, and R. Thorne, *Eur. Phys. J. C* **75**, 204 (2015), arXiv:1412.3989 [hep-ph].
- [125] E. Bothmann *et al.*, (2019), arXiv:1905.09127 [hep-ph].
- [126] S. Catani, F. Krauss, R. Kuhn, and B. R. Webber, *JHEP* **11**, 063 (2001), arXiv:hep-ph/0109231.
- [127] S. Höche, F. Krauss, S. Schumann, and F. Siegert, *JHEP* **05**, 053 (2009), arXiv:0903.1219 [hep-ph].
- [128] E. Re, *Eur. Phys. J. C* **71**, 1547 (2011), arXiv:1009.2450 [hep-ph].
- [129] S. Frixione, E. Laenen, P. Motylinski, B. R. Webber, and C. D. White, *JHEP* **07**, 029 (2008), arXiv:0805.3067 [hep-ph].
- [130] T. Gleisberg and S. Höche, *JHEP* **12**, 039 (2008), arXiv:0808.3674 [hep-ph].
- [131] S. Schumann and F. Krauss, *JHEP* **03**, 038 (2008), arXiv:0709.1027 [hep-ph].
- [132] S. Höche, F. Krauss, M. Schönherr, and F. Siegert, *JHEP* **09**, 049 (2012), arXiv:1111.1220 [hep-ph].
- [133] S. Höche, F. Krauss, M. Schönherr, and F. Siegert, *JHEP* **04**, 027 (2013), arXiv:1207.5030 [hep-ph].
- [134] F. Cascioli, P. Maierhofer, and S. Pozzorini, *Phys. Rev. Lett.* **108**, 111601 (2012), arXiv:1111.5206 [hep-ph].
- [135] A. Denner, S. Dittmaier, and L. Hofer, *Comput. Phys. Commun.* **212**, 220 (2017), arXiv:1604.06792 [hep-ph].
- [136] P. Nason and G. Zanderighi, *Eur. Phys. J. C* **74**, 2702 (2014), arXiv:1311.1365 [hep-ph].
- [137] ATLAS Collaboration, *JHEP* **09**, 145 (2014), arXiv:1406.3660 [hep-ex].
- [138] J. Pumplin, D. Stump, J. Huston, H. Lai, P. M. Nadolsky, *et al.*, *JHEP* **0207**, 012 (2002), arXiv:hep-ph/0201195 [hep-ph].
- [139] S. Alioli, P. Nason, C. Oleari, and E. Re, *JHEP* **07**, 060 (2008), arXiv:0805.4802 [hep-ph].
- [140] P. Golonka and Z. Was, *Eur. Phys. J. C* **45**, 97 (2006), arXiv:hep-ph/0506026.
- [141] N. Davidson, T. Przedzinski, and Z. Was, *Comput. Phys. Commun.* **199**, 86 (2016), arXiv:1011.0937 [hep-ph].
- [142] D. J. Lange, *Proceedings, 7th International Conference on B physics at hadron machines (BEAUTY 2000): Maagan, Israel, September 13–18, 2000*, *Nucl. Instrum. Meth. A* **462**, 152 (2001).

- [143] H. B. Hartanto, B. Jäger, L. Reina, and D. Wackerlo, *Phys. Rev. D* **91**, 094003 (2015), arXiv:1501.04498 [hep-ph].
- [144] A. D. Buzin, “Fitting function for asymmetric peaks,” (2007), arXiv:0711.4449 [physics.data-an].
- [145] J. Friedman, “Stochastic gradient boosting,” (2002), 367 pp.
- [146] A. Hoecker *et al.*, “TMVA - Toolkit for Multivariate Data Analysis,” (2007), arXiv:physics/0703039 [physics.data-an].
- [147] ATLAS Collaboration, *Eur. Phys. J. C* **74**, 3071 (2014), arXiv:1407.5063 [hep-ex].
- [148] ATLAS Collaboration, *Phys. Rev. D* **96**, 072002 (2017), arXiv:1703.09665 [hep-ex].
- [149] ATLAS Collaboration, “Calibration of the performance of b -tagging for c and light-flavour jets in the 2012 ATLAS data,” ATLAS-CONF-2014-046 (2014).
- [150] ATLAS Collaboration, “Calibration of b -tagging using dileptonic top pair events in a combinatorial likelihood approach with the ATLAS experiment,” ATLAS-CONF-2014-004 (2014).
- [151] D. de Florian, C. Grojean, F. Maltoni, C. Mariotti, *et al.*, (2016), arXiv:1610.07922 [hep-ph].
- [152] O. Bessidskaia Bylund (ATLAS), in *9th International Workshop on Top Quark Physics* (2016) arXiv:1612.00440 [hep-ph].
- [153] G. Aad *et al.* (ATLAS), *JHEP* **07**, 124 (2020), arXiv:2002.07546 [hep-ex].
- [154] ATLAS Collaboration, *Eur. Phys. J. C* **79**, 535 (2019), arXiv:1902.05759 [hep-ex].
- [155] F. Demartin, B. Maier, F. Maltoni, K. Mawatari, and M. Zaro, *Eur. Phys. J. C* **77**, 34 (2017), arXiv:1607.05862 [hep-ph].
- [156] ATLAS Collaboration, *Eur. Phys. J. C* **76**, 653 (2016), arXiv:1608.03953 [hep-ex].
- [157] “Trexitter,” <https://twiki.cern.ch/twiki/bin/viewauth/AtlasProtected/TtHFitter>.
- [158] W. Verkerke and D. P. Kirkby, eConf **C0303241**, MOLT007 (2003), arXiv:physics/0306116 [physics].
- [159] L. Moneta, K. Belasco, K. S. Cranmer, S. Kreiss, A. Lazzaro, *et al.*, PoS **ACAT2010**, 057 (2010), arXiv:1009.1003 [physics.data-an].
- [160] T. Junk, *Nucl. Instrum. Meth. A* **434**, 435 (1999), arXiv:hep-ex/9902006 [hep-ex].
- [161] A. L. Read, *Advanced Statistical Techniques in Particle Physics. Proceedings, Conference, Durham, UK, March 18–22, 2002*, *J. Phys. G* **28**, 2693 (2002), [,11(2002)].
- [162] ATLAS Collaboration, (2020), arXiv:2002.07546 [hep-ex].